Al-Farabi Kazakh National University

UDC 547.9(043.3) Manuscript rights

AHMAD IZAZ

Using advanced spectroscopic, and chromatographic techniques to study the biotransformation of steroidal drugs, and phytochemical constituents of *Tussilago farfara* L.

8D05301 – Chemistry

Thesis submitted in fulfillment of the requirements for the degree of
Doctor of Philosophy (PhD)

Scientific supervisors:

PhD., Associate Professor Kudaibergenova Bates Malikovna

Dr., Professor Muhammad Iqbal Choudhary

The Republic of Kazakhstan
Almaty, 2026

TABLE OF CONTENTS

NORMATIVE REFERENCES 5
LIST OF SYMBOLS AND ABBREVIATIONS 6
INTRODUCTION 9
1 Literature review 16
1.1 Overview of natural products 16
1.2 Natural products and drug discovery 16
1.3 Current advancements in natural products research 17
1.4 Traditional medicine systems 17
1.5 Challenges and new approaches in natural products research 18
1.6 Family Asteraceae, genus and species 18
1.6.1 Traditional uses of *Tussilago farfara* L 19
1.6.1.1 Phytochemistry 21
1.7 Pharmacological application 22
1.8 Biotransformation 27
1.8.1 Historical background 28
1.8.2 Agents of biotransformation 29
1.8.3 Process-driven use of biotransformation techniques 29
1.8.4 Significance and application of biocatalysis 30
1.8.5 Challenges in microbial transformation 31
1.8.6 Microbial transformation of steroids 31
2 Using advanced spectroscopic, and chromatographic techniques to study the phytochemical constituents of *Tussilago farfara* L 35
2.1 Introduction 35
2.2 Experimental 36
2.2.1 General experimental conditions 36
2.2.2 Instrumental methods for structural characterization 36
2.2.3 Chromatographic techniques 37
2.2.4 Ultra-performance liquid chromatography 37
2.2.5 Plant materials 37
2.2.6 Extraction procedure 38
2.2.7 Isolation and purification 39
2.2.8 Spectroscopic and spectrometric data of isolated compounds 42
2.2.9 Enzyme inhibition studies 48
2.2.9.1 Antileishmanial activity 48
2.2.9.1.1 *Leishmania major* Pteridine reductase 1 (*Lm*PTR-1) inhibitory assay 48
2.2.10 *In silico* studies 49
2.2.10.1 Molecular docking 49

2.2.10.2 Molecular dynamics (MD) simulations 49
2.3 Results and discussion 50
2.3.1 Optimization of UPLC 51
2.3.2 Structural elucidation 54
2.3.3 Enzyme expression and inhibition studies 73
2.3.4 *In silico* studies 78
2.3.4.1 Molecular docking 78
2.3.4.2 Molecular dynamics simulations 81
2.3.5 Structure – activity relationship (SAR) 84
2.4 Summary 84
2.5 Using advanced spectroscopic, and chromatographic techniques to study the biotransformation of steroidal drug methylprednisolone acetate via *Fusarium oxysporum* and *Penicillium chrysogenum* 86
2.6 Introduction 86
2.7 Experimental 87
2.7.1 Instrumental methods for structural characterization 87
2.7.2 Reagents and materials 88
2.7.3 Ultra performance liquid chromatography 88
2.7.4 Detection of compounds 89
2.7.5 Microbial cultures 89
2.7.5.1 Preparation of fungal cell culture and media 89
2.7.5.2 Fermentation and purification protocol with *Fusarium oxysporum* 91
and *Penicillium chrysogenum* 91
2.7.6 Isolation and purification 91
2.7.7 Spectroscopic and spectrometric data of isolated metabolites 94
2.7.8 *In vitro* studies 97
2.7.8.1 Aromatase inhibition assay 97
2.7.9 *In silico* studies 97
2.7.9.1 Ligand preparation 97
2.7.9.2 Protein preparation 98
2.7.9.3 Molecular docking studies 98
2.7.9.4 MM-GBSA tool for binding energy estimation 98
2.8 Results and discussion 99
2.8.1 Optimization of UPLC system 99
2.8.2 Structural elucidation 100
2.8.2.1 Proposed mechanism for synthesis of metabolite 2 105
2.8.3 *In vitro* aromatase inhibition assay 115
2.8.4 *In silico* studies 116
2.8.4.1 Molecular docking 116
2.8.5 Correlation between aromatase inhibition and molecular docking 120

2.8.6 Correlation between docking scores and binding energies 121
2.8.7 Structure–activity relationship (SAR) 122
2.9 Summary 122
3 Conclusion 124
REFERENCES 126

NORMATIVE REFERENCES

The following standards are referenced in this dissertation:

STSD 6709-72 — Distilled water. Technical conditions.

STSD 31460-2012 — Medicinal products. Ointments.

STSD 23932-90 — Laboratory glassware and equipment. General technical conditions.

STSD 1770-74 — Measuring laboratory glassware (Cylinders, beakers, flasks, test tubes). General technical conditions.

STSD 9147-80 — Porcelain tableware and laboratory equipment. Technical conditions.

STSD 10749.1-80 — Technical ethyl alcohol. Method for determining appearance.

STSD 24104-2001 — Laboratory scales.

STSD 28115-89 (ST SEV 6347-88) — Drying apparatuses and installations.

STSD R 56327-2014 — Medical electrical products. expert class Ultrasonic devices.

LIST OF SYMBOLS AND ABBREVIATIONS

The following abbreviations were used in the present study

Abbreviations	**Full Name**
TLC	Thin-layer chromatography
t_R	Retention time
CC	Column chromatography
HPLC	High performance liquid chromatography
UPLC	Ultra-performance liquid chromatography
GC	Gas chromatography
GC-MS	Gas chromatography-mass spectrometry
LC-MS	Liquid chromatography-mass spectrometry
BuOH	Butanol
$CHCl_3$	Chloroform
$CDCl_3$	Deuterated chloroform
EtOAc	Ethyl acetate
MeOH	Methanol
DCM	Dichloromethane
RI	Retention index
UV	Ultraviolet spectroscopy
Prep TLC	Preparative thin-layer chromatography
FT-IR	Fourier-transform infrared spectroscopy
EI	Electron ionization
1D-NMR	One-dimensional nuclear magnetic resonance spectroscopy
^{1}H-NMR	Proton nuclear magnetic resonance spectroscopy
2D-NMR	Two-dimensional nuclear magnetic resonance spectroscopy
COSY	Correlation spectroscopy
DEPT	Distortionless enhancement by polarization transfer
HMBC	Heteronuclear multiple bond correlation
HMQC	Heteronuclear multiple quantum correlation
ROESY	Rotating-frame Overhauser effect spectroscopy
NOESY	Nuclear Overhauser enhancement spectroscopy
NOE	Nuclear Overhauser effect
s	Singlet
br s	Broad singlet
d	Doublet
dd	Doublet of doublet
dt	Doublet of triplet
t	Triplet
q	Quartet

m	Multiplet
ppm	Parts per million
MHz	Megahertz
J value	Coupling constant
MS	Mass spectrometry
EI-MS	Electron ionization-mass spectrometry
HREI-MS	High-resolution electron ionization mass spectrometry
ESI-MS	Electrospray ionization-mass spectrometry
HRESI-MS	High-resolution electrospray ionization mass spectrometry
FAB-MS	Fast atom bombardment-mass spectrometry
m/z	Mass to charge ratio
Mol. Formula	Molecular formula
M. Weight	Molecular weight
Calcd	Calculated
WHO	World Health Organization
DMSO	Dimethyl sulfoxide
D_2O	Deuterium oxide
Ar	Aromatic
NA	Not active
NADPH	Nicotinamide adenine dinucleotide phosphate
SAR	Structure-activity relationship
IC_{50}	Half-maximal inhibitory concentration
MM-GBSA	Molecular Mechanics-Generalized Born with Surface Area solvation
MD	Molecular dynamics
*Lm*PTR-1	*Leishmania major* pteridine reductase-1
TRAIL	Tumor necrosis factor-related apoptosis-inducing ligand
RD cells	Rhabdomyosarcoma cell line
FMO	Flavin-containing monooxygenase
CYP	Cytochrome P450
SP	Standard precision
NTD	Neglected tropical diseases
µL	Microliter
µM	Micromolar
nM	Nanomolar
ns	Nanosecond
MIP	Molecularly imprinting polymer
TCM	Traditional Chinese Medicine
TKM	Traditional Korean Medicine
CZE	Capillary zone electrophoresis

Au	Gold
Ag	Silver
ARG	Arginine
MET	Methionine
PHE	Phenylalanine
CYS	Cysteine
GLY	Glycine
ALA	Alanine

INTRODUCTION

General description of the work. This Ph.D. dissertation focuses on the phytochemical investigation of *Tussilago farfara* L., and the biotransformation of selected steroidal substrate using modern spectroscopic (NMR, MS, FTIR, UV) and chromatographic (HPLC, UPLC) techniques to separate, identify, and evaluate the biological activity of both natural, and biotransformed compounds.

The study integrates to explore the phytochemical constituents of *Tussilago farfara* L. leading to the isolation of the twenty secondary metabolites, three of them (1, 14 and 20) are reported for the first time from this species. These compounds were examined for their ability to inhibit Pteridine Reductase-1 (PTR-1), a crucial *Leishmania* enzyme. Compounds 15–18 showed moderate PTR-1 inhibitory activity and favorable binding interactions, as supported by *in silico* study.

The study further investigates the *Fusarium oxysporum* and *Penicillium chrysogenum* for the microbial transformation of the selected steroidal substrate methylprednisolone acetate, yielding one new metabolite (2), and seven (3–9) known metabolites. Structural elucidation of these compounds was carried out using, NMR, MS, and FT-IR techniques. All metabolites (2–9) exhibited promising aromatase inhibitory activity than the standard drug exemestane under the assay conditions employed.

Relevance of the research work

Tussilago farfara or coltsfoot, is a medicinal plant that provides a sustainable, and environmentally friendly pathway for therapeutic research. *T. farfara* has more than 180 identified compounds which include phenolic acids, alkaloids, flavonoids, terpenoids, chromones, and volatile oils, many of which have been demonstrated to have anti-inflammatory, antioxidant, antiviral activities, and neuroprotective *etc*.

Therefore, the study of *T. farfara* provides a natural, renewable source of bioactive compounds, while microbial biotransformation of selected steroidal substrates represents a complementary strategy. Both strategies work together to promote the worldwide movement toward low-impact pharmaceutical manufacturing, sustainable drug discovery, and green chemistry.

Microbial biotransformation is becoming an increasingly important approach in current biotechnology, and drug development. It employs living organisms such as fungi, bacteria, and plant cell cultures to structurally modify complex organic compounds, including multifunctional, chiral, and inert compounds, typically in an aqueous medium, making the process cost-effective, and scalable.

Furthermore, this approach provides excellent enantio-, chemo-, stereo-, and regio-selectivity, enabling accurate molecular modifications. In addition, it adheres to the principle of green chemistry, resulting in minimal or non-toxic waste.

Consequently, this approach has an important in various industries, including pharmaceuticals, agriculture, food, and environmental management.

As the demand for eco-friendly, sustainable medication development rises, microbial transformation emerges as a crucial technique to develop biologically active compounds, particularly steroidal drugs, in a cost-effective, and environmentally friendly approach.

The aim of this study is to employ advanced spectroscopic and chromatographic techniques to investigate the phytochemical constituents of *Tussilago farfara* L. to explore the microbial biotransformation of selected steroidal substrate using fungal systems in a cost-effective and environmentally sustainable manner, and to evaluate the biological activities of the isolated phytochemicals and the resulting biotransformed derivatives.

The following tasks were set to accomplish the aim of the study:

1. to investigate and select the medicinal plant *Tussilago farfara* L., and the fungal strains *Fusarium oxysporum* and *Penicillium chrysogenum* relevant for sustainable drug discovery;
2. to perform systematic extraction, fractionation, isolation and purification of secondary metabolites from *Tussilago farfara* L., and to generate and purify fungal biotransformed steroidal metabolites using chromatographic techniques;
3. to elucidate the chemical structures of isolated compounds from *Tussilago farfara* L., and fungal biotransformed steroidal derivatives using advanced spectroscopic and spectrometric approaches;
4. to evaluate the *in vitro* antileishmanial activity (PTR-1 inhibition) of plant-derived compounds and the anti-aromatase activity of isolated biotransformed metabolites;
5. to support and validate experimental biological findings of plant-derived compounds and biotransformed steroids through *in silico* approaches, including molecular docking, molecular dynamics simulations, and binding energy calculations.

Object of the research: Isolation and characterization of secondary metabolites from the aerial parts of the medicinal plant *Tussilago farfara* L. Microbial biotransformation of methylprednisolone acetate using *Fusarium oxysporum* and *Penicillium chrysogenum*.

Subject of the research: Isolation, and chemical analysis of bioactive compounds from *Tussilago farfara* L. It also involves the synthesis of new metabolites through the fungal transformation of selected steroidal drug methylprednisolone acetate. Furthermore, the evaluation of both natural, and biotransformed compounds for their potential antileishmanial, and anti-aromatase activities respectively.

Research methods. A comprehensive methodological approach was employed including, advanced chromatographic techniques such as, high performance liquid chromatography (HPLC), and ultra-performance liquid chromatography (UPLC) for the isolation and purification of bioactive compounds from *T. farfara*, and biotransformed metabolites. Structural elucidation was carried out using spectroscopic techniques, including 1D (^{1}H, and ^{13}C), and 2D-NMR, and mass spectrometry (EI-MS, ESI-MS, and FAB-MS), Fourier-transform infrared (FT-IR) and UV-Vis spectroscopy. Furthermore, *in vitro*, and *in silico* studies were performed to assess the antileishmanial, and anti-aromatase activities of bioactive compounds of *T. farfara*, and biotransformed derivatives, respectively.

Scientific novelty of the research

This study contributes new knowledge such as, the isolation of three compounds (1, 14 and 20) reported for the first time from *Tussilago farfara* L., expanding the phytochemical profile of the plant. The study further investigates the microbial transformation of methylprednisolone acetate for the first time using selected fungal strains of *Fusarium oxysporum*, and *Penicillium chrysogenum* yielding a new metabolite. The biological potential of purified compounds was evaluated for antileishmanial, and anti-aromatase activities, which were further supported by *in silico* studies.

Main statement to be defended

1. The plant material of *Tussilago farfara* L. contains structurally diverse compounds (1–20), including simple phenolic acids, flavonoids, and caffeoylquinic acid derivatives, such as vanillic acid (1), (1S,3R,4R,5R)-3,5-di-*O*-caffeoylquinic acid (14), and 3,4,5-tri-*O*-caffeoylquinic acid methyl ester (20).

2. Microbial biotransformation of the selected steroidal substrate using the fungal strains *Fusarium oxysporum* and *Penicillium chrysogenum* affords regio- and stereoselective structural transformations, yielding one new metabolite, 20-(4′,5′-dimethyl-1′,3′-dioxolan-2-yl)-11β-hydroxypregn-4-ene-3,20-dione, and seven known metabolites.

Validity and reliability of the result obtained

This dissertation combines multi-technique validation, repeatability, and methodological rigor in both phytochemical, and biotransformation studies. In the phytochemical study of *Tussilago farfara* L., reliable botanical authentication and standardized extraction techniques (ethanol extraction, fractionation) were employed to ensure consistency. Advanced spectroscopic techniques such as ^{1}H-NMR (400–800 MHz), ^{13}C-NMR, EI-MS, ESI-MS, FAB-MS, UV, and FT-IR were used for structure confirmation. The reproducibility of biological results was demonstrated through reproducible IC_{50} values obtained from PTR-1 enzyme inhibition bioassays. *In silico* validation of inhibitory potential was achieved by molecular docking, and molecular dynamics simulations, which further supported

the consistency of ligand-receptor interactions. Similarly, biotransformation of methylprednisolone acetate was used to perform controlled microbial transformations under identical fermentation conditions. Subsequent isolation and purification techniques were carried out using TLC, column chromatography, Sephadex LH-20, HPLC, UPLC to ensure purity, and reproducibility. For structural elucidation, advanced spectroscopic techniques such as 1D/2D-NMR, EI-MS, ESI-MS, FAB-MS, and HR-MS were employed to confirm the structures with reliability. *In vitro* bioactivity studies demonstrated clear and reproducible IC_{50} values for aromatase inhibition, while *in silico* docking and MM-GBSA simulations further supported the binding stability, and affinity thereby improving computational robustness.

Theoretical and practical importance of the dissertation

This study merges two important disciplines of chemistry: medicinal plant phytochemistry, and selected steroidal substrate biotransformation which are both evaluated using sophisticated spectroscopic, chromatographic, and computational approaches. Furthermore, this study identified naturally occurring compounds with measurable anti-leishmanial activity against *Lm*PTR-1, providing a basis for future lead optimization studies.

In parallel, microbial biotransformation of steroidal drugs demonstrates the ability of microorganisms to generate structurally modified and biologically enhanced derivatives from existing drug, such as methylprednisolone acetate.

Together, these complementary approaches encourage the development of new drugs in two important fields: neglected tropical diseases through PTR-1 inhibition, and hormone-related cancers *via* aromatase inhibition.

Main results of the study:

The main findings of the study based on the phytochemical analysis of *Tussilago farfara* L., and the biotransformation of methylprednisolone acetate, are as follows:

1. The use of *Tussilago farfara* L. and fungal strains *Fusarium oxysporum* and *Penicillium chrysogenum* proved effective, enabling the successful isolation of diverse phytochemicals and the efficient biotransformation of methylprednisolone acetate into structurally modified metabolites.

2. Advanced chromatographic techniques, including TLC, column chromatography, Sephadex LH-20, HPLC, and UPLC, enabled the successful extraction, fractionation, and isolation of twenty secondary metabolites (1–20) from *Tussilago farfara* L. Additionally, microbial transformation of methylprednisolone acetate yielded eight metabolites, including one new metabolite (2), and seven known metabolites (3–9).

3. The structures of all isolated compounds and metabolites were elucidated using comprehensive spectroscopic and spectrometric techniques, including ^{1}H-

NMR, ^{13}CNMR, 2D-NMR, HRMS, EI-MS, FAB-MS, FT-IR, and UV/Vis spectroscopy. Among them, compounds 1, 14, and 20 were reported for the first time from this species. Biotransformation resulted in key structural modifications such as hydroxylation, ester cleavage, and keto reduction.

4. Biological evaluation revealed that compounds 15–18 exhibited moderate inhibition of *Lm*PTR-1, with compound 18 showing the highest activity (IC_{50} = 81.9 ± 1.12 µM). Furthermore, in the biotransformation study substrate 1, and its metabolites demonstrated promising anti-aromatase activity. Among them metabolite 4 exhibited enhanced inhibition (IC_{50} = 69.32 ± 0.17 nM) compared with both the substrate 1, and the standard drug exemestane under the experimental conditions.

5. Computational studies, including molecular docking, molecular dynamics simulations, and MM-GBSA analysis, supported strong and stable binding interactions of compounds with target enzymes. Caffeoylquinic acid derivatives (15–18) showed stable interactions with PTR-1, while steroidal metabolites (2–9), particularly metabolite 2, and 4 exhibited strong binding affinities toward aromatase, supporting their high inhibitory potential.

Author's contribution

The author independently conducted all stages of the research described in this dissertation, including:

1. A comprehensive evaluation of relevant literature.
2. Optimization of chromatographic profiling using TLC, HPLC, and UPLC for extraction, isolation, and spectroscopic analysis of natural compounds from *Tussilago farfara* L., as well as biotransformed metabolites derived from steroidal substrates.
3. Design, and optimization of microbial transformation method for methylprednisolone acetate, using *Fusarium oxysporum* and *Penicillium chrysogenum*.

In addition, the author prepared the figures, and tables through thorough data analysis interpretation, and composed the scientific narrative by integrating the results into logical conclusions.

Presentation of practical results

In addition to successfully isolating plant-derived compounds, and steroidal metabolites, the experimental results were presented in international scientific conference (MMDR-8, ICCBS, Karachi, Pakistan 2023). The results contribute to drug discovery research through enzymatic inhibition studies and are relevant to academic and research communities in medicinal chemistry, pharmacognosy, and pharmaceutical sciences.

Publications

The results of this study have been published in reputable academic journals. The author has published three original research papers (two related to plant phytochemistry and one on biotransformation), and one review articles in international peer-reviewed journals indexed by Scopus, including:

1. Ahmad I. et al. "Caffeoylquinic acid derivatives isolated from *Tussilago farfara* L. as potential antileishmanial agents: *in vitro* and *in silico* studies" // *Natural Product Research.* 2026, P. 1-9. https://doi.org/10.1080/14786419.2026.2613766. *(Experimental work, data analysis, writing original draft, validation, review and editing).*
2. Ahmad I. et al. "Coltsfoot (*Tussilago farfara* L.; Asteraceae): Modern methods of extraction, phytochemistry, nanoparticles synthesis, ethnopharmacology, and biological activities" // *Natural Product Research*. 2025, P. 1-20. https://doi.org/10.1080/14786419.2025.2548616. *(Experimental work, data analysis, writing original draft, validation, review and editing).*
3. Ahmad I. et al. "Aromatase (CYP19A1) Inhibitory Activity of Coltsfoot (*Tussilago farfara* L.) Phytochemicals: *In Vitro* and *in Silico* Evaluation" // *Erurasian chemico-technological journal*. 2025, Vol 27, No (4), P. 315–321. https://doi.org/10.18321/ectj1678. *(Experimental work, data analysis, writing original draft, validation, review and editing).*
4. I. Ahmad. et al., Fungal-Mediated Transformation of Methylprednisolone Acetate into Potent Aromatase Inhibitors: *In vitro* and *in silico* Studies" // *Journal of Molecular Structure*. 2026, Vol 1364, P. 145890. https://doi.org/10.1016/j.molstruc.2026.145890. *(Experimental work, data analysis, writing original draft, validation, review and editing).*

Structure of the dissertation as follows: 4 chapters, 36 tables, 36 figures, 47 supplementary figures, and 267 references within a total of 188 pages.

Acknowledgment. I am deeply grateful to **Allah Almighty**, the Most Beneficent and the Most Merciful, for His countless blessings, strength, and guidance that enabled me to complete this challenging journey. I also offer my sincere respect to the Holy **Prophet Muhammad** (Peace Be Upon Him).

I express my heartfelt appreciation to my supervisor, **Dr. Kudaibergenova Bates** Malikovna (Associate Professor), for her continuous guidance, valuable suggestions, and unwavering support throughout this research.

I am profoundly thankful to my esteemed co-supervisor, **Prof. Dr. M. Iqbal Choudhary** (*H.I., S.I., T.I.*) for his visionary leadership, and for providing an outstanding research environment at ICCBS.

I would also like to thank **Prof. Dr. Atia-tul-Wahab** (ICCBS) for her technical assistance during my research, and **Dr. Salar Hafez-Ghoran** and **Dr. Shamsher Ali** for their continuous encouragement and confidence-building support.

Finally, I extend my deepest gratitude to my parents, brothers especially, **Irshad Ahmad**, sister, extended family, and my friend **Ahmad Said** for their prayers, encouragement, and unwavering support throughout this journey.

1 Literature review

1.1 Overview of natural products

Natural products, which can be classified as primary and secondary metabolites, are derived from natural sources such as plants, animals, and microbes [1]. Secondary metabolites, like alkaloids, flavonoids, and terpenoids, exhibit biological activities but do not directly contribute to growth, whereas primary metabolites, such as amino acids, carbohydrates, and lipids, are essential for growth, and development. Due to their pharmacological importance, secondary metabolites are commonly referred to as natural products [2]. Nature has long been a primary source of clothing, food, medicine, and shelter. Plants have been widely recognized for their medicinal properties, and have made significant contributions to traditional healthcare systems worldwide [3, 4].

It is estimated that more than half of the world's rural population continues to rely on medicinal plants for their medical requirements [5]. Historical texts, including cuneiform tablets from Mesopotamia (c. 2600 B.C.), documented the use of oils from myrrh (*Commiphora*), and cypress (*Cupressus sempervirens*) to treat coughs, inflammation, and colds [6]. Natural products are essential to modern industry, and medicine by providing raw materials for drugs development. Notable examples are quinine, and artemisinin derived from the bark of *Cinchona officinalis,* and *Artemisia annua* effective against malaria [7].

1.2 Natural products and drug discovery

Natural compounds produced by microbes, and plants have long served as valuable resources in drug development. They produced a wide range of bioactive and structurally diverse compounds, many of which have been developed into clinically important drugs such as morphine, penicillin, artemisinin, and paclitaxel [8]. It is estimates that nearly 80% of the global population relies on natural products-based remedies for healthcare [9]. Even in developed countries, natural product-derived medicines remain an important component of medical systems [10]. Notably, 12 of the top 25 pharmaceutical treatments in the world are derived from natural sources [11].

Natural products continue to play an important part in contemporary drug discovery efforts in pharmaceutical companies and research institutions. Over the last 200 years, extensive research into their chemical, and biological properties has resulted in the production of drugs for a variety of disorders, as well as the expansion of synthetic, and medicinal chemistry [12]. Between 2005 and 2010, nineteen natural product-based drugs were approved worldwide to treat cancer, infectious, neurological, cardiovascular, and inflammatory diseases [8].

Although terrestrial plants have historically been the primary source of bioactive compounds, recent research has shown that the marine environment, which

make up over 70% of the earth's surface, provide a significant untapped resource. Marine organisms produce a variety of unique metabolites with significant pharmacological potential [13].

1.3 Current advancements in natural products research

Plant secondary metabolites are extracted, and characterized, and used in agriculture, medicine, and food. More efficient methods must be employed instead of costly, and time-consuming techniques. One of the most widely used methods for separating plant-based compounds involved molecularly imprinted polymers (MIPs) [14]. Rosmarinic acid was extracted from a complicated mixture of rosemary extract (*Rosmarinus officinalis* L.) using bulk imprinted polymers and the molecularly imprinted solid phase extraction (MISPE) [15]. Solanesol is one of the active compounds found in tobacco leaves. MIPs were employed as a stationary phase in flash chromatography for the development, and testing of a solanesol extraction process [16].

The membrane filtration method is also utilized in the natural product isolation process. Many fungi produce bioactive compounds with significant pharmacological relevance. Valuable compounds have been identified from fungal extracts using membrane technology, specifically nanofiltration [17]. Additionally, advances in analytical, and computational techniques, notably hyphenated procedures such as LC-NMR, and LC-MS have enabled direct structural evaluation of complex natural compounds from the small extract volume. These strategies accelerate the process of discovering, and developing of new pharmacological leads from natural sources while reducing the need for lengthy isolation procedures [18].

1.4 Traditional medicine systems

Traditional medicine with its origins in ancient plant-based methods, has long been essential to the prevention, and treatment of diseases. Human interaction with harmful, and medicinal plants contributed to the evolution of knowledge, which was then passed down orally and in writing [19]. The World Health organization (WHO) defines traditional medicine as "culturally based knowledge, and methods for healing and sustaining health" [20]. Traditional Chinese Medicine (TCM), Ayurveda, Kampo, Traditional Korean Medicine (TKM), and Unani medicine are important systems that are still used today [19]. Ancient manuscripts from China, Egypt, Mesopotamia, and India document the widespread use of herbal treatments [21]. Herbal medicine was systemized by Greco-Roman intellectuals such as Hippocrates and Galen, and it was later preserved by Arab scientists, particularly Avicenna [22].

The finding of active compounds such as salicin, and morphine in the nineteenth century marked the beginning of the modern era, and led to the

development of pharmaceuticals that are still used today. Traditional medicine is an important part of worldwide healthcare and cultural heritage.

1.5 Challenges and new approaches in natural products research

Natural products continue to be a key source of therapeutic leads due to their diverse structures, and bioactivities. Despite improvements in combinatorial chemistry, approximately one in 5,000 compounds is clinically approved, making the discovery process costly, and time-consuming [23]. Natural products are regaining appeal in drug discovery due to the recent incorporation of modern approaches such as high-throughput screening, computational modeling, genomics, and proteomics. Molecular biology, and genome mining facilitate the identification of new targets, and bioactive substances [21, 24], whereas techniques such as LC-MS, LC-NMR assist in dereplication to prevent repeated purification of known compounds [19].

At the molecular level, computational approaches (such as molecular docking and reverse docking) aid in virtual screening, and mechanism elucidation [25]. Moreover, metabolic engineering and synthetic chemistry enhance drug-like properties while promoting sustainability. To address existing challenges, researchers increasingly apply synthetic biology for sustainable chemical synthesis, examine compound-target interactions, and employ powerful analytical techniques. Natural products research is moving toward system-level, and tailored therapy as a result of constant advancements [26].

1.6 Family Asteraceae, genus and species

With over 1,600 genera and 25,000 species worldwide, the family Asteraceae is one of the largest flowering plant families [27]. It includes medicinal plants like wormwood, and chamomile as well as common food crops such as chicory, lettuce, and sunflower. Asteraceae species flourish in a wide range of habitats globally, with the exception of Antarctica [28]. Pharmacologically, their bioactivity is linked to a range of phytochemicals, including lignans, saponins, polyphenols, phenolic acids, sterols, essential oils, and polysaccharides [29].

Tussilago farfara is the only species of the genus *Tussilago*. It belongs to the family Asteraceae. It is also known as a "winter flower," or "beehive" [30, 31]. The height of this perennial plant ranges from 5-15 cm [32]. Large populations of the plant can be found in China, Korea, North Africa, and Europe [33, 34]. It has been used traditionally in medicine [32], for example, to treat cough, asthma, and bronchitis [35]. Flavonoids [36], chromones [37], sesquiterpenoids [38], volatile oils [39], alkaloids [40], and chlorogenic acids [41] are among the many phytochemicals found in *T. farfara*, according to numerous studies. Additionally, the plant has anti-inflammatory [42], antioxidant [43], antibacterial [44], cytoprotective [36], and

anticancer activities [45]. The traditional uses, phytochemistry, and pharmacological application of *Tussilago farfara* L. are shown in Figure 1.

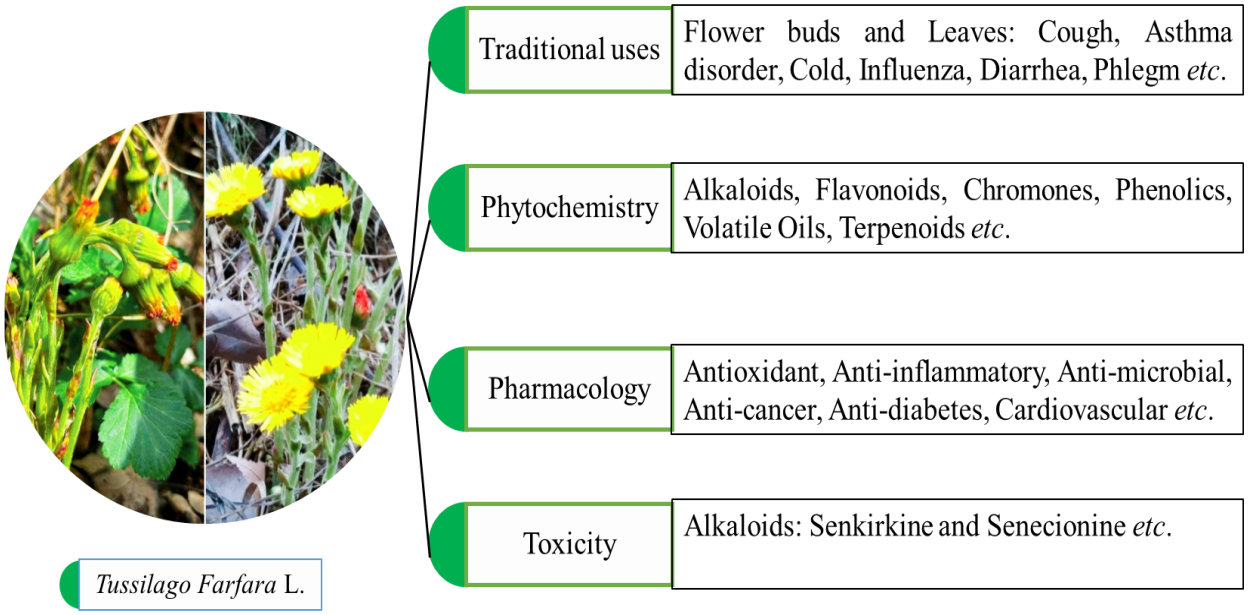


Figure 1 – Traditional uses, phytochemistry, and pharmacology of *Tussilago farfara* L

1.6.1 Traditional uses of *Tussilago farfara* L

According to the 15th edition of Chinese Pharmacopoeia (New Edition), *T. farfara* possesses warm, pungent, and mildly bitter properties. It is used to treat hemoptysis, bloody phlegm, asthma, atrophic lung disease, and acute or chronic cough, and is also believed moisturize the lungs [46]. *T. farfara* smoke inhalation was suggested by Song Dynasty pharmacist Su Song, and Tu Jing Ben Cao as a cough remedy [47]. There have also been reports of antiviral activity against enterovirus 71 infections [48]. Using network pharmacology, and molecular docking, the pharmacological potential of coltsfoot compounds against COVID-19 has been investigated [49, 50]. It has been shown that coltsfoot constituents may bind to SARS-CoV-2 3CL protease, and ACE2, thereby regulating multiple signaling pathways.

Coltsfoot leaves have been used to treat wounds in the Balkans. Tea prepared from the plant has also been traditionally used to treat cancer [51]. Its traditional uses in different countries are summarized in Table 1.

Table 1 – Traditional uses of *Tussilago farfara* in different countries

Countries	**Parts of the *T. farfara***	**Traditional Uses**	**References**
China	Plant	Used to treat cough, excessive phlegm, and asthma, as well as chest tightness in chronic bronchitis, emphysema, and bronchial asthma.	[52]
North America	Roots and Leaves	Asthma, and Tuberculosis.	[53]
Russia	Leaves	Asthma, bronchitis, common cold, and sedative. Additionally, it can be used topically to treat furunculosis and assist digestion. It is also effective as an analgesic.	[54]
North Africa, Europe, Siberia	Flower and leaves	Cough, and bronchial infections.	[55]
Asia, Bulgaria	Root and leaves	Chest pains, bronchial infections, coughing, asthma, influenza, and chronic bronchitis.	[56]
Canada, and USA	Flowers, buds Leaves and roots	Influenza, asthma, colds, gastroenteritis, diarrhea, and metabolic stimulation, external wound care, and blood purification.	[57]
Japan	Blooming flower	Evaluate in Inbred strain ACI rats	[58]
India	Whole plant	Disease related to respiratory tract.	[59]
Poland	Leaves	It can be used topically to treat furunculosis and assist digestion. It is also effective as an analgesic.	[55]
Western Ukraine, and Romania	Leaves	Food wrapping (sarma rolls)	[60]

1.6.1.1 Phytochemistry

Numerous studies have been done on phytochemistry of the *Tussilago farfara* L. Up to January 2025, more than 184 compounds have been identified [61]. These comprise phenolcarboxylic acids (ferulic, *p*-hydroxybenzoic), sesquiterpenoids (tussilagone), alkaloids (senecionine, tussilagine, senkirkine), fatty acids (capric, palmitic, stearic, and octadecene derivatives), carbohydrates (inulin, sucrose, pectin), latex, steroids (stigmasterol, β-sitosterol), and flavonoids (quercetin, rutin, kaempferol) [62]. Among the identified volatile constituents are 4,4-Dimethyltetracyclo[5.2.1.02,6.03,5]decane, Phytol, *n*-nonadecane, and *n*-tetradecane [63].

Alkaloids: *T. farfara* contains a number of alkaloids. It also includes pyrrolizidine alkaloids such as senkirkine, and senecionine, which are particularly known for their toxicity [64], leading to limitations or prohibitions in certain nations [59]. For fast identification, and measurement, capillary zone electrophoresis (CZE) is used. A statistical study of critical parameters, and reproducibility suggested that the CZE method provides sufficient resolution and internal uniformity [65].

Flavonoids: About 23 flavonoids, and glycosides have been identified in coltsfoot. Kaempferol, and quercetin have diverse anticancer properties [66]. Rutin has been linked to hypoglycemia [67]. The flavonoids in the methanolic extract of coltsfoot leaves were detected using gas chromatography-mass spectrometry (GC-MS) [68].

Chromones: Chromones have been isolated and identified from the extract of flower buds of the plant using chemical, and spectroscopic techniques [36], an enantiomer such as 1-[(4S)-3,4-dihydro-4-hydroxy-2,2-dimethyl-2H-1-benzopyran-6-yl]-ethenone [69].

Phenolics: In *T. farfara*, phenolic acids are the predominant class of organic acids [59]. These compounds include derivatives of phenylpropane, phenylpropanoic acid esters, and phenylmethane [44]. Important phenolic acids that contribute to antioxidant activity include 3,5-dicaffeoylquinic acids, 3,4-dicaffeoylquinic acids, and 5-dicaffeoylquinic acids [70]. Maltase inhibition is correlated with the quantity of caffeoyl groups [71]. The Folin–Ciocalteu and HPLC-DAD techniques were used to measure the total and individual phenolic acids [32, 44]. NMR, MS and IR, techniques were used to purify, and structurally validate phenylpropanoic esters [72, 73].

Volatile oils: Coltsfoot has few volatile oils, particularly in its leaves [39, 74]. Although compositional diversity has been noted in studies [75], molecular composition in relation to extraction procedures has yet to be investigated. Essential oils were extracted using hydrodistillation in a Clevenger-like system. The oils from buds, and stalks were identified using GC, and GC-MS, whereas the oils from coltsfoot flowers were evaluated using GC-FID/GC-MS [76].

Terpenoids: *Tussilago farfara* has sesquiterpenoids, and triterpenoids. Sesquiterpenoids contain bisabolane, and oplopane types, as well as their esters. New compounds such as tussfararin D, and farfarone A-D have recently been identified [34]. They were isolated by preparative column chromatography, HPLC and then quantified using UHPLC-MRM-HR [77]. Pentacyclic triterpenoids such as arnidiol, faradiol, and bauerenol were also identified in flower buds [78].

1.7 Pharmacological application

Tussilago farfara extracts, and purified compounds have been shown to be effective against respiratory disorders, inflammation, liver, malignancies (breast, colon, lung), diabetes, neuropathies, cardiovascular, and neurological diseases [59, 79]. Table 2 lists the primary pharmacological effects.

T. farfara's antioxidant property has been demonstrated using a variety of *in vitro*, and *in vivo* studies. The plant extracts showed antibacterial, and antioxidant activities [80], with aerial parts having the maximum antioxidant capacity. Sugars, and flavonoid glycosides such as isoquercitrin, apigenin, and quercetin-3-*O*-β-D-glucopyranoside have been connected to this significant antioxidant property [81]. A study conducted on Iranian *T. farfara* specimens found a substantial association between phenolic content, and antioxidant activity [32]. Furthermore, antioxidative activity was observed in human bronchial epithelial cell lines exposed to hydrogen peroxide-induced oxidative stress, indicating the plant's ability to defend against reactive oxygen species [82].

T. farfara has demonstrated promising anticancer efficacy in both cellular, and animal research. *T. farfara* displayed cytotoxic, and anti-proliferative properties as measured by the MTT assay. Bud-derived sesquiterpenoids showed considerable anticancer activity, and were used in the green synthesis of gold (Au) and silver (Ag) nanoparticles, which increased their medicinal value [83]. Methanolic fractions from *T. farfara's* leaf, and stem increased tumor necrosis factor-related apoptosis-inducing ligand (TRAIL) sensitivity in resistant Huh7 hepatocellular cancer cells, indicating promise as a TRAIL sensitizer [84]. The reported anticancer mechanisms included mitosis inhibition in tumor cells, immune response increase, and facilitation of microtubule aggregation during mitotic progression [85]. In addition, polysaccharide fractions from the plant caused apoptosis in leukemia, and lung cancer cell lines *in vitro,* increasing the plant's chemotherapeutic potential.

T. farfara's anti-inflammatory properties are mostly due to its sesquiterpenoid concentration. Almost half of the isolated sesquiterpenoids had significant inflammation-reducing properties [86]. Tussilagone (TGN) has been explored as a potential treatment drug for psoriasis, a chronic inflammatory skin disorder [87]. Furthermore, sesquiterpenoids inhibited NO generation in LPS-stimulated RAW 264.7 macrophage cells, with IC_{50} values ranging from 3.5 to 60.29 μM [88].

In vitro studies have shown that *T. farfara's* ethyl acetate (EtOAc) fraction protects cortical neurons from oxidative, glutamate-induced, and NO-induced damage at doses ranging from 0.1 to 30 μg/mL [89]. The active component, 7*β*-(3-ethyl-*cis*-crotonoyloxy)-1*α*-(2-methylbutyryloxy)-3,14-dehydro-Z-notonipetranone (ECN), activated the Nrf2/HO-1 signaling pathway in both *in vitro*, and *in vivo* models. However, optimal dose data is limited [90]. Flower bud extracts, and sesquiterpenoids, including ECN, tussilagonone, and 14-acetoxy-7*β*-(3′-ethyl-*cis*-crotonoyloxy)-1*α*-(2′-methylbutyryloxy)-notonipetranone, have been demonstrated to block the NF-κB pathway. This reduces the synthesis of inflammatory mediators such as TNF-α, NO, and PGE_2, while also scavenging reactive oxygen species (ROS) [91].

Different extracts from various parts of *T. farfara* have shown efficacy against both Gram-positive and Gram-negative bacteria in terms of antiviral and antibacterial activity. These include *Salmonella typhimurium*, *Pseudomonas aeruginosa*, *Escherichia coli*, *Bacillus cereus*, *Micrococcus flavus*, and *Staphylococcus aureus* [75, 92]. Furthermore, employing human rhabdomyosarcoma cell line (RD cells), and CCFS/KMC systems, the antiviral effectiveness of coltsfoot against enterovirus 71 (EV71) was verified *in vitro*. Protein synthesis suppression, and viral replication inhibition are thought to be key components of the antiviral process [93].

Additionally, the herb shows encouraging benefits on the cardiovascular system. Tussilagone improved peripheral hemodynamics in a dose-dependent manner, especially in canine models of hemorrhagic shock [94]. Pharmacological drugs such as phentolamine, and verapamil greatly decreased, but did not entirely eliminate, the effect of tussilagone-induced contraction of rabbit aortic strips in a Ca^{2+}-free solution. This indicates that tussilagone might work by directly stimulating the contraction of vascular smooth muscle, and increasing the release of catecholamine [95].

T. farfara also possesses antidiabetic, and anti-obesity effects. The methanolic extracts inhibited glucosidase enzymes, whereas the EtOAc extracts inhibited amylase [92]. Caffeoylquinic acid derivatives effectively suppressed α-glucosidase activity, with efficacy proportional to the amount of caffeoyl moieties attached to the quinic acid scaffold [71].

Lastly, the plant has demonstrated immunostimulant properties. Polysaccharides from *T. farfara* protected female C57BL/6 mice with Lewis lung cancer by boosting hematopoietic regeneration, and working synergistically with polychemotherapy [48]. These polysaccharides also have a stimulating effect on granulopoiesis, similar to the commercial granulocyte colony-stimulating factor (CSF) drug Neupogen. This suggests a function in reducing chemotherapy-induced immunosuppression [103].

Due to the therapeutic potential of *Tussilago farfara* and the growing demand for plant-derived bioactive compounds, comprehensive scientific studies are highly required. The study would help investigate phytochemical constituents of *T. farfara*, and evaluate its biological effects, particularly antileishmanial activity. Moreover, structure-activity relationship (SAR) studies would also be carried out to gain more insights into the molecular origin of the reported bioactivity.

An attempt was also made to isolate sufficient bioactive compounds for future modification through biotransformation. However, this did not yield sufficient amount, the experiment was continued using a commercially available drug (methylprednisolone acetate) as the substrate.

Table 2 – Pharmacological studies of *Tussilago farfara* L

Activity	Model used	Plant part	Type of extract	Result	References
Antioxidant	*In vitro;* DPPH, Lipid peroxidation homogenates	Buds	EtOAc fraction, MeOH extract	IC_{50} = 6.3 µg/mL in lipid peroxidation assay, and IC_{50} = 14.3 µg/mL in DPPH assay	[89]
Antioxidant	*In vitro;* DPPH, and pyrogallol autoxidation assays	Buds	EtOAc, *n*-BtOH fraction, and EtOH (70%) extract	All fraction show scavenging activity. EtOAc and *n*-BuOH shows higher activities than aqueous fraction	[96]
Anti-cancer	*In vitro*; Mice leukemia cells (L1210)	Aerial	Methylene chloride and MeOH extract	71% inhibition by MeOH extracts, and 92% inhibition by CH_2Cl_2	[97]
Anti-inflammatory	*In vitro;* Murine macrophage cell line (RAW 264.7)	Buds	1*α*,5*α*-bisacetoxy-8-angeloyloxy-3*β*,4*β*-epoxy-bisabola-7(14)-10-dien-2-one	Inhibition of arachidonic acid and I-NOS (71.1%) with IC_{50} = 8.9 µM	[98]
Anti-inflammatory	*In vitro;* Lipopolysaccharide (LPS)-stimulated macrophages	Buds	Tussilagone	Inhibited the production of NO, TNF-α, and PGE_2	[99]
Neuroprotective	*In vitro;* Cell culture of cortical	Buds	EtOAc, and MeOH fraction	Arachidonic acid-induce inhibition, with an IC_{50} = 0.64 µg/Ml	[89]

Table 2 (continued)					
Antimicrobial	*In vitro;* Liquid dilution	Rhizome, aerial parts	EtOH extract	*B. cereus*: 16.63/62.5 mg/mL	[100]
Antitussive	*In vivo*; Ammonium-induced cough, Mouse model	Buds	Aqueous extracts	Period increased by 47%, and cough frequency decreases by 48%	[101]
Expectorant	*In vivo*; Injection (intraperitoneal) of phenol red solution (Mouse model)	Buds	Aqueous extract	Strong expectorant activity. Increased by 42% of tracheal phenolsulfonphthalein excretion	[101]
Anti-obesity and antidiabetic	*In vitro*; Caffeoylquinic acid.	Buds	EtOAc, and MeOH extract	EtOAc extract showed promising anti-amylase activity, and MeOH extract exhibited activity against glucosidase	[92]
Cardiovascular system	*In vivo*; Tussilagone in dog	Buds	MeOH extract	Strong presser effect on the peripheral, particularly in hemorrhagic shock	[102]

1.8 Biotransformation

Microbial transformation is a key technique in biotechnology, and medicinal chemistry that involves structural alterations of organic compounds using a variety of biocatalytic systems. These living cell system include microorganisms, as well as plants, and animal cultures. Microorganisms include bacteria, fungi, parasites, and so forth. Since ancient times, biotransformation has been used to synthesize particular compounds with medicinal benefit from widely available precursor molecules [104, 105]. This produces compounds with high regio-, stereo-, chemo-, and enantio-selectivity under mild reaction conditions (i.e., non-extreme temperature, pressure, and pH) in solution. Biotransformation has been effectively used to alter the structural properties of chiral, multifunctional, and inert compounds without the need for protection, deprotection, or functional group activation procedures. Nowadays, biocatalytic methods are recognized to adhere to the green chemistry strategy since they use biological catalysts that are non-toxic, low-cost, renewable, and environmentally benign, and they produce less or no toxic waste than traditional methods [106-109].

Biotransformation has the advantage of retaining the starting material's original carbon backbone. These reactions play an important role in drug detoxification, and nutrient removal. The biotransformation process, also known as metabolic reactions, often convert chemicals into more polar forms that are excreted more rapidly from the body. They are part of the body's natural defense mechanism against xenobiotics [110-112].

There are two categories of microbial transformation reactions. Type 1 involves the use of enzymes including amidase, esterase, flavin-containing monooxygenase (FMO), and cytochrome P450 (CYP) to add polar groups to functional moieties. Enzymes like N-acetyltransferase, glucuronosyltransferase, and sulfotransferase catalyze type II conjugation processes, which involve the attachment of hydrophilic molecules like glucuronic acid, and sulfate to accessible functional groups [113, 114]. Scientists are constantly trying to improve the capacity of living cells and biocatalysts to change structures effectively, and economically. Applications for these transformations can be found in polymer science, food technology, medicine, agriculture, and environmental management. Microbial transformations are becoming increasingly important in drug research, and development processes [115, 116].

Biotransformation can be divided into two types on the basis of nature, and origin;

- Xenobiotic biotransformation: which involves the transformation of substances foreign to the organism. Terpenes, and steroids compounds serve as examples [117].

- Biosynthetically guided biotransformation: substrates for this category are analogs of natural biosynthetic intermediates. The conversion of kaurane to gibberellins is a prominent example [118].

1.8.1 Historical background

The usage of biotransformation extends to ancient times. Around 5000 BC, people converted sugar to ethanol, and ultimately to acetic acid. By 800 BC, the process of hydrolyzing casein with chymosin to make cheese was widely used. The earliest industrial biotransformation, the bio-oxidation of ethanol to acetic acid, was recorded by Orleans in 1670 [119].

In 1921, Hirsch and Neuberg employed *Saccharomyces cerevisiae* to biocondensate benzaldehyde, and acetaldehyde to produce 1-hydroxy-1-phenyl-2-propanone [120, 121].

Reichstein had a significant breakthrough in organic synthesis in 1934 when he converted sorbitol to sorbose through regioselective oxidation [122]. Androst-4-ene-3,17-dione was converted to its 17-hydroxy counterpart by *S. cerevisiae* in 1937. Progesterone transformation was industrialized in 1952 by Murray, and Peterson of Upjohn Co. using *Rhizopus sp*., to formed 11-α hydroxylation [123].

Notable example include the conversion of sucrose into glucose, and fructose by invertase during World War II [124], the microbial synthesis of acrylamide from acrylonitrile by *Brevibacterium* sp. in the 1980s [125], the biocatalytic synthesis of pantolactone by *Fusarium oxysporum* [126], the stereospecific hydroxylation of cyclohexanone carboxy esters by *Kloekra magna* [127], the synthesis of testolactone from testosterone by *Penicillium notatum* [128], and the conversion of β-ionone into fragrance agents by *A. niger*, and *Cunninghamella blakesleeana* [129]. Some enzymatic classes involved in biotransformation reaction are shown in Figure 2.

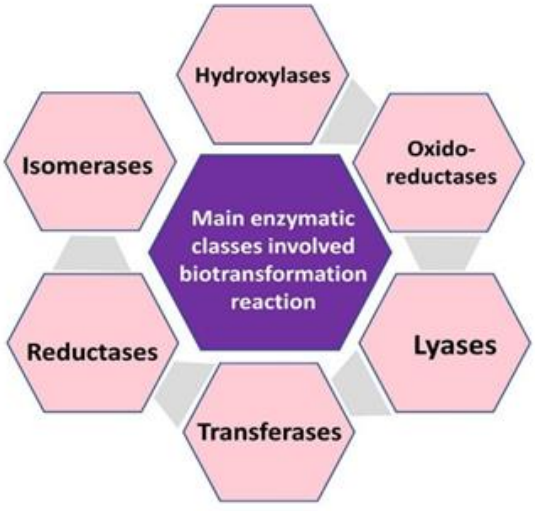


Figure 2 – Enzymatic classes involved in biotransformation reactions

1.8.2 Agents of biotransformation

Fungi and Bacteria: Whole microbial colonies (fungi or bacteria) are utilized in whole-cell biotransformation. These systems comprise a broad set of enzymes capable of performing various reactions. Fungi are particularly beneficial for food fermentation, and antibiotic synthesis. Industrially, *Rhizopus,* and *Mucor* strains are used to produce organic acid, and perform hydroxylation processes [130]. *Fusarium lini, Curvularia lunata, Aspergillus alliaceus,* and *Gibberella fujikuroi* have all been shown to convert spirolactone into hydroxylated compounds [131]. *Cunninghamella echinulata,* and *Cunninghamella blakesleeana* converted nandrolone to its analogues [132]. *Aspergillus niger,* and *Aspergillus flavus* altered the structural properties of artemether [133]. The bioconversion of taxol, an anticancer drugs, to more hydroxylated derivatives by *Streptomyces species* [134].

Plant cell suspension cultures: Plant cell suspension cultures have been utilized for the biotransformation of xenobiotic compounds, serving as viable alternative source of enzymes. Plant cell cultures offer effective methods for producing extremely valuable substances for medications, food, and cosmetics [135]. Numerous factors contribute to the widespread adoption of this technique, including the ease with which these cell cultures can proliferate in a laboratory setting, the reproducibility of the reactions, and their capacity to generate large quantities of modified metabolites. Progesterone (pregn-4-ene-3,20-dione) was microbially transformed utilizing *Catharanthus roseus* plant cell suspension cultures [136]. *Catharanthus roseus* cell suspension cultures were used to structurally alter (-)-Caryophyllene oxide [137]. *Picea abies* cell suspension culture was used to structurally change the organic molecule α-pinene into *trans*-verbenol, and verbenone [138]. Ethynodiol diacetate, used in birth control tablets, was converted into its derivatives utilizing plant cell suspension cultures of *Azadirachta indica*, and *Ocimum basilicum* [139].

1.8.3 Process-driven use of biotransformation techniques

Given the complexity and cost of drug development [140], structural modification of current medications through biotransformation can reduce development risks while enhancing overall efficiency [141], [142]. When chemical synthesis has reached its limits, microbial transformation provides regio- and stereoselective methods under mild, and green conditions. Combinatorial biocatalysts, and genome mining enhance its capabilities [143]. Schematic representation of whole-cell, and enzymatic biocatalysis is shown in Figure 3.

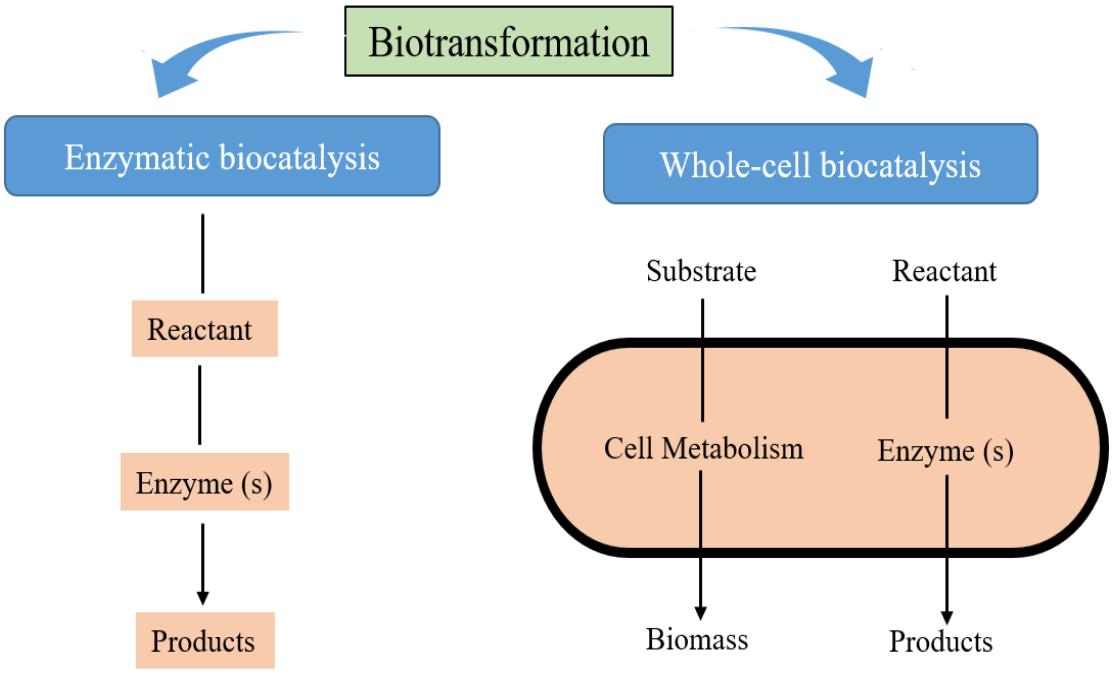


Figure 3 – Schematics representation of enzymatic, and whole-cell biocatalysis

1.8.4 Significance and application of biocatalysis

Drug development is a difficult, expensive, and multidisciplinary process that starts with identifying therapeutic targets, and progresses to lead optimization, and biological testing [104]. Microbial transformation is an effective way to change chiral, multifunctional, or inert compounds, especially when typical synthetic techniques are difficult or expensive [106, 144]. Unlike traditional synthesis, which frequently uses toxic chemicals, several protection/deprotection processes, and significant energy inputs, microbial reactions are environmentally friendly, occurring in aqueous media under mild conditions. These biocatalytic methods have great stereo-, and regioselectivity while remaining cost-effective and scalable. Furthermore, they greatly minimize the E-factor, a critical metric of environmental effect that represents the ratio of waste to product, and is consistent with green chemistry principles [145]. Microbial transformation helps to produce safer, and more sustainable industrial medication manufacturing procedures by utilizing non-toxic, biodegradable biological catalysts [107].

Biotransformation offers strong regio-, stereo-, enantio-, and chemo-selectivity, allowing for precise chemical alterations that can improve drug pharmacodynamics, and aid in drug repurposing. As a result, it has become an important tool in the production of new drugs. Many pharmaceutical companies currently employ biocatalysis on scale ranging from 1 kg to 100 kg in their drug research, and development pipelines. This technology is essential for producing

optically pure compounds, which are increasingly in demand across the pharmaceutical, fine chemical, food, and agrochemical industries [146-148].

Biotransformation is also employed for large-scale chemical production, with annual outputs surpassing 10,000 tons, demonstrating its expanding importance in worldwide sustainable manufacturing. Several research articles, reviews, and patents have emphasized this trend in recent years [106, 147, 149]. Chemical synthesis combined with biocatalysis is useful for creating a wide range of products, including food ingredients, agrochemical intermediates, medicines, enzymes, vaccines, and antibiotics [105, 150]. Importantly, biotransformation provides a sustainable, and cost-effective alternative to traditional methods for synthesizing chiral molecules, particularly those with complex structures, and high stereoselectivity, making it an essential technology for producing high-value, optically active compounds [151, 152].

1.8.5 Challenges in microbial transformation

Despite its widespread use, microbial transformation faces some challenges, the most prominent is the low solubility of organic substrates in aqueous media [153]. Enhancing substrate solubility is critical for efficient biotransformation. Organic compounds are frequently fed into microbial cell culture media using saturated solutions of 1,2-propanediol, acetone, methanol, dimethyl sulfoxide, and dimethyl formamide. Many research groups used cyclodextrins to increase the solubility, which has facilitated the transformation of compounds [154, 155]. The immobilization of enzymes or complete cells in a stable matrix, as proven by Mahato's group, a significant achievement in the field, increasing operating efficiency, and cell stability while lowering expenses [156]. Although it is preferable to use non-aqueous systems for biocatalytic processes, Although, it is preferable to use non-aqueous systems for biocatalytic processes, microbial enzymes usually exhibit lower catalytic activity. According to the recent study, a variety of microbial cell cultures can be modified to function in organic solvents. For example, by lyophilizing an aqueous solution containing a high reaction rate in the presence of non-buffer salt, a Subtilisin Carlsberg preparation can be obtained that becomes practically insoluble in most organic solvents [157].

1.8.6 Microbial transformation of steroids

The basic structure of steroidal compounds is made up of four fused rings. Three six-membered (rings A, B, and C) and one five-membered (ring D) derived from cyclopentanoperhydrophenanthrene (Figure 4). Different steroids possess functional groups that are attached to the fundamental hydrocarbon skeleton. Cholesterol is an essential steroid found in mammalian cell membranes. It is served as a precursor for a variety of steroids. In addition, a range of hormones, including sex hormones found in vertebrates, are biosynthesized from cholesterol.

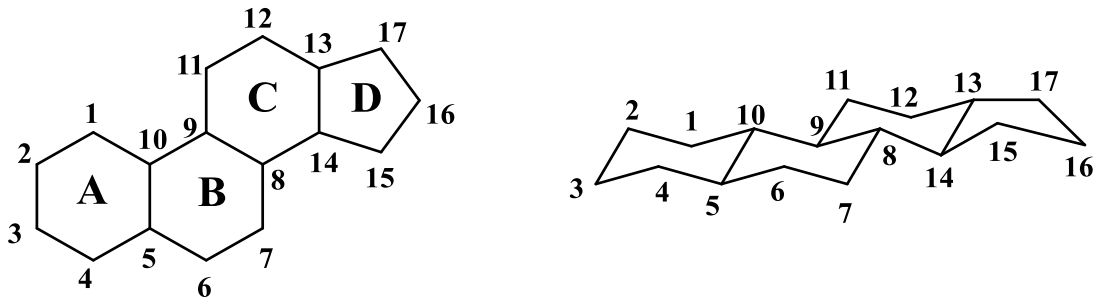


Figure 4 – Basic structure of steroid

Microbial transformation was first used in industry in 1952, when Murray and Peterson of the Upjohn Company reported the bioconversion of hormones, and steroidal drugs using microbial cultures, representing a key milestone in this field [123]. Since the 1950s, extensive research has been conducted on the derivatization of steroids like progesterone, and cortisol using microbial transformation [158].

One of the primary benefits of microbial transformation is its ability to change inactive or inaccessible sites on the steroid skeleton that are difficult to address with traditional chemical approaches. Such reactions frequently require expensive, and hazardous catalysts, making them less practical, and economically burdensome [159]. In contrast, microbial cultures provide an efficient, and site-specific solution that is both cost-effective and environmentally friendly. A diverse range of microorganisms have now been identified as capable of catalyzing reactions at nearly every point on the steroid core, decreasing synthesis steps and eliminating the requirement for complicated reagents in academic and industrial environments.

Examples of biotransformation include:

- *Curvularia* species allow androstenedione to undergo 11*α/β*-hydroxylation [160].
- The production of 7*α*,14*α*-dihydroxyprogesterone and 6*β*,14*α*-dihydroxyprogesterone by *Musor griseocyanus* [161].
- *Bacillus,* and *Mucor piriformis* strains efficiently convert the neuroactive steroid pregnenolone [162, 163].
- *Cunninghamella elegans,* and *Gibberella fujikuroi* produce different pregnenolone metabolites [164].

These examples demonstrate the wide spectrum of natural, and synthetic steroidal analogues with substantial therapeutic potential that can be produced through microbial transformation. Some recent biotransformed drugs are listed in Table 2, and shown in Figure 5.

Table 3 – Microbial transformation of some bioactive steroids

Compounds	Biological System	Transformation	Ref
Methasterone (21)	*Cunninghamella blakesleeana*, *Macrophimina phaseclina*	Hydroxylation, oxidation	[165]
Astragenol (22)	*Alternaria eureka*, *Neosartorya hiratsukae*	Hydroxylation cleavage, oxidation, epoxidation	[166]
Cycloastragenol (23)	*Alternaria eureka*, *Neosartorya hiratsukae*	Hydroxylation cleavage, oxidation, epoxidation	[166]
Methylstenbolone (24)	*Cunninghamella blakesleeana*, *Macrophimina phaseclina*	Hydroxylation, oxidation	[167]
Ethisterone (25)	*Cunninghamella blakesleeana*, *Aspergillus niger*	Hydroxylation	[168]
Testosterone (26)	*Aspergillus wenti*, *Cladosporium sphaeospermum*	Hydroxylation, dihydroxylation, trihydroxylation	[169]
Progesterone (27)	*Rhizopus microspores* var. *oligosporus*, *Aspergillus sojae*	Hydroxylation, Baeyer- Villiger oxidation	[170]
Neoruscogenin (28)	*Alternaria eureka*, *Neosartorya hiratsukae*	Cleavage, oxygenation, oxidation, acetylation, epoxidation, dehydration	[171]
Ruscogenins (29)	*Cunninghamella blakesleeana*	Hydroxylation, oxidation	[171]
Medrysone (30)	*Neurospora crassa*, *Cunninghamella blakesleeana*	Hydroxylation, oxidation	[172]
Spironolactone (31)	*Gibberella fujikuroi*, *Curvularia lunata*, *Fusarium lini*, *Aspergillus alliaceus*	Dehydrogenation, hydroxylation	[130]

Table 3 (continued)			
Mibolerone (32)	*Cunninghamella elegans*, *Cunninghamella blakesleeana*	Hydroxylation	[173]

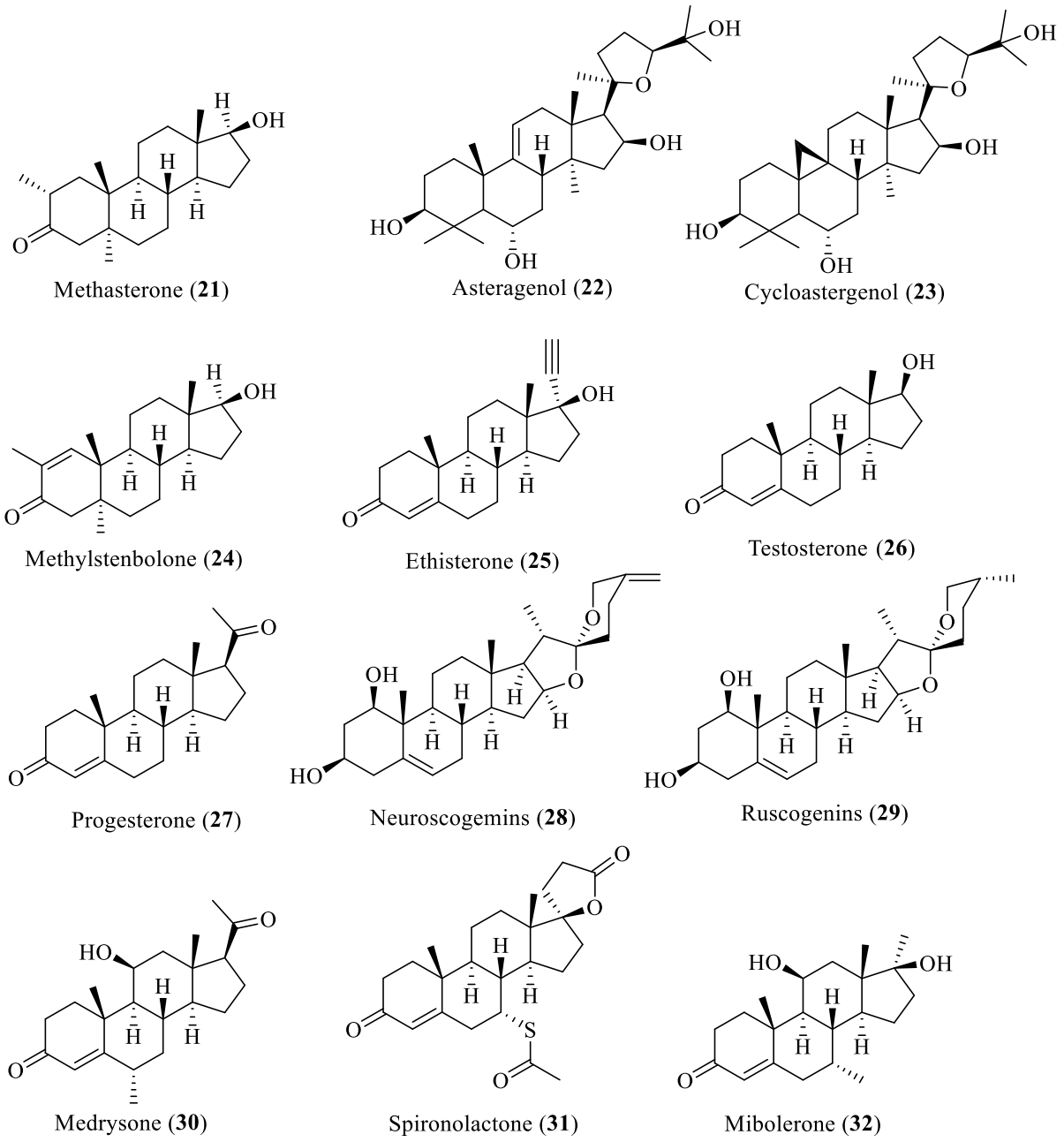


Figure 5 – Recently used steroidal drugs in biotransformation

2 Using advanced spectroscopic, and chromatographic techniques to study the phytochemical constituents of *Tussilago farfara* L

2.1 Introduction

Tussilago farfara L. (also known as coltsfoot) is a perennial herbaceous plant that belongs to the family Asteraceae and is the only species in the genus *Tussilago*. It is extensively recognized for its therapeutic potential, and induced in the pharmacopoeias of several countries [174]. Coltsfoot has been used traditionally in many cultures to treat respiratory disorders such as persistent cough, asthma, and bronchial infections [175]. In the United States, the roots are traditionally used to treat whooping cough, and asthma, whereas in Norway and other parts of Europe, dried and cut leaves are often incorporated into teas to treat chest problems [55]. Moreover, Chinese Traditional Medicine emphasizes the use of flower buds, which are often processed by honey-frying to increase detoxifying qualities, and reduce toxicity [36, 176].

Coltsfoot is used in European folk medicine to treat gastrointestinal problems, skin wounds, urinary tract infections, inflammatory, and eye ailments as well as in respiratory disorders [177]. This diverse range of applications highlights the plant's ethnobotanical relevance, and has prompted scientific research into its phytochemistry, and pharmacological properties.

Tussilago farfara has shown a wide range of biological features in contemporary pharmaceutical study [178]. These include anti-inflammatory [179], antioxidant [32, 180], antimicrobial [181], neuroprotective [182], platelet anti-aggregatory [183], and anticancer effects [45]. These bioactivities are attributed to its diverse chemical constituents, including alkaloids [184], flavonoids [182], chromones [37], phenolic acids [32], volatile oils [39], terpenoids [185], and sesquiterpenoids [38].

Among these chemicals, tussilagone (TSL) has gained special interest due to its anti-inflammatory, and antioxidant properties. However, the presence of pyrrolizidine alkaloids **(**PAs) in coltsfoot raises serious concerns due to their hepatotoxic, genotoxic, and carcinogenic effects. The concentration of PAs varies significantly depending on the plant part, region, and processing method [176]. To address these safety issues, attempts have begun to create coltsfoot variants free of PAs, such as those developed in Austria. Consequently, careful phytochemical characterization, quality control methods including, HPLC-ESI MS, direct infusion-ESI MS, HPTLC and HILIC/ESI-QTOF-MS are crucial when considering the coltsfoot-derived therapeutic products [186].

In addition to its medical applications, coltsfoot is consumed as a food component in some cultures, necessitating a better understanding of its safety profile. Furthermore, investigations into its ecology have revealed that the plant

reproduces efficiently via clonal development, which may have an impact on its phytochemical consistency, and potential for widespread cultivation [187].

Considering the rich phytochemical composition of *T. farfara*, and the reported biological activities, it is a good source for the discovery of new therapeutic agents. Leishmaniasis is a neglected tropical disease caused by *Leishmania* parasites, with approximately 350 million people in 88 countries are at risk of this infection. Current treatments limited by toxicity, cost, and drug resistance [188]. PTR1 plays a crucial role in the parasite folate and pterin metabolic pathway and serves as a metabolic bypass for dihydrofolate reductase (DHFR) inhibition, making it essential for parasite survival and an attractive target for antileishmanial drug development [189]. Therefore, the development of safe and effective antileishmanial agents is urgently needed to overcome the limitations of existing treatment [190].

Given the therapeutic potential of *Tussilago farfara* L., and the growing interest in isolating plant-derived bioactive compounds, there is an urgent need for comprehensive scientific investigations. This research aimed to investigate the phytochemical composition of *T. farfara* L. and assess its biological activities, particularly its antileishmanial potential. In addition, preliminary phytochemical investigations were conducted to identify steroid-like constituents that could serve as substrates for subsequent biotransformation studies. During fractionation, a sterol-type compound was detected and isolated from dichloromethane (DCM) fraction, which initially supported this approach. However, the compound was obtained in insufficient quantity and purity to enable extensive microbial transformation experiments and biological evaluation. Therefore, a commercially available steroidal substrate, methylprednisolone acetate, was selected as an alternative model compound for the biotransformation studies.

2.2 Experimental

2.2.1 General experimental conditions

Different techniques were applied to isolate various secondary metabolites from *Tussilago farfara* L., and to elucidate their structures.

2.2.2 Instrumental methods for structural characterization

The structures of the compounds were determined using 1D, 2D-NMR spectroscopy. The spectra were recorded on an Avance NMR spectrometer operating at 400, 500, 600, and 800 MHz (Bruker, Switzerland) in CD_3OD and $CDCl_3$. DEPT-90 and DEPT-135 experiments were performed to record the multiplicity of carbon signals. Mass spectra were recorded on HX 110 mass spectrometers equipped with a DA5000 data system and a JMS-600 instrument (Jeol, Japan). EI-MS analyses were performed at an ionization energy of 70 eV with a probe temperature of 250 °C. FAB-MS analyses were performed in positive-ion mode. The mass spectral data were acquired over the range *m/z* 5–3000. ESI-MS analyses were performed in

positive-ion mode over the mass range *m/z* 50–2000 using a capillary voltage of 4500 V, and a source temperature of 200 °C. The Bruker Vector 22 FT-IR spectrometer (France) was used for the IR analysis. Ultraviolet spectra were recorded in methanol using the Shimadzu UV-240 spectrophotometer (Shimadzu Corporation, Tokyo, Japan).

2.2.3 Chromatographic techniques

Normal-phase silica gel open-column chromatography (70-230 mesh, Merck, Germany) was used for fractionation, preparative TLC plates (20 × 20, 0.5 mm thickness, Merck, Germany), Sephadex LH-20 column chromatography (140–550 mesh, Sigma-Aldrich, USA), and normal-phase and reverse-phase HPLC (High-performance liquid chromatography) were employed for final purification. Under UV light, TLC plates were examined for fluorescent compounds at 366 nm, and for fluorescence quenching at 254 nm. Various spraying reagents, including vanillin, and ceric sulfate solution, were used to further visualize the spots on pre-coated TLC plates.

2.2.4 Ultra-performance liquid chromatography

Samples were analyzed using an ultra-performance liquid chromatography (UPLC) system an Agilent Technologies 1260 Infinity coupled with DAD. An Eclipse C18 column (4.6mm x 50mm, 5 µm particles size Agilent) was used for the chromatographic separation of metabolites. The solvent system was operated at a flow rate of 1 mL/min, which was adjusted before the experiment, and contained deionized water as mobile phase A and methanol as mobile phase B. The compounds were detected at 254 nm.

2.2.5 Plant materials

The aerial parts (8 kg) of the plant *Tussilago farfara* were collected in April 2023 from the Ile-Ala-Tau State National Natural Park near Almaty, Kazakhstan (42°48′30″–43°19′35″ N, 76°30′12″–77°50′27″ E; altitude: approximately 800 m above sea level). The plant materials were authenticated by Prof. G. T. Sitpayeva, Institute of Botany and Phytointroduction, Almaty, Kazakhstan, based on the Flora of Kazakhstan (Accession number: 3318). Figure 6 shows the buds and blooming flowers of *T. farfara* L.



Figure 6 – *Tussilago farfara* L. (**a**) flower buds and (**b**) blooming flowers

2.2.6 Extraction procedure

Air-dried buds of *Tussilago farfara* L. (8 kg) were sonicated for 40 minutes at 40°C in triplicate using 75% ethanol (20 L × 3). A rotary vacuum evaporator was used to concentrate all the crude extracts, resulting in a sticky residue (1.6 kg). After the crude extract was suspended in distilled water, it was fractionated using *n*-hexane, ethyl acetate, and *n*-BuOH (6 L × 3 for each solvent). All organic solvent fractions and water fraction were evaporated under low pressure and stored at –20°C for further isolation and purification. The study workflow is shown in Figure 7.

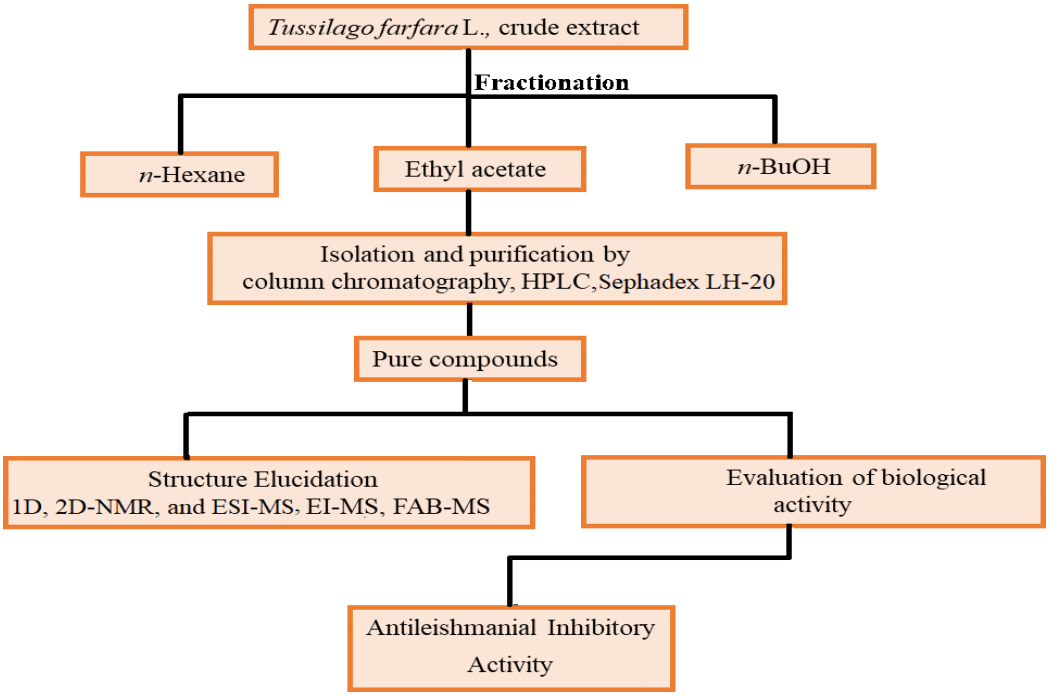


Figure 7 – Schematic diagram of purification, characterization, and biological activity of bioactive compounds of *Tussilago farfara* L

2.2.7 Isolation and purification

The EtOAc-soluble fraction (80 g) was subjected to column chromatography over silica gel (4000 g; 200-300 mesh). Initially, a gradient elution using *n*-hexane/EtOAc (100:0, 90:10, 80:20, 70:30, 60:40, 50:50, 40:60, 30:70, 20:80, 10:90, and 0:100 *v/v*; each 4 L) was employed, followed by EtOAc/MeOH (97:0, 95:5, 93:7, 90:10, 85:15, 80:20, 70:30, 50:50, and 0:100 *v/v*; each 4 L), yielding a total of 160 fractions. These were subsequently pooled into 16 subfractions based on thin-layer chromatography (TLC) profiles using *n*-hexane/EtOAc as the mobile phase and visualized via vanillin-sulfuric acid (VS) spray and heating. Fraction F-5 (1.3 g) was separated on silica gel (65 g, 300-400 mesh) using a gradient of EtOAc/MeOH (100:0, 98:2, 95:5, 93:7, 90:10, and 85:15 *v/v*; each 30 mL), yielding three subfractions (F5a-F5c). Subfraction F-5a (45 mg) was purified via Sephadex LH-20 chromatography (MeOH as eluent) to afford 10 fractions. Combined fractions 3-8 (20 mL each) afforded compounds 1 (5.3 mg, TLC: *n*-hexane/EtOAc 60:40; R_f = 0.4; detected under UV_{254} and VS spray), and 2 (4 mg, TLC: *n*-hexane/EtOAc 60:40; R_f = 0.5; detected under UV_{254} and VS spray). F-5b (126 mg) was chromatographed on silica gel (6.3 g, 300-400 mesh) using a stepwise gradient of DCM/MeOH (100:0, 99:1, 98:2, 97:3, 95:5, and 90:10 *v/v*; each 10 mL). Three subfractions were collected, from which compounds 3 (8.5 mg, TLC: DCM/MeOH 98:2; R_f = 0.5) and 4 (9 mg, TLC: *n*-hexane/EtOAc 4:6; R_f = 0.4) were isolated. Both compounds were visualized under UV_{254} and by VS spray. F-5c (114 mg) was fractionated using Sephadex LH-20 with MeOH as eluent. Combined fractions 3-4 (10 mL each) afforded compound 5 (6 mg, TLC: DCM/MeOH 97:3 with 1% acetic acid; R_f = 0.4; detection: as above). F-6 (20 mg) was processed via Sephadex LH-20 (MeOH, 10 mL/fraction), yielding compound 6 (4.5 mg, TLC: DCM/MeOH 97:3; R_f = 0.36; visualized under UV_{254} and iodine vapor). F-7 (320 mg) was subjected to column chromatography (16 g, 300-400 mesh) using a stepwise gradient of DCM/MeOH (100:0, 99:1, 98:2, 97:3, 95:5, 93:7, 90:10, 87:13, 84:16, and 80:20 *v/v*; each 10 mL). Two subfractions were collected, from which compounds 7 and 8 (30 mg and 4 mg; TLC: *n*-hexane/EtOAc 1:1 with 1% acetic acid, R_f = 0.59 and 0.53, respectively; UV_{254} detection and VS spray) were purified. Fraction 8 (3 g) was subjected to silica gel (150 g, 300-400 mesh), eluted with EtOAc/MeOH (100:0, 99:1, 98:2, 97:3, 95:5, 93:7, 90:10, 87:13, 84:16, and 80:20, *v/v*; each 50 mL), yielding three subfractions (F8a-F8c). F-8a (1g) was loaded on a Sephadex LH-20 column and washed with MeOH (50 mL/fraction), and combined fractions 34-38 yielded compound 9 (15 mg, TLC: *n*-hexane/EtOAc 1:1 with 1% acetic acid, R_f = 0.5; UV_{254} detection and VS spray). F-8b (1g) was similarly processed to afford compound 10 (7 mg, TLC: *n*-hexane/EtOAc 60:40 with 1.5% acetic acid, R_f = 0.44; UV_{254} detection and VS spray). F-8c (300 mg) was purified by silica gel column chromatography (15 g, 300-400 mesh), and eluted with gradient of EtOAc/DCM (100:0, 97:3, 95:5, 93:7, 90:10,

87:13, 84:16, and 80:20, *v/v*; each 10 mL), affording 30 subfractions. Combined fractions 3-14 (110 mL) were further subjected to a Sephadex LH-20 column (MeOH, 20 mL each fraction) to yield compounds 11 (100 mg, R_f = 0.5), 12 (80 mg, R_f = 0.35), and 13 (11 mg, R_f = 0.4; all analyzed by TLC using EtOAc/*n*-hexane 6:4 (*v/v*) with a few drops of acetic acid, and detected under UV_{254} and VS spray). F-9 (100 mg) was subjected to reverse-phase recycling HPLC (water/MeOH 50:50, 20 mL each fraction) to isolate compounds 14 (3 mg, t_R = 18.5 min, TLC: DCM/MeOH 95:5, R_f = 0.4), 15 (18 mg, t_R = 46 min, TLC: DCM/MeOH 95:5, R_f = 0.45), 16 (25 mg, t_R = 40 min, TLC: DCM/MeOH 90:10, R_f = 0.4), 17 (3 mg, t_R = 20 min, TLC: DCM/MeOH 90:10 with 1% acetic acid, R_f = 0.5), 18 (7 mg, t_R = 104 min, TLC: DCM/MeOH 90:10 (*v/v*) with few drops of acetic acid, R_f = 0.6), and 19 (4 mg, t_R = 100 min, TLC: DCM/MeOH 92:8 (*v/v*), with 1% acetic acid, R_f = 0.57). Eventually, F-10 (100 mg) was subjected to a Sephadex-LH-20 column chromatography (MeOH, 20 mL/fraction), afforded compound 20 (10 mg, TLC: DCM/MeOH 92:8 with 1% acetic acid, R_f = 0.6). All compounds 14-20 were visualized under UV_{254} and VS spray. The structures of all isolated compounds were elucidated using comprehensive spectroscopic techniques, including 1D and 2D-NMR, fast atom bombardment (FAB), and electron ionization mass spectrometry (EI-MS). Figure 8 represents the schematic diagram of the isolated compounds and Figure 9 shows the structures of elucidated compounds.

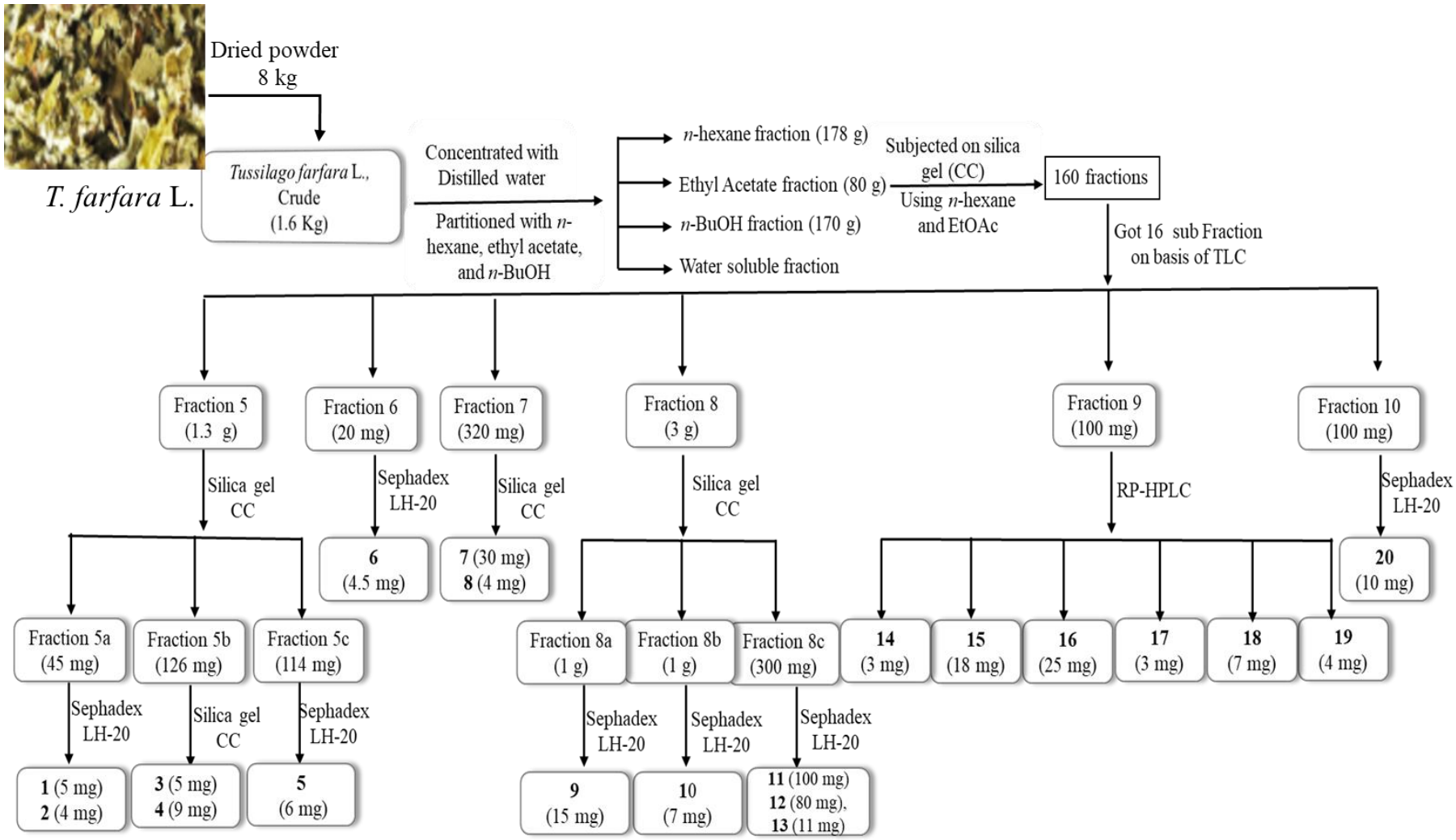
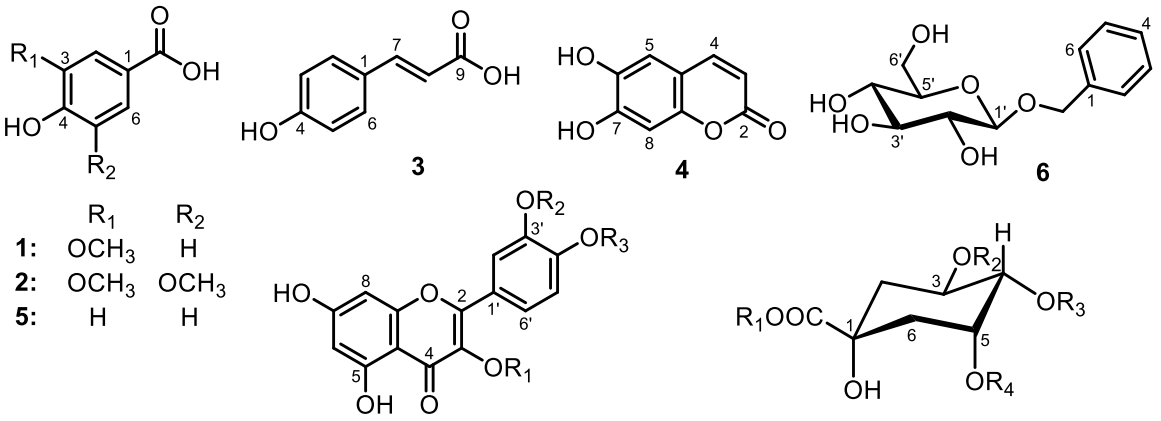


Figure 8 – Schematic diagrams of the isolated compounds from *Tussilago farfara* L



	R_1	R_2
1:	OCH_3	H
2:	OCH_3	OCH_3
5:	H	H

3 **4** **6**

	R_1	R_2	R_3
7:	OH	OH	OH
8:	OGlu	OH	OH
9:	OH	OH	OGlu
10:	ORut	OH	OH
11:	OH	H	OH
12:	OGlu	H	OH
13:	ORut	H	OH

	R_1	R_2	R_3	R_4
14:	H	Caffeoyl	H	Caffeoyl
15:	H	Caffeoyl	H	Caffeoyl
16:	H	Caffeoyl	Caffeoyl	H
17:	H	H	Caffeoyl	Caffeoyl
18:	CH_3	Caffeoyl	Caffeoyl	H
19:	CH_3	Caffeoyl	H	Caffeoyl
20:	CH_3	Caffeoyl	Caffeoyl	Caffeoyl

Figure 9 – Structures of isolated compounds from *Tussilago farfara* L

2.2.8 Spectroscopic and spectrometric data of isolated compounds

The structures of all isolated compounds were elucidated using 1D and 2D-NMR, including ^{13}C-NMR, and EI-MS, ESI-MS, and FAB-MS. The chemical structures are shown in Figure 9.

The mass spectrometric data of the isolated compounds are summarized in Table 4. The details of all purified compounds are provided below.

4-hydroxy-3-methoxybenzoic acid (1)

Common name	:	vanillic acid
Physical state	:	light yellowish powder
UV (MeOH) λ_{max} (nm)	:	282
IR (KBr disk) ν_{max} (cm^{-1})	:	3400–3100 (OH), 1688 (C=O)
Calculated monoisotopic mass	:	168.04
EI-MS *m/z* (observed)	:	168.2 ($M^{+\bullet}$)
Molecular formula	:	$C_8H_8O_4$
^{1}H-NMR (CD_3OD, 400 MHz) δ	:	Table 5

4-hydroxy-3,5-dimethoxybenzoic acid (2)

Common name	:	syringic acid
Physical state	:	white powder
UV (MeOH) λ_{max} (nm)	:	274
IR (KBr disk) ν_{max} (cm^{-1})	:	3300–2950 (OH), 1690

(C=O)

Calculated monoisotopic mass	:	198.05
EI-MS *m/z* (observed)	:	198.2 ($M^{+\bullet}$)
Molecular formula	:	$C_9H_{10}O_5$
^{1}H-NMR (CD_3OD, 400 MHz) δ	:	Table 6

(2E)-3-(4-hydroxyphenyl)prop-2-enoic acid (3)

Common name	:	*trans-p*-Coumaric acid
Physical state	:	white powder
UV (MeOH) λ_{max} (nm)	:	310
IR (KBr disk) ν_{max} (cm^{-1})	:	3500–3300 (OH), 1680 (C=O)
Calculated monoisotopic mass	:	164.05
EI-MS *m/z* (observed)	:	164.1 ($M^{+\bullet}$)
Molecular formula	:	$C_9H_8O_3$
^{1}H-NMR (acetone-d_6, 400 MHz) δ	:	Table 7

6,7-dihydroxy-2H-1-benzopyran-2-one (4)

Common name	:	esculetin
Physical state	:	light yellow powder
UV (MeOH) λ_{max} (nm)	:	360
IR (KBr disk) ν_{max} (cm^{-1})	:	3380–2990 (OH), 1715 (C=O)
Calculated monoisotopic mass	:	178.03
EI-MS *m/z* (observed)	:	178.1 ($M^{+\bullet}$)
Molecular formula	:	$C_9H_6O_4$
^{1}H-NMR (acetone-d_6, 400 MHz) δ	:	Table 8

4-Hydroxybenzoic acid (5)

Common name	:	*p*-Hydroxybenzoic acid
Physical state	:	white amorphous solid
UV (MeOH) λ_{max} (nm)	:	290
IR (KBr disk) ν_{max} (cm^{-1})	:	3450–2800 (OH), 1692 (C=O)
Calculated monoisotopic mass	:	138.03
EI-MS *m/z* (observed)	:	138.1 ($M^{+\bullet}$)
Molecular formula	:	$C_7H_6O_3$
^{1}H-NMR (CD_3OD, 400 MHz) δ	:	Table 9

(2R,3S,4S,5R,6R)-2-(hydroxymethyl)-6-(phenylmethoxy)oxane-3,4,5-triol (6)

Common name	:	benzyl *β*-D-glucoside
Physical state	:	white powder
UV (MeOH) λ_{max} (nm)	:	270

IR (KBr disk) ν_{max} (cm^{-1})	:	3430–3050 (OH), 2920 (aliphatic C-H), 1600 (C=C)
Calculated monoisotopic mass	:	270.11
ESI-MS *m/z* (observed)	:	271.1 $[M+H]^+$
Molecular formula	:	$C_{13}H_{18}O_6$
^{1}H-NMR (CD_3OD, 400 MHz) δ	:	Table 10

2-(3,4-dihydroxyphenyl)-3,5,7-trihydroxy-4H-chromen-4-one (7)

Common name	:	quercetin
Physical state	:	yellow powder
UV (MeOH) λ_{max} (nm)	:	302
IR (KBr disk) ν_{max} (cm^{-1})	:	3452–3100 (OH), 1665 (C=O)
Calculated monoisotopic mass	:	302.04
EI-MS *m/z* (observed)	:	302.3 ($M^{+\bullet}$)
Molecular formula	:	$C_{15}H_{10}O_7$
^{1}H-NMR (CD_3OD, 400 MHz) δ	:	Table 11

2-(3,4-dihydroxyphenyl)-5,7-dihydroxy-3-[(2S,5S,6R)-3,4,5-trihydroxy-6-(hydroxymethyl)oxan-2-yl]oxychromen-4-one (8)

Common name	:	quercetin-3-*O*-*β*-D-glucoside
Physical state	:	light yellow powder
UV (MeOH) λ_{max} (nm)	:	358
IR (KBr disk) ν_{max} (cm^{-1})	:	3400–3200 (OH), 1660 (C=O)
Calculated monoisotopic mass	:	464.10
ESI-MS *m/z* (observed)	:	465.1 $[M+H]^+$
Molecular formula	:	$C_{21}H_{20}O_{12}$
^{1}H-NMR (CD_3OD, 400 MHz) δ	:	Table 12

3,5,7-trihydroxy-2-[3-hydroxy-4-[3,4,5-trihydroxy-6-(hydroxymethyl)oxan-2-yl]oxyphenyl]chromen-4-one (9)

Common name	:	quercetin-4′-*O*-glucoside
Physical state	:	yellow powder
UV (MeOH) λ_{max} (nm)	:	356
IR (KBr disk) ν_{max} (cm^{-1})	:	3300–3100 (OH), 1690 (C=O)
Calculated monoisotopic mass	:	464.10
ESI-MS *m/z* (observed)	:	465.1 $[M+H]^+$
Molecular formula	:	$C_{21}H_{20}O_{12}$
^{1}H-NMR (CD_3OD, 400 MHz) δ	:	Table 13

2-(3,4-dihydroxyphenyl)-5,7-dihydroxy-3-[(2*S*,3*R*,4*S*,5*S*,6*R*)-3,4,5-trihydroxy-6-[[(2*R*,3*R*,4*R*,5*R*,6*S*)-3,4,5-trihydroxy-6-methyloxan-2-yl]oxymethyl]oxan-2-yl]oxychromen-4-one (10)

Common name	:	quercetin-3-rutinoside (Rutin)
Physical state	:	yellow crystal
UV (MeOH) λ_{max} (nm)	:	358
IR (KBr disk) ν_{max} (cm^{-1})	:	3410–3050 (OH), 2723 (C-H), 1664 (C=O)
Calculated monoisotopic mass	:	610.15
ESI-MS *m/z* (observed)	:	611.4 $[M+H]^+$
Molecular formula	:	$C_{27}H_{30}O_{16}$
^{1}H-NMR (CD_3OD, 400 MHz) δ	:	Table 14

3,5,7-trihydroxy-2-(4-hydroxyphenyl)-4H-chromen-4-one (11)

Common name	:	kaempferol
Physical state	:	yellow needle
UV (MeOH) λ_{max} (nm)	:	368
IR (KBr disk) ν_{max} (cm^{-1})	:	3420–3310 (OH), 1653 (C=O)
Calculated monoisotopic mass	:	286.05
EI-MS *m/z* (observed)	:	286.2 ($M^{+\bullet}$)
Molecular formula	:	$C_{15}H_{10}O_6$
^{1}H-NMR (CD_3OD, 400 MHz) δ	:	Table 15

5,7-dihydroxy-2-(4-hydroxyphenyl)-3-[(2*S*,3*R*,4*S*,5*S*,6*R*)-3,4,5-trihydroxy-6-(hydroxymethyl)oxan-2-yl]oxychromen-4-one (12)

Common name	:	astragalin
Physical state	:	yellow needle
UV (MeOH) λ_{max} (nm)	:	350
IR (KBr disk) ν_{max} (cm^{-1})	:	3350–3100 (OH), 1695 (C=O)
Calculated monoisotopic mass	:	448.10
ESI-MS *m/z* (observed)	:	449.1 $[M+H]^+$
Molecular formula	:	$C_{21}H_{20}O_{11}$
^{1}H-NMR (CD_3OD, 400 MHz) δ	:	Table 16

5,7-dihydroxy-2-(4-hydroxyphenyl)-3-[(2*S*,3*R*,4*S*,5*S*,6*R*)-3,4,5-trihydroxy-6-[[(2*R*,3*R*,4*R*,5*R*,6*S*)-3,4,5-trihydroxy-6-methyloxan-2-yl]oxymethyl]oxan-2-yl]oxychromen-4-one (13)

Common name	:	kaempferol 3-*O*-rutinoside
Physical state	:	yellow powder
UV (MeOH) λ_{max} (nm)	:	340

IR (KBr disk) ν_{max} (cm^{-1}) : 3370-2900 (OH), 1656 (C=O)
Calculated monoisotopic mass : 594.16
ESI-MS *m/z* (observed) : 595.3 $[M+H]^+$
Molecular formula : $C_{27}H_{30}O_{15}$
^{1}H-NMR (CD_3OD, 400 MHz) δ : Table 17

(1S, 3*R*, 4R, 5*R*)-3,5-bis[[(*E*)-3-(3,4-dihydroxyphenyl)prop-2-enoyl]oxy]-1,4-dihydroxycyclohexane-1-carboxylic acid (14)

Common name : 3,5-di-*O*-Caffeoylquinic acid
Physical state : brown powder
UV (MeOH) λ_{max} (nm) : 326
IR (KBr disk) ν_{max} (cm^{-1}) : 3400–3050, (OH), 1719 (carboxylic, C=O), 1680 (conjugated ester, C=O)
Calculated monoisotopic mass : 516.13
ESI-MS *m/z* (observed) : 517.1 $[M+H]^+$
Molecular formula : $C_{25}H_{24}O_{12}$
^{1}H-NMR (CD_3OD, 400 MHz) δ : Table 18

(1S, 3*R*, 4S, 5*R*)-3,5-bis[[(*E*)-3-(3,4-dihydroxyphenyl)prop-2-enoyl]oxy]-1,4-dihydroxycyclohexane-1-carboxylic acid (15)

Common name : 3,5-di-*O*-Caffeoylquinic acid
Physical state : brown powder
UV (MeOH) λ_{max} (nm) : 326
IR (KBr disk) ν_{max} (cm^{-1}) : 3420–3100 (OH), 1719 (carboxylic, C=O), 1680 (conjugated ester, C=O)
Calculated monoisotopic mass : 516.13
ESI-MS *m/z* (observed) : 517.1 $[M+H]^+$
Molecular formula : $C_{25}H_{24}O_{12}$
^{1}H-NMR (CD_3OD, 400 MHz) δ : Table 19

(1*S*,3*R*,4*S*,5*R*)-3,4-bis[[(*E*)-3-(3,4-dihydroxyphenyl)prop-2-enoyl]oxy]-1,5-dihydroxycyclohexane-1-carboxylic acid (16)

Common name : 3,4-Di-*O*-caffeoylquinic acid
Physical state : white powder
UV (MeOH) λ_{max} (nm) : 327
IR (KBr disk) ν_{max} (cm^{-1}) : 3350–3090 (OH), 1725 (carboxylic, C=O), 1687 (conjugated ester, C=O)
Calculated monoisotopic mass : 516.13
ESI-MS *m/z* (observed) : 517.1 $[M+H]^+$

Molecular formula	:	$C_{25}H_{24}O_{12}$
^{1}H-NMR (CD_3OD, 400 MHz) δ	:	Table 20

(1S,3R,4R,5R)-4,5-bis[[(E)-3-(3,4-dihydroxyphenyl)prop-2-enoyl]oxy]-1,5-dihydroxycyclohexane-1-carboxylic acid (17)

Common name	:	4,5-Di-*O*-caffeoylquinic acid
Physical state	:	white powder
UV (MeOH) λ_{max} (nm)	:	328
IR (KBr disk) ν_{max} (cm^{-1})	:	3400–3150 (OH), 1710 (carboxylic, C=O), 1694 (conjugated ester, C=O)
Calculated monoisotopic mass	:	516.13
ESI-MS *m/z* (observed)	:	517.1 $[M+H]^+$
Molecular formula	:	$C_{25}H_{24}O_{12}$
^{1}H-NMR (CD_3OD, 400 MHz) δ	:	Table 21

Methyl (1*S*,3*R*,4*R*,5*R*)-3,4-bis[[(*E*)-3-(3,4-dihydroxyphenyl)prop-2-enoyl]oxy]-1,5-dihydroxycyclohexane-1-carboxylate (18)

Common name	:	3,4-Di-*O*-caffeoylquinic acid methyl ester
Physical state	:	white powder
UV (MeOH) λ_{max} (nm)	:	326
IR (KBr disk) ν_{max} (cm^{-1})	:	3390–3150 (OH), 1704 (Non conjugated ester, C=O), 1698 (Conjugated ester, C=O)
Calculated monoisotopic mass	:	530.14
FAB-MS *m/z* (observed)	:	531.0 $[M+H]^+$
Molecular formula	:	$C_{26}H_{26}O_{12}$
^{1}H-NMR (CD_3OD, 400 MHz) δ	:	Table 22

Methyl (3*R*,5*R*)-3,5-bis[[(*E*)-3-(3,4-dihydroxyphenyl)prop-2-enoyl]oxy]-1,4-dihydroxycyclohexane-1-carboxylate (19)

Common name	:	3,5-Di-*O*-caffeoylquinic acid methyl ester
Physical state	:	white powder
UV (MeOH) λ_{max} (nm)	:	326
IR (KBr disk) ν_{max} (cm^{-1})	:	3410–3050 (OH), 1725 (Non conjugated ester, C=O), 1684 (Conjugated ester, C=O)
Calculated monoisotopic mass	:	530.14
FAB-MS *m/z* (observed)	:	531.3 $[M+H]^+$
Molecular formula	:	$C_{26}H_{26}O_{12}$
^{1}H-NMR (CD_3OD, 400 MHz) δ	:	Table 23

Methyl (3R,5R)-3,4,5-tris[[(E)-3-(3,4-dihydroxyphenyl)prop-2-enoyl]oxy]-1-hydroxycyclohexane-1-carboxylate (20)

Common name	:	3,4,5-Tri-*O*-caffeoylquinic acid methyl ester
Physical state	:	white powder
UV (MeOH) λ_{max} (nm)	:	330
IR (KBr disk) ν_{max} (cm^{-1})	:	3450–3100 (OH), 1720 (Non conjugated ester, C=O), 1670 (conjugated ester, C=O)
Calculated monoisotopic mass	:	692.17
ESI-MS *m/z* (observed)	:	693.1 $[M+H]^+$
Molecular formula	:	$C_{35}H_{32}O_{15}$
^{1}H-NMR (CD_3OD, 400 MHz) δ	:	Table 24

2.2.9 Enzyme inhibition studies

2.2.9.1 Antileishmanial activity

2.2.9.1.1 *Leishmania major* Pteridine reductase 1 (*Lm*PTR-1) inhibitory assay

Recombinant *Lm*PTR-1 was obtained via cloning of the PTR-1 gene into pET28a$^+$-TEV vector, followed by its expression in BL21 (DE3) cell line. The cloning, expression, and purification of the recombinant enzyme were carried out in collaboration with Prof. Dr. Humaira Zafar (HEJ Research Institute of Chemistry, Karachi, Pakistan). Subsequently, the recombinant enzyme was purified by HisTrap HP 5mL column chromatography following an optimized protocol (Figure 14) [200]. The *in vitro* inhibitory activity of the purified enzyme was assessed in a buffer containing 20 mM sodium acetate and 20 mM NaCl at pH 4.5 (adjusted using glacial acetic acid). A final DMSO level of 5% was applied to all samples, including controls, before the test compounds were dispensed into 96-well transparent polystyrene plates. Using a multi-channel pipette (Eppendorf Research® plus), the final reaction mixture including *Lm*PTR-1, biopterin and cytochrome C was added to each well. An ELISA spectrophotometer was used to record the initial absorbance at λ 550 nm after the 96-well plate was incubated for 10 minutes at 30°C. The reaction was started in the second phase by adding NADPH (final concentration: 500 μM), and it was then incubated for 40 minutes at 30°C [191]. The results were converted into percent inhibition values and analyzed using GraphPad Prism (version 8.0). Trimethoprim was used as the positive control, while the negative control consisted of the complete assay mixture containing *Lm*PTR-1 enzyme, biopterin, NADPH, and 5% DMSO, but without the test compound. All compounds were tested in triplicate (n = 3), and the results are expressed as mean ± standard deviation (SD). IC_{50} values were calculated by nonlinear regression analysis using a four-parameter logistic model in GraphPad Prism (Version 8), with 95% confidence intervals generated during curve fitting where applicable. Figure 15 shows the percent inhibition plot of compounds 15–18 along with standard (trimethoprim).

2.2.10 *In silico* studies

2.2.10.1 Molecular docking

To explore the ligand-receptor interaction profile and the physicochemical properties of the complex in a dynamic context, computational profiling of the prepared inhibitors (*in silico*) were performed. The protein (PDB ID: 1E92) was prepared for this purpose with the protein preparation wizard (Maestro, Schrödinger) [192]. The OPLS4 force field was used to minimize the protein by optimizing parameters such as forming disulfide bonds between cystines ≤ 3.2 Å apart, adding missing side chains and loops, removing water molecules beyond 5 Å of the hetero group, and forming zero-order bonds with metals [193].

Similarly, ligand preparation was carried out using LigPrep (an *in-built* suite in Maestro, Schrodinger) while preserving the ligands' original chiralities [194]. The next step was to build a receptor grid around the pteridine reductase-1 (PTR1) active site while retaining the cofactor NADPH. Thus, GLIDE (an integrated suite in Maestro and Schrodinger) was employed to dock in standard precision (SP) mode while keeping the ligand flexible [195]. Figure 17 shows molecular docking profiles of *Lm*PTR-1 complexes with compounds 15–18, along with standard inhibitor (trimethoprim).

2.2.10.2 Molecular dynamics (MD) simulations

A simulation study was also performed to examine protein-ligand interactions, focusing on the protein's conformational changes in a dynamic setting [196]. To evaluate the stability of the ligand-receptor protein over the 100 ns simulation period. Typical MD protocols include minimization, heating, equilibrium and production phases.

Thus, the default protocol was used to set up the OPLS4 force field. Using the TIP3P solvent model, the compounds were placed in a box with an orthorhombic shape, and the temperature maintained at 300 K using the NPT ensemble [197]. This was achieved by combining a Nose-Hoover chain thermostat with Martyna-Tobias-Klein barostat modules [198, 199]. Results were presented in the form of a simulated interaction diagram.

2.3 Results and discussion

Twenty secondary metabolites were purified from the ethyl acetate-soluble fraction of *T. farfara* using chromatographic techniques such as silica gel open column chromatography, Sephadex LH-20, and normal- and reverse-phase preparative recycling HPLC and UPLC. The purified compounds (1–20) [200], including vanillic acid (1), syringic acid (2), trans-*p*-coumaric acid (3), esculetin (4), *p*-hydroxybenzoic acid (5), benzoyl *β*-D-glucoside (6**)**, quercetin (7), isoquercitrin (8), quercetin 4′-*O*-glucoside (9), rutin (10), kaempferol (11), astragalin (12), kaempferol 3-*O*-rutinoside (13), (1S,3R,4R,5R)-3,5-di-*O*-caffeoylquinic acid (14), (1S,3R,4S,5R)-3,5-di-*O*-caffeoylquinic acid (15), 3,4-di-*O*-caffeoylquinic acid (16), 4,5-di-*O*-caffeoylquinic acid (17), 3,4-di-*O*-caffeoylquinic acid methyl ester (18), 3,5-di-*O*-caffeoylquinic acid methyl ester (19), and 3,4,5-tri-*O*-caffeoylquinic acid methyl ester (20) (Figure 9). The findings were based on extensive spectroscopic investigation, including 1D and 2D-NMR, FAB-MS, EI-MS, and ESI-MS and confirmed by comparison with previously published data.

Although *Tussilago farfara* is known to contain pyrrolizidine alkaloids (PAs) associated with safety concerns, none of the compounds isolated in the present study belonged to this class; however, the occurrence of PAs in other fractions should be considered in future safety evaluations of coltsfoot-derived therapeutic products.

The corresponding NMR and MS spectra, along with other supplementary characterization data, are provided in the Appendices. Mass spectrometric data for compounds 1–20 isolated from *Tussilago farfara* L., including molecular formula, ionization mode, ion type, calculated monoisotopic mass, and observed m/z values, are given in Table 4.

Table 4 – Mass spectrometric data of isolated compounds (1–20)

Compound	Molecular formula	Ionization mode	Ion type	Calculated monoisotopic mass (Da)	[a]Observed m/z	Figure [b]S
1	$C_8H_8O_4$	[c]EI	$M^{+\bullet}$	168.04	168.2	S3
2	$C_9H_{10}O_5$	EI	$M^{+\bullet}$	198.05	198.2	S4
3	$C_9H_8O_3$	EI	$M^{+\bullet}$	164.05	164.1	S5
4	$C_9H_6O_4$	EI	$M^{+\bullet}$	178.03	178.1	S6
5	$C_7H_6O_3$	EI	$M^{+\bullet}$	138.03	138.1	S7
6	$C_{13}H_{18}O_6$	[d]ESI (+)	$[M+H]^+$	270.11	271.1	S8
7	$C_{15}H_{10}O_7$	EI	$M^{+\bullet}$	302.04	302.3	S9
8	$C_{21}H_{20}O_{12}$	ESI (+)	$[M+H]^+$	464.10	465.1	S10
9	$C_{21}H_{20}O_{12}$	ESI (+)	$[M+H]^+$	464.10	465.1	S11
10	$C_{27}H_{30}O_{16}$	ESI (+)	$[M+H]^+$	610.15	611.4	S12
11	$C_{15}H_{10}O_6$	EI	$M^{+\bullet}$	286.05	286.2	S13

Table 4 (continued)						
12	$C_{21}H_{20}O_{11}$	ESI (+)	$[M+H]^+$	448.10	449.1	S14
13	$C_{27}H_{30}O_{15}$	ESI (+)	$[M+H]^+$	594.16	595.3	S15
14	$C_{25}H_{24}O_{12}$	ESI (+)	$[M+H]^+$	516.13	517.1	S16
15	$C_{25}H_{24}O_{12}$	ESI (+)	$[M+H]^+$	516.13	517.1	S19
16	$C_{25}H_{24}O_{12}$	ESI (+)	$[M+H]^+$	516.13	517.1	S20
17	$C_{25}H_{24}O_{12}$	ESI (+)	$[M+H]^+$	516.13	517.1	S21
18	$C_{26}H_{26}O_{12}$	[e]FAB (+)	$[M+H]^+$	530.14	531.0	S22
19	$C_{26}H_{26}O_{12}$	FAB (+)	$[M+H]^+$	530.14	531.3	S23
20	$C_{35}H_{32}O_{15}$	ESI (+)	$[M+H]^+$	692.17	693.1	S24

[a]Observed m/z: experimentally observed mass-to-charge ratio; [b]S: supplementary figure; [c]EI: electron ionization mass spectrometry (low-resolution); [d]ESI (+); electrospray ionization mass spectrometry in positive-ion mode (low-resolution); [e]FAB (+): fast atom bombardment mass spectrometry in positive-ion mode (low-resolution).

2.3.1 Optimization of UPLC

Optimization of ultra performance liquid chromatography (UPLC) conditions is essential to achieve efficient separation with reduced analysis time. In the present study, UPLC columns of different lengths (150, 100, and 50 mm) were evaluated to optimize chromatographic performance. Shorter columns, particularly C18 columns (50 mm), are widely reported to provide faster analysis with acceptable resolution, making them suitable for rapid screening of natural products [201]. Therefore, an Eclipse C18 column (4.6 × 50 mm, 5 µm) was selected due to its ability to deliver excellent separation within a shorter retention time, whereas longer columns required extended run times for comparable resolution. The mobile phase composition also plays a critical role in peak resolution and sensitivity. A binary solvent system consisting of water (A) and methanol (B) was employed which is commonly used in reversed-phase liquid chromatography [202]. Gradient elution is known to improve separation efficiency for compounds with varying polarity [203]. Accordingly, a gradient system starting from 90% A to 95% B was optimized to achieve effective separation within a 12-minute runtime, which is align with rapid UPLC screening protocols reported in the literature [204]. The use of a low injection volume (5 µL) and a flow rate of 1 mL/min ensured optimal peak shape and reproducibility. The chromatographic profile of *Tussilago farfara* L. exhibited well-resolved peaks, indicating high selectivity and sensitivity of the method. For instance, compound 7 showed a retention time of 6.92 minutes with a symmetrical peak and good baseline separation, suggesting adequate purity and efficient detection (Figure 10). Similar observations have been reported for UPLC-based phytochemical profiling, where sharp and symmetrical peaks indicate high column

efficiency and proper method optimization [201]. However, for complete purification, preparative reverse-phase HPLC was further employed, as UPLC is primarily a screening and analytical tool rather than a preparative technique.

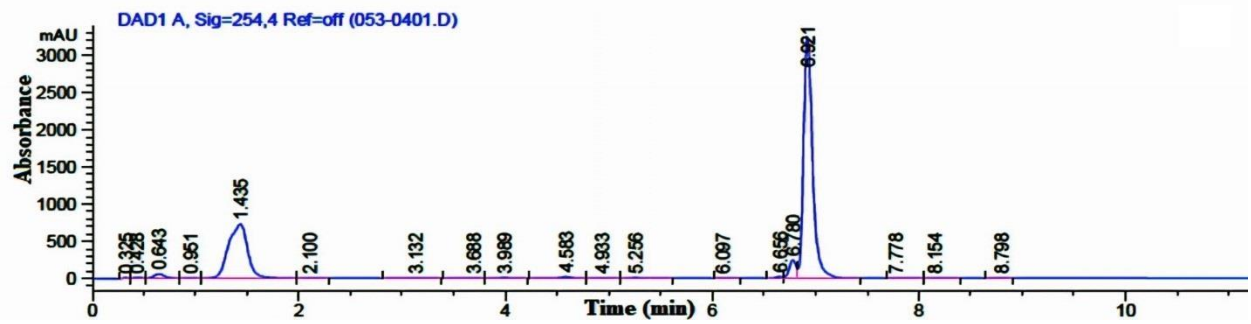


Figure 10 – UPLC-DAD chromatogram of quercetin (7) at 254 nm

Compound 10 exhibited a retention time of 0.88 minutes under the optimized UPLC conditions (Figure 11). Such early elution indicated that the compound has high polarity and weak interaction with the hydrophobic stationary phase, suggesting that the selected solvent system was not optimal for its retention compared to compound 7. In reversed-phase chromatography, highly polar compounds elute earlier due to reduced retention on the nonpolar stationary phase [203]. Despite this limitation, the chromatographic behavior provided useful insights into the compound's purity and polarity, confirming that compound 10 is more polar than compound 7. Based on this observation, the solvent system was subsequently adjusted during preparative HPLC to improve retention and achieve better purification.

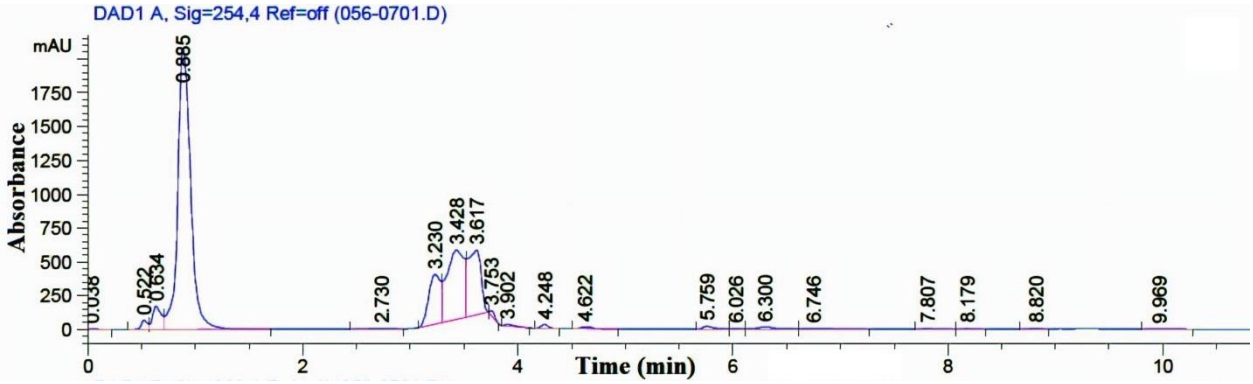


Figure 11 – UPLC-DAD chromatogram of quercetin-3-rutinoside (10) at 254 nm

To ensure reproducibility, all UPLC parameters and solvent conditions were kept constant. The chromatogram of kaempferol (11) in Figure 12 showed a retention time of 7.26 minutes with a sharp and well-resolved peak, indicating efficient separation. In reversed-phase chromatography, compounds with lower

polarity exhibit stronger interaction with the hydrophobic stationary phase and thus elute later [203]. Accordingly, kaempferol, being less polar than compounds 7 and 10, demonstrated a longer retention time due to increased hydrophobic interactions. This chromatographic behavior is consistent with literature reports and aids in distinguishing structurally related flavonoids based on polarity and retention characteristics [201].

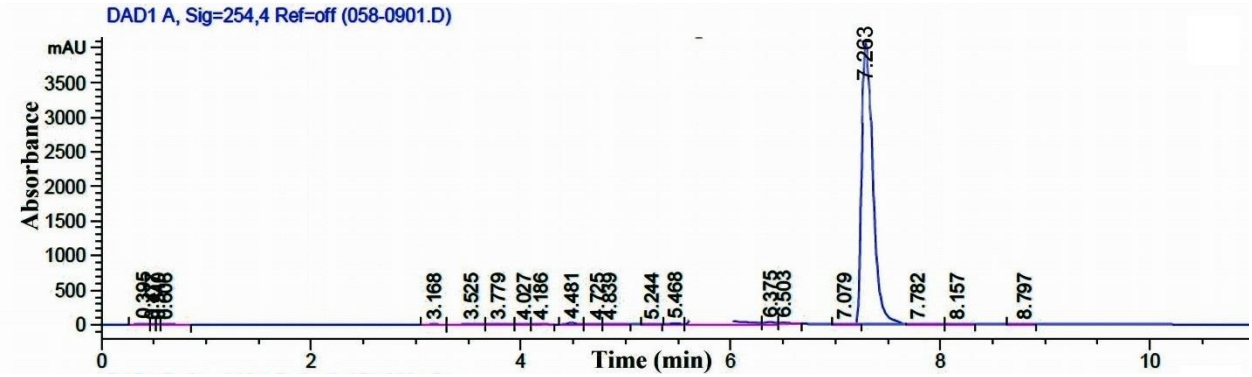


Figure 12 – UPLC-DAD chromatogram of kaempferol (11) at 254 nm

All chromatographic parameters were maintained constant to ensure consistency. Compounds 17, 16, and 15 exhibited retention times of 5.79, 6.28, and 6.73 minutes, respectively (Figure 13). Peak assignments were made based on retention times and correlation with spectral data. The slight differences in retention times suggest the presence of structural isomers or closely related analogues, where minor variations in stereochemistry and functional group orientation influence polarity and chromatographic behavior. Such differences are commonly observed in reversed-phase chromatography, where even small structural changes can affect retention [202, 203]. The relatively shorter retention times compared to compounds 7 and 11 indicate higher polarity. The chromatogram showed clear baseline separation and well-resolved peaks, demonstrating excellent selectivity and sensitivity. The semi-purified compounds were further purified using preparative reverse-phase HPLC.

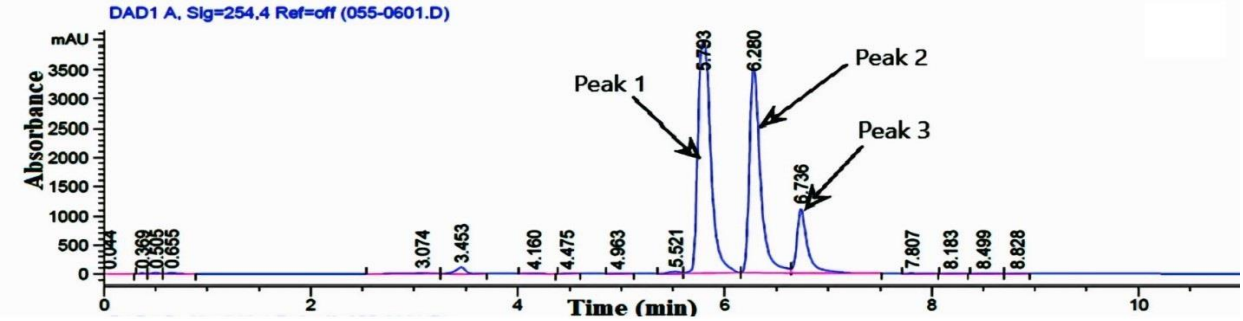


Figure 13 – UPLC-DAD chromatogram of compound 17 (Peak 1)**,** compound 16 (peak 2), and compound 15 (peak 3) at 254 nm

2.3.2 Structural elucidation

The ethyl acetate extract of *Tussilago farfara* L., was subjected to repeated column chromatography, which included open column silica gel chromatography, normal phase, reverse phase preparative recycling HPLC and Sephadex LH-20 chromatography to purify twenty secondary metabolites. To identify the purified compounds, various characterization techniques were used, including 1D, and 2D-NMR, EI-MS, ESI-MS, and FAB-MS. The identification of compounds 1–20 was based on spectroscopic data, which were then compared with previously published data. The chemical structures of all purified compounds are shown in Figure 9.

Vanillic acid (1)

Compound 1 was obtained as a light yellowish powder; EI-MS: *m/z* 168.2 ($M^{+\bullet}$), consistent with the molecular formula $C_8H_8O_4$. The IR spectrum exhibited characteristic absorptions for hydroxyl and carbonyl groups at 3400-3100 cm^{-1} (OH), and 1688 cm^{-1} (C=O), respectively. Based on the analysis of ^{1}H-NMR, and EI-MS, as well as comparisons with previously reported spectral data, the structure of compound 1 was deduced as vanillic acid [205]. This compound was isolated from the *T. farfara* for the first time. The ^{1}H-NMR spectral data are given in Table 5, while the corresponding ^{1}H-NMR and mass spectra are provided in Appendix A (Figures S3).

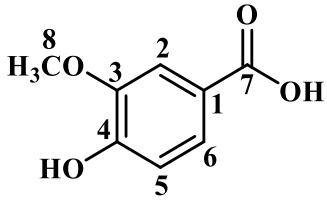


Table 5 – ^{1}H-NMR chemical shift data of compound 1

Carbon	δ_H (*J* in Hz)	Multiplicity
1	-	[a]C
2	7.57, d, *J* = 1.6 Hz, 1H	CH
3	-	C
4	-	C
5	6.75, d, *J* = 8.4 Hz, 1H	CH
6	7.47, dd, $J_{6/5,\ 6/2}$ = 8.0 Hz, 2.0 Hz, 1H	CH
7	-	C
8	3.87, s, 3H	CH_3

[a]C: quaternary carbons

Syringic acid (2)

Compound 2 was obtained as a white powder; EI-MS: *m/z* 198.2 ($M^{+\bullet}$), consistent with the molecular formula $C_9H_{10}O_5$. The IR spectrum showed characteristic absorptions for hydroxyl and carbonyl at 3300-2950 cm^{-1} (OH), and 1690 cm^{-1} (C=O), respectively. Based on the analysis of NMR, and EI-MS, and comparison with previously published data, the structure of compound 2 was assigned as syringic acid [206]. The ^{1}H-NMR spectral data are presented in Table 6, while the corresponding ^{1}H-NMR and mass spectra are provided in Appendix A (Figures S4).

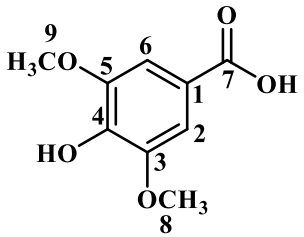


Table 6 – ^{1}H-NMR chemical shift data of compound 2

Carbon	δ_H (*J* in Hz)	Multiplicity
1	-	[a]C
2	7.31, s, 1H	CH
3	-	C
4	-	C
5	-	C
6	7.31, s, 1H	CH
7	-	C
8	3.8, s, -OCH_3, 3H	CH_3
9	3.8, s, -OCH_3, 3H	CH_3

[a]C: quaternary carbons

***trans-p*-Coumaric acid (3)**

Compound 3 was obtained as a white powder; EI-MS: *m/z* 164.1 ($M^{+\bullet}$), consistent with the molecular formula $C_9H_8O_3$. The IR spectrum exhibited characteristic absorptions for hydroxyl, and carbonyl groups at 3500-3300 cm^{-1} (OH), and 1680 cm^{-1} (C=O), respectively. Based on the NMR, and EI-MS spectral analysis, as well as comparison with previously reported data compound 3 was deduced as *trans-p*-Coumaric acid [207]. The ^{1}H NMR spectral data are given in Table 7. The corresponding ^{1}H-NMR and mass spectra are provided in Appendix A (Figures S5).

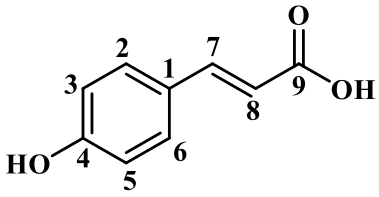


Table 7 – ^{1}H-NMR chemical shift data of compound 3

Carbon	δ_H (*J* in Hz)	Multiplicity
1	-	[a]C
2	7.42, d, *J* = 8.8 Hz, 1H	CH

Table 7 (continued)		
3	6.79, d, *J* = 8.8 Hz, 1H	CH
4	-	C
5	6.79, d, *J* = 8.8 Hz, 1H	CH
6	7.42, d, *J* = 8.8 Hz, 1H	CH
7	7.53, d, *J* = 16.0 Hz, 1H	CH
8	6.30, d, *J* = 16.0 Hz, 1H	CH
9	-	C

[a]C: quaternary carbons

Esculetin (4)

Compound 4 was obtained as a yellow powder; EI-MS: *m/z* 178.1 ($M^{+\bullet}$), consistent with the molecular formula $C_9H_6O_4$. The IR spectrum showed absorptions at 3380-2990 cm^{-1} (OH), and 1715 cm^{-1} (C=O), respectively. Based on NMR, and EI-MS analyses, together with comparison with literature data, the structure of compound 4 was assigned as esculetin [208]. The ^{1}H-NMR spectral data are presented in Table 8. The corresponding ^{1}H-NMR and mass spectra are provided in Appendix A (Figure S6).

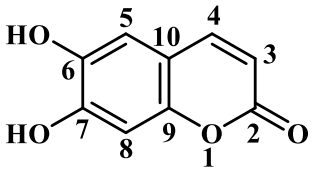


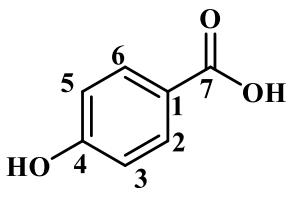
Table 8 – ^{1}H-NMR chemical shift data of compound 4

Carbon	δ_H (*J* in Hz)	Multiplicity
1	-	*
2	-	[a]C
3	5.99, d, *J* = 9.6 Hz, 1H	CH
4	7.69, d, *J* = 9.6 Hz, 1H	CH
5	6.88, s, 1H	CH
6	-	C
7	-	C
8	6.63, s, 1H	CH
9	-	C
10	-	C

*: oxygen atom at this position (no ^{1}H or ^{13}C NMR signal); [a]C: quaternary carbons

***p*-Hydroxybenzoic acid (5)**

Compound 5 was obtained as a yellow powder; EI-MS: *m/z* 138.1 ($M^{+\bullet}$), consistent with the molecular formula $C_7H_6O_3$. The IR spectrum exhibited characteristic peaks for hydroxyl, and carbonyl functionalities 3450-2800 cm^{-1} (OH), and 1692 cm^{-1} (C=O), respectively. Based on NMR, and EI-MS analyses,



together with comparison with literature data compound 5 was deduced as *p*-Hydroxybenzoic acid [209]. The ^{1}H-NMR spectral data are given in Table 9, while the corresponding ^{1}H-NMR and mass spectra are provided in Appendix A (Figure S7).

Table 9 – ^{1}H-NMR chemical shift data of compound 5

Carbon	δ_H (*J* in Hz)	Multiplicity
1	-	[a]C
2	7.87, d, *J* = 8.4 Hz, 1H	CH
3	6.80, d, *J* = 8.4 Hz, 1H	CH
4	-	[a]C
5	6.80, d, *J* = 8.4 Hz, 1H	CH
6	7.87, d, *J* = 8.4 Hz, 1H	CH
7	-	C

[a]C: quaternary carbons

Benzyl *β*-D-glucoside (6)

Compound 6 was obtained as a white powder; ESI-MS (+): *m/z* 271.1 $[M+H]^{+}$, consistent with the molecular formula $C_{13}H_{18}O_6$. IR spectrum exhibited the absorptions at 3430-3050 cm^{-1} (OH), and 1600 cm^{-1} (C=C), respectively. Based on NMR and ESI-MS analyses, together with comparison of the obtained spectral data with previously reported data, confirmed the structure of compound 6 as benzyl *β*-D-glucoside [210]. The ^{1}H-NMR spectral data are presented in Table 10. The corresponding ^{1}H-NMR and mass spectra are provided in Appendix A (Figure S8).

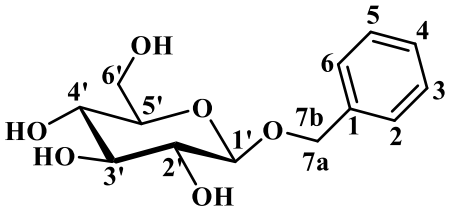


Table 10 – ^{1}H-NMR chemical shift data of compound 6

Carbon	δ_H (*J* in Hz)	Multiplicity
1	-	[a]C
2	7.43, brd, *J* = 7.2 Hz, 1H	CH
3	7.34, dd, *J* = 7.6 Hz, 6.8 Hz, 1H	CH
4	7.28, d, *J* = 6.8 Hz, 1H	CH
5	7.34, dd, $J_{5/6,\ 5/4}$ = 7.6 Hz, 6.8 Hz, 1H	CH
6	7.43, brd, *J* = 7.2 Hz, 1H	CH
7[a]	4.85, d, *J* = 10.5 Hz, 1H	CH
7b	4.68, d, *J* = 12.0 Hz, 1H	CH
1′	4.36, d, *J* = 7.6 Hz, 1H	CH
2′	3.21-3.31, m, 1H	CH

Table 10 (continued)		
3′	3.21-3.31, m, 1H	CH
4′	3.21-3.31, m, 1H	CH
5′	3.21-3.31, m, 1H	CH
6′ a	3.88, dd, $J_{6a'/5', 6a'/4'}$ = 2.0 Hz, 1.6 Hz, 1H	CH
6′ b	3.91, dd, $J_{6b'/5', 6b'/4'}$ = 11.6 Hz, 5.5 Hz, 1H	CH

[a]C: quaternary carbons

Quercetin (7)

Compound 7 was obtained as a yellow powder; EI-MS: *m/z* 302.3 ($M^{+\bullet}$), consistent with the molecular formula $C_{15}H_{10}O_7$. The IR spectrum displayed absorptions at 3452-3100 cm^{-1}(OH), and 1665 cm^{-1} (C=O), respectively. Based on NMR, and EI-MS spectral analyses as well as comparison with published data, the structure of compound 7 was deduced as quercetin [211]. The ^{1}H-NMR spectral data are given in Table 11, while the corresponding ^{1}H-NMR and mass spectra are provided in Appendix A (Figure S9).

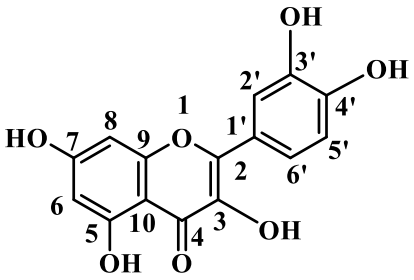


Table 11 – ^{1}H-NMR chemical shift data of compound 7

Carbon	δ_H (*J* in Hz)	Multiplicity
1	-	*
2	-	[a]C
3	-	C
4	-	C
5	-	C
6	6.25, d, *J* = 1.6 Hz, 1H	CH
7	-	C
8	6.51, d, *J* = 1.6 Hz, 1H	CH
9	-	C
10	-	C
1′	-	C
2′	7.81, d, *J* = 2.0 Hz, 1H	CH
3′	-	C
4′	-	C
5′	6.99, d, *J* = 8.4 Hz, 1H	CH
6′	7.69, dd, $J_{6'/5', 6'/2'}$ = 8.4 Hz, 2.0 Hz, 1H	CH

*: oxygen atom at this position (no ^{1}H or ^{13}C NMR signal); [a]C: quaternary carbons

Quercetin-3-*O*-*β*-D-glucoside (8)

Compound 8 was obtained as a yellow powder; ESI-MS (+): *m/z* 465.1 $[M+H]^+$, corresponding with the molecular formula $C_{21}H_{20}O_{12}$. Hydroxyl, and carbonyl functionalities showed absorptions at 3400-3200 cm^{-1} (OH), 1660 cm^{-1} (C=O), respectively in IR spectrum. Based on NMR, and ESI-MS, as well as comparison with previously reported data compound 8 was assigned as quercetin-3-*O*-*β*-D-glucoside [212]. The ^{1}H-NMR spectral data are presented in Table 12. The corresponding ^{1}H-NMR and mass spectra are provided in Appendix A (Figure S10).

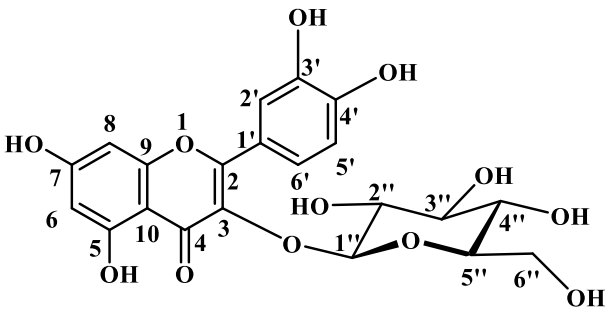


Table 12 – ^{1}H-NMR chemical shift data of compound 8

Carbon	δ_H (*J* in Hz)	Multiplicity
1	-	*
2	-	[a]C
3	-	C
4	-	C
5	-	C
6	6.18, d, *J* = 1.8 Hz, 1H	CH
7	-	C
8	6.39, d, *J* = 2.0 Hz, 1H	CH
9	-	C
10	-	C
1′	-	C
2′	7.70, d, *J* = 2.0 Hz, 1H	CH
3′	-	C
4′	-	C
5′	6.87, d, *J* = 2.0 Hz, 1H	CH
6′	7.59, dd, $J_{6'/5',\ 6'/2'}$ = 8.4 Hz, 2.6 Hz, 1H	CH
1″	5.25, d, *J* = 7.6 Hz, 1H	CH
2″	3.72, dd, $J_{2''/1'',\ 2''/3''}$ = 11.9 Hz, 2.2 Hz, 1H	CH
3″	3.58, dd, $J_{3''/2'',\ 3''/4''}$ = 11.9 Hz, 5.3 Hz, 1H	CH
4″	3.49, m, 1H	CH
5″	3.41-3.35, m, 1H	CH
6″	3.22, m, 2H	CH_2

*: oxygen atom at this position (no ^{1}H or ^{13}C NMR signal); [a]C: quaternary carbons

Quercetin-4′-*O*-glucoside (9)

Compound 9 was obtained as a yellow powder; ESI-MS (+): *m/z* 465.1 $[M+H]^+$, consistent with the molecular formula $C_{21}H_{20}O_{12}$. The IR spectrum exhibited absorptions at 3300-3100 cm^{-1} (OH), and 1660 cm^{-1} (C=O), respectively. Based on NMR, ESI-MS spectral data analyses and comparison with previously reported data the compound 9 was deduced as quercetin-4′-*O*-glucoside [213]. The ^{1}H-NMR spectral data are presented in Table 13, while the corresponding ^{1}H-NMR and mass spectra are provided in Appendix A (Figure S11).

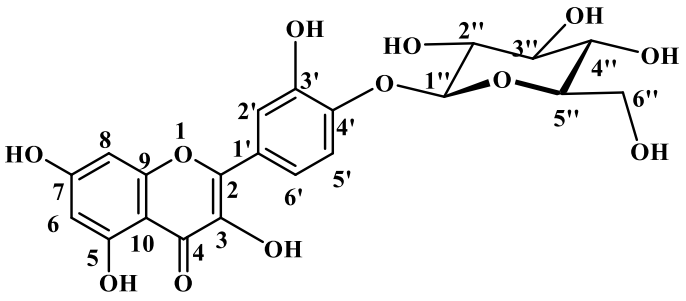


Table 13 – ^{1}H-NMR chemical shift data of compound 9

Carbon	δ_H (*J* in Hz)	Multiplicity
1	-	*
2	-	[a]C
3	-	C
4	-	C
5	-	C
6	6.19, d, *J* = 1.9 Hz, 1H	CH
7	-	C
8	6.40, d, *J* = 2.1 Hz, 1H	CH
9	-	C
10	-	C
1′	-	C
2′	7.77, d, *J* = 1.9 Hz, 1H	CH
3′	-	C
4′	-	C
5′	7.32, d, *J* = 8.6 Hz, 1H	CH
6′	7.73, dd, $J_{6'/5', 6'/2'}$ = 8.6 Hz, 1.9 Hz, 1H	CH
1″	4.91, d, *J* = 7.6 Hz, 1H	CH
2″	3.95, dd, $J_{2''/1'', 2''/3'}$ = 12.0 Hz, 1.7 Hz, 1H	CH
3″	3.76, dd, $J_{3''/2'', 3''/4''}$ = 11.9 Hz, 5.3 Hz, 1H	CH
4″	3.40-3.57, m, 1H	CH
5″	3.40-3.57, m, 1H	CH
6″	3.40-3.57, m, 2H	CH_2

*: oxygen atom at this position (no ^{1}H or ^{13}C NMR signal); [a]C: quaternary carbons

Quercetin-3-rutinoside (10)

Compound 10 was obtained as a yellow solid; ESI-MS (+): *m/z* 611.4 $[M+H]^+$, corresponding with the molecular formula $C_{27}H_{30}O_{16}$. The IR spectrum exhibited characteristic absorptions for hydroxyl, and carbonyl groups at 3410-3050 cm^{-1} (OH), 1664 cm^{-1} (C=O), respectively. Based on spectral analysis of NMR, ESI-MS, and comparison with previous published data the structure of compound 10 was assigned as quercetin-3-rutinoside [211]. The ^{1}H-NMR spectral data are presented in Table 14. The ^{1}H-NMR and mass spectra are shown in Appendix A (Figure S12).

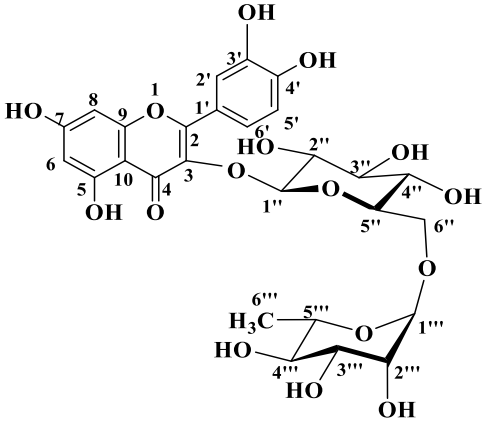


Table 14 – ^{1}H-NMR chemical shift data of compound 10

Carbon	δ_H (*J* in Hz)	Multiplicity
1	-	*
2	-	[a]C
3	-	C
4	-	C
5	-	C
6	6.04, d, *J* = 2.0 Hz, 1H	CH
7	-	C
8	6.19, d, *J* = 1.6 Hz, 1H	CH
9	-	C
10	-	C
1′	-	C
2′	7.66, d, *J* = 2.0 Hz, 1H	CH
3′	-	C
4′	-	C
5′	6.84, d, *J* = 8.4 Hz, 1H	CH
6′	7.63, dd, $J_{6'/5', 6''/2'}$ = 8.4 Hz, 2.0 Hz, 1H	CH
1″	4.94, d, *J* = 7.7 Hz, 1H	CH
2″	4.51, brs, 1H	CH
3″	3.82, dd, $J_{3''/2'', 3''/4''}$ = 10.8 Hz, 6.0 Hz, 1H	CH
4″	3.64, dd, $J_{4''/5'', 4''/3''}$ = 3.4 Hz, 1.6 Hz, 1H	CH
5″	3.57, m, 1H	CH
6″	3.55, m, 2H	CH_2
1‴	3.48-3.33, m, 1H	CH

Table 14 (continued)		
2‴	3.48-3.33, m, 1H	CH
3‴	3.48-3.33, m, 1H	CH
4‴	3.48-3.33, m, 1H	CH
5‴	3.48-3.33, m, 1H	CH
6‴	1.16, d, $J_{6'''/5'''}$ = 6.0 Hz, 3H	CH_3

*: oxygen atom at this position (no ^{1}H or ^{13}C NMR signal); [a]C: quaternary carbons

Kaempferol (11)

Compound 11 was obtained as a yellow powder; EI-MS: *m/z* 286.2 ($M^{+\bullet}$), consistent with the molecular formula $C_{15}H_{10}O_6$. The IR spectrum exhibited absorptions at 3420-3310 cm^{-1} (OH), and 1653 cm^{-1} (C=O), respectively. Based on NMR, and EI-MS spectral analyses, as well as comparisons with previously reported data, the structure of compound 11 was deduced as kaempferol [214]. The ^{1}H-NMR spectral data are presented in Table 15, while the corresponding ^{1}H-NMR and mass spectra are provided in Appendix A (Figure S13).

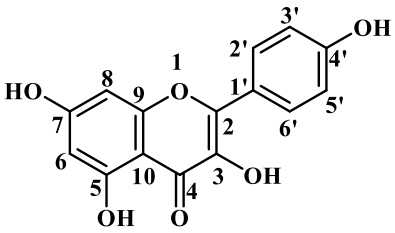


Table 15 – ^{1}H-NMR chemical shift data of compound 11

Carbon	δ_H (*J* in Hz)	Multiplicity
1	-	*
2	-	[a]C
3	-	C
4	-	C
5	-	C
6	6.18, d, $J_{6/8}$ = 2.0 Hz, 1H	CH
7	-	C
8	6.39, d, $J_{8/6}$ = 2.0 Hz, 1H	CH
9	-	C
10	-	C
1′	-	C
2′	8.10, d, $J_{3'/2', 5'/6'}$ = 8.8 Hz, 1H	CH
3′	6.92, d, $J_{3'/2', 5'/6'}$ = 8.8 Hz, 1H	CH
4′	-	C
5′	6.92, d, $J_{3'/2', 5'/6'}$ = 8.8 Hz, 1H	CH
6′	8.10, d, $J_{3'/2', 5'/6'}$ = 8.8 Hz, 1H	CH

*: oxygen atom at this position (no ^{1}H or ^{13}C NMR signal); [a]C: quaternary carbons

Kaempferol 3-*O*-glucoside (12)

Compound 12 was obtained as a yellow needle; ESI-MS (+): *m/z* 449.1 $[M+H]^+$, consistent with the molecular formula $C_{21}H_{20}O_{11}$. The hydroxyl, and carbonyl functionalities showed absorptions at 3350-3100 cm^{-1} (OH), 1695 cm^{-1} (C=O), respectively in the IR spectrum. Based on NMR, and ESI-MS spectral analysis, and comparison with previously reported data, the structure of compound 12 was identified as kaempferol 3-*O*-glucoside [215]. The ^{1}H-NMR spectral data are given in Table 16. The ^{1}H-NMR and mass spectra are shown in Appendix A (Figure S14).

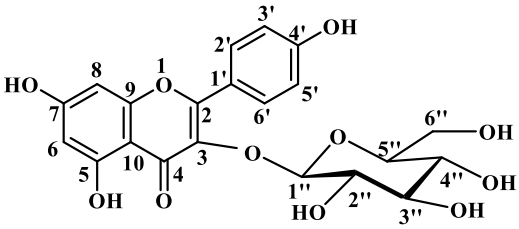


Table 16 – ^{1}H-NMR chemical shift data of compound 12

Carbon	δ_H (*J* in Hz)	Multiplicity
1	-	*
2	-	[a]C
3	-	C
4	-	C
5	-	C
6	6.05, d, $J_{6/8}$ = 2.0 Hz, 1H	CH
7	-	C
8	6.20, d, $J_{8/6}$ = 2.0 Hz, 1H	CH
9	-	C
10	-	C
1′	-	C
2′	8.02, d, $J_{2'/3', 6'/5'}$ = 8.8 Hz, 1H	CH
3′	6.85, d, $J_{3'/2', 5'/6'}$ = 8.8 Hz, 1H	CH
4′	-	C
5′	6.85, d, $J_{3'/2', 5'/6'}$ = 8.8 Hz, 1H	CH
6′	8.02, d, $J_{2'/3', 6'/5'}$ = 8.8 Hz, 1H	CH
1″	5.08, d, $J_{1''/2''}$ = 7.6 Hz, 1H	CH
2″	3.35, m, 1H	CH
3″	3.30, m, 1H	CH
4″	3.27, m, 1H	CH
5″	3.18, m, 1H	CH
6″	3.66, m, 2H	CH_2

*: oxygen atom at this position (no ^{1}H or ^{13}C NMR signal); [a]C: quaternary carbons

Kaempferol 3-*O*-rutinoside (13)

Compound 13 was obtained as a yellow powder; ESI-MS (+): *m/z* 595.3 $[M+H]^+$, consistent with the molecular formula $C_{27}H_{30}O_{15}$. The IR spectrum showed absorptions at 337-2900 cm^{-1} (OH), and 1656 cm^{-1} (C=O), respectively. Based on NMR, and ESI-MS spectral analysis as well as comparisons with previously reported data, the structure of compound 13 was deduced as kaempferol 3-*O*-rutinoside [216]. The ^{1}H-NMR spectral data are presented in Table 17, while the corresponding ^{1}H-NMR and mass spectra are provided in Appendix A (Figure S15).

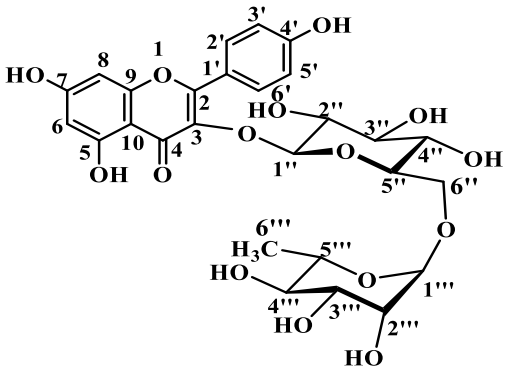


Table 17 – ^{1}H-NMR chemical shift data of compound 13

Carbon	δ_H (*J* in Hz)	Multiplicity
1	-	*
2	-	[a]C
3	-	C
4	-	C
5	-	C
6	6.05, d, $J_{6/8}$ = 2.0 Hz, 1H	CH
7	-	C
8	6.19, d, $J_{8/6}$ = 1.6 Hz, 1H	CH
9	-	C
10	-	C
1′	-	C
2′	8.05, d, $J_{2'/3', 6'/5'}$ = 8.8 Hz, 1H	CH
3′	6.87, d, $J_{3'/2', 5'/6'}$ = 8.8 Hz, 1H	CH
4′	-	C
5′	6.87, d, $J_{3'/2', 5'/6'}$ = 8.8 Hz, 1H	CH
6′	8.05, d, $J_{2'/3', 6'/5'}$ = 8.8 Hz, 1H	CH
1″	4.98, d, $J_{1''/2''}$ = 7.4 Hz, 1H	CH
2″	3.19, m, 1H	CH
3″	3.25, m, 1H	CH
4″	3.10, m, 1H	CH
5″	3.35, m, 1H	CH
6a″	3.82, d, $J_{6a''/5''}$ = 9.4 Hz, 1H	CH
6b″	3.50, bd, $J_{6b''/5''}$ = 10.0 Hz, 1H	CH

Table 17 (continued)		
1‴	4.51, s, 1H	CH
2‴	3.35, m, 1H	CH
3‴	3.65, brs, m, 1H	CH
4‴	3.15, m, 1H	CH
5‴	3.65, brs, 1H	CH
6‴	1.15, d, $J_{6'''/5'''}$ = 6.0 Hz, 3H	CH_3

*: oxygen atom at this position (no ^{1}H or ^{13}C NMR signal); [a]C: quaternary carbons

(1*S*,3*R*,4*R*,5*R*)-3,5-Di-*O*-caffeoylquinic acid (14)

Compound 14 was obtained as a brown powder; ESI-MS (+): *m/z* 517.1 $[M+H]^+$, corresponding with the molecular formula $C_{25}H_{24}O_{12}$. The IR spectrum exhibited absorptions at 3400-3050 cm^{-1} (OH), and carbonyls at 1719 cm^{-1} (carboxylic, C=O), 1680 cm^{-1} (conjugated ester, C=O), respectively. Based on spectral analysis of NMR, and ESI-MS, as well comparison with previously reported data, the structure of compound 14 was deduced as 3,5-Di-*O*-caffeoylquinic acid [217]. The relative configuration at C-4 was established from a strong NOESY correlation between H-4 and H-5, indicating that these protons are spatially close and located on the same face of the ring (Figure S17). This assignment was further supported by the observed coupling pattern which is consistent with the proposed stereochemical arrangement. The ^{1}H-NMR spectral data are presented in Table 18, and HPLC chromatogram used for purity assessment is presented in Appendix A (Figure S1), while The ^{1}HNMR and mass spectra are shown in Figure S16.

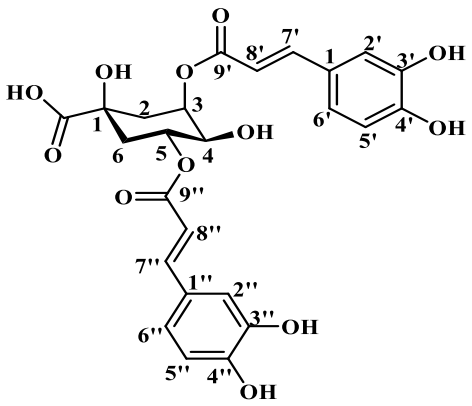


Table 18 – ^{1}H-NMR chemical shift data of compound 14

Carbon	δ_H (*J* in Hz)	Multiplicity
1	-	[a]C
2	2.09-2.28, m, 2H	CH_2
3	5.37, d, $J_{3/5}$ = 2.9 Hz, 1H	CH
4	3.90, dd, $J_{4/5,\ 4/3}$ = 9.36 Hz, 3.28 Hz, 1H	CH
5	5.56, m, 1H	CH
6	2.09-2.28, m, 2H	CH_2
1′	-	C
2′	6.97, m, 1H	CH
3′	-	C

Table 18 (continued)		
4′	-	C
5′	6.77, brs, m, 1H	CH
6′	7.07, d, $J_{6'/5'}$ = 8.4 Hz, 1H	CH
7′	7.62, d, $J_{7'/8'}$ = 15.9 Hz, 1H	CH
8′	6.42, d, $J_{8'/7'}$ = 16.0 Hz, 1H	CH
9′	-	C
1″	-	C
2″	6.95, m, 1H	CH
3″	-	C
4″	-	C
5″	6.75, brs, m, 1H	CH
6″	7.04, d, $J_{6''/5''}$ = 8.4, 1H	CH
7″	7.59, d, $J_{7''/8''}$ = 15.9 Hz, 1H	CH
8″	6.28, d, $J_{8''/7''}$ = 16.0 Hz, 1H	CH
9″	-	C

[a]C: quaternary carbons

(1*S*,3*R*,4*S*,5*R*)-3,5-Di-*O*-caffeoylquinic acid (15)

Compound 15 was obtained as an amorphous powder; ESI-MS (+): *m/z* 517.1 $[M+H]^+$, consistent with the molecular formula $C_{25}H_{24}O_{12}$. The IR spectrum showed absorptions at 3420-3100 cm^{-1} (OH), and 1719 cm^{-1} (carboxylic, C=O), 1680 cm^{-1} (conjugated ester, C=O), respectively. Based on NMR, and ESI-MS spectral analysis, and comparison with previously reported data, the structure of 15 was deduced as 3,5-Di-*O*-caffeoylquinic acid [218]. The relative configuration at C-4 was established from a strong NOESY correlation between H-4 and H-3, indicating that these protons are spatially close and located on the same face of the ring (Figure S19). The stereochemical assignment was further supported by the coupling pattern, which was consistent with the proposed configuration at C-4. The ^{1}H-NMR spectral data are given in Table 19, and HPLC chromatogram is provided in Appendix A (Figure S1), while the corresponding ^{1}H-NMR and mass spectra are provided in Figure S18.

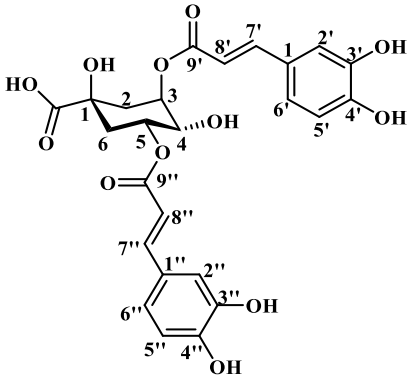


Table 19 – ^{1}H-NMR chemical shift data of compound 15

Carbon	δ_H (*J* in Hz)	Multiplicity
1	-	[a]C
2	2.12-2.31, m 2H	CH_2

Table 19 (continued)		
3	5.41, m, 1H	CH
4	3.97, dd, $J_{4/3,\ 4/5}$ = 7.6 Hz, 2.4 Hz, 1H	CH
5	5.41, m, 1H	CH
6	2.12-2.31, m, 2H	CH_2
1′	-	C
2′	7.05, m, 1H	CH
3′	-	C
4′	-	C
5′	6.78, d, $J_{5'/6',\ 5''/6''}$ = 8.4 Hz, 1H	CH
6′	6.96, $J_{6'/5',\ 6''/5''}$ = 8.4 Hz, 1H	CH
7′	7.62, d, $J_{7'/8'}$ = 15.6 Hz, 1H	CH
8′	6.37, d, $J_{8'/7'}$ = 16.0 Hz, 1H	CH
9′	-	C
1″	-	C
2″	7.05, m, 1H	CH
3″	-	C
4″	-	C
5″	6.78, d, $J_{5'/6',\ 5''/6''}$ = 8.4 Hz, 1H	CH
6″	6.96, $J_{6'/5',\ 6''/5''}$ = 8.4 Hz, 1H	CH
7″	7.58, d, $J_{7''/8''}$ = 15.6 Hz, 1H	CH
8″	6.28, d, $J_{8''/7''}$ = 16.0 Hz, 1H	CH
9″	-	C

[a]C: quaternary carbons

3,4-Di-*O*-caffeoylquinic acid (16)

Compound 16 was obtained as an amorphous powder; ESI-MS (+): *m/z* 517.1 $[M+H]^+$, corresponding with the molecular formula $C_{25}H_{24}O_{12}$. The IR spectrum exhibited characteristic absorptions at 3350-3090 cm^{-1} (OH), and 1725 cm^{-1} (carboxylic, C=O), 1687 cm^{-1} (conjugated ester, C=O), respectively. Based on the analysis of ^{1}H-NMR, and ESI-MS data, as well as comparisons with previously reported data, the structure of compound 16 was deduced as 3,4-Di-*O*-caffeoylquinic acid [218]. The ^{1}H-NMR spectral data are listed in Table 20. The HPLC chromatogram is provided in Appendix A (Figure S1), while the corresponding ^{1}H-NMR and mass spectra are provided in Figure S20.

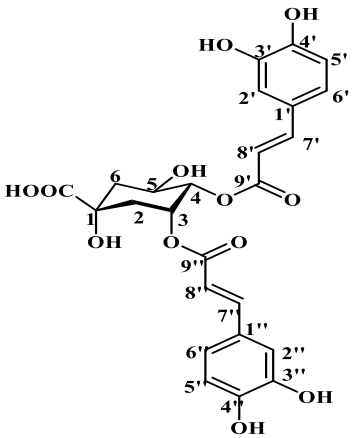


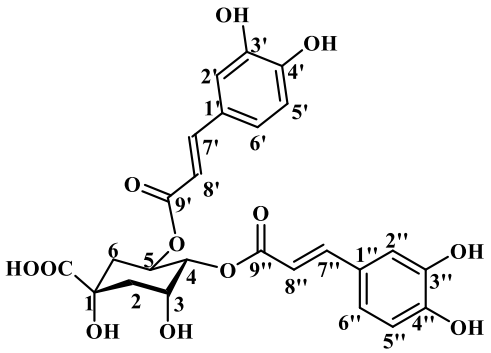
Table 20 – ^{1}H-NMR chemical shift data of compound 16

Carbon	δ_H (*J* in Hz)	Multiplicity
1	-	[a]C
2	2.22-2.35, m, 2H	CH_2
3	5.63, d, $J_{3/4}$ = 2.7 Hz, 1H	CH
4	5.02, dd, $J_{4/3,\ 4/5}$ = 2.8 Hz, 2.7 Hz, 1H	CH
5	4.34, m, 1H	CH
6	2.22-2.35, m, 2H	CH_2
1′	-	C
2′	7.02, d, $J_{2'/3'}$ = 4.0 Hz, 1H	CH
3′	-	C
4′	-	C
5′	6.76, d, $J_{5'/6'}$ = 7.8 Hz, 1H	CH
6′	6.92, m, 1H	CH
7′	7.57, d, $J_{7'/8'}$ = 15.9 Hz, 1H	CH
8′	6.29, d, $J_{8'/7'}$ = 15.6 Hz, 1H	CH
9′	-	C
1″	-	C
2″	7.01, d, $J_{2''/3''}$ = 5.6 Hz, 1H	CH
3″	-	C
4″	-	C
5″	6.73, d, $J_{5''/6''}$ = 7.8 Hz, 1H	CH
6″	6.92, m, 1H	CH
7″	7.53, d, $J_{7''/8''}$ = 15.9 Hz, 1H	CH
8″	6.27, d, $J_{8''/7''}$ = 15.6 Hz, 1H	CH
9″	-	C

[a]C: quaternary carbons

4, 5-Di-*O*-caffeoylquinic acid (17)

Compound 17 was obtained as white powder; ESI-MS (+): *m/z* 517.1 $[M+H]^+$, consistent with the molecular formula $C_{25}H_{24}O_{12}$. The IR spectrum exhibited absorptions at 3400-3150 cm^{-1} (OH), and 1710 cm^{-1} (carboxylic, C=O), 1694 cm^{-1} (conjugated ester, C=O), respectively. Based on NMR, and ESI-MS spectral data analysis, and comparison with previously reported data, the structure of compound 17 was deduced as 4, 5-Di-*O*-caffeoylquinic acid [218]. The ^{1}H-NMR



spectral data are provided in Table 21. The HPLC chromatogram used for purity assessment is presented in Appendix A (Figure S2), while the corresponding ^{1}H-NMR and mass spectra are provided in Figure S21.

Table 21 – ^{1}H-NMR chemical shift data of compound 17

Carbon	**δ_H (*J* in Hz)**	**Multiplicity**
1	-	[a]C
2	2.35, m, 2H	CH_2
3	3.98, brs m, 1H	CH
4	5.31, m, 1H	CH
5	5.40, brs m, 1H	CH
6	2.19, d, m, 2H	CH_2
1′	-	C
2′	7.05, m, 1H	CH
3′	-	C
4′	-	C
5′	6.77, m, 1H	CH
6′	6.96, m, 1H	CH
7′	7.59, d, $J_{7'/8'}$ = 16.0 Hz, 1H	CH
8′	6.34, d, $J_{8'/7'}$ = 16.0 Hz, 1H	CH
9′	-	C
1″	-	C
2″	7.05, m, 1H	CH
3″	-	C
4″	-	C
5″	6.77, m, 1H	CH
6″	6.96, m, 1H	CH
7″	7.55, d, $J_{7''/8''}$ = 16.0 Hz, 1H	CH
8″	6.21, d, $J_{8''/7''}$ = 16.0 Hz, 1H	CH
9″	-	C

[a]C: quaternary carbons

3,4-Di-*O*-caffeoylquinic acid methyl ester (18)

Compound 18 was obtained as white powder; ESI-MS (+): *m/z* 531.0 $[M+H]^+$, corresponding to the molecular formula $C_{26}H_{26}O_{12}$. The IR spectrum showed absorptions at 3390-3150 cm^{-1} (OH), and 1704 cm^{-1} (non conjugated ester, C=O), 1698 cm^{-1} (conjugated ester, C=O), respectively. Based on NMR, and ESI-MS, as well as comparison with previously reported data, the structure of compound 18 was assigned as 3,4-Di-*O*-caffeoylquinic acid methyl ester [219]. The ^{1}H-NMR spectral data are presented in Table 22, and the HPLC chromatogram is provided in Appendix A (Figure S2), while NMR and mass spectra are shown in Figure S22.

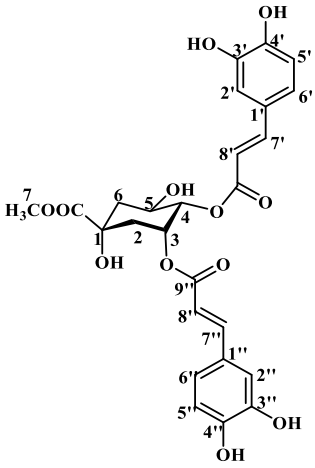


Table 22 – ^{1}H-NMR chemical shift data of compound 18

Carbon	δ_H (*J* in Hz)	Multiplicity
1	-	[a]C
2	2.10-2.34, m, 2H	CH_2
3	5.55, d, $J_{3/4}$ = 4.8 Hz, 1H	CH
4	5.11, d, $J_{4/3}$ = 8.0 Hz, 1H	CH
5	4.35, m, 1H	CH
6	2.10-2.34 m, 2H	CH_2
7	3.71, s, 3H	CH_3
1′	-	C
2′	7.02, brs, 1H	CH
3′	-	C
4′	-	C
5′	6.75, m, 1H	CH
6′	6.93, m, 1H	CH
7′	7.61, d, $J_{7'/8'}$ = 16.0 Hz, 1H	CH
8′	6.30, d, $J_{8'/7'}$ = 16.0 Hz, 1H	CH
9′	-	C
1″	-	C
2″	7.02, brs, 1H	CH
3″	-	C
4″	-	C
5″	6.75, m, 1H	CH
6″	6.93, m, 1H	CH
7″	7.51, d, $J_{7''/8''}$ = 16.0 Hz, 1H	CH

Table 22 (continued)		
8″	6.17, d, $J_{8''/7''}$ = 16.0 Hz, 1H	CH
9″	-	C

[a]C: quaternary carbons

3,5-Di-*O*-caffeoylquinic acid methyl ester (19)

Compound 19 was obtained as white powder; ESI-MS (+): *m/z* 531.3 $[M+H]^+$, consistent with the molecular formula $C_{26}H_{26}O_{12}$. The IR spectrum exhibited absorptions at 3410-3050 cm^{-1} (OH), and 1725 cm^{-1} (non-conjugated ester, C=O), 1684 (Conjugated ester, C=O), respectively. Based on spectral analysis of NMR, and ESI-MS, as well as comparisons with previously reported data, the structure of compound 19 was deduced as 3,5-Di-*O*-caffeoylquinic acid methyl ester [220]. The ^{1}H-NMR spectral data are given in Table 23. The HPLC chromatogram is provided in Appendix A (Figure S2), while the corresponding ^{1}H-NMR and mass spectra are provided in Figure S23.

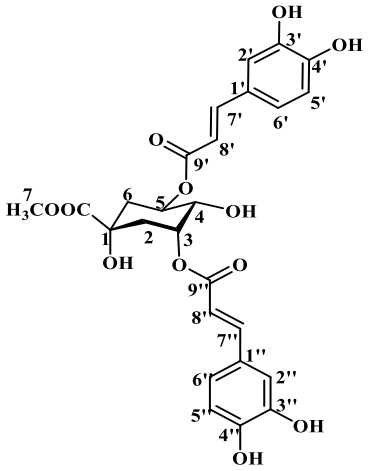


Table 23 – ^{1}H-NMR chemical shift data of compound 19

Carbon	δ_H (*J* in Hz)	Multiplicity
1	-	[a]C
2	2.26-2.32, m, 2H	CH_2
3	5.28, d, $J_{3/4}$ = 8.0 Hz, 1H	CH
4	3.96, d, $J_{4/5}$ = 4.4 Hz, 1H	CH
5	5.38, d, $J_{5/4}$ = 4.8 Hz, 1H	CH
6	2.10-2.14, m, 2H	CH_2
7	3.67, s, 3H	CH_3
1′	-	C
2′	7.04, m, 1H	CH
3′	-	C
4′	-	C
5′	6.77, d, $J_{5'/6''}$ = 8.0 Hz, 1H	CH
6′	6.95, br. d, $J_{6'/5',\ 6''/5''}$ = 8.2 Hz, 1H	CH
7′	7.61, d, $J_{7'/8'}$ = 16.0 Hz, 1H	CH
8′	6.34, d, $J_{8'/7'}$ = 16.0 Hz, 1H	CH
9′	-	C
1″	-	C
2″	7.04, m, 1H	CH

Table 23 (continued)		
3″	-	C
4″	-	C
5″	6.75, d, $J_{5''/6''}$ = 8.0 Hz, 1H	CH
6″	6.95, d, $J_{6'/5', 6''/5''}$ = 8.2 Hz, 1H	CH
7″	7.54, d, $J_{7''/8''}$ = 16.0 Hz, 1H	CH
8″	6.21, d, $J_{8''/7''}$ = 16.0 Hz, 1H	CH
9″	-	C

[a]C: quaternary carbons

3,4,5-Tri-*O*-caffeoylquinic acid methyl ester (20)

Compound 20 was obtained as white powder; ESI-MS (+): *m/z* 693.1 $[M+H]^+$, corresponding to the molecular formula $C_{35}H_{32}O_{15}$. The IR spectrum showed absorptions at 3450-3100 cm^{-1} (OH), and 1720 (non-conjugated ester, C=O), 1670 (conjugated ester, C=O), respectively. Baes on NMR, and ESI-MS spectral analysis, as well as comparison previously reported data, the structure of compound 20 was deduced as 3,4,5-Tri-*O*-caffeoylquinic acid methyl ester [221]. The ^{1}H-NMR spectral data are presented in Table 24, and NMR and mass spectra are shown in Appendix A (Figure S24).

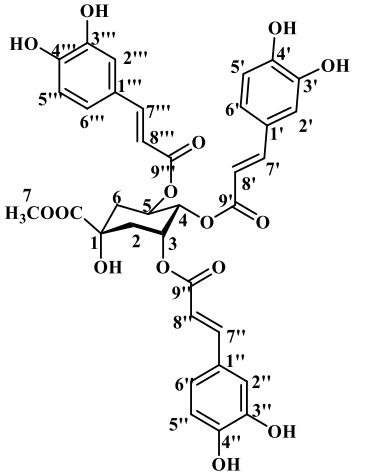


Table 24 – ^{1}H-NMR chemical shift data of compound 20

Carbon	δ_H (*J* in Hz)	Multiplicity
1	-	[a]C
2	2.05-2.30, m, 2H	CH_2
3	5.13, m, 1H	CH
4	4.36, m, 1H	CH
5	5.66, m, 1H	CH
6	3.32, m, 2H	CH_2
7	3.34, s, 3H	CH_3
1′	-	C
2′	7.04, m, 1H	CH
3′	-	C
4′	-	C
5′	6.77, m, 1H	CH
6′	6.91, m, 1H	CH
7′	7.61, d, $J_{7'/8'}$ = 16.0 Hz, 1H	CH

Table 24 (continued)		
8′	6.29, brd, $J_{8'/7'}$ = 16.0 Hz, 1H	CH
9′	-	C
1″	-	C
2″	7.04, m, 1H	CH
3″	-	C
4″	-	C
5″	6.77, m, 1H	CH
6″	6.91, m, 1H	CH
7″	7.57, d, $J_{7''/8''}$ = 16.0 Hz, 1H	CH
8″	6.25, brd, $J_{8''/7''}$ = 16.0 Hz, 1H	CH
9″	-	C
1‴	-	C
2‴	7.04, m, 1H	CH
3‴	-	C
4‴	-	C
5‴	6.77, m, 1H	CH
6‴	6.91, m, 1H	CH
7‴	7.53, d, $J_{7'''/8'''}$ = 16.0 Hz, 1H	CH
8‴	6.21, d, $J_{8'''/7'''}$ = 16.0 Hz, 1H	CH
9‴	-	C

[a]C: quaternary carbons

2.3.3 Enzyme expression and inhibition studies

The expression and purification of recombinant *Leishmania major* pteridine reductase-1 (*Lm*PTR-1) were optimized using Tris-HCl buffer (pH 8.0). SDS-PAGE analysis confirmed successful purification, revealing a single prominent band at approximately 38 kDa, corresponding to the expected molecular weight of the enzyme (Figure 14).

The purified enzyme *Lm*PTR-1 was sequentially used in *in vitro* inhibition assays to evaluate the activity of isolated caffeic acid derivatives. Natural products are an important source of drug development against neglected tropical diseases (NTDs). Phenolic secondary metabolites, particularly biflavonoids, have been reported to exhibit significant inhibition of *Lm*PTR-1 [222, 223]. The current study therefore investigated the inhibitory effects of caffeic acid derivatives against *Lm*PTR-1. In particular, compounds 15–18 exhibited mild to moderate inhibitory activity (Figure 15). Among them, compounds 17 (3,4-di-*O*-caffeoylquinic acid methyl ester) and 18 (3,4-di-*O*-caffeoylquinic acid) exhibited the highest inhibitory activity, with IC_{50} values of 93.9 ± 1.25 μM, and 81.9 ± 1.12 μM, respectively (Table 25). While, compounds 15 and 16 showed weaker inhibition (IC_{50} > 100 μM). The

higher activity observed for compounds 17 and 18 compared with compounds 15 and 16 suggests that the positional arrangement of the caffeoyl groups plays an important role in PTR-1 inhibition. The weak activity of compounds 15 and 16 suggests that not all dicaffeoylquinic acid derivatives contribute similarly to enzyme inhibition, highlighting the influence of subtle structural differences on biological activity. Given that no standard inhibitor of *Lm*PTR-1 has been reported in the literature, trimethoprim, a known inhibitor of dihydrofolate reductase-thymidylate synthase (DHFR-TS), an enzyme with a related function, was used as a reference inhibitor (IC_{50} = 21.07 ± 1.60 μM) [224].

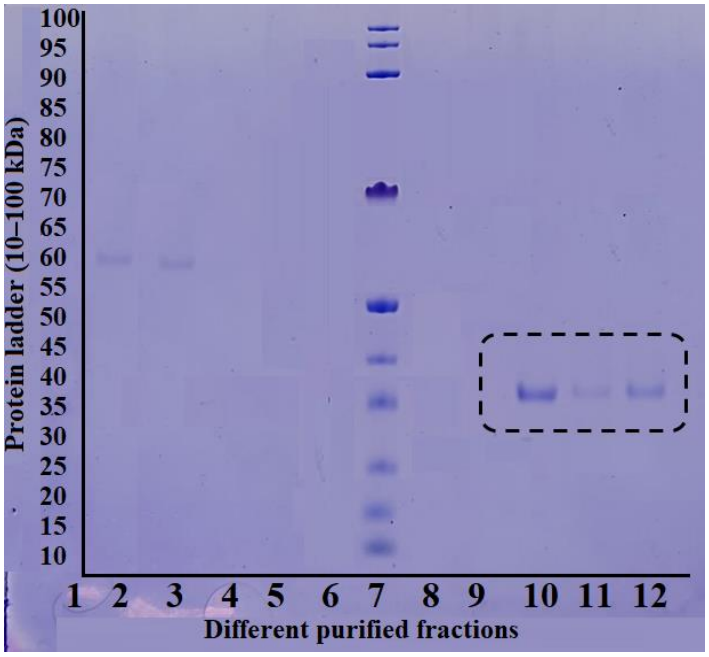


Figure 14 – Expression and Purification of PTR1: Gel electrophoresis results obtained after His-trap column chromatography. Lane 7th contains the ladder, whereas lane 10th, 11th, and 12th contains the purified fractions of PTR1

Table 25 – *Lm*PTR-1 inhibitory activity of isolated compounds 1-20

Compounds	**% Inhibition (500 μM)**	**IC_{50} (μM) ± SD**	**[c]ΔIC$_{50}$ vs Trimethoprim (μM)**
1	25	NA[b]	NA[b]
2	35	NA[b]	NA[b]
3	25	NA[b]	NA[b]
4	28	NA[b]	NA[b]
5	30	NA[b]	NA[b]
6	44	NA[b]	NA[b]
7	25	NA[b]	NA[b]
8	27	NA[b]	NA[b]
9	15	NA[b]	NA[b]

Table 25 (continued)			
10	15	NA[b]	NA[b]
11	19	NA[b]	NA[b]
12	20	NA[b]	NA[b]
13	25	NA[b]	NA[b]
14	25	NA[b]	NA[b]
15	85	198.7 ± 1.37	+177.63 ± 2.11
16	73	122.1 ± 1.15	+101.03 ± 1.97
17	88	93.9 ± 1.25	+72.84 ± 2.03
18	92	81.9 ± 1.12	+60.83 ± 1.95
19	28	NA[b]	NA[b]
20	32	NA[b]	NA[b]
Trimethoprim[a]	92	21.07 ± 1.60	0.00

[a]Positive control; [b]NA: Not Active; [c]ΔIC_{50}: positive (+) values indicate lower potency compared to Trimethoprim

Although compounds 17 and 18 were less active than trimethoprim, their moderate lead-level inhibitory activity highlights caffeoylquinic acid derivatives as promising scaffolds for further structural optimization and antileishmanial drug development. Non-linear regression analysis further confirmed the dose-dependent inhibition of compounds 15–18, and the corresponding dose–response curves, together with that of the reference inhibitor, are shown in Figure 16.

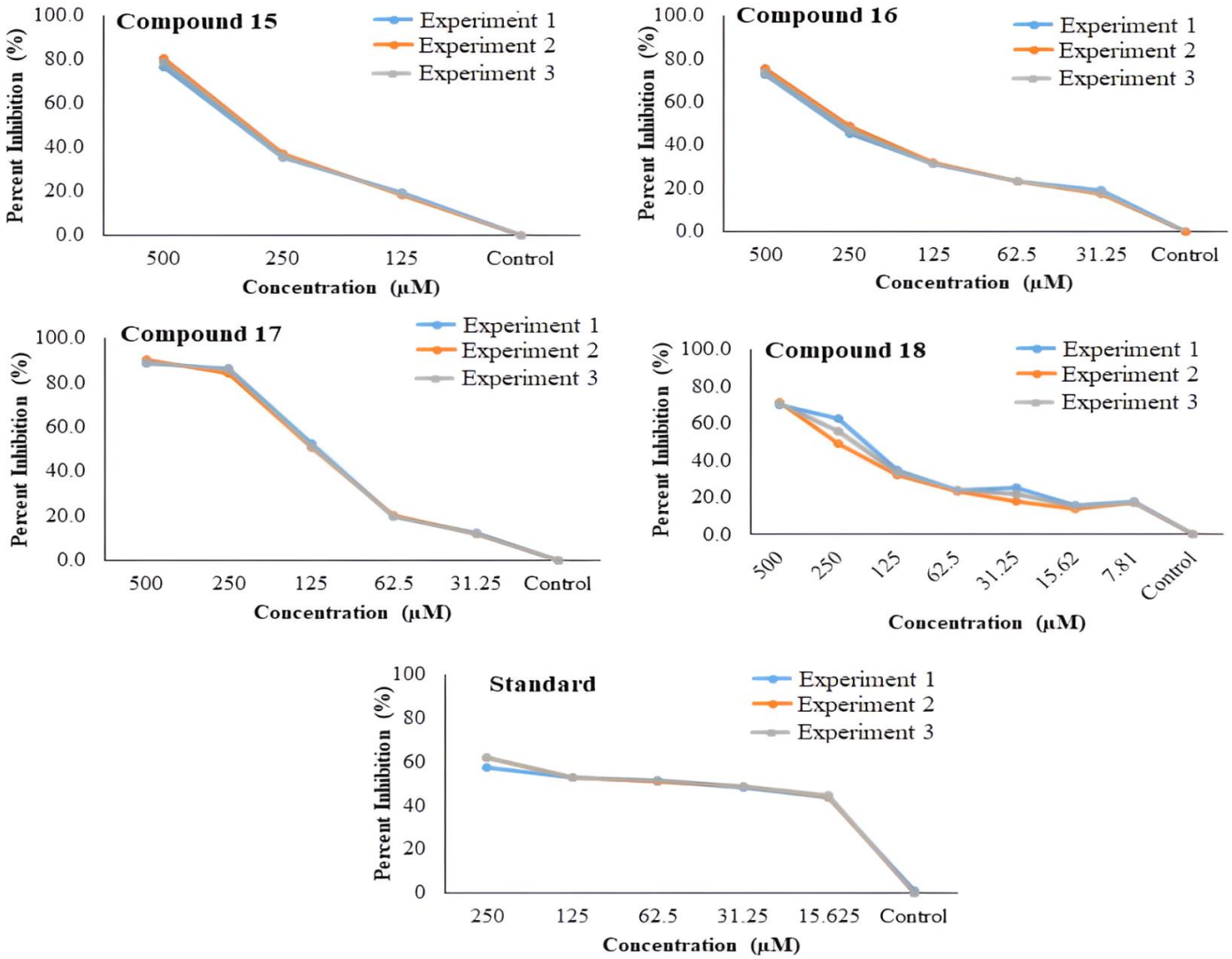


Figure 15 – The x-axis represents the compound concentration (µM), while the y-axis shows percentage inhibition (%) of compounds 15–18 and the standard drug trimethoprim

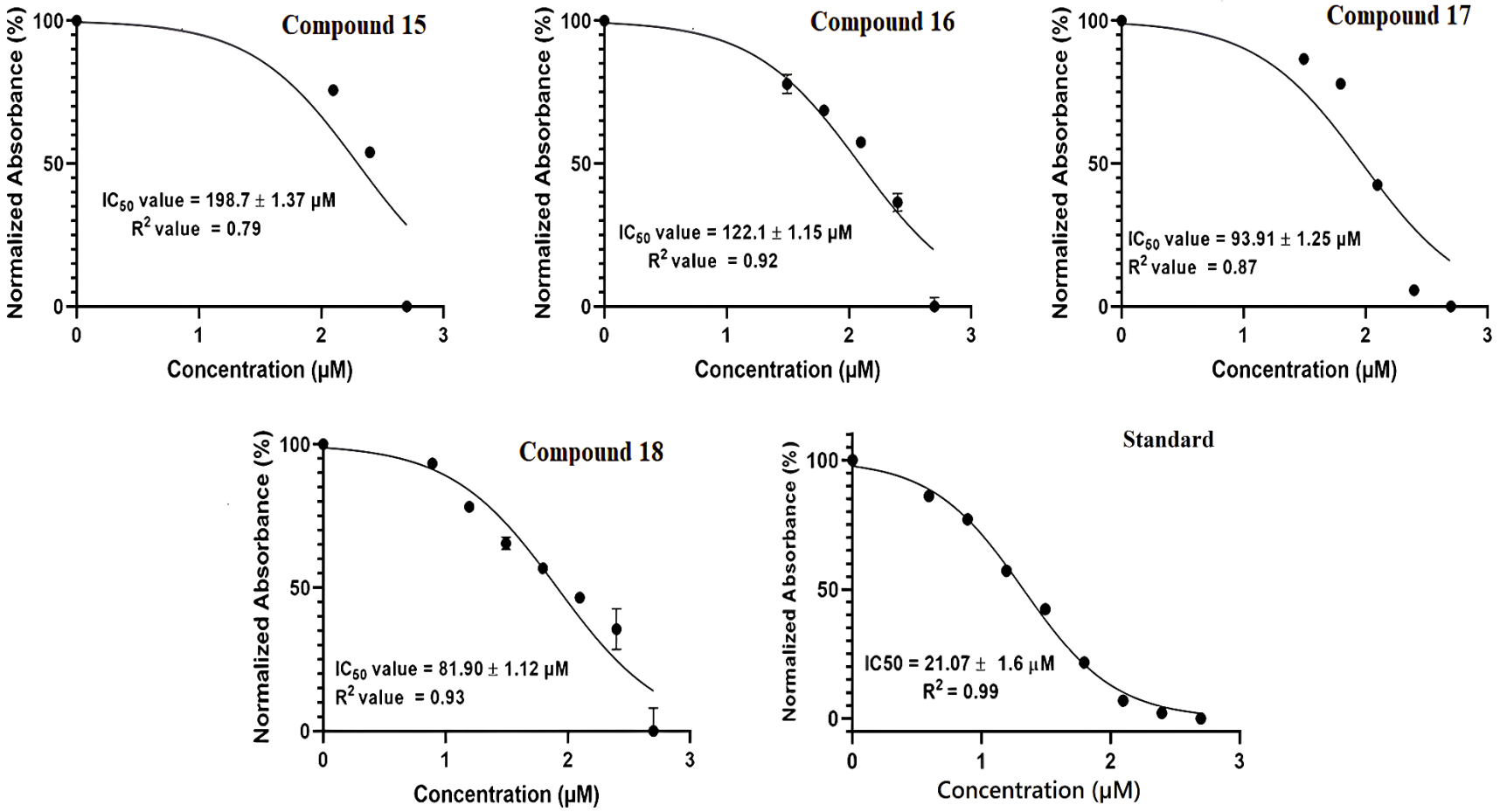


Figure 16 – Dose dependent curves of compounds 15–18 obtained by non-linear regression analysis. The x-axis of the curve indicates the Log inhibitor concentration (µM) for compounds 15–18, where Log 500 = 2.698 and the y-axis shows the normalized absorbance or extent of inhibition (%)

2.3.4 *In silico* studies

2.3.4.1 Molecular docking

Docking studies further indicated the inhibitory effect of compounds 15–18 against *Lm*PTR-1. These studies provide insight into the atomic-level interactions between ligands and proteins. In compound 15, ring A exhibited π-π stacking interaction, and formed an aromatic hydrogen interaction with the binding site's Tyr194, and Phe113 residues, respectively. Ring-B also interacted with Gly240 by a second hydrogen bond. Similarly, ring C, and the carbonyl of Phe113 formed a hydrogen bond. Compound 15 showed a docking score of –4.81. It is important to remember that during the docking process, the cofactor (NADPH) remained intact. Similarly, compounds 16 and 17 established a π-π stacking interaction between ring A, and the catalytic triad's Phe113, whereas compound 16 established extra hydrogen bonds between ring-B's carbonyl groups, and the binding pocket's HIE241 residue (Figure 17). Additionally, the hydrogens of ring-A in compounds 16, and 17 interacted with the active site's HOH2109, and HOH2110. The calculated docking score of compound 16, and 17 are –7.79, and –2.86 respectively. Compound 18, an unmethylated derivative of compound 17, showed various interactions including two hydrogen bonds via carbonyl groups on ring B, and Val230, as well as a π-π stacking interaction with the Phe113 residue. The carbonyl group of compound 18 bridging rings B, and C was found to have two aromatic hydrogen bonds with Phe113. Additionally, it demonstrated hydrogen bonding interactions with the active site's HOH2110, HOH2075, and Gly240 residues. The calculated docking score of compound 18 was –2.31 (Table 26).

In the case of trimethoprim (standard) a typical inhibitor two hydrogen bonds were found with the Tyr194, and Ser111 of the binding pocket, whereas π-π stacking interaction was also seen with Phe113 (Figure 18). Trimethoprim had a docking score of –5.51, and formed two π-π stacking contacts with Phe113, and a salt bridge with Asp232 indicating the importance of key residues in *Lm*PTR-1 inhibition (Table 26).

Table 26 – Computational profiling of potential leads (15–18) and the inhibitor (trimethoprim) on the basis of docking scores, residues involved interactions, prominent types of interactions, protein, and ligand RMSD

Compounds	Docking Scores	Docking residues in interactions	Types of interactions	Protein RMSD	Ligand RMSD
15	–4.81	Phe113, Tyr194, Gly240	π-π staking, CH-π, and hydrogen bonding	2.0-4.5 Å	1.6-6.4 Å (Stable after 10ns)

Table 26 (continued)					
16	–7.79	Phe113, HIE241, HOH2109, HOH2110	π-π stacking, and hydrogen bonding	1.6-3.6 Å	1.5-10.5 Å (Stable after 40ns)
17	–2.86	Phe113, HOH2109, HOH2110	π-π stacking, and hydrogen bonding	2.0-4.5 Å	3-8 Å (Stable after 10ns)
18	–2.31	Phe113, Tyr194, Ser111, Gly240, HOH2110, HOH2075	π-π stacking, CH-π, and hydrogen bonding	2.0-3.2 Å	3.2-6.4 Å (Stable after 10ns)
Standard (trimethoprim)	–5.51	Phe113, Asp232	π-π stacking, and hydrogen bonding	2.4-5.4 Å	2.4-3.0 Å

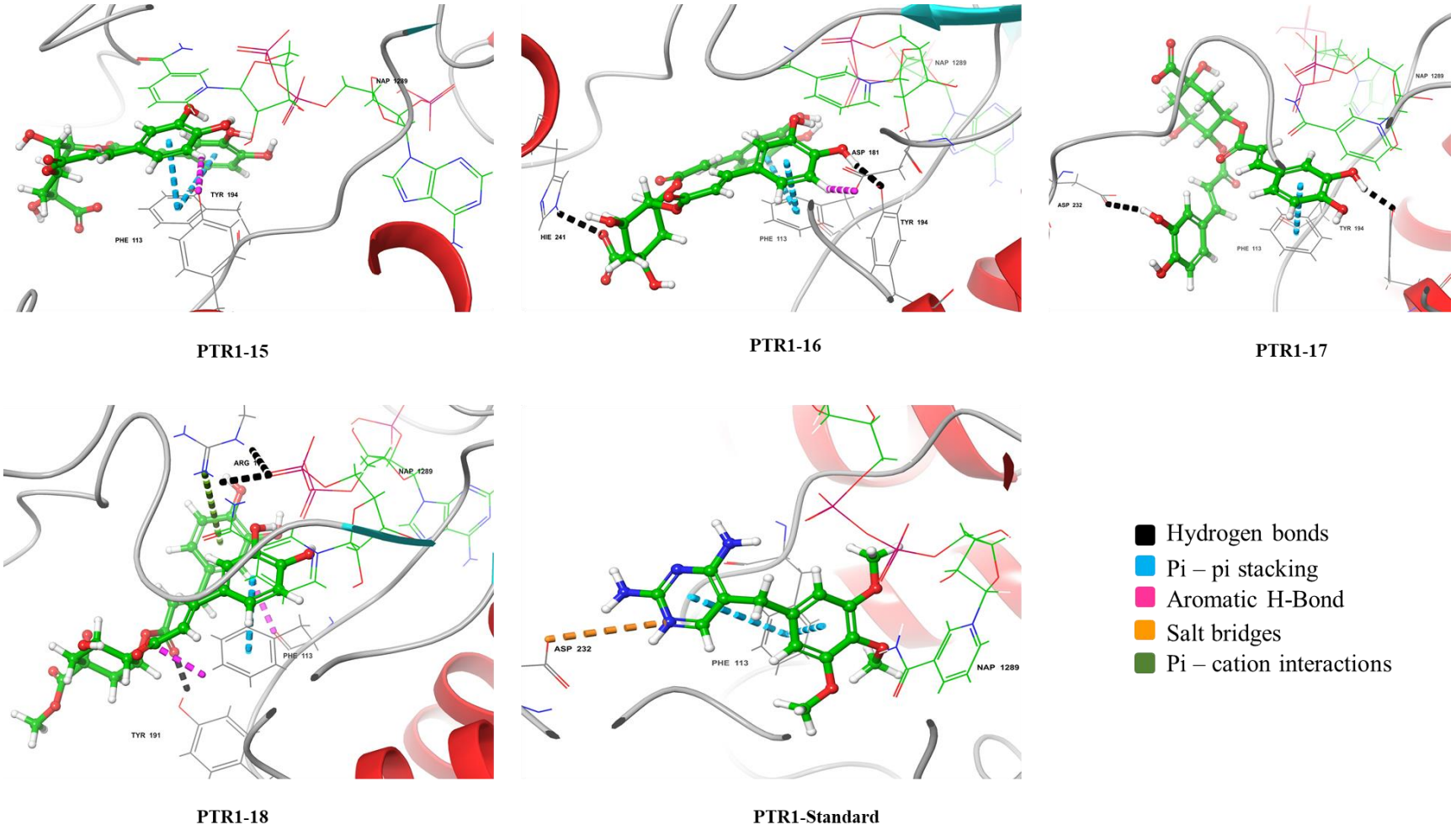


Figure 17 – Molecular docking profiles of PTR-1 complexes with compounds 15–18, along with standard inhibitor (trimethoprim)

2.3.4.2 Molecular dynamics simulations

Molecular dynamics simulations (MD) studies were conducted in order to examine the stability of these complexes in a dynamic context, as docking studies only give a static image of the protein-ligand interaction. Throughout the simulation, the root mean square deviation (RMSD) of compound 15 profile indicated the formation of a stable protein-ligand complex with fewer fluctuations (<3 Å) (Figure 18). A key interaction between compound 15, and the Lys244 residue is shown by the ligand-protein contact diagram through hydrogen bonding and water bridge formation, whereas Phe113 of the binding pocket displayed hydrophobic interactions (Figure 19).

Similarly, during the 100 ns simulation period, interaction of compound 15 with Tyr191, and Phe113 remained persistent for 37% and 74%, respectively. Likewise, the binding site's Tyr194, and Ser111 exhibited 53% and 63% of the total interactions with compound 15**,** respectively. In contrast, compound 16 displayed increased RMSD between 25–35 ns, which was thereafter stabilized, as shown in Figure 18. According to the simulation profile, a stable hydrophobic interaction between the ligand, and the key active-site residue Phe113 was formed. Ligand-protein contacts study showed that Phe113, and Tyr194 were responsible for 63% and 30% of interactions with compound 16, respectively (Figure 19).

The ligand interaction diagram showed hydrophobic interactions between compound 18, and Phe113 at the enzyme's binding site. Tyr191, and Lys244 formed strong interactions via hydrogen bonding and water bridges. Phe113 sustained contacts for only 31% of the simulated duration, indicating that compound 18 may exhibit weaker binding stability within the active site.

Trimethoprim, a typical inhibitor, induced noticeable backbone fluctuations during the initial 40 ns of simulation. The RMSD of the protein backbone stabilized after approximately 42 ns, and the complex remained stable throughout the trajectory. The ligand-protein complex has various interactions, including hydrophobic interactions, and hydrogen bonding between Phe113, and Tyr194. The ligand-protein contact analysis revealed hydrogen binding with Tyr194, hydrophobic interactions with Phe113 and π-cation interactions with Arg17.

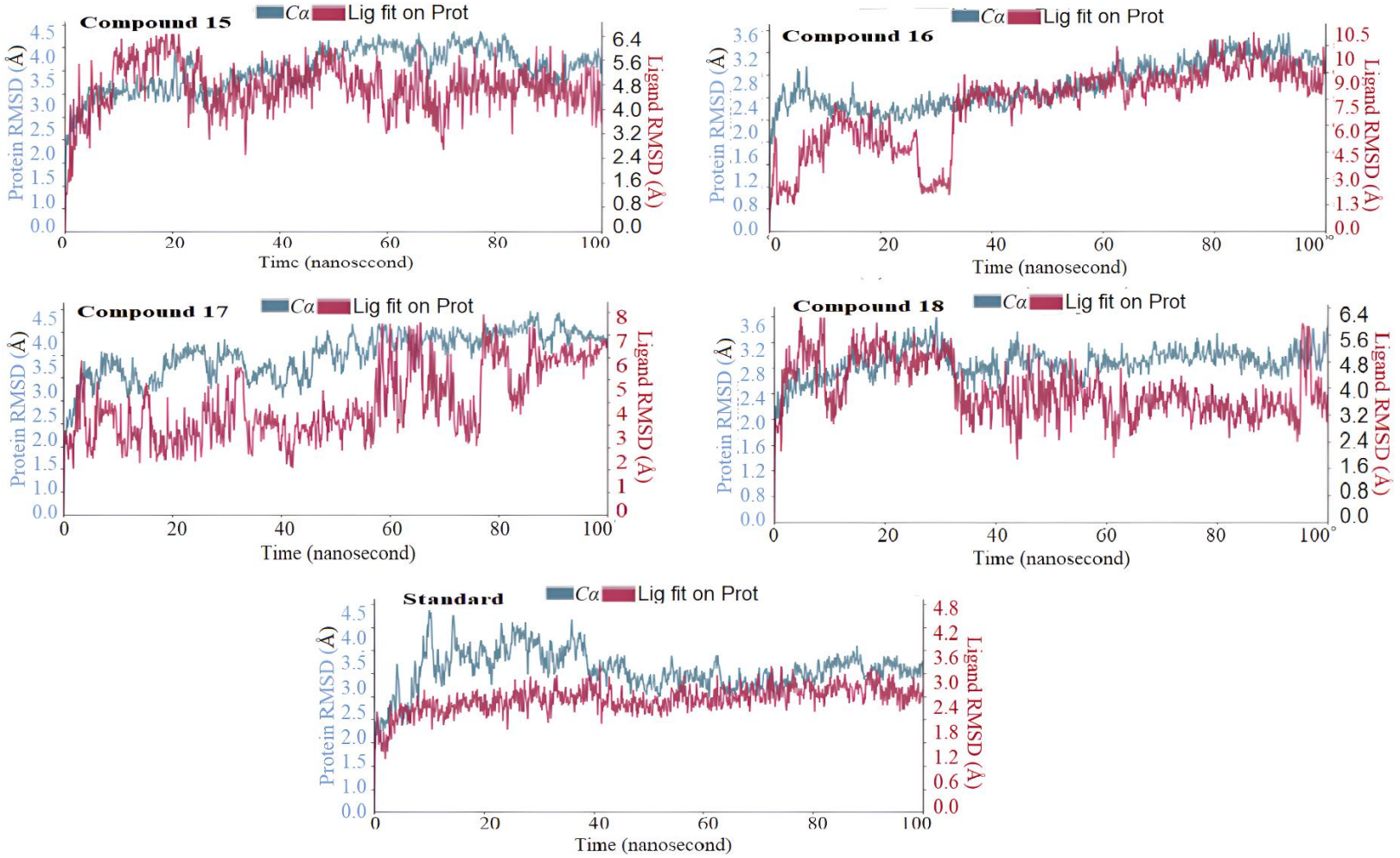


Figure 18 – Root mean square deviation (RMSD) analysis of the protein–ligand complexes during 100 ns molecular dynamics simulations for compounds 15–18 and the standard inhibitor. The blue curves represent fluctuations of the protein backbone (Cα atoms), while the red curves correspond to the ligand RMSD fitted to the protein (*LmPTR*-1)

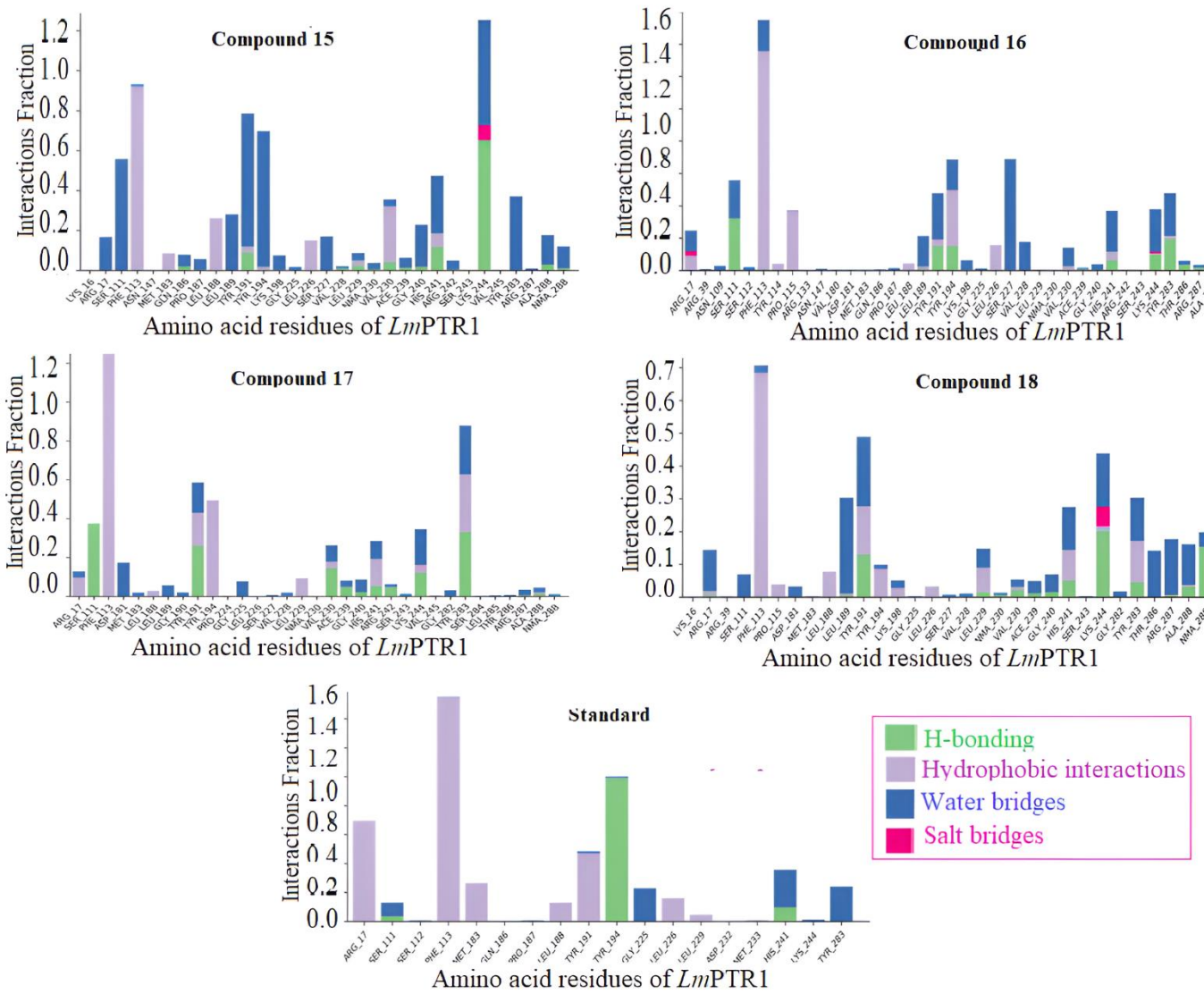


Figure 19 – Protein-ligand contacts at 100 ns simulation of compounds 15–18, and the standard with binding site residues of *Lm*PTR-1 protein

2.3.5 Structure – activity relationship (SAR)

The caffeoyl moieties at R_2 and R_4 in complex 15 formed persistent connections with important active-site residues, Tyr194, Ser111, and Tyr191, which were maintained for 74%, 63%, and 37% of the simulation period, respectively. The compound's binding potential was greatly influenced by these interactions, as indicated by its IC_{50} value of 198.7 ± 1.37 µM, and docking score of -4.81. For 63% of the simulation period, compound 16's hydrophobic contacts with Phe113 were maintained by the caffeoyl groups at R_2 and R_3. The increased hydrophobicity resulted in a stronger binding profile, as evidenced by a docking score of -7.79, and an IC_{50} value of 122.1 ± 1.15 µM. Compound 17 exhibited caffeoyl moieties at R_3 and R_4, while compound 18 had caffeoyl moieties at R_2 and R_3. Interestingly, complexes 16, 17, and 18 all have higher binding affinities than compound 15 due to the caffeoyl group at the R_3 position. Additionally, complex 18's methyl group enhanced inhibitory efficacy by contributing more non-covalent contacts. Thus, compound 18 with an IC_{50} of 81.9 ± 1.12 µM, demonstrated the highest activity, followed by compound 17 (IC_{50} = 93.9 ± 1.25 µM). Compounds 17, and 18 maintained contacts with Phe113 for 94% and 31% of the simulation time, respectively, which correlates with a stable RMSD profile and improved binding stability. These results are in line with molecular dynamics (MD) simulations.

2.4 Summary

This part of the PhD dissertation focuses on the phytochemical and biological study of *Tussilago farfara* L., an important medicinal plant. We conducted a phytochemical investigation of the ethanolic extract of *T. farfara*, resulting in the isolation and characterization of twenty secondary metabolites, namely vanillic acid (1), syringic acid (2), *trans*-*p*-coumaric acid (3), esculetin (4), *p*-hydroxybenzoic acid (5), benzyl β-D-glucoside (6), quercetin (7), quercetin-3-*O*-β-D-glucoside (8), quercetin-4′-*O*-glucoside (9), quercetin-3-*O*-rutinoside (10), kaempferol (11), kaempferol-3-*O*-glucoside (12), kaempferol-3-*O*-rutinoside (13), (1*S*,3*R*,4*R*,5*R*)-3,5-di-*O*-caffeoylquinic acid (14), (1*S*,3*R*,4*S*,5*R*)-3,5-di-*O*-caffeoylquinic acid (15), 3,4-di-*O*-caffeoylquinic acid (16), 4,5-di-*O*-caffeoylquinic acid (17), 3,4-di-*O*-caffeoylquinic acid methyl ester (18), 3,5-di-*O*-caffeoylquinic acid methyl ester (19), and 3,4,5-tri-*O*-caffeoylquinic acid methyl ester (20). Among these, compounds 1, 14, and 20 are reported from *Tussilago farfara* for the first time. The structures of compounds 1–20 were identified by extensive NMR (1D and 2D), and mass spectrometric studies (EI-MS, ESI-MS, FAB-MS). *Leishmania major* Pteridine reductase-1 (*Lm*PTR-1) is a vital enzyme for parasite survival and serves as a promising drug target. All purified compounds were evaluated for antileishmanial activity *in vitro*. However, only compounds 15–18 showed moderate anti PTR-1 inhibitory activities, with IC_{50} values between 81.9 and 198.7 µM. *In*

silico studies revealed strong interactions between compounds 15–18 and the PTR-1 enzyme. Based on these findings, quinic acid derivatives having caffeoyl moieties can be further investigated for designing new PTR-1 inhibitors. Hence, further studies are required to validate their activity.

2.5 Using advanced spectroscopic, and chromatographic techniques to study the biotransformation of steroidal drug methylprednisolone acetate via *Fusarium oxysporum* and *Penicillium chrysogenum*

2.6 Introduction

Biotransformation techniques have evolved as very effective approaches for structural modification in a wide range of organic molecules. This method uses biocatalysts such as whole microorganisms, plant cells, or isolated enzymes which are inexpensive, environmentally friendly, and non-toxic. Oxidation, dehydrogenation, chlorination, reduction, aromatization, methylation, demethylation, and rearrangements are examples of reactions that normally take place under mild conditions (ambient temperature, pressure, and pH). Biotransformation can reduce the number of steps needed to produce desired products by removing the requirement for toxic reagents, protection/deprotection strategies, and harsh activation procedures. As a result, these procedures produce less chemical waste, and are more environmentally friendly than conventional synthetic approaches.

One of the most significant advantages of biotransformation is its ability to maintain the carbon backbone of the original molecules while introducing functional group. This makes it very valuable in the realm of drug discovery, and development, where biocatalysis is commonly used to create libraries of compounds based on basic pharmacophores. These chemical libraries are then tested for a variety of biological activities throughout the lead discovery, and optimization phases [111, 225-229].

Natural compounds, such as steroids, terpenes, and flavonoids, have been proven beneficial in treating cancer, immune system abnormalities, cardiovascular illnesses, and bacterial, viral, and fungal infections for decades. Natural products can be difficult to derivatize due to their asymmetric cores and inert hydrocarbon skeletons. Biotransformation using microorganisms (bacteria or fungi), plant cell cultures, or purified enzymes is an efficient method for producing derivaties or structural mimics of natural compounds. Enzymes catalyze the process, producing regio-, stereo-, and chemo-selective products. Because of the selective nature of biological catalysts (enzymes), biotransformation techniques are currently being employed successfully in a variety of industries, including medicine, agriculture, polymers, and the food industry [230-232].

Among natural products, steroids are an important class of physiologically active molecule. Several steroid-based medications have been developed in recent decades for anti-aromatase, anticancer, anti-inflammatory, antileishmanial, antibacterial, anti-androgenic, anabolic, and contraceptive effects. Despite their therapeutic efficacy, these compounds have been linked to gynecomastia, lower fertility in males, masculinization in females and children, and more significant

dangers such as blood clotting, hypertension, hepatic neoplasms, and carcinomas [233, 234].

Aromatase (CYP19A1) is an important enzyme in estrogen biosynthesis that catalyzes the conversion of androgens into estrogens. Extreme estrogen production has been associated with the development and progression of hormone-dependent disorders, particularly estrogen receptor-positive breast cancer. Consequently, aromatase inhibition has become an established therapeutic strategy for the treatment of postmenopausal breast cancer [235]. Although several aromatase inhibitors are currently available, their long-term use may be associated with side effects and drug resistance, creating a continuing need for the discovery of new and more effective inhibitors. Due to their structural similarity to natural enzyme substrates, steroidal compounds represents an important class of aromatase inhibitors [236]. Therefore, in order to reduce the adverse impact of existing steroidal drugs, it is necessary to develop new derivatives of steroidal drugs that are safe, effective, selective, and have better pharmacokinatic properties.

In light of these concerns, biotransformation offers a promising strategy for generating safer and more effective analogues through the modification of steroidal drugs. Bypassing the need for protection, and activation steps, biotransformation enables the efficient modification of a broad variety of organic molecules in an environmentally safe manner [237, 238].

Based on the preliminary phytochemical investigations of *T. farfara* described in the previous chapter, a sterol-sterol-type compound was detected from dichloromethane fraction. However, due to low yield, and purity the investigation proceeded with a commercially available drug, methylprednisolone acetate (1). Two fungal strains, *Fusarium oxysporum* (Figure 23) and *Penicillium chrysogenum* (Figure 24) were employed to produce eight metabolites (2–9). Among these, metabolite 2 was identified as a new metabolite, whereas metabolites 3–9 were known metabolites. The substrate 1 and all eight metabolites were then assessed for their aromatase inhibition activity to investigate potential improvements in biological efficacy.

2.7 Experimental

Various chromatographic and spectroscopic techniques were used to isolate and characterize metabolites of methylprednisolone acetate (1).

2.7.1 Instrumental methods for structural characterization

Metabolite structures were elucidated using 1D and 2D-NMR, including ^{13}C-NMR. ^{1}H-NMR spectra were recorded on Avance spectrometers at 400, 500, 600, and 800 MHz (Bruker, Switzerland) in CD_3OD and $CDCl_3$. To determine the multiplicity of carbon signals, DEPT-90, and DEPT-135 experiments were performed. Mass spectra were recorded on HX 110 mass spectrometers equipped

with a DA5000 data system and a JMS-600 instrument (Jeol, Japan). EI-MS analyses were performed at an ionization energy of 70 eV with a probe temperature of 250 °C. FAB-MS analyses were performed in positive-ion mode, and mass spectral data were acquired over the range *m/z* 5–3000. ESI-MS analyses were performed in positive-ion mode over the mass range *m/z* 50–2000 using a capillary voltage of 4500 V, and a source temperature of 200 °C. High-resolution electrospray ionization mass spectrometry (HRESI-MS) analyses were performed in positive-ion mode using a MAT 95XP (Thermo Finnigan, USA) mass spectrometer. The Bruker Vector 22 FT-IR spectrometer (France) was used for the IR analysis. A Buchi 560 apparatus (Switzerland) was used to determine melting point. Ultraviolet spectra were recorded in methanol using the Shimadzu UV 240 spectrophotometer (Shimadzu Corporation, Tokyo, Japan).

2.7.2 Reagents and materials

All solvents were purchased from Fisher Scientific (UK). Methylprednisolone acetate (1) (*m/z* 416; $C_{24}H_{32}O_6$) was purchased from Pfizer Karachi, Pakistan. The media components were purchased from DaeJung Chemicals and Metals Company Limited (Korea), Oxoid Limited (UK), Sigma-Aldrich (Germany), Scharlau Chemicals and Reagents (Spain), and VWR Chemicals (UK). The initial purification of metabolites was accomplished using open column chromatography with silica gel (Merck 200-300 mesh). For final purification Sephadex LH-20 column chromatography (140–550 mesh, Sigma-Aldrich, USA), and normal and reverse-phase preparative HPLC (LC 908, Japan) were employed. To analyze the degree of transformation and purity, a thin-layer chromatography (TLC) was used on pre-coated silica gel 60 GF_{254} (20 × 20 cm, 0.25 mm, Merck, Germany) plates. The spots on TLC plates were observed using UV light (λ = 254, and 366 nm), and spraying reagents (*i.e.*, vanillin/sulfuric acid and ceric sulfate). Human placental aromatase was obtained from human placental tissues provided by Sobhraj Maternity Hospital, Karachi, Pakistan.

2.7.3 Ultra performance liquid chromatography

Samples were analyzed using an ultra-performance liquid chromatography (UPLC) system (Agilent Technologies 1260 Infinity) coupled with a diode-array detector (DAD). An Eclipse C18 column (4.6 mm x 50 mm, 5 μm particle size; Agilent) was used for the chromatographic separation of metabolites. The solvent system consisted of deionized water as mobile phase A, and methanol as mobile phase B, pumped at a constant flow rate of 1 mL/min, which was optimized prior to the experiments.

2.7.4 Detection of compounds

Metabolites were detected with under UV light (254 nm) and/or spraying with reagents such as ceric sulfate, and vanillin-sulfuric acid spray.

Ceric Sulfate: 1 mL of a saturated solution of ceric sulfate [$Ce(SO_4)_2$] in 65% sulfuric acid [H_2SO_4] was diluted with 20 mL of distilled water.

Vanillin: Vanillin (1 g) was dissolved in 50% ethanol (50 mL), followed by dropwise addition of concentrated H_2SO_4.

2.7.5 Microbial cultures

The microorganisms were obtained from the following sources:

- American Type Culture Collection (ATCC), USA.
- Northern Regional Research Laboratories (NRRL), USA.
- International Mycological Institute (IMI), UK.
- Institute of Fermentation, Osaka (IFO), Japan.

SDA slants were used to grow microorganisms which were then stored at 4 °C prior to use.

2.7.5.1 Preparation of fungal cell culture and media

Specific media were prepared for various fungal cultures. Ingredients for growth media of various fungi are as follows:

***Penicillium chrysogenum* (ATCC9178):** The growth medium for *Penicillium chrysogenum* consisted of the following components per liter of distilled water:

Glycerol (5.0 mL)	Yeast extract (5.0 g)
NaCl (5.0 g)	KH_2PO_4 (5.0 g)
Peptone (5.0 g)	Glucose (10.0 g)

***Fusarium oxysporum* (ATCC76616):** The medium for *Fusarium oxysporum* included the following ingredients per liter of distilled water:

Glycerol (10.0 mL)	Yeast extract (5.0 g)
NaCl (5.0 g)	KH_2PO_4 (5.0 g)
Peptone (5.0 g)	Glucose (10.0 g)

***Cunninghamella elegans* (ATCC36112):** The medium for *Cunninghamella elegans* included the following ingredients per liter of distilled water:

Glycerol (10.0 mL)	Yeast extract (5.0 g)
NaCl (5.0 g)	KH_2PO_4 (5.0 g)
Peptone (5.0 g)	Glucose (10.0 g)

***Rhizopus stolonifer* (ATCC 10404):** *Rhizopus stolonifer* (ATCC 10404) growth medium was formulated according to the following chemicals per liter of distilled water:

Peptone (5.0 g)	Yeast extract (3.0 g)
NaCl (5.0 g)	KH_2PO_4 (5.0 g)
Glucose (20.0 g)	

***Fusarium lini* (NRRL 2204):** The medium for *Fusarium lini* consisted of the following ingredients per liter of distilled water:

Glycerol (10.0 mL)	Yeast extract (5.0 g)
NaCl (5.0 g)	KH_2PO_4 (5.0 g)
Peptone (5.0 g)	Glucose (10.0 g)

***Cephalosporium aphidicola* (IMI 68689):** Medium for *Cephalosporium aphidicola* (IMI 68689) was composed of the following reagents per liter of distilled water:

Glycine (2.0 g)	Yeast extract (5.0 g)
KCl (1.0 g)	KH_2PO_4 (1.0 g)
$MgSO_4.7H_2O$ (2.0 g)	Glucose (50.0 g)
Gibberella trace element solution (GTES) (2.0 mL).	

***Gibberella fujikuroi* (ATCC 10704):** *Gibberella fujikuroi* (ATCC 10704) medium includes the following ingredients per liter of distilled water:

$MgSO_4.7H_2O$ (1.0 g)	NH_4NO_3 (1.0 g),
GTES (2.0 mL),	KH_2PO_4 (5.0 g)
Glucose (80.0 g)	

***Aspergillus niger* (ATCC 10549)**: *Aspergillus niger* (ATCC 10549) was grown in medium, which included the following reagents per liter of distilled water:

Glycerol (10.0 mL)	Yeast extract (3.0 g)
NaCl (5.0 g)	KH_2PO_4 (1.0 g)
Peptone (5.0 g)	Glucose (10.0 g)

***Macrophomina phaseolina* (KUCC 730):** The chemicals for medium of *Macrophomina phaseolina* (KUCC-730) was the same as that of *C. elegans*.

***Curvularia lunata* (NRRL 2178):** The medium for *C. lunata* was the same as that for *C. elegans*.

Gibberella Trace Element Solution: Following constituents were mixed in 100 mL of distilled water:

$Mo(NH_4)_3$ (0.01g)	$FeSO_4.7H_2O$ (0.1 g)
$Co(NO_3)3$ (0.01 g)	$ZnSO_4.7H_2O$ (0.16 g)
$MnSO_4.7H_2O$ (0.01 g)	$CuSO_4.5H_2O$ (0.1 g)

All ten microbial strains were initially screened on a small scale using methylprednisolone acetate (1) as the substrate. Biotransformation progress was monitored by TLC analysis and comparison with substrate and fungal blank controls. Based on substrate conversion efficiency and the appearance of new metabolite spots, *Fusarium oxysporum* and *Penicillium chrysogenum* were selected for large-scale fermentation and further investigation.

2.7.5.2 Fermentation and purification protocol with *Fusarium oxysporum* and *Penicillium chrysogenum*

Eighteen (18) L, and fifteen (15) L of culture medium were prepared for *F. oxysporum*, and *P. chrysogenum* respectively, and autoclaved at 121°C for 10 minutes. The sterilized media were then transferred to 20 Erlenmeyer flasks (12 of *FO*, and 8 of *PC*), each holding 1.5 L of media. Each flask received five days old fungal culture and was incubated at 20 ± 2 °C with a shaker set at 121 rpm. After observing acceptable growth, 7.5 g of substrate (methylprednisolone acetate) was mixed in 100 mL of methanol, and evenly distributed 375 mg per flask. The mixture was placed on a rotary shaker at 20 ± 2 °C for 15 days. To stop the reaction one liter of ethyl acetate was added to each flask after 15 days. The filtrates were extracted three times with EtOAc (25 L × 3), and then concentrated under reduced pressure on a rotary evaporator after being dried with anhydrous sodium sulfate (Na_2SO_4). The microbial transformations protocol is shown in Figure 20.

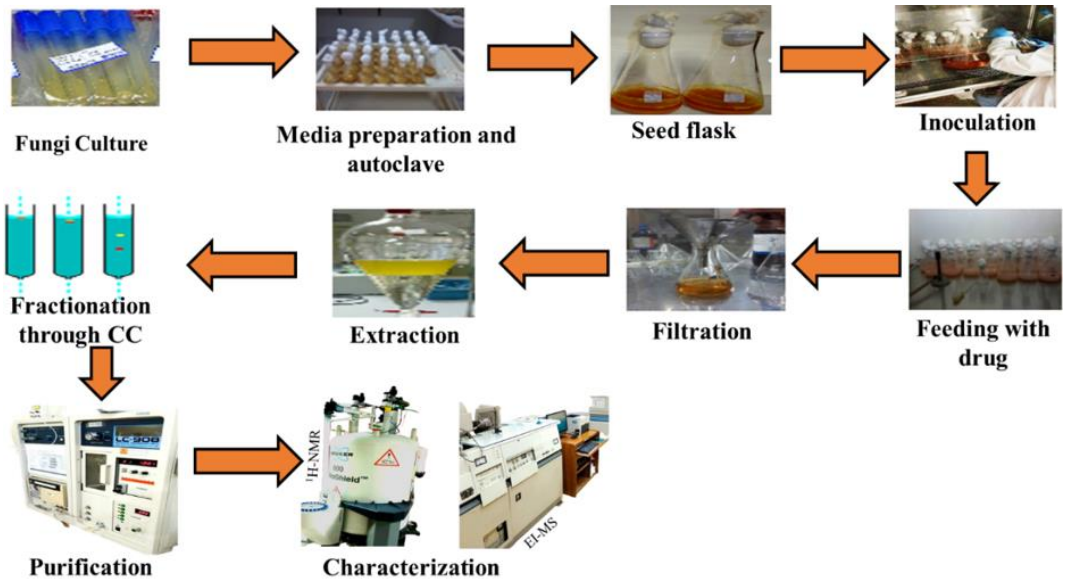


Figure 20 – Experimental protocol of microbial transformation

2.7.6 Isolation and purification

Eight (8.0) g, and six (6.0) g of sticky brown extract were obtained from the incubation of drug (1) with *F. oxysporum* and *P. chrysogenum*, respectively. The crude extract (8 g) of *F. oxysporum* was fractionated using a gradient elution of *n*-hexane and ethyl acetate (100:0 to 0:100), followed by gradient elution of ethyl acetate-methanol (100:0 to 50:50), using a silica-gel (200–300 mesh) column (150 cm × 7.0 cm). Three major fractions (F-1 to F-3) were obtained from column chromatography. Thin-layer chromatography (TLC) was used to determine the fraction profiles. Chloroform, and methanol were used to elute the semi-purified

fractions on HPLC (normal phase). This resulted in the purification of metabolite 2 ($CHCl_3$: MeOH; 98.5/1.5, t_R = 35 min, 5 mg); Rf = 0.67 (TLC, silica gel GF_{254}, $CHCl_3$/MeOH 4:0.1, v/v) from Fr-1, and 3 (DCM: MeOH; 90/10, t_R = 40 min, 7 mg); Rf = 0.37 (TLC, silica gel GF_{254}, $CHCl_3$/MeOH 4:0.1, v/v) from Fr-2. Fr-3 (4 g) was subjected to silica-gel column chromatography with DCM, and methanol to yield three subfractions (Fr-4a to Fr-4c). Fr-4a (300 mg) was extracted by HPLC (normal phase) with chloroform, and methanol ($CDCl_3$: MeOH; 90:10 v/v), yielding metabolite 4 (t_R = 38 min, 5 mg); Rf = 0.36 (TLC, silica gel GF_{254}, $CHCl_3$/MeOH 4:0.1, v/v). Fr-4b (1.5 g) was first extracted on a silica gel column, then eluted with *n*-hexane, and ethyl acetate (100:0 to 0:100, v/v), yielding metabolite 5 (300 mg); Rf = 0.34 (TLC, silica gel GF_{254}, $CHCl_3$/MeOH 4:0.2, v/v). Colorless crystals were obtained after slow solvent evaporation at room temperature. Metabolite 6 (4 mg); Rf = 0.50 (TLC, silica gel GF_{254}, $CHCl_3$/MeOH 4:0.2, v/v), 7 (6 mg); Rf = 0.38 (TLC, silica gel GF_{254}, $CHCl_3$/MeOH 4:0.2, v/v), and 8 (5 mg); Rf = 0.32 (TLC, silica gel GF_{254}, $CHCl_3$/MeOH 4:0.2, v/v), were obtained from Fr-4c (1.2 g) using DCM, and MeOH (100:0 to 85:15, v/v) in a silica gel column chromatography. Figure 21 shows the fermentation, extraction, isolation and purification of metabolites (2-8).

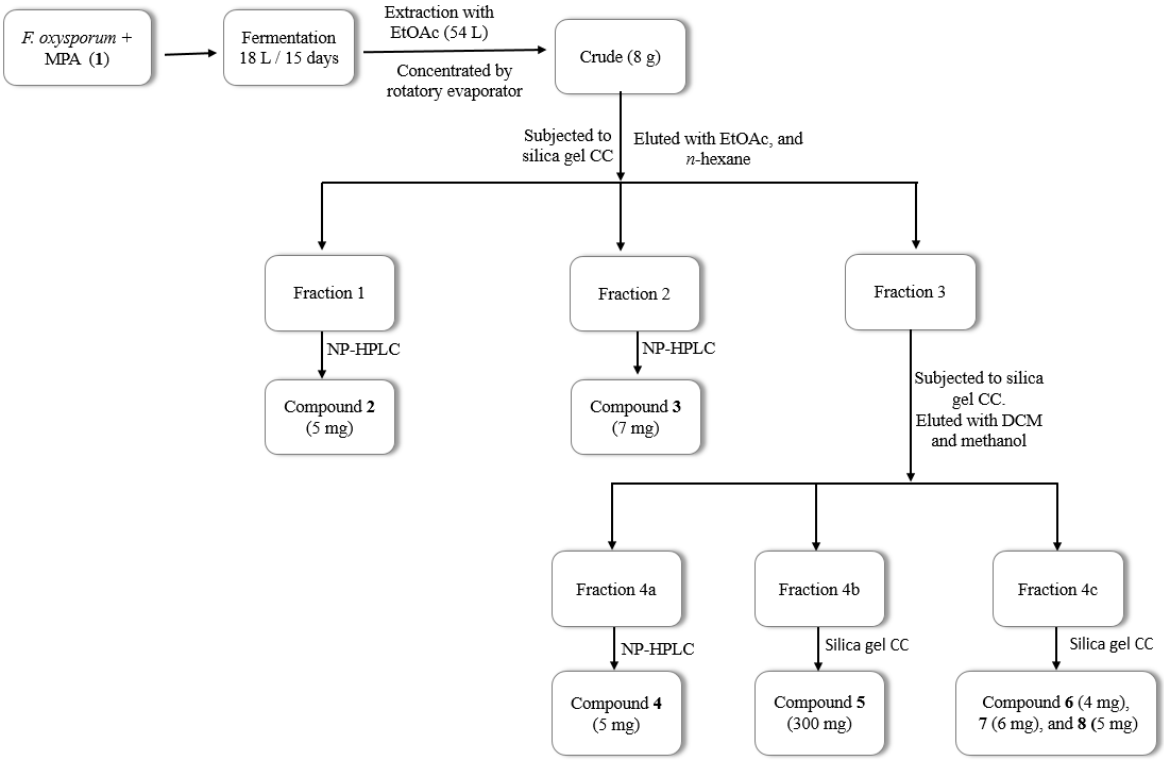


Figure 21 – Fermentation, extraction, isolation, and purification of metabolites using *Fusarium oxysporum*

The crude extract from *Penicillium chrysogenum* (6 g) was subjected to column chromatography with gradient elution of DCM, and MeOH (100:00 to 90:10 v/v), yielding two fractions (F-1 and F-2). Fr-1 (3.5 g) was further purified on a silica gel column using *n*-hexane, and ethyl acetate (100:0 to 0:100, v/v) to get metabolite 3 (8 mg), and 5 (9 mg). The profile of Fr-2 (250 mg) was checked by TLC, followed by purification with HPLC (normal phase) using DCM, and methanol (94:6 v/v), which resulted in the isolation of metabolite 8 (t_R = 20 min, 6 mg), and metabolite 9 (t_R = 32 min, 5 mg); Rf = 0.50 (TLC, silica gel GF_{254}, $CHCl_3$/MeOH 4:0.2, v/v). Figure 22 illustrates the isolation and purification of metabolites 3, 5, and 8-9.

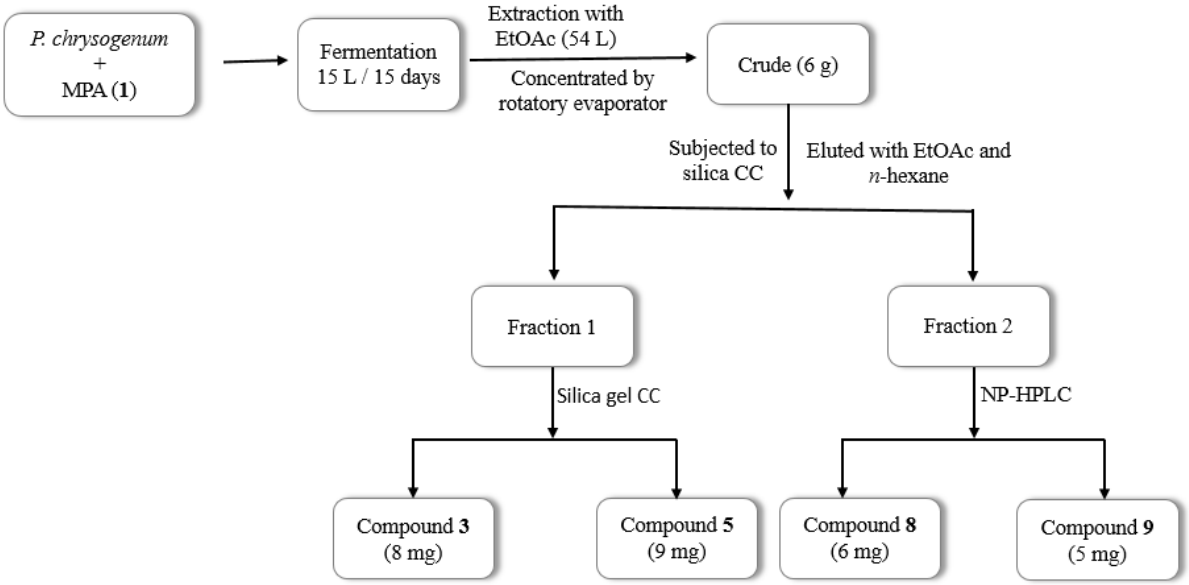


Figure 22 – Fermentation, extraction, isolation, and purification of metabolites using *Penicillium chrysogenum*

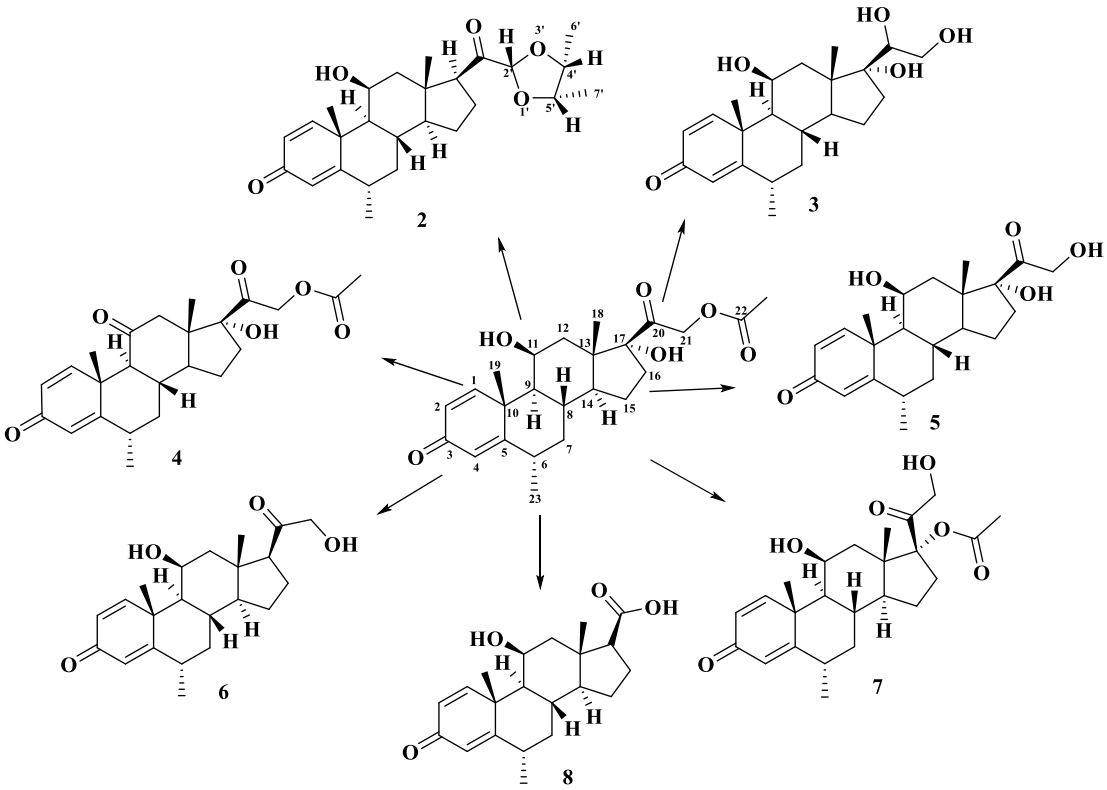


Figure 23 – Biotransformation of methylprednisolone acetate with *Fusarium oxysporum*

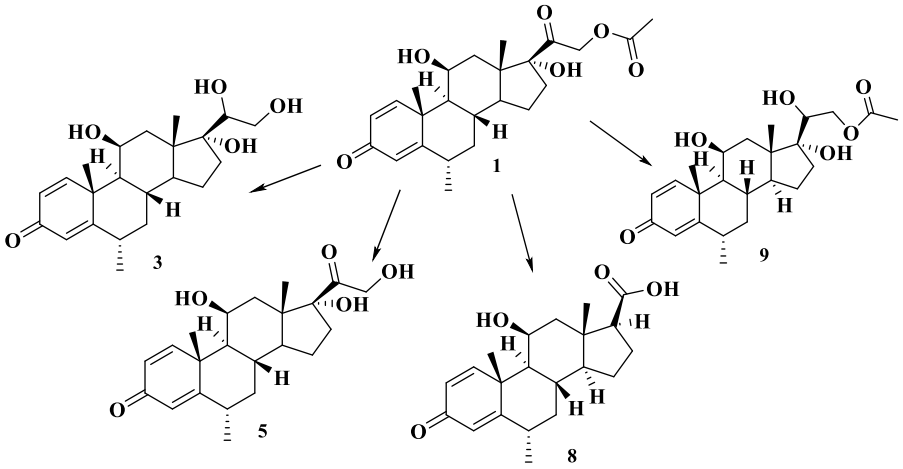


Figure 24 – Biotransformation of methylprednisolone acetate with *Penicillium chrysogenum*

2.7.7 Spectroscopic and spectrometric data of isolated metabolites

Metabolites 2–9 were structurally elucidated using 1D and 2D NMR techniques, including ^{1}H and ^{13}C-NMR spectroscopy [239]. Their structures are shown in Figure 23, and Figure 24. The mass spectrometric data of the isolated metabolites are summarized in Table 27.

20-(4′,5′-Dimethyl-1′,3′-dioxolan-2-yl)-11β-hydroxypregn-4-ene-3,20-dione (2)

Physical state	:	white solid
Melting point	:	178–180 °C
UV ($CHCl_3$) λ_{max} (nm)	:	245
IR ($CHCl_3$) ν_{max} (cm^{-1})	:	3485 (OH), 1716, 1654 (C=O), and 1614 (C=C)
Calculated monoisotopic mass	:	428.25
HRESI-MS *m/z* (observed)	:	429.2633 $[M+H]^+$
Molecular formula	:	$C_{26}H_{36}O_5$
^{1}H-NMR ($CDCl_3$, 500 MHz) δ	:	Table 28
^{13}C-NMR ($CDCl_3$, 125 MHz) δ	:	Table 28

11β,17α,20,21-tetrahydroxy-6α-methylpregna-1,4-dien-3-one (3)

Physical state	:	white solid
UV (MeOH) λ_{max} (nm)	:	245
IR ($CHCl_3$) ν_{max} (cm^{-1})	:	3409 (OH), and 1653 (C=O)
Calculated monoisotopic mass	:	376.22
EI-MS *m/z* (observed)	:	376.4 ($M^{+\bullet}$)
Molecular formula	:	$C_{22}H_{32}O_5$
^{1}H-NMR (CD_3OD, 400 MHz) δ	:	Table 29
^{13}C-NMR (CD_3OD, 125 MHz) δ	:	Table 29

21-acetyloxy-17α-hydroxy-6α-methylpregna-1,4-dien-3,11,20-trione (4)

Physical state	:	white solid
UV (MeOH) λ_{max} (nm)	:	243
IR ($CHCl_3$) ν_{max} (cm^{-1})	:	3428 (OH), 1748, 1727, 1706 (C=O) and 1655 (C=C)
Calculated monoisotopic mass	:	414.20
ESI-MS *m/z* (observed)	:	415.2 $[M+H]^+$
Molecular formula	:	$C_{24}H_{30}O_6$
^{1}H-NMR (CD_3OD, 800 MHz) δ	:	Table 30
^{13}C-NMR (CD_3OD, 150 MHz) δ	:	Table 30

11β,17α,21-trihydroxy-6α-methylpregna-1,4-dien-3,20-dione (5)

Physical state	:	white solid
UV (MeOH) λ_{max} (nm)	:	246
IR ($CHCl_3$) ν_{max} (cm^{-1})	:	3405 (OH), and 1713 (C=O)
Calculated monoisotopic mass	:	374.20
ESI-MS *m/z* (observed)	:	375.1 $[M+H]^+]^+$
Molecular formula	:	$C_{22}H_{30}O_5$

^{1}H-NMR (CD_3OD, 500 MHz) δ	:	Table 31
^{13}C-NMR (CD_3OD, 100 MHz) δ	:	Table 31

11β,21-dihydroxy-6α-methylpregna-1,4-dien-3,20-dione (6)

Physical state	:	white solid
UV (MeOH) λ_{max} (nm)	:	241
IR ($CHCl_3$) ν_{max} (cm^{-1})	:	3422 (OH), 1715, and 1655 (C=O)
Calculated monoisotopic mass	:	358.21
ESI-MS *m/z* (observed)	:	359.3 $[M+H]^+$
Molecular formula	:	$C_{22}H_{30}O_4$
^{1}H-NMR (CD_3OD, 800 MHz) δ	:	Table 32
^{13}C-NMR (CD_3OD, 150 MHz) δ	:	Table 32

17α-acetoxy-11β,21-dihydroxy-6α-methylpregna-1,4-dien-3,20-dione (7)

Physical state	:	white solid
UV (MeOH) λ_{max} (nm)	:	245
IR ($CHCl_3$) ν_{max} (cm^{-1})	:	3420 (OH), 1724, and 1654 (C=O)
Calculated monoisotopic mass	:	416.22
ESI-MS *m/z* (observed)	:	417.2 $[M+H]^+$
Molecular formula	:	$C_{24}H_{32}O_6$
^{1}H-NMR (CD_3OD, 800 MHz) δ	:	Table 33
^{13}C-NMR (CD_3OD, 201 MHz) δ	:	Table 33

11β-hydroxy-6α-methyl-3-oxoandrosta-1,4-diene-17β-carboxylic acid (8)

Physical state	:	white solid
UV (MeOH) λ_{max} (nm)	:	246
IR ($CHCl_3$) ν_{max} (cm^{-1})	:	3386 (OH), 1724, and 1654 (C=O)
Calculated monoisotopic mass	:	344.19
ESI-MS *m/z* (observed)	:	345.2 $[M+H]^+$
Molecular formula	:	$C_{21}H_{28}O_4$
^{1}H-NMR (CD_3OD, 800 MHz) δ	:	Table 34
^{13}C-NMR	:	Not recorded

21-acetyloxy-11β,17α,20-trihydroxy-6α-methylpregna-1,4-dien-3-one (9)

Physical state	:	white solid
UV (MeOH) λ_{max} (nm)	:	244
IR ($CHCl_3$) ν_{max} (cm^{-1})	:	3437 (OH), 1728, and 1656 (C=O)
Calculated monoisotopic mass	:	418.23
EI-MS *m/z* (observed)	:	418.3 ($M^{+\bullet}$)
Molecular formula	:	$C_{24}H_{34}O_6$

^{1}H-NMR (CD_3OD, 400 MHz) δ	:	Table 35
^{13}C-NMR (CD_3OD, 150 MHz) δ	:	Table 35

2.7.8 *In vitro* studies

2.7.8.1 Aromatase inhibition assay

The human placental aromatase inhibition assay was performed using 96-well black fluorescent microplate with a total reaction volume of 100 µL. The test compounds were initially dissolved in DMSO, and further diluted with methanol. Acetonitrile was used to dissolve the substrate 7-methoxy-4-(trifluoromethyl)coumarin (MFC). Human placental microsomes containing aromatase were prepared from placental tissues obtained from Sobhraj Maternity Hospital, Karachi, Pakistan, and used as the enzyme source. The preparation of placental microsomes and aromatase inhibition assays was carried out in collaboration with the Dr. Panjwani Center for Molecular Medicine and Drug Research, (ICCBS), University of Karachi, Pakistan, under the supervision of Prof. Dr. Muhammad Iqbal Choudhary. A solution of 0.1 M potassium phosphate buffer (pH 7.4) was used to prepare the human placental microsomal suspension. After mixing the microsomes, and the substrate (MFC, 50 µM), the final concentration of human placental aromatase was adjusted to 2 mg/mL. Each well received 47 µL of the enzyme/substrate mixture and 3 µL of test compound at various concentrations. After 5 minutes of pre-incubation at 37°C, the reaction was initiated by adding 50 µL of NADPH (1 mM), bringing the final incubation volume to 100 µL. The plate was then incubated at 37 °C for 20 minutes. The reaction was stoped by adding 37 µL of acetonitrile containing 0.1 M Tris base. And then the fluorescence of each well was measured using a Varioskan Lux multimode microplate reader at an excitation wavelength of 400 nm (emission 540 nm) [238, 239]. Exemestane was used as the positive control, while the negative control consisted of the complete reaction mixture containing aromatase, substrate, and the corresponding solvent (DMSO/methanol) but without the test compound. Background fluorescence was determined from the wells containing enzyme-substrate mixture by adding stop solution before the addition of NADPH. Under the assay conditions, product production was linear with respect to time and protein concentration. The IC_{50} values were determined from concentration–response curves generated in triplicate (n = 3) using GraphPad Prism (version 8) [241, 242]. Nonlinear regression analysis with a four-parameter logistic model was used for curve fitting, and 95% confidence intervals were calculated where applicable.

2.7.9 *In silico* studies

2.7.9.1 Ligand preparation

The ligand preparation was performed by using the *LigPrep* tool, which involved a series of steps to optimize the molecular structures. These steps include

torsion optimization to relieve steric hindrances, strains, and assignment of appropriate protonation states at a physiological pH range of 7.0 ± 2.0. This comprehensive preparation protocol ensured that the ligands (metabolites) 2–9 were accurately represented in their most biologically relevant forms [242-244].

2.7.9.2 Protein preparation

The protein structure (PDB ID: 4KQ8) (human aromatase) was prepared, and minimized using Schrödinger's Maestro 2023-1 software. The OPLS4e force field was used to assign partial charges, and protons, while the Prime module filled missing loops, and created bonds to metal ions. PROPKA predicted the protein's pKa, and restricted minimization optimized heavy atoms, and hydrogens, easing steric hindrance.

2.7.9.3 Molecular docking studies

Molecular docking studies were performed by using the Glide 6.9 module of Schrödinger 2023-1. The reported crystal structure of protein aromatase (PDB ID: 4KQ8) was used for ligand docking, with a 10×10×10 Å grid box centered around the co-crystallized ligand (4-Androstene-3,17-dione), defining the binding site. The Glide XP module was employed for ligand docking, and the resulting best-docked conformations were analyzed to interpret the final results [245, 246].

2.7.9.4 MM-GBSA tool for binding energy estimation

The Prime MM-GBSA tool was employed to estimate the binding free energy, and affinities of the protein-ligands complexes. This tool re-ranked the docked conformations obtained from Glide XP docking for each ligand, and estimated their binding energies in kcal/mol. The binding energies reflects binding affinities, with more negative values indicating a stronger binding [247-249].

2.8 Results and discussion

2.8.1 Optimization of UPLC system

Samples were analyzed using an ultra-performance liquid chromatography (UPLC) system (Agilent Technologies 1260 Infinity) coupled with a diode array detector (DAD). Chromatographic separation was achieved using an Eclipse C18 column (4.6 × 50 mm, 5 µm). Column length optimization (150, 100, and 50 mm) revealed that shorter columns provide faster analysis with acceptable resolution, particularly suitable for steroidal compounds, whereas longer columns improve resolution at the expense of extended run time. Therefore, the 50 mm column was selected to achieve rapid and efficient separation. A binary mobile phase consisting of deionized water (A) and methanol (B) was employed, as methanol–water systems are commonly used for steroid analysis in reversed-phase chromatography [250]. The flow rate was maintained at 1.0 mL/min to ensure optimal peak shape and reproducibility.

A gradient elution from 90% A to 95% B was applied to accommodate compounds of varying polarity, as increasing organic solvent concentration facilitates the separation of structurally similar steroidal metabolites. Under these optimized conditions metabolite 8 (peak 1), and metabolite 4 (peak 2) were successfully resolved (Figure 25). The observed differences in retention behavior can be attributed to variations in polarity and functional groups, where metabolite 8, bearing a carboxylic acid functionality, elutes earlier due to increased polarity, while metabolite 4, containing acetoxy and ketone groups, shows relatively higher retention due to increased hydrophobic interactions with the stationary phase. This behavior is consistent with reported reversed-phase chromatographic patterns of steroid derivatives [251].

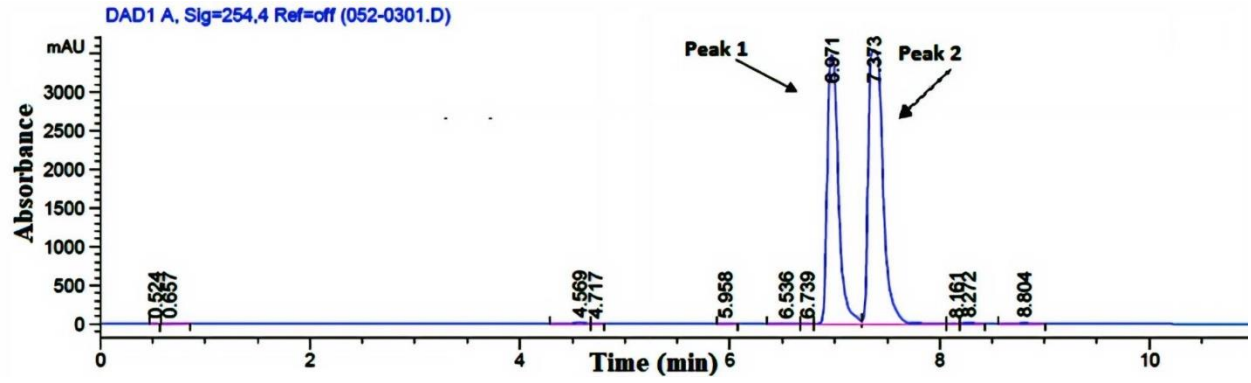


Figure 25 – UPLC-DAD chromatogram of metabolite 8 (peak 1), and metabolite 4 (peak 2) at 245 nm

2.8.2 Structural elucidation

Incubation of methylprednisolone acetate (1) with *Fusarium oxysporum* yielded one new metabolite (2), and six known metabolites (3-8), as shown in Figure 23. Similarly, incubation with *Penicillium chrysogenum* resulted four metabolites (3, 5, 8, and 9), as shown in Figure 24. The formation of hydroxylated and reduced metabolites demonstrates the regio- and stereoselective nature of fungal biocatalysis. Similar transformations have been reported for steroid substrates by microbial systems, highlighting the ability of fungi to introduce structural modifications that are difficult to achieve selectively through conventional chemical synthesis [252, 253]. The structure of the new metabolite 2, as well as known metabolites 3–9, were elucidated using NMR, and MS techniques, and compared with published data. The corresponding NMR and MS spectra, along with other supplementary characterization data, are provided in the Appendices.

Mass spectrometric data including molecular formula, ionization mode, ion type, calculated monoisotopic mass, and observed m/z values for metabolites 2–9, are given in Table 27.

Table 27 – Mass spectrometric data of metabolites 2–9

Compound	Molecular formula	Ionization mode	Ion type	Calculated monoisotopic mass (Da)	Calculated m/z	[a]Observed m/z	[b]Mass error (ppm)	Figure
2	$C_{26}H_{36}O_5$	[d]HRESI (+)	$[M+H]^+$	428.25	429.2636	429.2633	0.5	29
3	$C_{22}H_{32}O_5$	[e]EI	$M^{+\bullet}$	376.22		376.4		[c]S36
4	$C_{24}H_{30}O_6$	[f]ESI (+)	$[M+H]^+$	414.20		415.2		S38
5	$C_{22}H_{30}O_5$	ESI (+)	$[M+H]^+$	374.20		375.1		S40
6	$C_{22}H_{30}O_4$	ESI (+)	$[M+H]^+$	358.21		359.3		S42
7	$C_{24}H_{32}O_6$	ESI (+)	$[M+H]^+$	416.22		417.2		S44
8	$C_{21}H_{28}O_4$	ESI (+)	$[M+H]^+$	344.19		345.2		S45
9	$C_{24}H_{34}O_6$	EI	$M^{+\bullet}$	418.23		418.3		S46

[a]Observed m/z: experimentally observed mass-to-charge ratio; [b]Mass error (ppm): mass error (ppm) and calculated m/z values are reported only for compound 2, which was analyzed by HRESI-MS; [c]S: supplementary figure; [d]HRESI (+): high-resolution electrospray ionization mass spectrometry in positive-ion mode; [e]EI: electron ionization mass spectrometry (low-resolution); [f]ESI (+): electrospray ionization mass spectrometry in positive-ion mode (low-resolution).

Metabolite 2: High-resolution electrospray ionization mass spectrometry (HRESI-MS) supported the molecular formula $C_{26}H_{36}O_5$ based on its $[M+H]^+$ peak at *m/z* 429.2633 as shown in Figure 29, consistent with an additional moiety relative to the substrate 1. The IR spectrum of $CHCl_3$ exhibited absorption bands at 3485 cm^{-1} (OH), 1716 (ketone C=O), 1654 cm^{-1} (conjugated C=O), and 1614 cm^{-1} (C=C), confirming the existence of hydroxyl, keto, and olefinic functionalities in the molecule.

Significant differences were observed between the ^{1}H- (Figure 28), and ^{13}C-NMR spectra (Figure 30) of metabolite 2, and the substrate 1 (Table 28). Signals corresponding to the acetal-related methylene at δ_H 1.16, and methine at δ_H 4.93 disappeared, while new peaks for a dioxolane ring appeared. The ^{1}H-NMR spectra revealed a singlet at δ_H 5.05 (H-2′), and multiplets at δ_H 3.63, and 3.64 (H-4′ and H-5′), as well as a multiplet at δ_H 1.29-1.22 (C-6′ and C-7′) of the dioxolane ring. Additionally, the presence of a multiplet at δ_H 2.78 suggested the loss of the 17α-OH [254]. The ^{13}C-NMR spectra showed new carbon signals at δ_C 101.3 (C-2′), 79.1 (C-4′), and 80.2 (C-5′), confirming the incorporation of a 4′,5′-dimethyl-1′,3′-dioxolane moiety. Downfield carbon signals at δ_C 186.6, and 206.4 were due to the presence of two ketone groups as shown in Figure 30.

The attachment of substituent was further verified using HMBC correlations. Proton H-2′ (δ_H 5.05) showed long-range correlations with C-17 (δ_C 57.6), C-20 (δ_C 206.4), C-4′ (δ_C 79.1), and C-5′ (δ_C 80.2), indicating attachment of dioxolane ring at C-20. Additionally, HMBC correlations of C-4′ and C-5′ to the methyl carbons C-6′ and C-7′ (δ_C 17) indicated the presence of dimethyl substitution. Moreover, a triplet at δ_H 2.78 showed HMBC correlations with carbon signals at δ_C 206.4 (C-20), δ_C 44.4 (C-13), δ_C 23.5 (C-16), and δ_C 16.5 (18-CH_3), confirming its assignment as 17α-H. COSY analysis (Figure 27) confirmed the absence of vicinal proton coupling to H-2′ (δ_H 5.05), confirming its position.

The relative stereochemistry of the dioxolane moiety was determined *via* NOESY analysis (Figure 27). Proton H-2′ (δ_H 5.05) exhibited spatial correlations with H-4′ and H-5′ (δ_H 3.64 and 3.63), and methyl groups (C-6′ and C-7′), indicating a *cis*-orientation. NOESY correlations between H-2′, and protons at δ_H 0.94 (C-18), and δ_H 2.12 (C-8) supported the *cis*-configuration of the 4′,5′-dimethyl-1′,3′-dioxolane ring.

Metabolite 2 was assigned as 20-(4′,5′-Dimethyl-1′,3′-dioxolan-2-yl)-11β-hydroxypregn-4-ene-3,20-dione (Figure 26) [254]. The HPLC chromatogram used for purity assessment is presented in Appendix B (Figure S25), while the corresponding 2D-NMR including COSY, HMBC, and NOESY, and ^{13}C-NMR spectra are provided in Figures S27–S33.

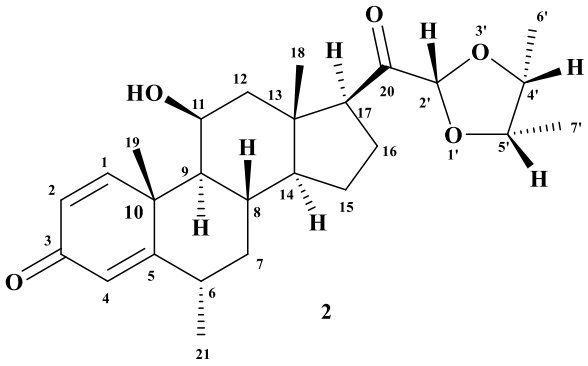


Figure 26 – Chemical structures of biotransformed metabolite 2 through *F. oxysporum*

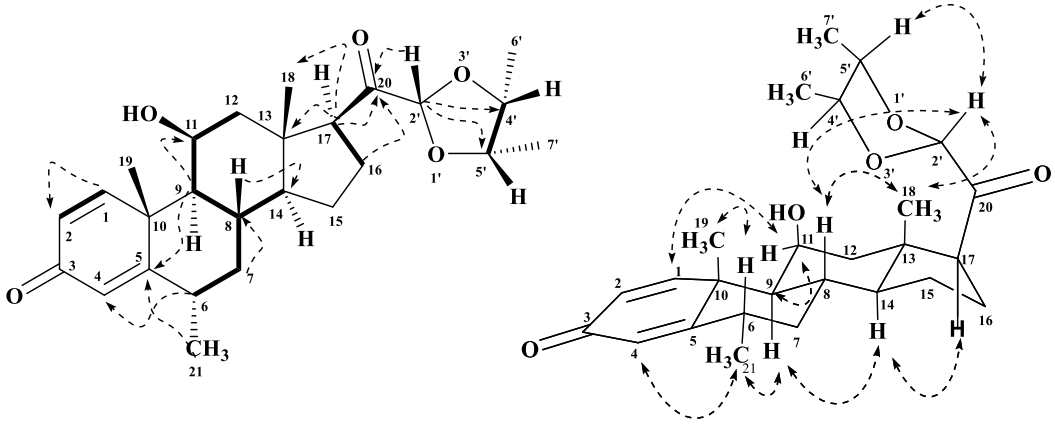


Figure 27 – Key COSY (▬), HMBC (⋯➝), and NOESY (🡻🡹) correlations of metabolite 2

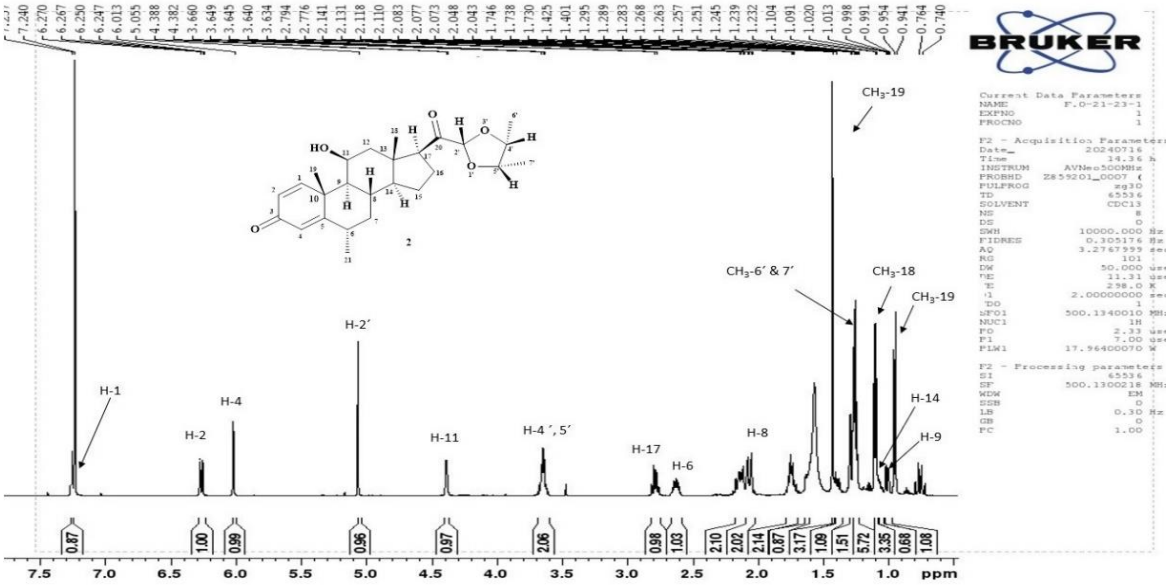


Figure 28 – ^{1}H-NMR spectrum of metabolite 2.

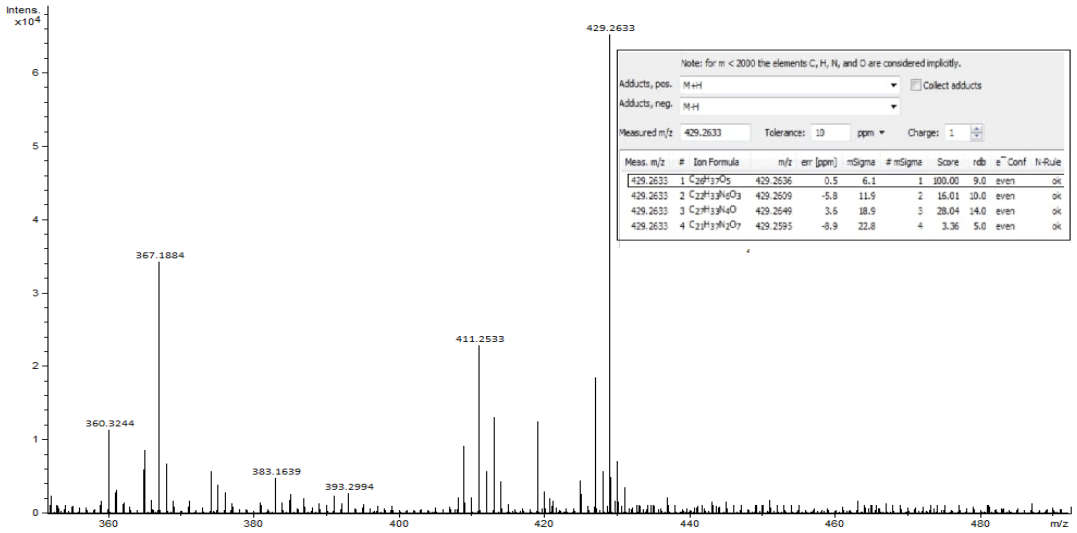


Figure 29 – HRESI-MS spectrum of metabolite 2

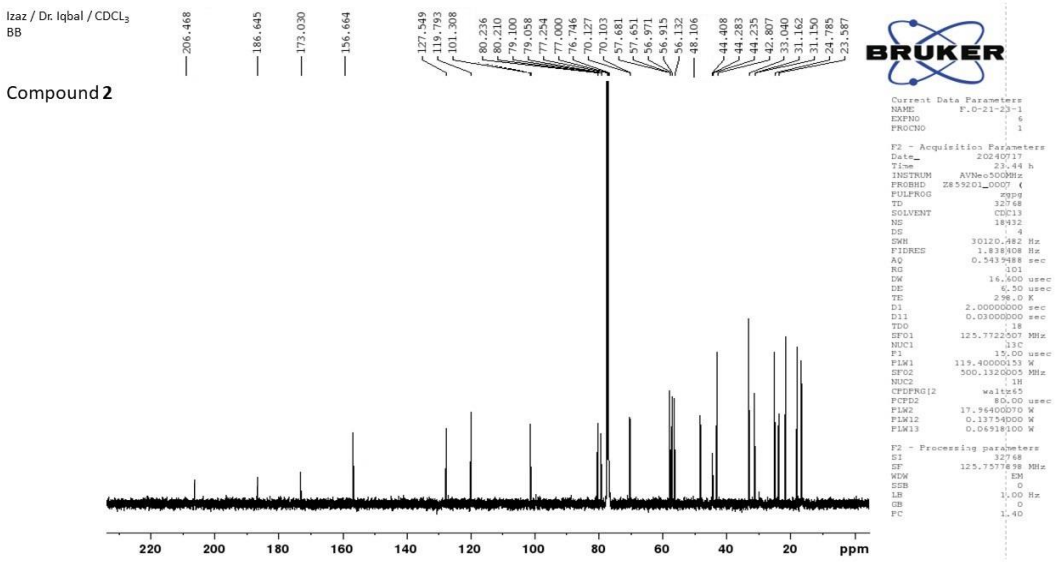


Figure 30 – Broadband-decoupled (BB) ^{13}C-NMR spectrum of metabolite 2

Table 28 – ^{1}H, and ^{13}C-NMR chemical shift data (*J* in Hz) of metabolite 2[a]

No.	2		
	δ_C	δ_H (*J* in Hz)	Multiplicity
1	156.7	7.25, d, $J_{1/2}$ = 10.0 Hz, 1H	CH
2	127.5	6.27, d, $J_{2/1,\ 2/4}$ = 10.0 Hz, 1H	CH
3	186.6	-	[b]C
4	119.8	6.01, m, 1H	CH
5	173.1	-	C
6	33.0	2.65, m, 1H	CH

Table 28 (continued)			
7	42.8	2.07, m; 0.75, m, 2H	CH_2
8	31.1	2.12, m. 1H	CH
9	56.9	1.02 (1H, dd, $J_{9/11,\,9/8}$ = 11.5 Hz, 3.5 Hz, 1H	CH
10	44.4	-	C
11	70.1	4.38, m, 1H	CH
12	48.1	2.08, m; 1.60, m, 2H	CH_2
13	44.4	-	C
14	57.7	1.07, m, 1H	CH
15	24.7	1.74, m; 1.39, m, 2H	CH_2
16	23.5	2.14, m; 1.73, m, 2H	CH_2
17	57.6	2.78, m. 1H	CH
18	16.5	0.94, d, J = 5.6 Hz, 3H	CH_3
19	21.4	1.42, s, 3H	CH_3
20	206.4	-	C
2′	101.3	5.05, s, 1H	CH
4′	79.1	3.64, m, 1H	CH
5′	80.2	3.63, m, 1H	CH
6′, 7′	17.7	1.29-1.22, m, 6H	$2CH_3$
21	16.3	1.09, d, $J_{22/6}$ = 6.5 Hz, 3H	CH_3

2[a]: ^{1}H- and ^{13}C-NMR ($CDCl_3$; 500 and 125 MHz); [b]C: quaternary carbons

The formation of metabolites 2–9 was confirmed through control experiments conducted under identical fermentation conditions. Negative controls containing the substrate and culture medium, but lacking the fungal strain, were subjected to the same incubation, extraction, and chromatographic procedures. None of the metabolites were detected in any of the control experiments, whereas they were exclusively observed in cultures containing both the fungal strain and the substrate, confirming their origin as true fungal biotransformation products.

2.8.2.1 Proposed mechanism for synthesis of metabolite 2

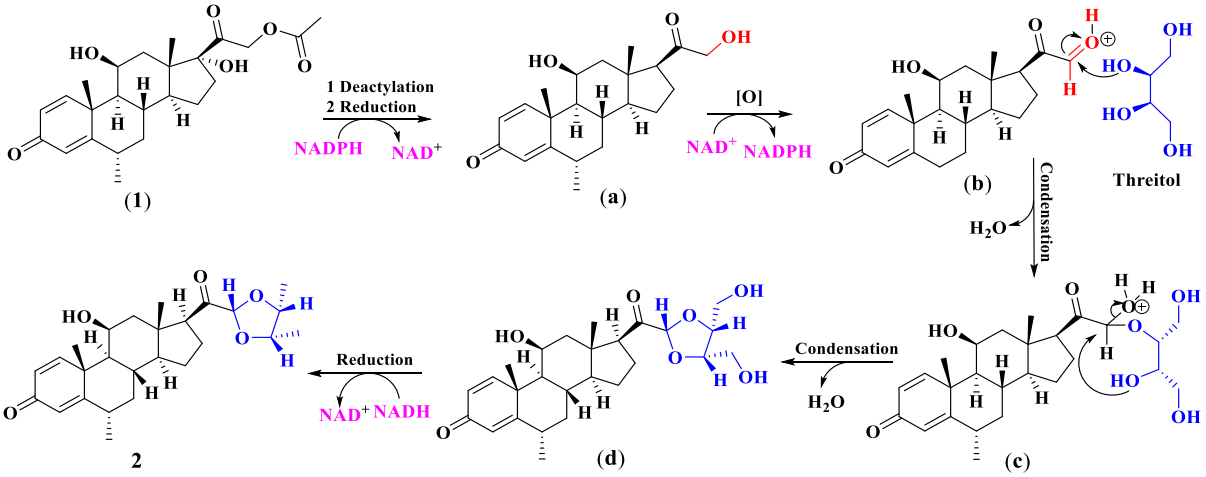
A possible mechanism for the synthesis of metabolite 2 is provided in Scheme 1 based on its structural features, and known fungal biotransformation pathways. Isolated cytochrome P450 monooxygenases from *Fusarium oxysporum* have been knwon to catalyze regio-, and stereoselective oxidation reactions, transforming unactivated hydrocarbon C-H bonds of steroidal substrates into C-OH functionality under mild conditions [255]. Such enzymes might be able to catalyze hydroxylation by high-valent iron-oxo species (Fe^{4+}), which could abstract a hydrogen atom from the steroidal substrate, and then an oxygen-rebound step to introduce a hydroxyl group (OH) at an sp^3-hybridized carbon center [256]. Members of the genus

Fusarium, including *F. oxysporum*, are known to catalyze selective hydroxylation of steroidal drugs. In this study, metabolite 8 is likely produced from regioselective hydroxylation, whereas metabolite 4 from an oxidative pathway, collectively demonstrating the broad oxidative capacity of fungal biocatalysts [257].

Metabolite 5, which is another biotransformed product, could to be produced through deacetylation, but metabolite 7 is appeared to be the result of an acetyl rearrangement reaction. Similarly, a reductive deacetylation mechanism is proposed to produce metabolite 2, and 6.

In the first step of metabolite 2 synthesis, substrate 1 undergoes esterase-catalyzed deacetylation at C-21, a reaction commonly associated with enzymatic hydrolysis of ester functional groups, yielding a free C-21 (a) hydroxyl group. The C-21 hydroxyl further oxidized to an aldehyde (b), while the C-17 hydroxyl simultaneously reduced *via* a dehydrogenase-type enzyme, and the NAD^+/NADH use as a redox cofactor [258]. The highly electrophilic aldehyde undergoes acetalization with threitol moiety at C-2, and C-3 hydroxyl groups through elimination of two water molecules, the polyol (threitol) originates from fungal carbohydrate metabolism under fermentation conditions [259-261]. Further reduction of terminal hydroxyl groups (d) occurred through reductases enzyme, afforded metabolite 2 [262].

The identification of metabolite 2 expands the known metabolic profile of methylprednisolone acetate and demonstrates the ability of fungal biocatalysts to generate structurally novel steroidal derivatives. This finding highlights the potential of microbial biotransformation as a valuable approach for producing new molecules of pharmaceutical interest.



Scheme 1 – Tentative fungal biotransformation pathway for the formation of metabolite (2) from substrate 1 *via* esterase-mediated deacetylation**,** NAD^+/NADH-dependent oxidation, and intramolecular acetalization.

11β,17α,20,21-tetrahydroxy-6α-methylpregna-1,4-dien-3-one (3)

Metabolite 3 was obtained as a white solid, UV λ_{max} 245 nm; the molecular ion peak ($M^{+\bullet}$) at m/z 376.4 ($C_{22}H_{32}O_5$) in the EI-MS spectrum consistent with ester hydrolysis, followed by hydroxylation in substrate 1 (m/z 416).

The IR ($CHCl_3$) spectrum showed the presence of ketone carbonyl group at 1653 cm^{-1}, and OH at 3409 cm^{-1}. The ^{13}C-NMR spectrum is lacks the quaternary carbon around δ_C 214 (C-20), and shows two new signals at δ_C 76, and δ_C 65, suggesting dihydroxylation in metabolite 3 at the C-20, and 21 positions. The presence of OH groups at C-20, and C-21 were also supported by the ^{1}H-NMR spectrum which displayed signals for a new methine protons at δ_H 3.77 (C-20), and δ_H 3.65 (C-21) (Table 29) [263]. The new OH groups were assigned at C-20 based on the HMBC correlations of H-20 (δ_H 3.77) with C-21 (δ_C 65), and H-21 (δ_H 3.65) with C-20 (δ_C 76), and C-17 (δ_C 86), respectively. The known metabolite 3 was thus identified as 11β,17α,20,21-tetrahydroxy-6α-methylpregna-1,4-dien-3-one. The HPLC chromatogram is provided in Appendix B (Figure S25), and the corresponding ^{1}H-NMR, ^{13}C-NMR, and mass spectra are provided in Figures S36–S37.

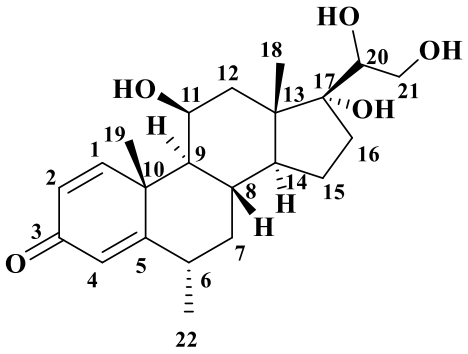


Table 29 – ^{1}H-, and ^{13}C-NMR chemical shift data of metabolite 3[a]

Carbon	δ_C	δ_H (*J* in Hz)	Multiplicity
1	160.9	7.49, d , $J_{1/2}$ = 10.0 Hz, 1H	CH
2	127.3	6.25, dd , $J_{1/2, 2/4}$ = 10.0 Hz, 1.6 Hz, 1H	CH
3	189.0	-	[b]C
4	119.6	5.97, m, 1H	CH
5	178.0	-	[b]C
6	34.3	2.75, m, 1H	CH
7	44.7	2.17, m; 0.82, m, 2H	CH_2
8	32.6	2.21, m, 1H	CH
9	58.2	0.96, dd, $J_{9/11, 9/8}$ = 11.2 Hz, 3.6 Hz, 1H	CH
10	43.2	-	[b]C
11	71.1	4.35, m, 1H	CH
12	42.1	1.99, m; 1.77,m, 2H	CH_2
13	46.3	-	[b]C
14	51.5	1.56, m, 1H	CH
15	25.1	1.85, m; 1.44, m, 2H	CH_2

Table 29 (continued)			
16	34.5	1.74, m; 1.32, m, 2H	CH_2
17	86.1	-	[b]C
18	18.0	1.11, m, 3H	CH_3
19	21.9	1.49, s, 3H	CH_3
20	76.3	3.77, m, 1H	CH
21	65.3	3.65, m, 2H	CH_2
22	17.8	1.23, m, 3H	CH_3

3[a]: ^{1}H- and ^{13}C-NMR (CD_3OD; 400 and 125 MHz); [b]C: quaternary carbons

21-acetyloxy-17α-hydroxy-6α-methylpregna-1,4-dien-3,11,20-trione (4)

A white solid powder of metabolite 4 was isolated. UV λ_{max} 243 nm; ESI-MS (+) of metabolite 4 showed molecular ion peak $[M+H]^+$ at m/z 415.2 ($C_{24}H_{30}O_6$), which is 2 a.m.u lower than that of the substrate 1. This suggested that one hydroxyl group has been oxidized to a ketone. Absorption bands in the IR ($CHCl_3$) spectrum at 3428 cm^{-1} represents OH, and 1748 cm^{-1}, 1727 cm^{-1}, 1706 cm^{-1}, and 1655 cm^{-1} indicate the presence of multiple carbonyl groups (ketone and ester), and olefinic functionalities, respectively. The ^{1}H-NMR spectrum (Table 30) lacks the methine proton at δ_H 4.40 (C-11), which is present in substrate 1 [264]. Additionally, the appearance of new quaternary carbon (δ_C 211) in the ^{13}C-NMR spectrum indicated oxidation of the C-11 hydroxyl group. The position of the new ketone group was deduced on the basis of HMBC correlations of H-12 (δ_H 2.950 and 2.323), and H-9 (δ_H 2.087) with C-11 (δ_C 211). Metabolite 4 was assigned as 21-acetyloxy-17α-hydroxy-6α-methylpregna-1,4-dien-3,11,20-trione. The HPLC chromatogram used for purity assessment is presented in Appendix B (Figure S25), while the corresponding ^{1}H-NMR, ^{13}C-NMR, and mass spectra are provided in Figures S38–S39.

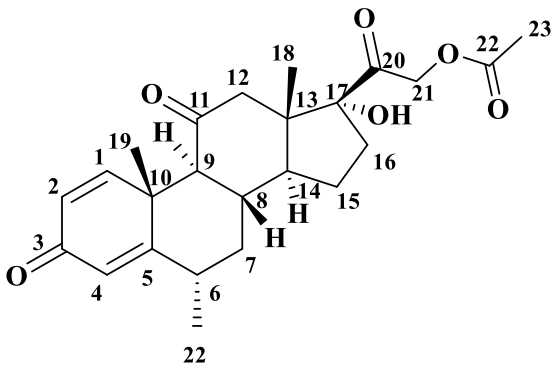


Table 30 – ^{1}H-, and ^{13}C-NMR chemical shift data of metabolite 4[a]

Carbon	**δ_C**	**δ_H (*J* in Hz)**	**Multiplicity**
1	158.8	7.80, d , $J_{1/2}$ = 10.4 Hz, 1H	CH
2	127.3	6.19, dd , $J_{1/2, 2/4}$ = 9.6 Hz, 1.6 Hz, 1H	CH
3	188.7	-	[b]C
4	121.8	6.07, m 1H	CH
5	174.1	-	[b]C

Table 30 (continued)			
6	34.5	2.69, m 1H	CH
7	43.5	2.09, m; 1.02, m, 2H	CH_2
8	37.3	2.22, m 1H	CH
9	61.7	2.09, m, 1H	CH
10	44.3	-	[b]C
11	211.5	-	[b]C
12	52.6	2.95; 2.323, m, 2H	CH_2
13	48.2	-	CH
14	50.7	2.40, m, 1H	CH
15	24.0	1.99, m; 1.504, m, 2H	CH_2
16	35.2	2.70, m; 1.695, m, 2H	CH_2
17	89.4	-	[b]C
18	15.7	0.64, s, 3H	CH_3
19	19.6	1.46, s, 3H	CH_3
20	207.0	-	CH
21	69.4	4.93, overlap, 2H	CH_2
22	172.3	-	[b]C
23	20.3	2.12, s, 3H	CH_3
24	17.9	1.16, d, $J_{22/6}$ = 6.4 Hz, 3H	CH_3

4[a]: ^{1}H- and ^{13}C-NMR (CD_3OD; 800 and 150 MHz); [b]C: quaternary carbons

11β,17α,21-trihydroxy-6α-methylpregna-1,4-dien-3,20-dione (5)

Metabolite 5 was appeared as a white solid. UV λ_{max} 246 nm; the ESI-MS (+) of metabolite 5 showed the molecular ion peak $[M+H]^+$ at m/z 375.1 ($C_{22}H_{30}O_5$), indicating the loss of the ester group present in compound 1. The IR ($CHCl_3$) spectrum showed absorbances at 3405 cm^{-1} confirming the hydroxyl, while 1713 cm^{-1}, and 1648 cm^{-1} represents the ketone groups functionality. The ^{1}H-NMR spectrum of metabolite 5 lacks the signals of the ester group and showed methylene protons at δ_H 4.62 (m) of C-21 (Table 31). The H-21 (δ_H 4.62) showed HMBC correlations with C-20 (δ_C 214) which indicated hydroxylation at C-21 [265]. Finally, metabolite (5) was assigned as 11β,17α,21-trihydroxy-6α-methylpregna-1,4-dien-3,20-dione. The corresponding ^{1}H-NMR, ^{13}C-NMR, and mass spectra are provided in Appendix B (Figures S40–S41).

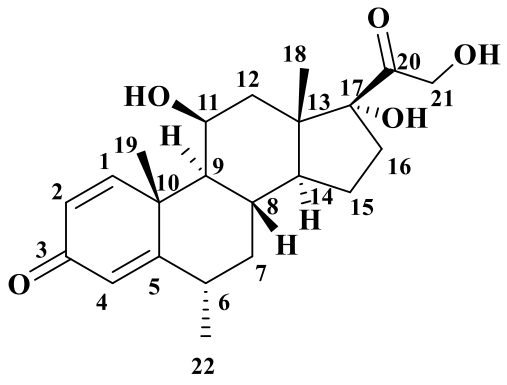


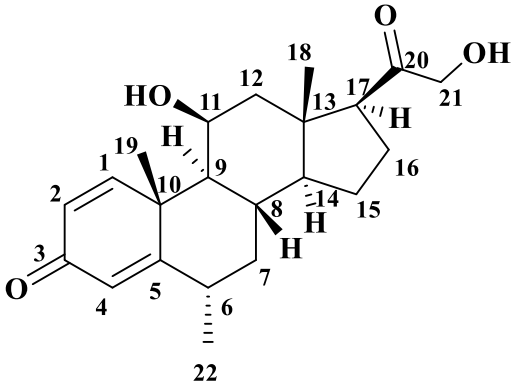
Table 31 – ^{1}H-, and ^{13}C-NMR chemical shift data of metabolite 5[a]

Carbon	δ_C	δ_H (*J* in Hz)	Multiplicity
1	158.5	7.46, d, $J_{1/2}$ = 10.0 Hz, 1H	CH
2	128.7	6.26, dd, $J_{2/1,\ 2/4}$ = 10.5 Hz, 2.0 Hz, 1 [H]	CH
3	187.4	-	[b]C
4	121.1	5.99, m, 1H	CH
5	174.5	-	[b]C
6	34.2	2.75, m, 1H	CH
7	41.4	2.16, m; 0.84, m, 2H	CH_2
8	32.7	2.27, m, 1H	CH
9	57.6	0.98, dd, $J_{9/11,\ 9/8}$ = 11.5 Hz, 3.5 Hz, 1H	CH
10	44.5	-	[b]C
11	70.8	4.40, m, 1H	CH
12	39.4	1.99, m; 1.60, m, 2H	CH_2
13	45.9	-	CH
14	53.0	1.71, m, 1H	CH
15	25.5	2.72, m; 1.46, m 2H	CH_2
16	35.3	1.80, m; 1.44, m, 2H	CH_2
17	90.7	-	[b]C
18	17.9	0.90, s, 3H	CH_3
19	22.2	1.47, s, 3H	CH_3
20	214.2	-	[b]C
21	68.7	4.62, m, 2H	CH_2
22	18.8	1.13, d, $J_{22/6}$ = 6 Hz, 3H	CH_3

5[a]: ^{1}H- and ^{13}C-NMR (CD_3OD; 500 and 100 MHz); [b]C: quaternary carbons

11β,21-dihydroxy-6α-methylpregna-1,4-dien-3,20-dione (6)

Metabolite 6 was isolated as a white solid. UV λ_{max} 241 nm; ESI-MS (+) showed the molecular ion peak $[M+H]^+$ at m/z 359.3 ($C_{22}H_{30}O_4$), consistent with loss of the ester, hydroxylation at C-21, and replacement of the C-17 hydroxyl with a proton. Absorption bands in the IR ($CHCl_3$) spectrum at 3422 cm^{-1}, 1715 and 1655 cm^{-1} indicated the presence of OH, and ketone functionalities, respectively. The ^{1}H-NMR spectrum revealed a methine proton at δH 2.50 (C-17) and a hydroxyl proton at δH 4.189 (C-21) (Table 32) [265]. The ^{13}C-



NMR spectrum showed a new methine carbon at δC 60 (C-17), supporting the modification at this position. HMBC correlations of H-17 (δ_H 2.50) with C-20 (δC 211) and H-21 (δ_H 4.189) with C-20 (δ_C 211) confirmed the positions of these protons. The known metabolite 6 was deduced as 11β,21-dihydroxy-6α-methylpregna-1,4-dien-3,20-dione. The corresponding ^{1}H-NMR, ^{13}C-NMR, and mass spectra are provided in Appendix B (Figures S42–S43).

Table 32 – ^{1}H-, and ^{13}C-NMR chemical shift data of metabolite 6[a]

Carbon	δ_C	δ_H (*J* in Hz)	Multiplicity
1	160.6	7.47, d, $J_{1/2}$ = 10.4 Hz, 1H	CH
2	127.4	6.25, dd, $J_{1/2, 2/4}$ = 9.6 Hz, 1.6 Hz, 1H	CH
3	189.0	-	[b]C
4	119.7	5.98, m, 1H	CH
5	177.7	-	C
6	34.4	2.75, m, 1H	CH
7	44.3	2.12, m; 0.771, m, 2H	CH_2
8	32.9	2.19, 1H	CH
9	57.8	1.02, dd, $J_{9/11, 9/8}$ = 11.4 Hz, 3.2 Hz, 1H	CH
10	46.2	-	C
11	70.4	4.34, m, 1H	CH
12	48.2	2.09, m; 1.552, m, 2H	CH_2
13	45.1	-	CH
14	52.6	1.68, m, 1H	CH
15	24.7	1.74, m, 1.426, m, 2H	CH_2
16	23.3	2.19, m; 1.758, m, 2H	CH_2
17	60.1	2.50, m, 1H	CH
18	16.2	0.92, s, 3H	CH_3
19	21.9	1.47, s, 3H	CH_3
20	211.7	-	C
21	69.9	4.19, m, 2H	CH_2
22	18.0	1.13, d, $J_{22/6}$ = 6 Hz, 3H	CH_3

6[a]: ^{1}H- and ^{13}C-NMR (CD_3OD; 800 and 200 MHz); [b]C: quaternary carbons

17α-acetoxy-11β,21-dihydroxy-6α-methylpregna-1,4-dien-3,20-dione (7)

Metabolite 7 was obtained as a white solid. UV λ_{max} 245 nm; the molecular ion peak $[M+H]^+$ at m/z 417.2 ($C_{24}H_{32}O_6$) in the ESI-MS (+) spectrum indicated the removal of ester group from C-21, esterification at C-17, and hydroxylation at C-21 relative to substrate 1 (m/z 416). The IR ($CHCl_3$) spectrum displayed absorptions at 3420 cm^{-1} (OH), 1724 and 1654 cm^{-1} (C=O), and 1612 cm^{-1} (C=C) [266]. The ^{13}C-

NMR spectrum showed a quaternary carbon at δ_C 207 (C-20), and methylene carbon at δ_C 67 corresponding to C-21. The ^{1}H-NMR spectrum supported hydroxylation at C-21 with methylene proton signals at δ_H 4.258 (C-21) (Table 33). The new OH group was assigned at C-21 based on HMBC correlations of H-21 (δ_H 4.258) with C-20 (δ_C 207). Metabolite 7 was assigned as 17α-acetoxy-11β,21-dihydroxy-6α-methylpregna-1,4-dien-3,20-dione. The ^{1}H-NMR, and mass spectra are provided in Appendix B (Figures S44).

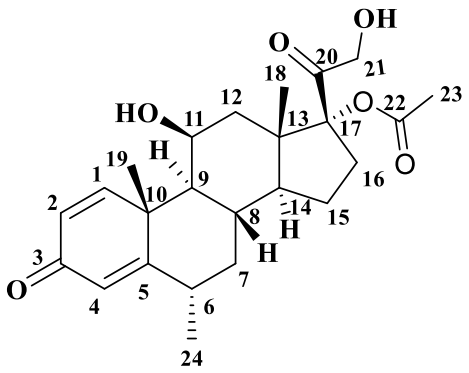


Table 33 – ^{1}H-, and ^{13}C-NMR chemical shift data of metabolite 7[a]

Carbon	δ_C	δ_H (*J* in Hz)	Multiplicity
1	160.5	7.47, d , $J_{1/2}$ = 9.6 Hz, 1H	CH
2	127.5	6.27 , dd, $J_{1/2, 2/4}$ = 10.4 Hz, 1.6 Hz, 1H	CH
3	189.9	-	[b]C
4	119.8	5.99, m, 1H	CH
5	177.5	-	C
6	34.4	2.76, m, 1H	CH
7	44.3	2.16, m; 0.84, m, 2H	CH_2
8	32.6	2.26, m, 1H	CH
9	57.5	1.04, dd, $J_{9/11, 9/8}$ = 11.2 Hz, 4.0 Hz, 1H	CH
10	46.1	-	C
11	70.4	4.42, m, 1H	CH
12	40.4	2.04, m; 1.72, m, 2H	CH_2
13	48.3	-	CH
14	53.0	1.64, m, 1H	CH
15	25.0	1.80, m; 1.51, m, 2H	CH_2
16	31.2	2.84, m; 1.81, m, 2H	CH_2
17	95.5	-	C
18	17.1	0.96, s, 3H	CH_3
19	20.9	1.48, s, 3H	CH_3
20	207.0	-	C
21	67.5	4.26, s, 2H	CH_2
22	172.5	-	C
23	21.9	1.99, s, 3H	CH_3
24	18.0	1.13, d, $J_{21/6}$ = 6.4 Hz, 3H	CH_3

7[a]: ^{1}H- and ^{13}C-NMR (CD_3OD; 800 and 150 MHz); [b]C: quaternary carbons

11*β*-Hydroxy-6*α*-methyl-3-oxoandrosta-1,4-diene-17*β*-carboxylic Acid (8)

A white solid of metabolite 8 was obtained. UV λ_{max} 246 nm; ESI-MS (+) showed molecular ion peak $[M+H]^+$ at m/z 345.2 ($C_{21}H_{28}O_4$), suggesting removal of the side chain at C-20 with formation of a carboxylic acid and dehydroxylation at C-17. Absorption bands in the IR ($CHCl_3$) spectrum at 3386 cm^{-1}, 1728 and 1654 cm^{-1} indicating the presence of OH, and ketone functionalities.

The ^{1}H-NMR spectrum showed a methine proton at C-17 (δ_H 2.259), and the ^{13}C-NMR signal at δ_C 57 supports dehydroxylation at C-17 (Table 34). HSQC analysis showed no CH_2 cross peaks or carbon signals at δ_C 65–69 corresponding to C-21, further supporting the absence of the C-21 hydroxyl group. The position of the new methine proton was deduced on the basis of HMBC correlations of H-17 (δ_H 2.26) with C-20 (δ_C 178) [265]. The metabolite 8 was assigned as 11*β*-Hydroxy-6*α*-methyl-3-oxoandrosta-1,4-diene-17*β*-carboxylic acid. The HPLC chromatogram used for purity assessment is presented in Appendix B (Figure S26), while ^{1}H-NMR, and mass spectra are provided in Figures S45.

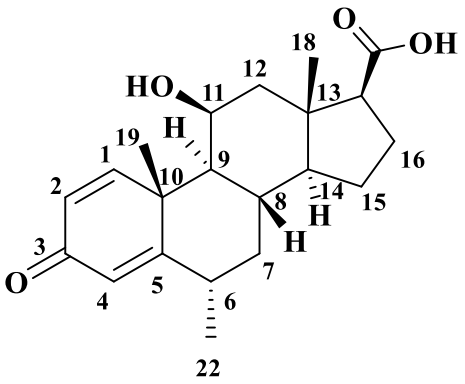


Table 34 – ^{1}H-, and ^{13}C-NMR chemical shift data of metabolite 8[a]

Carbon	[b]δ_C	δ_H (*J* in Hz)	Multiplicity
1	-	7.49, d , $J_{1/2}$ = 10.4 Hz, 1H	CH
2	-	6.25, dd, $J_{1/2,\ 2/4}$ = 9.6 Hz, 1.6 Hz, 1H	CH
3	-	-	[c]C
4	-	5.98, m, 1H	CH
5	-	-	C
6	-	2.74, m, 1H	CH
7	-	2.14, m; 0.79, m, 2H	CH_2
8	-	2.17, m, 1H	CH
9	-	0.99, overlap, 1H	CH
10	-	-	C
11	-	4.32, m, 1H	CH
12	-	2.26, m; 1.41, m, 2H	CH_2
13	-	-	CH
14	-	1.07, m, 1H	CH
15	-	1.73, m; 1.43, m, 2H	CH_2
16	-	2.08, m; 1.43, m, 2H	CH_2
17	-	2.26, m, 1H	CH

Table 34 (continued)			
18	-	1.00, s, overlap, 3H	CH_3
19	-	1.48, s, 3H	CH_3
20	-	-	C
21	-	1.12, d, $J_{21/6}$ = 6.4 Hz, 3H	CH_3

8[a]: ^{1}H-NMR (CD_3OD; 800); [b]δ: indicated ^{13}C not performed; [c]C: quaternary carbons

21-acetyloxy-11β,17α,20-trihydroxy-6α-methylpregna-1,4-dien-3-one (9)

Metabolite 9 was obtained as a white solid. UV λ_{max} 244 nm; the EI-MS spectrum showed molecular ion peak ($M^{+\bullet}$) at m/z 418.3 ($C_{24}H_{34}O_6$), suggesting reduction of C-20 carbonyl group. The IR ($CHCl_3$) spectrum showed the presence of ketonic carbonyl at 1728 and 1654 cm^{-1}, and OH group at 3437 cm^{-1}. In the ^{1}H-NMR spectrum, a methine proton at δ_H 3.96 corresponding to C-20 was observed, supporting hydroxylation (Table 35). In the ^{13}C-NMR spectrum, the C-20 carbonyl signal at δ_C 214 disappeared and a new signal appeared at δ_C 74, further confirming hydroxylation at C-20 [264]. The new OH group was placed at C-20 based on the HMBC correlations of H-20 (δ_H 3.96) with C-21 (δ_C 68) confirming hydroxylation. The metabolite 9 was thus identified as 21-acetyloxy-11β,17α,20-trihydroxy-6α-methylpregna-1,4-dien-3-one. The HPLC chromatogram is provided in Appendix B (Figure S26), while the corresponding ^{1}H-NMR, ^{13}C-NMR, and mass spectra are provided in Figures S46–S47.

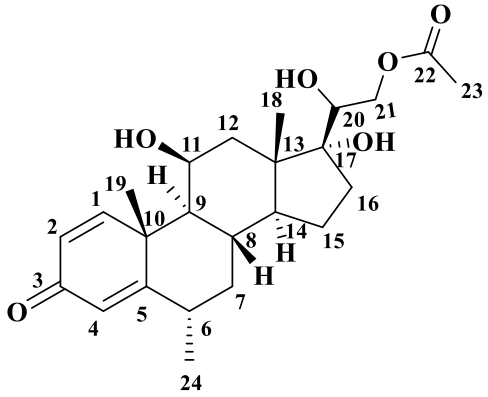


Table 35 – ^{1}H-, and ^{13}C-NMR chemical shift data of metabolite 9[a]

Carbon	δ_C	δ_H (*J* in Hz)	Multiplicity
1	160.9	7.49, d , $J_{1/2}$ =10 Hz, 1H	CH
2	127.3	6.25, dd , $J_{1/2, 2/4}$ =10 Hz, 1.6H	CH
3	189.0	-	[b]C
4	119.6	5.97, m, 1H	CH
5	178.1	-	[b]C
6	34.0	2.74, m, 1H	CH
7	44.7	2.14, m; 0.823, m, 2H	CH_2
8	32.6	2.20, m, 1H	CH
9	58.3	0.95, m, 1H	CH
10	41.8	-	[b]C
11	71.0	4.35, m, 1H	CH

Table 35 (continued)			
12	42.1	2.01, m; 1.768, m, 2H	CH_2
13	46.3	-	CH
14	51.5	1.54, m, 1H	CH
15	25.1	1.73, m; 1.32, m, 2H	CH_2
16	34.4	1.87, m; 1.45, m, 2H	CH_2
17	85.7	-	^{b}C
18	17.6	1.11, overlap, 3H	CH_3
19	21.9	1.48, s, 3H	CH_3
20	74.2	3.96, dd, $J_{20/21, 21/20}$ = 8.4 Hz, 2.8 Hz, 1H	CH
21	68.3	4.18, m, 2H	CH_2
22	173.3	-	^{b}C
23	20.9	2.05, s, 3H	CH_3
24	18.3	1.12, overlap, 3H	CH_3

9[a]: ^{1}H- and ^{13}C-NMR (CD_3OD; 400 and 150 MHz); [b]C: quaternary carbons

2.8.3 *In vitro* aromatase inhibition assay

We evaluated the *in vitro* inhibitory effects of methylprednisolone acetate (1) and its metabolites against human placental aromatase. The substrate 1, and its metabolites 2–9 showed promising results. The substrate 1 showed an IC_{50} of 184.4 ± 0.25 nM, slightly higher inhibitory activity than the standard aromatase inhibitor exemestane (IC_{50} = 210 ± 0.16 nM). The biotransformed metabolites exhibited strong inhibitory potential with IC_{50} values ranging from 69.32 to 184.4 nM. Metabolite 4 showed the strongest inhibitory activity, with an IC_{50} value of 69.32 ± 0.17 nM, followed 3 (IC_{50} of 86.33 ± 0.85 nM), 9 (IC_{50} = 131.40 ± 0.29 nM), 2 (IC_{50} = 139.3 ± 0.31 nM), 5 (IC_{50} = 141.2 ± 0.25 nM), 6 (IC_{50} = 171.7 ± 0.24 nM), 7 (IC_{50} = 173.8 ± 0.28 nM), and 8 (IC_{50} = 177.5 ± 0.31 nM).

The IC_{50} values, docking scores, and MM-GBSA (kcal/mol) binding energies of metabolites 2–9 are listed in Table 36, and illustrated in Figures 31–33 respectively. The higher aromatase inhibitory activity of several metabolites compared to the parent compound demonstrates the impact of microbial structural modification on bioactivity. In particular metabolites 3 and 4, showed promising improvement in the inhibition of an enzyme, suggesting that selective fungal transformations can improve pharmacological properties. Similar to the previous study, microbial transformations of steroidal substrates may lead to the formation of structurally modified metabolites with altered biological activities and enhanced therapeutic potential. Hence, microbial biotransformation is a selective, green and valuable process to generate bioactive steroidal analogues for drug discovery and development [267].

Overall, these findings demonstrate the potential of fungal biotransformation to improve the aromatase inhibitory activity of steroidal compounds. Further studies are required to fully explore the therapeutic potential of these metabolites.

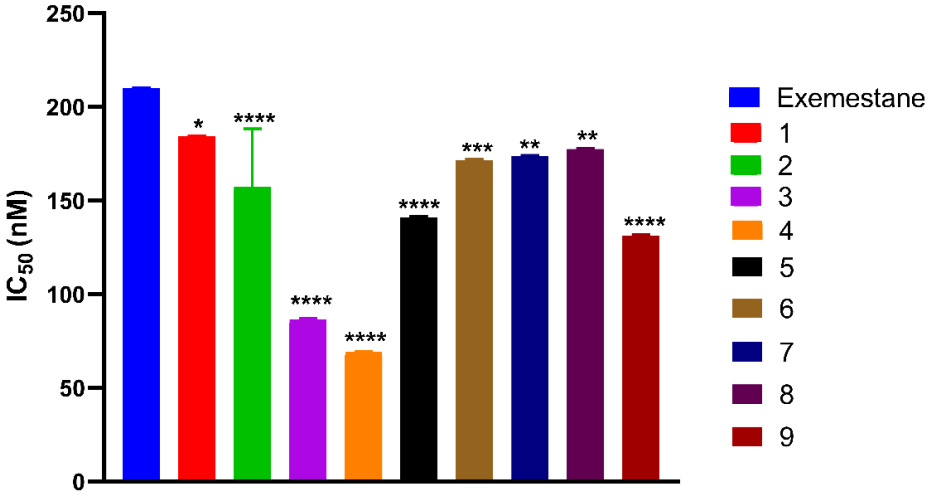


Figure 31 – Comparison of the IC_{50} values of substrate 1, and metabolites 2–9 against human placental aromatase, with Exemestane as the reference standard. Dose–response curves were generated using various concentrations of test compounds. Data represent mean ± SD from three independent experiments (n = 3). Statistical analysis was performed by one-way ANOVA (**p < 0.001, ****p < 0.0001; ns, non-significant) using GraphPad Prism 8.0

2.8.4 *In silico* studies

2.8.4.1 Molecular docking

A molecular docking study was conducted to evaluate the interactions between biotransformed metabolites (2–9) and the target enzyme aromatase. The findings predicted the binding conformation of the compounds within active site. Key residues including, leucine (LEU), arginine (ARG), methionine (MET), tryptophan (TRP), phenylalanine (PHE), cysteine (CYS), glycine (GLY), and alanine (ALA) were played critical roles in protein-ligand interactions.

Furthermore, functional groups such as carbonyl, hydroxyl, and oxygen atoms engaged in π–π, and hydrogen bonding interactions with aromatase offering important information about the compounds' inhibitory mechanism. Significant protein-ligand interactions were identified from the molecular docking analysis. The docking scores of the biotransformed compounds ranged from –4.87 to –7.01 (Figure 32), which are more favorable than that of standard drug exemestane (–6.01). Metabolite 2 exhibited the highest docking score (–7.01), followed by metabolites 4 (–6.85), 1 (–6.75), 8 (–6.67), 9 (–6.53), 3 (–6.11), 5 (–5.57), 6 (–5.15), and 7 (–4.87).

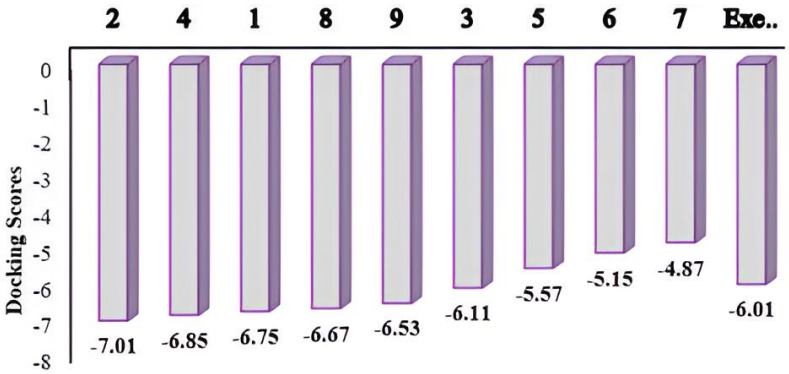


Figure 32 –Molecular docking scores of substrate 1, its metabolites 2–9 and standard drug (Exe; exemestane) for aromatase inhibition

Molecular Mechanics Generalized Born Surface Area (MM-GBSA) calculations were performed using VSGB (Variable Dielectric Surface Generalized Born) solvation model, OPLS4 force field to analyze the binding energies, and complex stabilities of metabolites 2–9 complexed with human placental aromatase. This indicating strong interactions and high affinity toward the aromatase receptor domain. The results demonstrated a direct correlation between binding energy, and complex stability with binding energies, ranging between –92.12 to –46.40 kcal/mol. The MM-GBSA analyses revealed that metabolite 2 showed the highest binding affinity (–92.12 kcal/mol), followed by metabolite 4 (–89.65 kcal/mol), substrate 1 (–86.39 kcal/mol), 9 (–82.81 kcal/mol), 5 (–67.17 kcal/mol), 3 (–63.92 kcal/mol), 7 (–62.41 kcal/mol), 6 (–60.27 kcal/mol), and 8 (–46.40 kcal/mol). Hence, these metabolites were identified as promising aromatase inhibitors, supported by their stronger binding affinities predicted through the *in silico* studies (Figure 33, and Table 36).

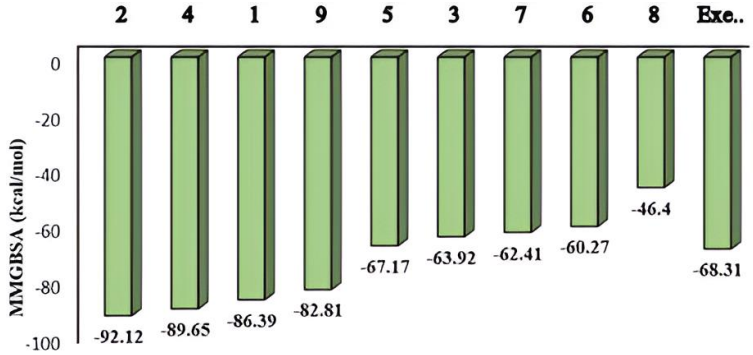


Figure 33 – Binding energy of substrate 1, and its metabolites 2–9 and standard drug (Exe; exemestane) for aromatase inhibition

The substrate 1 formed hydrogen bonds with key amino acid residues, contributing to its stability within the active site of receptor protein. Specifically, the carbonyl group at C-3, formed a hydrogen bond with MET 374, while the carbonyl

group at C-20 formed a hydrogen bond with GLY 439, a critical residue located at the active site of the receptor protein (Figure 34).

In metabolite 2, the carbonyl group at C-20 was involved in hydrogen bonding with two critical amino acid residues: GLY 439, and ALA 438. Moreover, metabolite 3 forms two distinct hydrogen bonding interactions. Specifically, the OH group at C-17 formed a hydrogen bond with MET 374, while the OH group attached at C-21, established a hydrogen bond with LEU 477. These interactions contributed to a favorable binding energy of the protein-ligand complex. The carbonyl group at C-3 of metabolite 4 formed a hydrogen bond with MET 374, while C-11 established an aromatic hydrogen bond with TRP 224, a critical residue within the active site of the receptor protein. Furthermore, the carbonyl group at C-20 formed a hydrogen bond with GLY 439. In metabolite 5, the OH group at C-11 of formed an aromatic hydrogen bond with TRP 224. Additionally, the OH at C-17, and carbonyl group at C-20 established hydrogen bonds with LEU 372, and MET 374, respectively. The metabolite 6 interacted *via* the carbonyl group at C-3, and established an aromatic hydrogen bond with PHE 148. While, in metabolite 7, the C-3 carbonyl group formed an aromatic hydrogen bond with MET 374, a critical residue within the receptor domain. Furthermore, the CO groups at C-20 established two hydrogen bonds: one with ALA 438, and another with GLY 439. In metabolite 8, the C-3 carbonyl group (CO) formed a hydrogen bond, and a salt bridge with ARG 115. Additionally, the carbonyl group at C-20 formed an aromatic hydrogen bond with PHE 134, a critical residue at the active site of the receptor protein. In case of metabolite 9, the hydroxyl group at C-17, and the hydroxyl group at C-20 both formed hydrogen bonds with CYS 437, a key residue within the receptor domain. All of the identified aromatase inhibitors 1-9 exhibited higher binding affinities, as compared to the reference inhibitor, exemestane (–68.31 kcal/mol). These findings highlighted the role of ligand's functional groups, and residues of aromatase contributing to enzyme inhibitory activity (Figure 34, and Table 36).

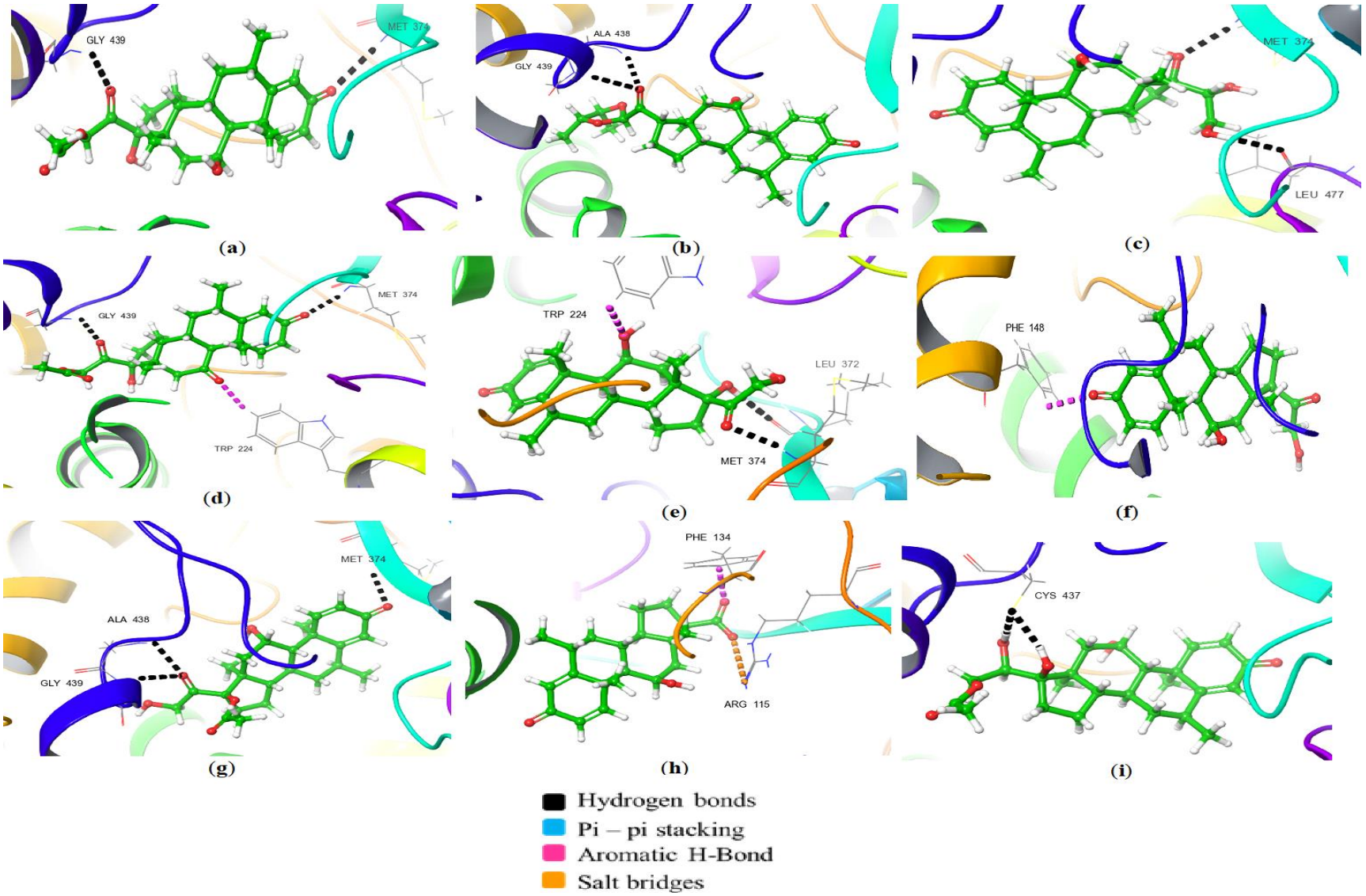


Figure 34– 3D Docked conformations of metabolites (**a**) 1, (**b**) 2, (**c**) 3, (**d**) 4, (**e**) 5, (**f**) 6 (**g**) 7, (**h**) 8, and (**i**) 9, within the aromatase active site.

Table 36 – Comparison of IC_{50}, docking score, and MM-GBSA (kcal/mol) of metabolites 2–9

Compounds	**IC_{50} (nM) ± SD**	**Docking scores**	**MM-GBSA (kcal/mol)**	**[a]ΔIC_{50} vs Exemestane (nM)**
Methylprednisolone acetate (1)	184.4 ± 0.25	–6.75	–86.39	–25.6
2	139.3 ± 0.85	–7.01	–92.12	–70.7
3	86.33 ± 0.31	–6.11	–63.92	–123.6
4	69.32 ± 0.17	–6.85	–89.65	–140.7
5	141.2 ± 0.25	–5.57	–67.17	–68.8
6	171.7 ± 0.24	–5.15	–60.27	–38.3
7	173.8 ± 0.28	–4.87	–62.41	–36.2
8	177.5 ± 0.31	–6.67	–46.4	–32.5
9	131.4 ± 0.29	–6.53	–82.81	–78.6
[b]Exemestane	210.0 ± 0.16	–6.01	–68.31	0.00

[a]ΔIC_{50} = IC_{50} (Compounds) – IC_{50} (Exemestane); negative values indicate higher potency than exemestane; [b]standard drug.

2.8.5 Correlation between aromatase inhibition and molecular docking

The correlation plot between the enzyme inhibition (IC_{50} values), and docking scores for the series of compounds compared to exemestane is shown in Figure 35. Overall, a weak correlation was observed between IC_{50} values and docking scores. Although metabolites 4 and 9 exhibit relatively lower IC_{50} values and favorable docking scores, other metabolites 6–8 show higher IC_{50} values despite comparable docking scores. This variation suggests that while molecular docking provides useful insight into potential ligand–target interactions, experimental enzyme inhibition is influenced by additional factors such as solubility, conformational flexibility, enzyme dynamics, and assay conditions, leading to deviations from a perfect linear correlation. Therefore, docking results should be considered supportive mechanistic evidence rather than direct predictors of biological potency.

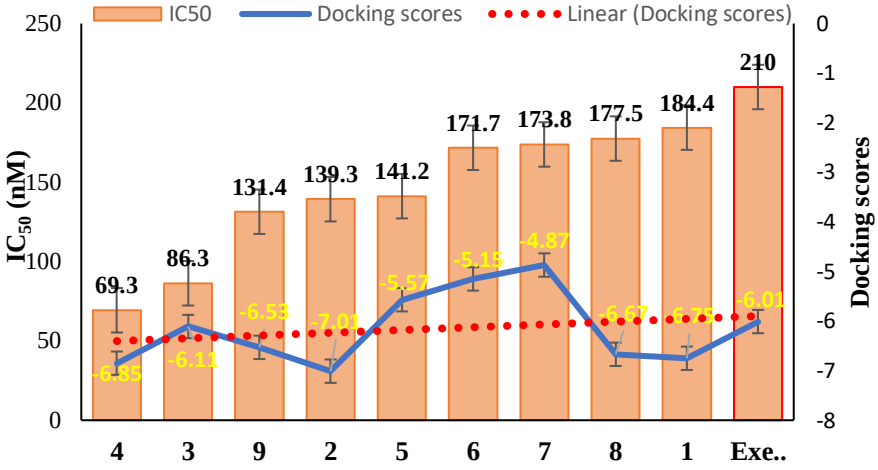


Figure 35 – Correlation between aromatase inhibition (IC_{50}) and molecular docking studies of substrate 1, its metabolites 2–9 and standard drug (Exe; exemestane)

2.8.6 Correlation between docking scores and binding energies

The moderate correlation between docking scores and binding energies (kcal/mol) for the tested compounds is shown in Figure 36. In general, compounds with more negative docking scores demonstrate stronger and more stable binding, as reflected by their lower binding energies. Among metabolites 2–9, metabolites 2 (–7.01) and 4 (–6.85) showed the most favorable results, while slight deviations are observed for metabolites 8 (–6.67), suggesting that the correlation is not entirely linear. These findings suggest that docking scores and MM-GBSA binding energies provide complementary information regarding ligand binding; however, both approaches represent computational estimations and should be interpreted in conjunction with the experimental inhibition data rather than as independent proof of biological activity.

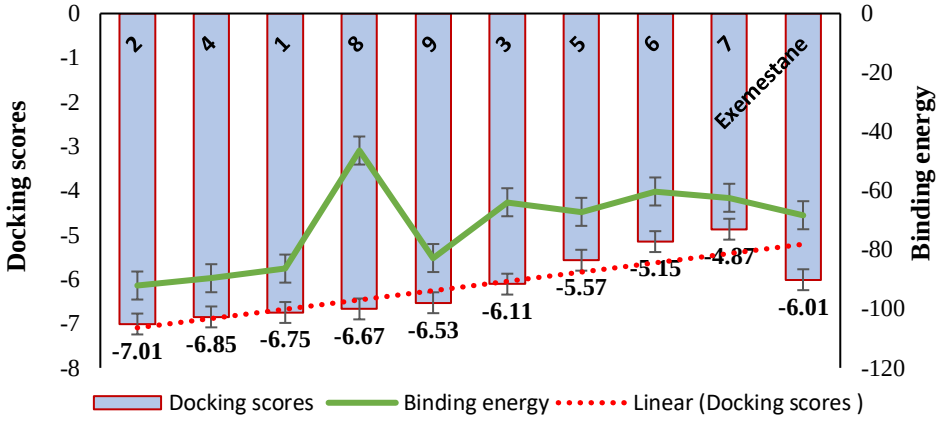


Figure 36 – Correlation between docking scores and binding energies (kcal/mol) of substrate 1, its metabolites 2–9 and standard drug exemestane

2.8.7 Structure–activity relationship (SAR)

The substrate 1 with hydroxyls at C-11 and C-17, a carbonyl at C-20, and an ester at C-21, showed moderate activity (IC_{50} of 184.4 nM). Its activity is stabilized by hydrogen bonding of the C-3 carbonyl with MET374 and the C-20 carbonyl with GLY439 in the aromatase active site. Metabolite 2, a new metabolite lacking the C-17 hydroxyl and featuring a cyclic acetal at C-21, displayed improved activity with an IC_{50} of 139.3 nM due to strong hydrogen bonds of the C-20 carbonyl with GLY439 and ALA438, contributing to the highest docking score and binding energy. Metabolite 3, with the C-20 carbonyl reduced to a hydroxyl and an additional hydroxyl at C-21, showed further enhancement with an IC_{50} of 86.33 nM. The C-17 hydroxyl forms a hydrogen bond with MET374, while the C-21 hydroxyl interacts with LEU477, demonstrating the advantage of dual hydrogen bonding for ligand stabilization. Metabolite 4, where the C-11 hydroxyl is oxidized to a carbonyl, exhibited the highest activity with an IC_{50} of 69.32 nM. Key interactions include a hydrogen bond and salt bridge of the C-3 carbonyl with ARG115, an aromatic hydrogen bond of the C-11 carbonyl with TRP224, and hydrogen bonding of the C-20 carbonyl with GLY439 and PHE134, collectively enhancing binding stability. Metabolites 5 to 8 showed weaker activity, with IC_{50} values ranging from 141.2 to 177.5 nM. Modifications such as addition of a hydroxyl at C-21, removal of C-17 hydroxyl, or esterification at C-17 provided limited improvement because they did not establish cooperative hydrogen bonding with key residues. Metabolite 9, with reduction of the C-20 carbonyl to a hydroxyl, demonstrated moderate activity with an IC_{50} of 131.4 nM, forming hydrogen bonds with CYS437 and highlighting the importance of multiple polar interactions.

Overall, carbonyl at C-11 and hydrogen bonding at C-20 and C-21 are critical for binding and activity. The C-17 hydroxyl can enhance or reduce stability depending on surrounding modifications. Metabolites 2, 3, and 4 exhibited the most promising aromatase inhibitory activities among the tested compounds.

2.9 Summary

This part of the thesis deals with the microbial transformation of the steroidal drugs methylprednisolone acetate (1) using selected microbial strains. Incubation of methylprednisolone acetate (1), *m/z* 416, $C_{24}H_{32}O_6$, with *F. oxysporum* yielded a new metabolite, 20-(4′,5′-dimethyl-1′,3′-dioxolan-2-yl)-11β-hydroxypregn-4-ene-3,20-dione (2), along with six known metabolites, 11β,17α,20,21-tetrahydroxy-6α-methylpregna-1,4-dien-3-one (3), 21-acetyloxy-17α-hydroxy-6α-methylpregna-1,4-dien-3,11,20-trione (4), 11β,17α,21-trihydroxy-6α-methylpregna-1,4-dien-3,20-dione (5), 11β,21-dihydroxy-6α-methylpregna-1,4-dien-3,20-dione (6), 17α-acetoxy-11β,21-dihydroxy-6α-methylpregna-1,4-dien-3,20-dione (7), 11β-hydroxy-6α-methyl-3-oxoandrosta-1,4-diene-17β-carboxylic acid (8) shown in Figure 23.

Similarly, incubation of 1 with *Penicillium chrysogenum* yielded four metabolites 3, 5, 8, and 21-acetyloxy-11β,17α,20-trihydroxy-6α-methylpregna-1,4-dien-3-one (9) shown in Figure 24. The aromatase-inhibitory potential of all metabolites was evaluated. Metabolite 2 (IC_{50} = 139.3 ± 0.31 nM), 3 (IC_{50} = 86.33 ± 0.85 nM), 4 (IC_{50} = 69.32 ± 0.17 nM), 5 (IC_{50} = 141.2 ± 0.25 nM), 6 (IC_{50} = 171.7 ± 0.24 nM), 7 (IC_{50} = 173.8 ± 0.28 nM), 8 (IC_{50} = 177.5 ± 0.31 nM), and 9 (IC_{50} = 131.4 ± 0.29 nM) were identified as promising inhibitors against aromatase. To conclude, metabolites 2, and 4 demonstrated favorable aromatase inhibition IC_{50} = 139.3 ± 0.31 nM, and IC_{50} = 69.32 ± 0.17 nM respectively, as compared to substrate 1 with IC_{50} = 184.4 ± 0.25 nM, and the standard drug exemestane IC_{50} = 210.0 ± 0.16 nM. These findings were further supported by computational analyses, which suggested favorable binding interactions for metabolite 2 and 4 with lower docking scores of –7.01 and –6.85, and promising binding affinities of –92.12 and –89.12 kcal/mol, respectively. These findings demonstrate the potential of fungal-mediated biotransformation to generate structurally diverse and biologically valuable steroid derivatives. Aromatase enzyme catalyzes key steps in the biosynthesis of estrogens, and therefore its inhibition is a validated approach for the treatment of estrogen receptor positive (ER+) breast cancers. Further *in vivo* studies are required to evaluate the therapeutic potential of these compounds.

3 Conclusion

1. The selection and investigation of the medicinal plant *Tussilago farfara* L., and the fungal strains *Fusarium oxysporum* and *Penicillium chrysogenum* were successfully accomplished as key components of this study. *Tussilago farfara* was chosen based on its well-documented traditional medicinal use and rich phytochemical profile, which was supported by the isolation of twenty secondary metabolites from 80 g of the ethyl acetate fraction. In parallel, the selected fungal strains demonstrated efficient and selective microbial biotransformation of methylprednisolone acetate, yielding eight metabolites 2–9 under controlled fermentation conditions. The combined use of plant-based natural products and microbial systems highlights their significance as sustainable and complementary biological resources for drug discovery and development.

2. Systematic extraction, fractionation, isolation, and purification of secondary metabolites from *Tussilago farfara* L. were performed using advanced chromatographic techniques, leading to the successful isolation of twenty compounds (1–20). Compounds were isolated and purified by column chromatography, flash chromatography, Sephadex LH-20, UPLC and preparative HPLC, with TLC used for monitoring. However, the quantity of isolated compounds was insufficient for subsequent biotransformation studies. Therefore, the study was extended to the microbial biotransformation of commercially available steroidal drug methylprednisolone acetate using *Fusarium oxysporum* and *Penicillium chrysogenum*, which yielded one new metabolite 2, and seven known metabolites 3–9 demonstrating the ability of fungal systems to generate structurally diverse steroidal derivatives with high regio- and stereoselectivity.

3. The chemical structures of the isolated phytochemicals and fungal-derived metabolites were successfully determined using advanced spectroscopic techniques, including ^{1}H-NMR, ^{13}C-NMR, and 2D-NMR, EI-MS, ESI-MS, FAB-MS, HRMS, and IR analyses, facilitating structural characterization. Among the isolated compounds from *Tussilago farfara* L., compounds 1, 14, and 20 were reported for the first time from this plant, expanding its phytochemical profile. Structural analysis of the biotransformed metabolites revealed important modifications such as hydroxylation, dehydroxylation, ester cleavage, ester cyclization, and keto reduction, demonstrating the specificity of microbial enzymatic systems in modifying steroidal frameworks.

4. The purified compounds were comprehensively evaluated for their biological activities using well-established *in vitro* assays, revealing promising pharmacological potential. The phytochemicals isolated from *Tussilago farfara* L., particularly the caffeoylquinic acid derivatives (15–18), demonstrated moderate antileishmanial activity against *Leishmania major* through inhibition of the pteridine reductase-1 (*Lm*PTR-1) enzyme. Among them, compound 18 exhibited the highest

inhibitory activity (IC_{50} = 81.9 ± 1.12 µM). However, in comparison to the standard drug trimethoprim (IC_{50} = 21.07 ± 1.60 µM), compound 18 displayed lower potency. In addition, the microbial biotransformation of methylprednisolone acetate resulted in structurally modified metabolites with enhanced biological performance. All metabolites 2–9 exhibited promising anti-aromatase activity, with metabolite 4 showing the highest activity with an IC_{50} of 69.32 ± 0.17 nM, and new metabolite 2 with an IC_{50} value of 139.3 ± 0.31 nM. Notably, these metabolites demonstrated improved activity compared to the substrate 1 (IC_{50} = 184.4 ± 0.25 nM) as well as the standard drug exemestane (IC_{50} = 210 ± 0.16 nM) under experimental conditions employed, indicating a notable enhancement in potency. These results highlight the effectiveness of microbial biotransformation in generating structurally optimized steroidal derivatives with improved pharmacological profiles.

5. The experimental findings were further supported by *in silico* studies, which provided detailed molecular-level insights into the observed biological activities. Molecular docking analysis of *Lm*PTR-1 inhibition revealed that compound 17 and 18 from *T. farfara* exhibited strong interactions with key active-site residues, including Phe113, Tyr194, Ser111, and Gly240. Notably, compound 18 formed multiple hydrogen bonds with Gly240, and π–π stacking interactions with Phe113, indicating a stable binding conformation. Similarly, biotransformed steroidal metabolites 2–9 exhibited strong binding affinities toward aromatase, as supported by molecular docking and MM-GBSA analyses. The metabolites interacted with key residues including MET374, GLY439, TRP224, LEU477, and CYS437 through hydrogen bonding and hydrophobic interactions. Among them, metabolite 2 and 4 exhibited the most favorable binding energies of −92.12 and −89.65 kcal/mol, respectively. Although the computational results generally supported the experimental findings, minor discrepancies between docking scores, binding energies, and IC_{50} values were observed, reflecting the simplified nature of computational models relative to complex biological systems. Overall, the integration of computational and experimental approaches provides a comprehensive understanding of enzyme inhibition mechanisms and highlights the potential of these compounds for future drug development.

REFERENCES

1 Sarker S. D., Nahar L. An introduction to natural products isolation // Nat Prod Iso. – **2012**. – P. 1-25.

2 Croteau R., Kutchan T. M., Lewis N. G. Natural products (secondary metabolites) // Pl ant Mol. Biol. – **2000**. – Vol. 24. – P. 1250-1319.

3 Mishra G., Singh P., Verma R., Kumar S., Srivastav S., Jha K., Khosa R. Traditional uses, phytochemistry and pharmacological properties of *Moringa oleifera* plant: An overview // Der Pharmacia Lettre. – **2011**. – Vol. 3, № 2. – P. 141-164.

4 Jamshidi-Kia F., Lorigooini Z., Amini-Khoei H. Medicinal plants: Past history and future perspective // J. Herbmed Pharmacol. – **2017**. – Vol. 7, № 1. – P. 1-7.

5 Achika J. I. A Review of the Phytochemistry and Pharmacology of *Lannea species*: // TJNPR. – **2018**. – Vol. 2, № 10. – P. 442-446.

6 Dias D. A., Urban S., Roessner U. A historical overview of natural products in drug discovery // Metabolites. – **2012**. – Vol. 2, № 2. – P. 303-336.

7 Saxena R., Sheoran A., Giri B., Davidson W. S. J. Purification strategies for microbial lipases // J. Microbiol. Methods. – **2003**. – Vol. 52, № 1. – P. 1-18.

8 Chen J., Li W., Yao H., Xu J. Insights into drug discovery from natural products through structural modification // Fitoterapia. – **2015**. – Vol. 103. – P. 231-241.

9 Cox B., Denyer J. C., Binnie A., Donnelly M. C., Evans B., Green D., Lewis J. A., Mander T. H., Merritt A. T., Valler M. J. Application of high-throughput screening techniques to drug discovery // Prog Med Chem. – **2000**. – Vol. 37. – P. 83-133.

10 Phillipson J. D. Human medicinal agents from plants, edited by AD Kinghorn and MF Balandrin, American Chemical Society, Washington, DC, **1993** No. of pages: 356, price US $89.95. ISBN 0-8412-2705-5 // Flavour Fragr. J. – P. 355.

11 Kinghorn A. Human medical agents from plants // ACS Symp. series. – 1993. – Vol. 525.

12 Berdy J. The discovery of new bioactive microbial metabolites: screening and identification // Bioactive metabolites from microorganisms. – **1989**. – Vol. 58. № 1. – P. 1-26.

13 Mayer A. M., Glaser K. B., Cuevas C., Jacobs R. S., Kem W., Little R. D., McIntosh J. M., Newman D. J., Potts B. C., Shuster D. E. The odyssey of marine pharmaceuticals: a current pipeline perspective // TIPS. – **2010**. – Vol. 31, № 6. – P. 255-265.

14 Baker Z. K., Sardari S. Molecularly imprinted polymer (MIP) applications in natural product studies based on medicinal plant and secondary metabolite analysis // Iran. Biomed. J. – **2021**. – Vol. 25, № 2. – P. 68-77.

15 Saad E. M., El Gohary N. A., Abdel-Halim M., Handoussa H., El Nashar R. M., Mizaikoff B. Molecularly imprinted polymers for selective extraction of rosmarinic acid from *Rosmarinus officinalis* L // Food Chem. – **2021**. – Vol. 335. – P. 127644.

16 Ma X., Meng Z., Qiu L., Chen J., Guo Y., Yi D., Ji T., Jia H., Xue M. J. Solanesol extraction from tobacco leaves by Flash chromatography based on molecularly imprinted polymers // J. Chromatogr. B. – **2016**. – Vol. 1020. – P. 1-5.

17 Williams S., Oatley D., Abdrahman A., Butt T., Nash R. Membrane technology for the improved separation of bioactive compounds // Procedia Eng. – **2012**. – Vol. 44. – P. 2112-2114.

18 Jaroszewski J. W. Hyphenated NMR methods in natural products research, Part 2: HPLC-SPE-NMR and other new trends in NMR hyphenation // Planta Medica. – **2005**. – Vol. 71, № 09. – P. 795-802.

19 Yuan H., Ma Q., Ye L., Piao G. J. M. The traditional medicine and modern medicine from natural products // Molecules. – **2016**. – Vol. 21, № 5. – P. 2-18.

20 Che C., George V., Ijinu T., Pushpangadan P., Andrae-Marobela K. Traditional medicine. Pharmacognosy // Pharmacogn. – **2017**. –. P-15-30.

21 Cragg G. M., Newman D. Natural products: a continuing source of novel drug leads // BBA-General Subjects. – **2013**. – Vol. 1830, № 6. – P. 3670-3695.

22 Gurnani N., Mehta D., Gupta M., Mehta B. Natural products: source of potential drugs // Afr J Basic Appl Sci. – **2014**. – Vol. 6, № 6. – P. 171-186.

23 Jachak S. M., Saklani A. Challenges and opportunities in drug discovery from plants // Current science. – **2007**. – P. 1251-1257.

24 Hubert J., Nuzillard J. M., Renault J. H. Dereplication strategies in natural product research: How many tools and methodologies behind the same concept? // Phytochem. Rev. – **2017**. – Vol. 16. – P. 55-95.

25 Cavasotto C. N., Aucar M. G., Adler N. S. Computational chemistry in drug lead discovery and design // Int. J. Quantum Chem. – **2019**. – Vol. 119, № 2. – P. 1-19.

26 Li F. S., Weng J. K. Demystifying traditional herbal medicine with modern approach // Nature plants. – **2017**. – Vol. 3, № 8. – P. 1-7.

27 Rolnik A., Olas B. J. The plants of the Asteraceae family as agents in the protection of human health // Int. J. Mol. Sci. – **2021**. – Vol. 22, № 6. – P. 1-10.

28 Flavonoids of the sunflower family (Asteraceae). / Bohm B. A., Stuessy T. F // Springer.- 2013.

29 Koc S., Isgor B. S., Isgor Y. G., Shomali Moghaddam N., Yildirim O. The potential medicinal value of plants from Asteraceae family with antioxidant defense enzymes as biological targets // Pharm. Biol. – **2015**. – Vol. 53, № 5. – P. 746-751.

30 Wang Y., Yang C., Jin M., Zhong J., Mei D., Wei X., Wang H. Isolation and identification of *Tussilago farfara* leaf spot caused by *Alternaria alternata* in China // Microb. Pathog. – **2022**. – Vol. 172. – P. 1-21.

31 Yu-Peng L., Kang Y., Hui M., Tao S. Polyhydroxylated eudesmane sesquiterpenoids and sesquiterpenoid glucoside from the flower buds of *Tussilago farfara* // Chin J Nat Medicines. – **2022**. – Vol. 20, № 4. – P. 301-308.

32 Norani M., Ebadi M.-T., Ayyari M. Volatile constituents and antioxidant capacity of seven *Tussilago farfara* L. populations in Iran // Sci. Hortic. – **2019**. – Vol. 257. – P. 1-7.

33 Jang H., Lee J. W., Lee C., Jin Q., Choi J. Y., Lee D., Han S. B., Kim Y., Hong J. T., Lee M. K. Sesquiterpenoids from *Tussilago farfara* inhibit LPS-induced nitric oxide production in macrophage RAW 264.7 cells // Arch Pharm Res. – **2016**. – Vol. 39. – P. 127-132.

34 Xu J., Sun X., Kang J., Liu F., Wang P., Ma J., Zhou H., Jin D.-Q., Ohizumi Y., Lee D. J. Chemical and biological profiles of *Tussilago farfara*: Structures, nitric oxide inhibitory activities, and interactions with iNOS protein // J. Funct. Foods. – **2017**. – Vol. 32. – P. 37-45.

35 Song K., Lee K. J., Kim Y. S. Development of an efficient fractionation method for the preparative separation of sesquiterpenoids from *Tussilago farfara* by counter-current chromatography // J. Chromatogr. A. – **2017**. – Vol. 1489. – P. 107-114.

36 Kang U., Park J., Han A.-R., Woo M. H., Lee J.-H., Lee S. K., Chang T.-S., Woo H. A., Seo E. K. Identification of cytoprotective constituents of the flower buds of *Tussilago farfara* against glucose oxidase-induced oxidative stress in mouse fibroblast NIH3T3 cells and human keratinocyte HaCaT cells // Arch. Pharm. Res. – **2016**. – Vol. 39. – P. 474-480.

37 Sun J., Yu J. H., Zhang J. S., Song X. Q., Bao J., Zhang H. Chromane enantiomers from the flower buds of *Tussilago farfara* L. and assignments of their absolute configurations // Chem Biodivers. – **2019**. – Vol. 16, № 3. – P. 1-9.

38 Song X.-Q., Yu J.-H., Sun J., Liu K.-L., Zhang J.-S., Zhang H. J. B. C. Bioactive sesquiterpenoids from the flower buds of *Tussilago farfara* // Bioorg. Chem. – **2021**. – Vol. 107. – P. 1-9.

39 Judzentiene A., Budiene J. Volatile oils of flowers and stems of *Tussilago farfara* L. from Lithuania // J. Essent. Oil-Bear. Plants. – **2011**. – Vol. 14, № 4. – P. 413-416.

40 Nedelcheva A., Kostova N., Sidjimov A. Pyrrolizidine alkaloids in *Tussilago farfara* from Bulgaria // Biotechnol. Biotechnol. Equip. – **2015**. – Vol. 29, № sup1. – P. 1-7.

41 Qin Z.-B., Zhang J., Wu X.-D., He J., Ding L.-F., Peng L.-Y., Li X.-Y., Li Y., Deng L., Guo Y.-D. Sesquiterpenoids from *Tussilago farfara* and their inhibitory effects on nitric oxide production // Planta medica. – **2014**. – Vol. 80, № 08/09. – P. 703-709.

42 Qin Kun Q. K., Liu CaiHong L. C., Qi YongXiu Q. Y., Li Ke L. K. Evaluation of antioxidant activity of polysaccharides from *Tussilago farfara* L. by Flow Injection Analysis // Asian J. Chem. – **2014**. – Vol. 26, № 2. – P. 3073–076**.**

43 Li W., Huang X., Yang X.-W. New sesquiterpenoids from the dried flower buds of *Tussilago farfara* and their inhibition on NO production in LPS-induced RAW264. 7 cells // Fitoterapia. – **2012**. – Vol. 83, № 2. – P. 318-322.

44 Uysal S., Senkardes I., Mollica A., Zengin G., Bulut G., Dogan A., Glamočlija J., Soković M., Lobine D., Mahomoodally F. M. Biologically active compounds from two members of the Asteraceae family: *Tragopogon dubius Scop*. and *Tussilago farfara* L // J. Biomol. Struct. Dyn. – **2019**. – P. 3269-3281.

45 Li H., Lee H. J., Ahn Y. H., Kwon H. J., Jang C.-Y., Kim W.-Y., Ryu J.-H. Tussilagone suppresses colon cancer cell proliferation by promoting the degradation of *β*-catenin // Biochem. Biophys. Res. Commun. – **2014**. – Vol. 443, № 1. – P. 132-137.

46 Chinese P. M. C. China. Pharmacopoeia of the People's Republic of China // CMSTP. – **2010**. – Vol. 292.

47 Hu N., Wang Z. Tu Jing Ben Cao [Illustrated Manual of Materia Medica], by Su S (1061) // FJSTP. – **1987**.

48 Yeh C.-F., Wang K.-C., Lu C.-Y., Chiang L.-C., Shieh D.-E., Yen M.-H., Chang J. S. Yakammaoto inhibits enterovirus 71 infection by reducing viral attachment, internalization, replication, and translation // KJMS. – **2015**. – Vol. 31, № 6. – P. 293-302.

49 Fan J. X. Mechanism of *Farfarae Flos* in Qingfei Paidu Decoction against COVID-19 based on network pharmacology and molecular docking // Zhong. Cao. Yao. – **2020**. – P. 2317-2325.

50 Pranskuniene Z., Balciunaite R., Simaitiene Z., Bernatoniene J. Herbal medicine uses for respiratory system disorders and possible trends in new herbal medicinal recipes during COVID-19 in pasvalys district, Lithuania // IJERPH. – **2022**. – Vol. 19, № 15. – P. 1-13.

51 Sak K., Jürisoo K., Raal A. Estonian folk traditional experiences on natural anticancer remedies: From past to the future // Pharm. Biol. – **2014**. – Vol. 52, № 7. – P. 855-866.

52 Commission C. P., %J S. P. C. Pharmacopoeia of the people's republic of china **2015** //. – 2015.

53 Hooper S. N., Chandler R. Herbal remedies of the Maritime Indians: phytosterols and triterpenes of 67 plants // Pharm. Biol. – **1984**. – Vol. 10, № 2. – P. 181-194.

54 Shikov A. N., Pozharitskaya O. N., Makarov V. G., Wagner H., Verpoorte R., Heinrich M. Medicinal plants of the Russian Pharmacopoeia; their history and applications // J. Ethnopharmacol. – **2014**. – Vol. 154, № 3. – P. 481-536.

55 Xue S.-Y., Li Z.-Y., Zhi H.-J., Sun H.-F., Zhang L.-Z., Guo X.-Q., Qin X.-M. Metabolic fingerprinting investigation of *Tussilago farfara* L. by GC–MS and multivariate data analysis // Biochem. Syst. Ecol. – **2012**. – Vol. 41. – P. 6-12.

56 Stoyanova M., Perifanova-Nemska M. Biologically active compounds from *Tussilago farfara* L // Mater. Sci. Eng. – **2021**– Vol. 1031. – P. 1-8.

57 Roeder E. Medicinal plants in Europe containing pyrrolizidine alkaloids // Pharmazie. – **1995**. – Vol. 50, № 2. – P. 83-98.

58. Hirono I., Mori H., Culvenor C. C. J. G. Carcinogenic activity of coltsfoot, *Tussilago farfara* l // J. Cancer Res. – **1976**. – Vol. 67, № 1. – P. 125-129.

59 Bota V. B., Neamtu A.-A., Olah N.-K., Chișe E., Burtescu R. F., Pripon Furtuna F. R., Nicula A.-S., Neamtu C., Maghiar A.-M., Ivănescu L. C. A Comparative analysis of the anatomy, phenolic profile, and antioxidant capacity of *Tussilago farfara* L. vegetative organs // Plants. – **2022**. – Vol. 11, № 13. – P. 1-20.

60 Dénes A., Papp N., Babai D., Czúcz B., Molnár Z. Wild plants used for food by Hungarian ethnic groups living in the Carpathian Basin // Acta Soc. Bot. Pol. – 2012. – Vol. 81, № 4. – P. 381-396.

61 Smyrska-Wieleba N., Wojtanowski K. K., Mroczek T. Comparative HILIC/ESI-QTOF-MS and HPTLC studies of pyrrolizidine alkaloids in flowers of *Tussilago farfara* and roots of *Arnebia euchroma* // Phytochem. Lett. – **2017**. – Vol. 20. – P. 339-349.

62 Norani M., Crawford A., Aliahmadi A., Ayyari M. Evaluation of *Tussilago farfara* L. Smoke by GC/MS: A Phytochemical Approach to a Traditional Medicine // Agrotech Ind. Crops. – **2023**. – Vol. 3, № 1. – P. 14-22.

63 Norani M., Ebadi M.-T., Yadegari M., Ayyari M. J. Study of Essential Oil and Effect of Temperature and Seed Appendages (pappus) on Germination Characteristics in Coltsfoot // JMPB. – **2024**. – Vol. 13, № 3. – P. 538-544.

64 Moreira R., Pereira D. M., Valentão P., Andrade P. B. Pyrrolizidine alkaloids: chemistry, pharmacology, toxicology and food safety // Int. J. Mol. Sci. – **2018**. – Vol. 19, № 6. – P. 1-22.

65 Lebada R., Schreier A., Scherz S., Resch C., Krenn L., Kopp B. Quantitative analysis of the pyrrolizidine alkaloids senkirkine and senecionine in *Tussilago*

farfara L. by capillary electrophoresis // IJPCBTech. – **2000**. – Vol. 11, № 6. – P. 366-369.

66 Xiong W., Chen X., Lv G., Hu D., Zhao J., Li S. J. Optimization of microwave-assisted extraction of bioactive alkaloids from lotus plumule using response surface methodology // J. Pharm. Anal. – **2016**. – Vol. 6, № 6. – P. 382-388.

67 Gao H. G. H., Huang Y. H. Y., Gao Bo G. B., Xu. P. Y. X. P., Inagaki C., Kawabata J. *α*-Glucosidase inhibitory effect by the flower buds of *Tussilago farfara* L // Food Chem. – **2008**. – Vol. 106, № 3. – P. 1195-1201.

68 Hleba L., Vuković N., Horská E., Petrová J., Sukdolak S., Kačániová M. J. Phenolic profile and antimicrobial activities to selected microorganisms of some wild medical plant from Slovakia // Asian Pac. J. Trop. Dis. – 2014. – Vol. 4, № 4. – P. 269-274.

69 Eckelmann J., Saggiomo V., Fischmann S., Lüning U. Binding of group 15 and group 16 oxides by a concave host containing an isophthalamide unit // Beilstein J. Org. Chem. – **2012**. – Vol. 8, № 1. – P. 11-17.

70 Tajner-Czopek A., Gertchen M., Rytel E., Kita A., Kucharska A. Z., Sokół-Łętowska A. Study of antioxidant activity of some medicinal plants having high content of caffeic acid derivatives // Antioxidants. – **2020**. – Vol. 9, № 5. – P. 1-21.

71 Gao H., Huang Y.-N., Gao B., Xu P.-Y., Inagaki C., Kawabata J. *α*-Glucosidase inhibitory effect by the flower buds of *Tussilago farfara* L // Food Chem. – **2008**. – Vol. 106, № 3. – P. 1195-1201.

72 Yang L., Jiang H., Hou A., Guo X., Man W., Yan M., Xing X., Yang B., Wang Q., Kuang H. Simultaneous determination of thirteen Q-markers in raw and processed *Tussilago farfara* L. By UPLC-QQQ-MS/MS coupled with chemometrics // Molecules. – **2019**. – Vol. 24, № 3. – P. 2-16.

73 Kuroda M., Ohshima T., Kan C., Mimaki Y. Chemical constituents of the leaves of *Tussilago farfara* and their aldose reductase inhibitory activity // Nat. Prod. Commun. – **2016**. – Vol. 11, № 11. – P. 1661-1664.

74 Liu Y.-f., Yang X.-w., Wu B. J. GC-MS analysis of essential oil constituents from buds of *Tussilago farfara* L // J. Chin. Pharm. Sci. – **2006**. – Vol. 15, № 1. – P. 10.

75 Boucher M.-A., Côté H., Pichette A., Ripoll L., Legault J. Chemical composition and antibacterial activity of *Tussilago farfara* (L.) essential oil from Quebec, Canada // Nat. Prod. Res. – **2020**. – Vol. 34, № 4. – P. 545-548.

76 Ferrer D. B., Venskutonis P. R., Talou T., Zebib B., Ferrer J. M. B., Merah O. J. Potential interest of *Tussilago farfara* (L.) whole plant of Lithuanian and French origin for essential oil extraction // Am. J. Essent. Oil. Nat. Prod. – **2016**. – Vol. 4, № 3. – P. 12-15.

77 Zhi H. J., Qin X. M., Sun H. F., Zhang L. Z., Guo X. Q., Li Z. Y. Metabolic fingerprinting of *Tussilago farfara* L. using ^{1}H-NMR spectroscopy and multivariate data analysis // Phyto Chem Anal. – **2012**. – Vol. 23, № 5. – P. 492-501.

78 Yaoita Y., Kikuchi M., Machida K. Terpenoids and related compounds from plants of the family Compositae (Asteraceae) // Nat. Prod. Commun. – **2012**. – Vol. 7, № 4. – P. 533-538.

79 Mackenzie A. J., Spina D., Page C. P. Models used in the development of antitussive drugs // Drug Discov. Today Dis. Models. – **2004**. – Vol. 1, № 3. – P. 297-302.

80 Dobravalskyte D., Talou T., Venskutonis P. R. Activity of natural antioxidants extracted from *greater calamint sweet cicily* and coltsfoot cultivated in Lithuania and France // Conference Proceedings of the 6th Baltic Conference on Food Science and Technology FOODBALT-2011, Jelgava, Latvia –, **2011**. – P. 5-6.

81 Kim M. R., Lee J. Y., Lee H. H., Aryal D. K., Kim Y. G., Kim S. K., Woo E.-R., Kang K. W. Antioxidative effects of quercetin-glycosides isolated from the flower buds of *Tussilago farfara* L // Food Chem. Toxicol. – **2006**. – Vol. 44, № 8. – P. 1299-1307.

82 Dragičević S., Kovacević D., Divac Rankov A., Nikolić A., Radojković D., Radović S. J. Evaluation of toxicity and antioxidative effects of *Tussilago farfara* and Verbascum thapsus water extracts in zebrafish and in bronchial epithelial cells // Arch. Biol. Sci. – **2019**. – Vol. 71, № 3. – P. 409-416.

83 Lee I. K., Kim K. H., Choi S. U., Lee J. H., Lee K. R. Phytochemical constituents of *Thesium chinense* TURCZ and their cytotoxic activities *in vitro* // Nat. Prod. Sci. – **2009**. – Vol. 15, № 4. – P 246-249.

84 Lee H. J., Cho H. S., Jun S. Y., Lee J. J., Yoon J. Y., Lee J. H., Song H. H., Choi S. H., Kim S. Y., Saloura V. *Tussilago farfara* L. augments TRAIL-induced apoptosis through MKK7/JNK activation by inhibition of MKK7-TIPRL in human hepatocellular carcinoma cells // Oncology reports. – **2014**. – Vol. 32, № 3. – P. 1117-1123.

85 Cao J., Qin X., Li Z. J. Synthesis of silver nanoparticles from the polysaccharide of farfarae flos and uncovering its anticancer mechanism based on the cell metabolomic approach // J. Proteome Res. – **2021**. – Vol. 21, № 1. – P. 172-181.

86 LI J. J. C. T., Drugs H. Research progress on sesquiterpenoids from *Tussilago farfara* // Zhongcaoyao. – **2017**. – P. 2964-2971.

87 Lee J., Song K., Hiebert P., Werner S., Kim T.-G., Kim Y. S. J. Tussilagonone ameliorates psoriatic features in keratinocytes and imiquimod-induced psoriasis-like lesions in mice via NRF2 activation // J. Invest. Dermatol. – **2020**. – Vol. 140, № 6. – P. 1223-1232.

88 Qin K., Liu C., Qi Y., Li K. J. Evaluation of Antioxidant Activity of Polysaccharides from *Tussilago farfara* L. by Flow Injection Analysis // Asian J. Chem. – **2014**. – Vol. 26, № 10. – P. 3073-3076.

89 Cho J., Kim H. M., Ryu J. H., Jeong Y. S., Lee Y. S., Jin C. Neuroprotective and antioxidant effects of the ethyl acetate fraction prepared from *Tussilago farfara* L // Biol. Pharm. Bull. – **2005**. – Vol. 28, № 3. – P. 455-460.

90 Lee J., Song K., Huh E., Oh M. S., Kim Y. S. Neuroprotection against 6-OHDA toxicity in PC12 cells and mice through the Nrf2 pathway by a sesquiterpenoid from *Tussilago farfara* // Redox biol. – **2018**. – Vol. 18. – P. 6-15.

91 Hwang J. H., Kumar V. R., Kang S. Y., Jung H. W., Park Y. K. J. Effects of flower buds extract of *Tussilago farfara* on focal cerebral ischemia in rats and inflammatory response in BV2 microglia // Chin. J. Integr. Med. – **2018**. – Vol. 24. – P. 844-852.

92 Uysal S., Senkardes I., Mollica A., Zengin G., Bulut G., Dogan A., Glamočlija J., Soković M., Lobine D., Mahomoodally F. M. J. Dynamics. Biologically active compounds from two members of the Asteraceae family: *Tragopogon dubius Scop*. and *Tussilago farfara* L // J. Biomol. Struct. Dyn. – **2019**. – Vol. 37, № 12. – P. 3269-3281.

93 Chiang Y. W., Yeh C. F., Yen M. H., Lu C. Y., Chiang L. C., Shieh D. E., Chang J. S. J. T. Flos farfarae inhibits enterovirus 71-induced cell injury by preventing viral replication and structural protein expression // Am. J. Chin. Med. – **2017**. – Vol. 45, № 02. – P. 299-317.

94 Li Y., Wang Y. The effects of tussilagone on the hemodynamics of conscious dogs and dogs during hemorrhagic shock // Yao xue xue bao = Acta pharm. Sin. – **1987**. – Vol. 22, № 7. – P. 486-490.

95 Li Y., Wang Y.. Pressor mechanism of tussilagone // Yao xue xue bao = Acta pharm. Sin. – **1986**. – Vol. 7, № 4. – P. 333-336.

96 Chang. T. L., Yan. P. L., Feng. C. H., Yu L. *In vitro* antioxidant activities of *Tussilago farfara*, a new record species to Changbai Mountain // Chin J Nat Med. – **2012**. – Vol. 10, № 4. – P. 260-262.

97 Goun E. A., Petrichenko V., Solodnikov S., Suhinina T., Kline M. A., Cunningham G., Nguyen C., Miles H. J. Anticancer and antithrombin activity of Russian plants // J. Ethnopharmacol. – **2002**. – Vol. 81, № 3. – P. 337-342.

98 Ryu J. H., Jeong Y. S., Sohn D. H. A new bisabolene epoxide from *Tussilago farfara*, and inhibition of nitric oxide synthesis in LPS-activated macrophages // J. Nat. Prod. – **1999**. – Vol. 62, № 10. – P. 1437-1438.

99 Hwangbo C., Lee H. S., Park J., Choe J., Lee J. H. The anti-inflammatory effect of tussilagone, from *Tussilago farfara,* is mediated by the induction of heme oxygenase-1 in murine macrophages // Int. Immunopharmacol. – **2009**. – Vol. 9, № 13-14. – P. 1578-1584.

100 Kokoska L., Polesny Z., Rada V., Nepovim A., Vanek T. Screening of some Siberian medicinal plants for antimicrobial activity // J. Ethnopharmacol. – **2002**. – Vol. 82, № 1. – P. 51-53.

101 Li Z. Y., Zhi H. J., Xue S. Y., Sun H. F., Zhang F. S., Jia J.-P., Xing J., Zhang L. Z., Qin X. M. J. Metabolomic profiling of the flower bud and rachis of *Tussilago farfara* with antitussive and expectorant effects on mice // J. Ethnopharmacol. – **2012**. – Vol. 140, № 1. – P. 83-90.

102 Li J., Zhang Z. Z., Lei Z. H., Qin X. M., Li Z. Y. J. NMR based metabolomic comparison of the antitussive and expectorant effect of *Farfarae Flos* collected at different stages // J. Pharm. Biomed. Anal. – **2018**. – Vol. 150. – P. 377-385.

103 Fan J. X. Mechanism of *Farfarae Flos* in Qingfei Paidu Decoction against COVID-19 based on network pharmacology and molecular docking // Zhongcaoyao. – **2020**. – P. 2317-2325.

104 Adams J. P., Brown M. J., Diaz-Rodriguez A., Lloyd R. C., Roiban G. D. Biocatalysis: A pharma perspective // Adv. Synth. Catal. – **2019**. – Vol. 361, № 11. – P. 2421-2432.

105 Sheldon R. A., Brady D., Bode M. L. The Hitchhiker's guide to biocatalysis: recent advances in the use of enzymes in organic synthesis // Chem. Sci. – **2020**. – Vol. 11, № 10. – P. 2587-2605.

106 Ottone C., Romero O., Aburto C., Illanes A., Wilson L. Biocatalysis in the winemaking industry: Challenges and opportunities for immobilized enzymes // Compr. Rev. Food Sci. Food Saf. – **2020**. – Vol. 19, № 2. – P. 595-621.

107 Sheldon R. A., Brady D. Broadening the scope of biocatalysis in sustainable organic synthesis // ChemSusChem. – **2019**. – Vol. 12, № 13. – P. 2859-2881.

108 Britton J., Majumdar S., Weiss G. A. Continuous flow biocatalysis // Chem. Soc. Rev. – **2018**. – Vol. 47, № 15. – P. 5891-5918.

109 Bianchini L. F., Arruda M. F., Vieira S. R., Campelo P. M., Grégio A. M., Rosa E. A. Microbial biotransformation to obtain new antifungals // Front. Microbiol. – **2015**. – Vol. 6. – P. 1-12.

110 Smitha M., Singh S., Singh R. J. Microbial biotransformation: a process for chemical alterations // J Bacteriol Mycol Open Access. – **2017**. – Vol. 4, № 2. – P. 47-51.

111 Cao H., Chen X., Jassbi A. R., Xiao J. Microbial biotransformation of bioactive flavonoids // Biotechnol. Adv. – **2015**. – Vol. 33, № 1. – P. 214-223.

112 Molina G., Pimentel M. R., Bertucci T., Pastore G. M. Application of fungal endophytes in biotechnological processes // Chem. Eng. Trans. – **2012**. – Vol. 27, № 10. – P. 289-294.

113 Romero-Fernández M., Paradisi F. Protein immobilization technology for flow biocatalysis // Curr. Opin. Chem. Biol. – **2020**. – Vol. 55. – P. 1-8.

114 Guarneri A., van Berkel W., Paul C. E. Alternative coenzymes for biocatalysis // NCBs. – **2018**. – P. 1-24.

115 Li Q., Wu T., Zhao L., Pei J., Wang Z., Xiao W. Highly efficient biotransformation of astragaloside IV to cycloastragenol by sugar-stimulated *β*-glucosidase and *β*-xylosidase from Dictyoglomus thermophilum // J. Microbiol. Biotechnol. – **2019**. – P. 1882-1893.

116 Choi J.-M., Han S.-S., Kim H.-S. J. B. a. Industrial applications of enzyme biocatalysis: Current status and future aspects // Biotechnol. Adv. – **2015**. – Vol. 33, № 7. – P. 1443-1454.

117 Alfarra H., Hasali N., Omar M. A lignolytic fungi with laccase activity isolated from Malaysian local environment for phytochemical transformation purposes // Int. Res. J. Biol. Sci. – **2013**. Vol. 2, № 7. – P. 51-54.

118 Takahashi J. A., Gomes D. C., Lyra F. H., Dos Santos G. F., Martins L. R. The remarkable structural diversity achieved in ent-kaurane diterpenes by fungal biotransformations // Molecules. – **2014**. – Vol. 19, № 2. – P. 1856-1886.

119 Liese A., Villela. F. M. Production of fine chemicals using biocatalysis // Curr. Opin. Biotechnol. – **1999**. – Vol. 10, № 6. – P. 595-603.

120 Neuberg C., Hirsch J. Über ein kohlenstoffketten knüpfendes ferment (carboligase) // Biochem. Z. – **1921**. – Vol. 115. – P. 282-310.

121 Becvarova H. Course of transformation of benzaldehyde by Saccharomyces cerevisiae // Fol. Microbiol. – **1963**. – Vol. 8. – P. 165-169.

122 Leuenberger H. Interrelations of chemistry and biotechnology-I. Biotransformation-a useful tool in organic chemistry // Pure Appl. Chem. – **1990**. – Vol. 62, № 4. – P. 753-768.

123 Murray H., Petrson H. Oxygenation of steroids by mucorales fungi // Chem Tech. – **1978**. – Vol. 8. – P. 662-672.

124 Nelson J., Griffin E. G. Adsorption of invertase // J. Am. Chem. Soc. – **1916.** – Vol. 38, № 5. – P. 1109-1115.

125 Asano Y., Yasuda T., Tani Y., Yamada H. A new enzymatic method of acrylamide production // Agric. Biol. Chem. – **1982**. – Vol. 46, № 5. – P. 1183-1189.

126 Wandrey C., Liese A., Kihumbu D. development. Industrial biocatalysis: past, present, and future // Org. Process Res. Dev. – **2000**. – Vol. 4, № 4. – P. 286-290.

127 Venisetty R., Ciddi V. Application of microbial biotransformation for the new drug discovery using natural drugs as substrates // Curr. Pharm. Biotechnol. – **2003**. – Vol. 4, № 3. – P. 153-167.

128 Bartmańska A., Dmochowska-Gładysz J., Huszcza E. Steroids' transformations in *Penicillium notatum* culture // Steroids. – **2005**. – Vol. 70, № 3. – P. 193-198.

129 Hartman D. A., Pontones M. E., Kloss V. F., Curley R. W., Robertson L. W. Models of retinoid metabolism: Microbial biotransformation of *α*-ionone and *β*-ionone // J. Nat. Prod. – **1988**. – Vol. 51, № 5. – P. 947-953.

130 Sultana N., Saify Z. S. Enzymatic biotransformation of terpenes as bioactive agents // J. Enzyme Inhib. Med. Chem. – **2013**. – Vol. 28, № 6. – P. 1113-1128.

131 Al-Aboudi A., Kana'an B. M., Zarga M. A., Bano S., Javed K., Choudhary M. I. Fungal biotransformation of diuretic and antihypertensive drug spironolactone with *Gibberella fujikuroi*, *Curvularia lunata*, *Fusarium lini*, and *Aspergillus alliaceus* // Steroids. – **2017**. – Vol. 128. – P. 15-22.

132 Baydoun E., Karam M., Khan M. S. A., Ahmad M. S., Smith C., Abdel-Massih R., Choudhary M. I. Microbial transformation of nandrolone with *Cunninghamella echinulata* and *Cunninghamella blakesleeana* and evaluation of leishmaniacidal activity of transformed products // Steroids. – **2014**. – Vol. 88. – P. 95-100.

133 Azizuddin, Iqbal M., Sherwani S. K. Biotransformation of *β*-Artemether by *Aspergillus niger* and *Aspergillus flavus*, and Antifungal Activity of Their Metabolites // Chem. Nat. Compd. – **2016**. – Vol. 52. – P. 62-66.

134 Chen T. S., Li X., Bollag D., Liu Y. C., Chang C. J. Biotransformation of taxol // Tetrahedron Lett. – **2001**. – Vol. 42, № 23. – P. 3787-3789.

135 Ochoa-Villarreal M., Howat S., Hong S., Jang M. O., Jin Y. W., Lee E. K., Loake G. Plant cell culture strategies for the production of natural products // BMB reports. – **2016**. – Vol. 49, № 3. – P. 149-158.

136 Asthana G. S., Asthana A. Sciences P. Biotransformation of progesterone to 17*α*-hydroxyprogesterone by using plant cell suspension culture of *Catharanthus roseus* // Int J Pharm Pharm Sci. – **2015**. –Vol. 7, № 4. – P. 7.362-368

137 Choudhary M. I., Siddiqui Z. A., Khan S., Saifullah, Musharraf S. G. Biotransformation of (–)-caryophyllene oxide by cell suspension culture of *Catharanthus roseus* // Z. Naturforsch. B. – **2006**. – Vol. 61, № 2. – P. 197-200.

138 VANEK T., Halik J., Vankova R., Valterova I. Formation of trans-verbenol and verbenone from *α*-pinene catalysed by immobilised Picea abies cells // Biosci. Biotechnol. Biochem. – **2005**. – Vol. 69, № 2. – P. 321-325.

139 Zafar S., Yousuf S., Kayani H. A., Saifullah S., Khan S., Al-Majid A. M., Choudhary M. I. Biotransformation of oral contraceptive ethynodiol diacetate with microbial and plant cell cultures // Chemistry Central Journal. – **2012**. – Vol. 6. – P. 1-8.

140 Vangala S., Pinjari J., Patole P., Ravindran S., Gangal R., Wangikar P., Basu S., Ahmed T., Rastogi H. Translational drug discovery research: Integration of medicinal chemistry, computational modeling, pharmacology, ADME, and toxicology // EDMI. – **2011**. – P. 1-54.

141 Arrowsmith J. Phase II failures: 2008–2010 // Nat. Rev. Drug Discov. – **2011**. – Vol. 10, № 5. – P. 328-329.

142 Fura A. Role of pharmacologically active metabolites in drug discovery and development // Drug Discov. Today. – 2006. – Vol. 11, № 3-4. – P. 133-142.

143 de Carvalho C. C. Whole cell biocatalysts: essential workers from nature to the industry // Microb. Biotechnol. – **2017**. – Vol. 10, № 2. – P. 250-263.

144 Alcántara A. J. Biotransformations in drug synthesis: a green and powerful tool for medicinal chemistry // J. Med. Chem. Drug Des. – **2018**. – Vol. 1, № 1. – P. 1-7.

145 Schulz S., Girhard M., Urlacher V. B. Biocatalysis: key to selective oxidations // ChemCatChem. – **2012**. – Vol. 4, № 12. – P. 1889-1895.

146 Ferrer M., Bargiela R., Martínez-Martínez M., Mir J., Koch R., Golyshina O. V., Golyshin P. N. Biodiversity for biocatalysis: A review of the α/β-hydrolase fold superfamily of esterases-lipases discovered in metagenomes // JBCBT. – **2015**. – Vol. 33, № 5-6. – P. 235-249.

147 Priyanka P., Tan Y., Kinsella G. K., Henehan G. T., Ryan B. Solvent stable microbial lipases: Current understanding and biotechnological applications // Biotechnol Lett. – **2019**. – Vol. 41. – P. 203-220.

148 Banerjee S., Singh S., Rahman L. U. Biotransformation studies using hairy root cultures—a review // Biotechnol. Adv. – 2012. – Vol. 30, № 3. – P. 461-468.

149 Basso A., Serban S. Industrial applications of immobilized enzymes—A review // Mol. Catal. – **2019**. – Vol. 479. – P. 461-468.

150 Borges K. B., de Souza Borges W., Durán-Patrón R., Pupo M. T., Bonato P. S., Collado I. G. Stereoselective biotransformations using fungi as biocatalysts // Tetrahedron Asymmetry. – **2009**. – Vol. 20, № 4. – P. 385-397.

151 Solano D. M., Hoyos P., Hernáiz M., Alcántara A., Sánchez-Montero J. Industrial biotransformations in the synthesis of building blocks leading to enantiopure drugs // Bioresour. Technol. – **2012**. – Vol. 115. – P. 196-207.

152 De Carvalho C. C. Enzymatic and whole cell catalysis: finding new strategies for old processes // Biotechnol. Adv. – **2011**. – Vol. 29, № 1. – P. 75-83.

153 Goetschel R., Bar R. Formation of mixed crystals in microbial conversion of sterols and steroids // Enzym. Microb. Technol. – **1992**. – Vol. 14, № 6. – P. 462-469.

154 Kumar R., Dahiya J., Singh D., Nigam P. Biotransformation of cholesterol using Lactobacillus bulgaricus in a glucose-controlled bioreactor // Bioresour. Technol. – **2001**. – Vol. 78, № 2. – P. 209-211.

155 Schlosser D., Irrgang S., Schmauder H. Steroid hydroxylation with free and immobilized cells of *Penicillium raistrickii* in the presence of *β*-cyclodextrin // Appl. Microbiol. Biotechnol. – **1993**. – Vol. 39. – P. 16-20.

156 Mahato R. I., Kawabata K., Nomura T., Takakura Y., Hashida M. J. Physicochemical and pharmacokinetic characteristics of plasmid DNA/cationic liposome complexes // J. Pharm. Sci. – **1995**. – Vol. 84, № 11. – P. 1267-1271.

157 Khmelnitsky Y. L., Welch S. H., Clark D. S., Dordick J. S. Salts dramatically enhance activity of enzymes suspended in organic solvents // J. Am. Chem. Soc. – **1994**. – Vol. 116, № 6. – P. 2647-2648.

158 Lee B., Brown W., Ryu D., Thoma R. Bioengineering. Sequential 11*α*-hydroxylation and 1-dehydrogenation of 16*α*-hydroxycortexolone // Biotechnol. Bioeng. – **1971**. – Vol. 13, № 4. – P. 503-515.

159 Coldham N. G., Sauer M. pharmacology a. Pharmacokinetics of [14C] genistein in the rat: gender-related differences, potential mechanisms of biological action, and implications for human health // Toxicol. Appl. Pharmacol. – **2000**. – Vol. 164, № 2. – P. 206-215.

160 Rabinovich M., Bolobova A., Vasil'Chenko L. Fungal decomposition of natural aromatic structures and xenobiotics: a review // Appl. Biochem. Microbiol. – **2004**. – Vol. 40. – P. 1-17.

161 Templeton J. F., Kumar V. S., Marat K., Kim R., Labella F., Cote D. J. New hydroxylation products of progesterone with *Mucor griseocyanus* // J. Nat. Prod. – **1987**. – Vol. 50, № 3. – P. 463-467.

162 Madyastha K., Joseph T. Transformation of dehydroepiandrosterone and pregnenolone by *Mucor piriformis* // Appl. Microbiol. Biotechnol. – **1995**. – Vol. 44. – P. 339-343.

163 Fernandes D., Loi B., Porte C. Biosynthesis and metabolism of steroids in molluscs // J. Steroid Biochem. Mol. Biol. – **2011**. – Vol. 127, № 3-5. – P. 189-195.

164 Choudhary M. I., Sultan S., Jalil S., Anjum S., Rahman A. A., Fun H. K. Microbial transformation of mesterolone // Chem. Biodivers. – **2005**. – Vol. 2, № 3. – P. 392-400.

165 Aamer M., Siddiqui M., Jabeen A., Irshad R., Khan F.-A., Choudhary M. I., Wang Y. Structural transformation of methasterone with *Cunninghamella blakesleeana* and *Macrophomina phaseolina* // RSC Adv. – **2022**. – Vol. 12, № 15. – P. 9494-9500.

166 Ekiz G. n., Yılmaz S., Yusufoglu H., Kırmızıbayrak P. B., Bedir E. J. Microbial transformation of cycloastragenol and astragenol by endophytic fungi isolated from astragalus species // J. Nat. Prod. – **2019**. – Vol. 82, № 11. – P. 2979-2985.

167 Aamer M., Siddiqui M., Jabeen A., Irshad R., Khan F.-A., Choudhary M. I., Wang Y. New anti-inflammatory and non-cytotoxic metabolites of

methylstenbolone obtained by microbial transformation // Bioorg. Chem. – **2022**. – Vol. 129. – P. 106187.

168 Aziz A., Bano S., Choudhary M. I. Microbial transformation of oral contraceptive ethisterone by *Aspergillus niger* and *Cunninghamella blakesleeana* // Steroids. – **2020**. – Vol. 154. – P. 1-5.

169 Yildirim K., Kuru A., Yılmaz Ş. Biotransformation of testosterone by Cladosporium sphaerospermum // JBCBT. – **2019**. – Vol. 37, № 6. – P. 409-413.

170 Javid M., Nickavar B., Vahidi H., Faramarzi M. A. Baeyer-Villiger oxidation of progesterone by *Aspergillus sojae* PTCC 5196 // Steroids. – **2018**. – Vol. 140. – P. 52-57.

171 Özçınar O. z., Tağ O. z. r., Yusufoglu H., Kivçak B., Bedir E. J. Biotransformation of neoruscogenin by the endophytic fungus *Alternaria eureka* // J. Nat. Prod. – **2018**. – Vol. 81, № 6. – P. 1357-1367.

172 Baydoun S., Wahab A.-t., Bano S., Imad R., Choudhary M. I. Microbial-catalysed derivatization of anti-cancer drug exemestane and cytotoxicity of resulting metabolites against human breast adenocarcinoma cell line (MCF-7) *in vitro* // Steroids. – **2016**. – Vol. 115. – P. 67-74.

173 Siddiqui M., Ahmad M. S., Wahab A.-t.-., Yousuf S., Fatima N., Naveed Shaikh N., Rahman A.-u.-., Choudhary M. I. Biotransformation of a potent anabolic steroid, mibolerone, with *Cunninghamella blakesleeana*, *C. echinulata*, and *Macrophomina phaseolina*, and biological activity evaluation of its metabolites // PLoS One. – **2017**. – Vol. 12, № 2. – P. 1-22.

174 Ahmad I., Kudaibergenova B., Ahmad M., Sadia M., Choudhary M. I., Hafez-Ghoran S. Coltsfoot (*Tussilago farfara* L.; Asteraceae): modern methods of extraction, phytochemistry, nanoparticles synthesis, ethnopharmacology, and biological activities // Nat. Prod. Res. – **2025**. –P. 1-20.

175 Tobyn G., Denham A., Whitelegg M. *Tussilago farfara*, coltsfoot // **Med Herb**. – **2011**. – P. 317-326.

176 Adamczak A., Opala B., Gryszczynska A., Buchwald W. Content of pyrrolizidine alkaloids in the leaves of coltsfoot (*Tussilago farfara* L.) in Poland // Acta Soc. Bot. Pol. – **2013**. – Vol. 82, № 4. – P. 289-293.

177 Rigat M., Valles J., Gras A., Iglésias J., Garnatje T. E. Plants with topical uses in the Ripollès district (Pyrenees, Catalonia, Iberian Peninsula): ethnobotanical survey and pharmacological validation in the literature // J. Ethnopharmacol. – **2015**. – Vol. 164. – P. 162-179.

178 Ahmad I., Atif M., Aldibekova G., Balpanova D., Zafar H., Sadia M., Ahmad M., Atia tul W., Kudaibergenova B., Choudhary u. I. Aromatase (CYP19A1) Inhibitory Activity of Coltsfoot (*Tussilago farfara* L.) Phytochemicals: *In Vitro* and *in Silico* Evaluation // Eurasian chem.-technol. j. – **2025**. – Vol. 27, № 4. –P. 315-321.

179 Kun C., Yi X., Chang-rui W., Tian-ming Z. Developments of separation, purification and quality control for the chemical constitutions of *Tussilago farfara* // NPRD. – **2014**. – Vol. 26, № 4. – P. 619.

180 Zhao Peng Z. P., Li Lin L. L., Tang ZhiShu T. Z., Li WenHong L. W. Isolation, characterization and antioxidant activities of polysaccharides from *Tussilago farfara* // Asian J. Chem. – **2012**. – Vol. 24, № 6. – P. 2707-2710.

181 Kačániová M., Hleba L., Petrová J., Felšöciová S., Pavelková A., Rovná K., Bobková A., Čuboň J. Antimicrobial activity of *Tussilago farfara* L // JMBFS. – **2013**. – Vol. 2, № special issue 2. – P. 1343-1350.

182 Zhao J., Evangelopoulos D., Bhakta S., Gray A. I., Seidel V. J. Antitubercular activity of Arctium lappa and *Tussilago farfara* extracts and constituents // J. Ethnopharmacol. – **2014**. – Vol. 155, № 1. – P. 796-800.

183 Hwang S.-B., Chang M. N., Garcia M. L., Han Q. Q., Huang L., King V. F., Kaczorowski G. J., Winquist R. J. L-652,469-a dual receptor antagonist of platelet activating factor and dihydropyridines from *Tussilago farfara* L // Eur. J. Pharmacol. – **1987**. – Vol. 141, № 2. – P. 269-281.

184 Song X. Q., Sun J., Yu J. H., Zhang J. S., Bao J., Zhang H. Prenylated indole alkaloids and lignans from the flower buds of *Tussilago farfara* // Fitoterapia. – **2020**. – Vol. 146. – P. 1-7.

185 Muravnik L. E., Kostina O. V., Shavarda A. L. Glandular trichomes of *Tussilago farfara* (senecioneae, asteraceae) // Planta. – **2016**. – Vol. 244. – P. 737-752.

186 Chen S., Dong L., Quan H., Zhou X., Ma J., Xia W., Zhou H., Fu X. J. A review of the ethnobotanical value, phytochemistry, pharmacology, toxicity and quality control of *Tussilago farfara* L.(coltsfoot) // J. Ethnopharmacol. – **2021**. – Vol. 267. – P. 1-19.

187 Pfeiffer T., Günzel C., Frey W. Distribution, Functional Ecology of Plants. Clonal reproduction, vegetative multiplication and habitat colonisation in *Tussilago farfara* (Asteraceae): a combined morpho-ecological and molecular study // Flora: Morphol. Distrib. Funct. Ecol. Plants. – **2008**. – Vol. 203, № 4. – P. 281-291.

188 Santiago-Silva, Kaio M., Priscila G. Camargo, and Marcelle LF Bispo. Promising molecular targets related to polyamine biosynthesis in drug discovery against leishmaniasis // Med. Chem. – **2023**. – Vol. 19, № 1. –. P. 2-9.

189 Vickers, Tim J., and Stephen M. Beverley. "Folate metabolic pathways in *Leishmania* // Essays in biochem. – 2011. – Vol. 51. –. P. 63-80.

190. Desjeux, Philippe. Leishmaniasis: current situation and new perspectives // Comp. Immunol. Microbiol. Infect. Dis. – **2004**. – Vol. 27, № 5. –. P. 305-318.

191 Shanks E. J., Ong H. B., Robinson D. A., Thompson S., Sienkiewicz N., Fairlamb A. H., Frearson J. A. Development and validation of a cytochrome c-

coupled assay for pteridine reductase 1 and dihydrofolate reductase // Anal. Biochem. – **2010**. – Vol. 396, № 2. – P. 194-203.

192 Gourley D. G., Schüttelkopf A. W., Leonard G. A., Luba J., Hardy L. W., Beverley S. M., Hunter W. N. Pteridine reductase mechanism correlates pterin metabolism with drug resistance in trypanosomatid parasites // Nat. Struct. Biol. – **2001**. – Vol. 8, № 6. – P. 521-525.

193 Lu C., Wu C., Ghoreishi D., Chen W., Wang L., Damm W., Ross G. A., Dahlgren M. K., Russell E., Von Bargen C. D. OPLS4: Improving force field accuracy on challenging regimes of chemical space // J. Chem. Theory Comput. – **2021**. – Vol. 17, № 7. – P. 4291-4300.

194 Johnston R. C., Yao K., Kaplan Z., Chelliah M., Leswing K., Seekins S., Watts S., Calkins D., Chief Elk J., Jerome S. V. Epik: p K a and Protonation State Prediction through Machine Learning // J. Chem. Theory Comput. – **2023**. – Vol. 19, № 8. – P. 2380-2388.

195 Yang Y., Yao K., Repasky M. P., Leswing K., Abel R., Shoichet B. K., Jerome S. V. Efficient exploration of chemical space with docking and deep learning // J. Chem. Theory Comput. – **2021**. – Vol. 17, № 11. – P. 7106-7119.

196 Bowers K. J., Chow E., Xu H., Dror R. O., Eastwood M. P., Gregersen B. A., Klepeis J. L., Kolossvary I., Moraes M. A., Sacerdoti F. D. Scalable algorithms for molecular dynamics simulations on commodity clusters // Proceedings of the 2006 ACM/IEEE Conference on Supercomputing – **2006**. – P. 1-13.

197 Mark P., Nilsson L. J. T. Structure and dynamics of the TIP3P, SPC, and SPC/E water models at 298 K // J. Phys. Chem. A. – **2001**. – Vol. 105, № 43. – P. 9954-9960.

198 Cheng A., Merz K. M. J. T. Application of the Nosé− Hoover chain algorithm to the study of protein dynamics // J. Phys. Chem. – **1996.** – Vol. 100, № 5. – P. 1927-1937.

199 Martyna G. J., Tobias D. J., Klein M. L. J. T. Constant pressure molecular dynamics algorithms // J. Chem. Phys. – **1994**. – Vol. 101, № 5. – P. 4177-4189.

200 Ahmad I., Hafez-Ghoran S., Yousuf M., Zafar H., Wahab A.-t., Yousuf S., Ahmad M., Gul I., Kudaibergenova B., Choudhary M. I. Caffeoylquinic acid derivatives isolated from *Tussilago farfara* L. as potential anti-leishmanial agents; *in vitro* and *in silico* studies // Nat. Prod. Res. – **2026**. –P. 1-9.

201 Nováková L., Matysová L., Solich P. Advantages of application of UPLC in pharmaceutical analysis // *Talanta*. –**2006**. Vol.–68, –P. 908-918.

202 M.W. Dong, Modern HPLC for practicing scientists // *John Wiley & Sons*. – **2006**.

203 Snyder LR., Kirkland JJ., Dolan JW. Introduction to modern liquid chromatography // *John Wiley & Sons*.–**2011**.

204 Swartz ME., UPLC™: An Introduction and Review // *J. Liq. Chromatogr. Relat. Technol*. –**2005**. Vol. –28, –P. 1253-1263.

205 Hayun H., Gavrila I., Silviana S., Siahaan A., Vonna R., Latifah M. Synthesis and antioxidant activity study of new mannich bases derived from vanillic acid // Rasayan J. Chem. – **2020**. – Vol. 13, № 1. – P. 131-138.

206 Świsłocka R. Spectroscopy B. Experimental (FT-IR, FT-Raman, ^{1}H, ^{13}C NMR) and theoretical study of alkali metal syringates // Mol. Biomol. Spectrosc. – **2013**. – Vol. 111. – P. 290-298.

207 Contardi M., Alfaro-Pulido A., Picone P., Guzman-Puyol S., Goldoni L., Benítez J. J., Heredia A., Barthel M. J., Ceseracciu L., Cusimano G. Low molecular weight ε-caprolactone-p-coumaric acid copolymers as potential biomaterials for skin regeneration applications // PloS One. – **2019**. – Vol. 14, № 4. – P. 1-18.

208 Li L., Xu L. W., Jiang Y. F., Xi C. J., Wang H. Q., Suo Y. R. Isolation, characterization and crystal structure of natural eremophilenolide from *Ligularia sagitta* // Z. Naturforsch. B. – **2004**. – Vol. 59, № 8. – P. 921-924.

209 Wang M., Zeng J., Zhu Y., Chen X., Guo Q., Tan H., Cui B., Song S., Deng Y. A 4-hydroxybenzoic acid-mediated signaling system controls the physiology and virulence of Shigella sonnei // Microbiol. Spectr. – **2023**. – Vol. 11, № 3. – P. 1-22.

210 Douros A., Hadjipavlou-Litina D., Nikolaou K., Skaltsa H. The occurrence of flavonoids and related compounds in *Cedrus brevifolia* A. Henry ex Elwes & A. Henry needles. Inhibitory potencies on lipoxygenase, linoleic acid lipid peroxidation and antioxidant activity // Plants. – **2017**. – Vol. 7, № 1. – P. 1-12.

211 Bukhari S. B., Memon S., Mahroof-Tahir M., Bhanger M. Spectroscopy B. Synthesis, characterization and antioxidant activity copper–quercetin complex // Spectrochim. Acta A Mol. Biomol. Spectrosc. – **2009**. – Vol. 71, № 5. – P. 1901-1906.

212 Costa D. A. d., Silva D. A., Cavalcanti A. C., Medeiros M. A. A. d., Lima J. T. d., Cavalcante J. M. S., Silva B. A. d., Agra M. d. F., Souza M. d. F. V. d. Chemical constituents from *Bakeridesia pickelii Monteiro* (Malvaceae) and the relaxant activity of kaempferol-3-O-beta-D-(6''-Ep-coumaroyl) glucopyranoside on guinea-pig ileum // Química Nova. – **2007**. – Vol. 30. – P. 901-903.

213 Rohman M. M., Hossain M. D., Suzuki T., Takada G., Fujita M. Quercetin-4′-glucoside: a physiological inhibitor of the activities of dominant glutathione S-transferases in onion (Allium cepa L.) bulb // Acta Physiol. Plant. – **2009**. – Vol. 31. – P. 301-309.

214 Chanaj-Kaczmarek J., Wojcińska M., Matlawska I. Phenolics in the *Tussilago farfara* leaves // Herba Pol. – **2013**. – Vol. 59, № 1. – P. 35-43.

215 Xiao Z., Wu H., Wu T., Shi H., Hang B., Aisa H. Kaempferol and quercetin flavonoids from *Rosa rugosa* // Chem. Nat. Compd. – **2006**. – Vol. 42, № 6. – P. 736-737.

216 S Osw P., HS Hussain F. Engineering. Isolation of kaempferol 3-O-rutinoside from Kurdish plant *Anchusa italica Retz*. and bioactivity of some extracts // Eurasian j. sci. eng. – **2020**. – Vol. 6, № 2. – P. 141-156.

217 Li Z. J., Cai L., Mei R. F., Dong J. W., Li S. Q., Yang X. Q., Zhou H., Yin T. P., Ding Z. T. A highly efficient transformation of cis-to trans-cinnamic acid derivatives by iodine // Tetrahedron Lett. – **2015**. – Vol. 56, № 52. – P. 7197-7200.

218 Wan C., Li S., Liu L., Chen C., Fan S. Caffeoylquinic acids from the aerial parts of *Chrysanthemum coronarium* L // Plants . – **2017**. – Vol. 6, № 1. – P. 1-7.

219 Yang A., Zhao A., Zheng Z., Shang Q., Zhang F., Han N., Yang L., Li C. Chemical constituents of the flower buds of *Tussilago farfara*. II // Chem. Nat. Compd. – **2018**. – Vol. 54. – P. 978-980.

220 Kim J. Y., Cho J. Y., Ma Y. K., Park K. Y., Lee S. H., Ham K. S., Lee H. J., Park K. H., Moon J. H. Dicaffeoylquinic acid derivatives and flavonoid glucosides from glasswort (*Salicornia herbacea* L.) and their antioxidative activity // Food Chem. – **2011**. – Vol. 125, № 1. – P. 55-62.

221 Merfort I. Caffeoylquinic acids from flowers of *Arnica montana* and *Arnica chamissonis* // Phytochemistry. – **1992**. – Vol. 31, № 6. – P. 2111-2113.

222 Murugesan A., Holmstedt S., Brown K. C., Koivuporras A., Macedo A. S., Nguyen N., Fonte P., Rijo P., Yli-Harja O., Candeias N. R. Design and synthesis of novel quinic acid derivatives: *in vitro* cytotoxicity and anticancer effect on glioblastoma // Future Med. Chem. – **2020**. – Vol. 12, № 21. – P. 1891-1910.

223 Hafez Ghoran S., Yousuf M., Zafar H., Abdjan M. I., Ayatollahi S. A., Atia-tul-Wahab, Aminah N. S., Kristanti A. N., Aziz-ur-Rehman, Choudhary M. I. *In vitro*, *in silico*, and STD-NMR studies of flavonoids from *Hypericum helianthemoides* (Spach) Boiss. against *Leishmania major* pteridine reductase 1 (Lm PTR1) // J. Biomol. Struct. Dyn. – **2024**. – P. 1-15.

224 Teixeira, B. V. F., Teles, A. L. B., Silva, S. G. D., Brito, C. C. B., Freitas, H. F. D., Pires, A. B. L. Castilho, M. S. Dual and selective inhibitors of pteridine reductase 1 (PTR1) and dihydrofolate reductase-thymidylate synthase (DHFR-TS) from *Leishmania chagasi* // J. Enzyme Inhib. Med. Chem. – **2019**. – Vol. 34, № 1. –. P. 1439-1450.

225 Choudhary M., Gupta S., Dhar M. K., Kaul S. Endophytic fungi-mediated biocatalysis and biotransformations paving the way toward green chemistry // Front. Bioeng. Biotechnol. – **2021**. – Vol. 9. – P. 1-10.

226 Buttgereit F., Bijlsma J. W., Strehl C. Will we ever have better glucocorticoids? // Clin. Immunol. – **2018**. – Vol. 186. – P. 64-66.

227 Gkantzou E., Chatzikonstantinou A. V., Fotiadou R., Giannakopoulou A., Patila M., Stamatis H. Trends in the development of innovative nanobiocatalysts and their application in biocatalytic transformations // Biotechnol. Adv. – **2021**. – Vol. 51. – P. 1-26.

228 Feng J., Wu Q., Zhu D., Ma Y. Biotransformation enables innovations toward green synthesis of steroidal pharmaceuticals // ChemSusChem. – **2022**. – Vol. 15, № 9. – P. 1-14.

229 Salter R., Beshore D. C., Colletti S. L., Evans L., Gong Y., Helmy R., Liu Y., Maciolek C. M., Martin G., Pajkovic N. Microbial biotransformation–an important tool for the study of drug metabolism // Xenobiotica. – **2019**. – Vol. 49, № 8. – P. 877-886.

230 Smith C., Khan M. S. A., Ahmad M. S., Farran D., Choudhary M. I., Baydoun E. Microbial transformation of oxandrolone with *Macrophomina phaseolina* and *Cunninghamella blakesleeana* // Steroids. – **2015**. – Vol. 102. – P. 39-45.

231 Choudhary M. I., Erum S., Atif M., Malik R., Khan N. T. Biotransformation of (20S)-20-hydroxymethylpregna-1, 4-dien-3-one by four filamentous fungi // Steroids. – 2011. – Vol. 76, № 12. – P. 1288-1296.

232 Siddiqui M., Choudhary M. I. Biotransformation studies on bioactive compounds: 25 years of interesting research at the ICCBS // Chem. Synth. – **2023**. – Vol. 25, № 3. – P. 1-50.

233 Maravelias C., Dona A., Stefanidou M., Spiliopoulou C. Adverse effects of anabolic steroids in athletes: a constant threat // Toxicol. Lett. – **2005**. – Vol. 158, № 3. – P. 167-175.

234 Maltais R., Tremblay M. R., Ciobanu L. C., Poirier D. J. Steroids and combinatorial chemistry // J. Comb. Chem. – **2004**. – Vol. 6, № 4. – P. 443-456.

235 Chumsri, S., Howes, T., Bao, T., Sabnis, G., Brodie, A. Aromatase, aromatase inhibitors, and breast cancer // J. Steroid Biochem. Mol. Biol. – **2011**. – Vol. – 125, № 1-2. –. P. 13-22.

236 Bhatnagar, A. S. (2007). The discovery and mechanism of action of letrozole // Breast Cancer Res. Treat. – **2007**. – Vol. 105. – P. 7-17.

237 Choudhary M. I., Siddiqui M., Yousuf S., Fatima N., Ahmad M. S., Choudhry H. Bio-catalytic structural transformation of anti-cancer steroid, drostanolone enanthate with *Cephalosporium aphidicola* and *Fusarium lini*, and cytotoxic potential evaluation of its metabolites against certain cancer cell lines // Front. Pharmacol. – **2017**. – Vol. 8. – P. 1-15.

238 Atia-tul-Wahab S. M., Ibrahim I., Hussain A., Ajandouz E., Hijazi A., Baydoun E., Choudhary M. I. *Cunninghamella blakesleeana*-mediated biotransformation of a contraceptive drug, desogestrel, and anti-MDR-Staphylococcus aureus activity of its metabolites // Bioorg Chem. – **2018**. – Vol. 77. – P. 52-158.

239 Ahmad I., Atif M., Kudaibergenova B., Zafar H., Hafez-Ghoran S., Atia tul W., Ahmad M., Sadia M., Ali S., Choudhary MI. Fungal-mediated transformation

of methylprednisolone acetate into potent aromatase inhibitors: *In vitro* and *in silico* studies // J. Mol. Struct. –**2026**. –Vol. 1364. – P. 145890.

240 Li H., Zhao Y., Chen L., Su Y., Li X., Jin L., Ge R. S. Triclocarban and triclosan inhibit human aromatase via different mechanisms // Biomed Res. Int. – **2017**. – Vol. 2017, № 1. – P. 1-7.

241 Ge H., Chen L., Su Y., Jin C., Ge R. S. Effects of folpet, captan, and captafol on human aromatase in JEG-3 cells // Pharmacol. – **2018**. – Vol. 102, № 1-2. – P. 81-87.

242 Zafar H., Anis R., Hafeez S., Aqeel Khan M., Zehra Basha F., Maslennikov I., Choudhary M. I. Identification of Non-steroidal Aromatase Inhibitors via *In silico* and *In vitro* Studies // Med. Chem. – **2023**. – Vol. 19, № 10. – P. 986-1001.

243 Aamer M., Atif M., Siddiqui M., Zafar H., Irshad R., Khan F.-A., Liang D., Choudhary M. I., Wang Y. Further transformation of fungal catalyzed transformed metabolite 11β-hydroxy-dianabol into new aromatase inhibitors // Bioorg. Chem. – **2025**. – Vol. 154. – P. 108025.

244 Sajid M., Siddiqui H., Atif M., Sharif R., Zafar H., Threadgill M. D., Choudhary M. I. Biodiversity. Synthesis, Aromatase Inhibition, Cytotoxicity and Molecular Docking Studies of New Fluorinated and Non-Fluorinated Thiourea Derivatives of Desloratadine // Chem. Biodiversity. – **2025**. – Vol. 22, № 3. – P. 1-14

245 Madhavi Sastry G., Adzhigirey M., Day T., Annabhimoju R., Sherman W. J. Protein and ligand preparation: parameters, protocols, and influence on virtual screening enrichments // J. Comput. Aided Mol. Des. – **2013**. – Vol. 27. – P. 221-234.

246 Repasky M. P., Shelley M., Friesner R. A. Flexible ligand docking with Glide // Curr Protoc Bioinformatics. – **2007**. – Vol. 18, № 1. – P. 1-36

247 Choudhary M. I., Shaikh M., tul-Wahab A.-., ur-Rahman A. *In silico* identification of potential inhibitors of key SARS-CoV-2 3CL hydrolase (Mpro) via molecular docking, MMGBSA predictive binding energy calculations, and molecular dynamics simulation // Plos One. – **2020**. – Vol. 15, № 7. – P. 1-15.

248 Atif M., Zafar H., Wahab A.-t.-., Choudhary M. I. Drug repurposing against fucosyltransferase-2 via docking, STD-NMR, and molecular dynamic simulation studies // PloS One. – **2024**. – Vol. 19, № 11. – P. 1-19.

249 Lagarias P., Barkan K., Tzortzini E., Stampelou M., Vrontaki E., Ladds G., Kolocouris A. J. Insights to the binding of a selective adenosine A3 receptor antagonist using molecular dynamic simulations, MM-PBSA and MM-GBSA free energy calculations, and mutagenesis // J. Chem. Inf. Model. – **2019**. – Vol. 59, № 12. – P. 5183-5197.

250 Hameedat F., Hawamdeh S., Alnabulsi S., Zayed A. High Performance Liquid Chromatography (HPLC) with Fluorescence Detection for Quantification of

Steroids in Clinical, Pharmaceutical, and Environmental Samples: A Review // Molecules. – **2022**. –Vol. 27 № 6. – P.1807.

251 McDonald JG., Matthew S., Auchus RJ. Steroid profiling by gas chromatography-mass spectrometry and high performance liquid chromatography-mass spectrometry for adrenal diseases // *Hormones & cancer*. – **2011**. – Vol. 2. № 6. – P. 324-332.

252 Siddiqui, M., Jabeen, A., Wang, Y., Wang, W., Choudhary, M. I. Whole-cell fungal-mediated structural transformation of anabolic drug metenolone acetate into potent anti-inflammatory metabolites // J. Adv. Res. – **2020**. – Vol. 24. – P. 69-78.

253 Borges, K. B., de Souza Borges, W., Durán-Patrón, R., Pupo, M. T., Bonato, P. S., Collado, I. G. Stereoselective biotransformations using fungi as biocatalysts // Tetrahedron: Asymmetry. – **2009**. – Vol. 20, № 4. – P. 385-397.

254 Pinto RMA., Salvador JAR., Le Roux C., Paixão JA. Bismuth(III) Triflate-Catalyzed Direct Conversion of Corticosteroids into Highly Functionalized 17-Ketosteroids by Cleavage of the C17-Dihydroxyacetone Side Chain // J. Org. Chem**.** –**2009**. Vol– 74, № 21. –P. 8488-8491.

255 Durairaj P., Malla S., Nadarajan SP., Lee PG., Jung E., Park H., Kim BG., Yun H., Fungal cytochrome P450 monooxygenases of *Fusarium oxysporum* for the synthesis of ω-hydroxy fatty acids in engineered Saccharomyces cerevisiae // Microbial Cell Factories. – **2015**. Vol. 14 –P. 2-16.

256 Newcomb M., Hollenberg PF., Coon MJ., Multiple mechanisms and multiple oxidants in P450-catalyzed hydroxylations, Arch. Biochem. Biophys. – **2003**. –Vol. 409.–P. 72-79.

257 Fernandes P., Cruz A., Angelova B., Pinheiro HM., Cabral JMS. Microbial conversion of steroid compounds: recent developments // Enzyme Microb. Technol. – **2003**. Vol. 32–.P 688-705.

258 Khan MF., Hof C., Niemcová P., Murphy CD. Recent advances in fungal xenobiotic metabolism: enzymes and applications // World J. Microbiol. Biotechnol. –**2023**. –Vol. 39. –P. 296.

259 Jennings DH., Polyol Metabolism in Fungi // Adv. Microb. Physiol. –**1985**. –Vol. 25. –P. 149-193.

260 Frensch B., Lechtenberg ., Kather M., Yunt Z., Betschart M., Kammerer B., Lüdeke S., Müller M., Piel J., Teufel R. Enzymatic spiroketal formation *via* oxidative rearrangement of pentangular polyketides // Nat. Commun. –**2021**. –Vol. 12. –P. 1-12.

261 Bilyk B., Oliveira GS., de Angelo RM., Almeida MO., Honorio KM., Leeper FJ., Dias MV., Leadlay PF. Enzyme-catalyzed spiroacetal formation in polyketide antibiotic biosynthesis // J. Am. Chem. Soc. –**2023**. –Vol. 144. –P. 14555-14563.

262 Castro MI., Loureiro-Dias MC., Glycerol utilization in *Fusarium oxysporum* var. lini: regulation of transport and metabolism // Microbiol. –**1991**. – Vol. 137. –P. 1497-1502.

263 Eisenberg R., Kudrimoti S., Hughes C. G., Maylin G. A., Tobin T. Synthesis, purification, and chemical characterization of 20-dihydro-6-methylprednisone, an isomeric metabolite of methylprednisolone in the horse, for use as an analytical standard // *Drug Test. Anal*. – **2014**. – Vol. 6, № 3. – P. 303-307.

264 Signoretti E. C., Valvo L., Savella A., Cavina G. J.. Purity evaluation of 6*α*-methylprednisolone acetate by HPLC // J. Pharm. Biomed. Anal. – **1993**. – Vol. 11, № 7. – P. 587-593.

265 Vree T., Verwey-van Wissen C., Lagerwerf A., Swolfs A., Maes R., Van Ooijen R., van Eikema Hommes O., Jongen P. J. Applications. Isolation and identification of the C6-hydroxy and C20-hydroxy metabolites and glucuronide conjugate of methylprednisolone by preparative high-performance liquid chromatography from urine of patients receiving high-dose pulse therapy // J. Chromatogr. B Biomed. Sci. Appl. – **1999**. – Vol. 726, № 1-2. – P. 157-168.

266 Murata N., Fujimori S., Ichihara Y., Sato Y., Yamaji T., Tsuboi H., Uchida M., Suzuki H., Yamada M., Oikawa T., Nemoto H. Synthesis and anti-tumor activity of a fluorinated analog of medroxyprogesterone acetate (MPA), 9*α*-fluoromedroxyprogesterone acetate (FMPA) // Chem. Pharm. Bull. – **2006**. – Vol. 54, № 11. – P. 1567-1570.

267 Donova, M. V., Egorova, O. V. Microbial steroid transformations: current state and prospects // Appl. Microbiol. Biotechnol. – **2012**. – Vol. 94, № 6. – P. 1423-1447.

Appendix A

Spectroscopic, mass spectrometric, and chromatographic data of isolated compounds from *Tussilago farfara* L.

Figures S1–S22 present the spectroscopic, spectrometric, and chromatographic characterization of compounds obtained *Tussilago farfara* L., including NMR spectra, EI-MS/ESI-MS/FAB-MS evidence, and HPLC chromatograms used for structural elucidation and purity assessmen.

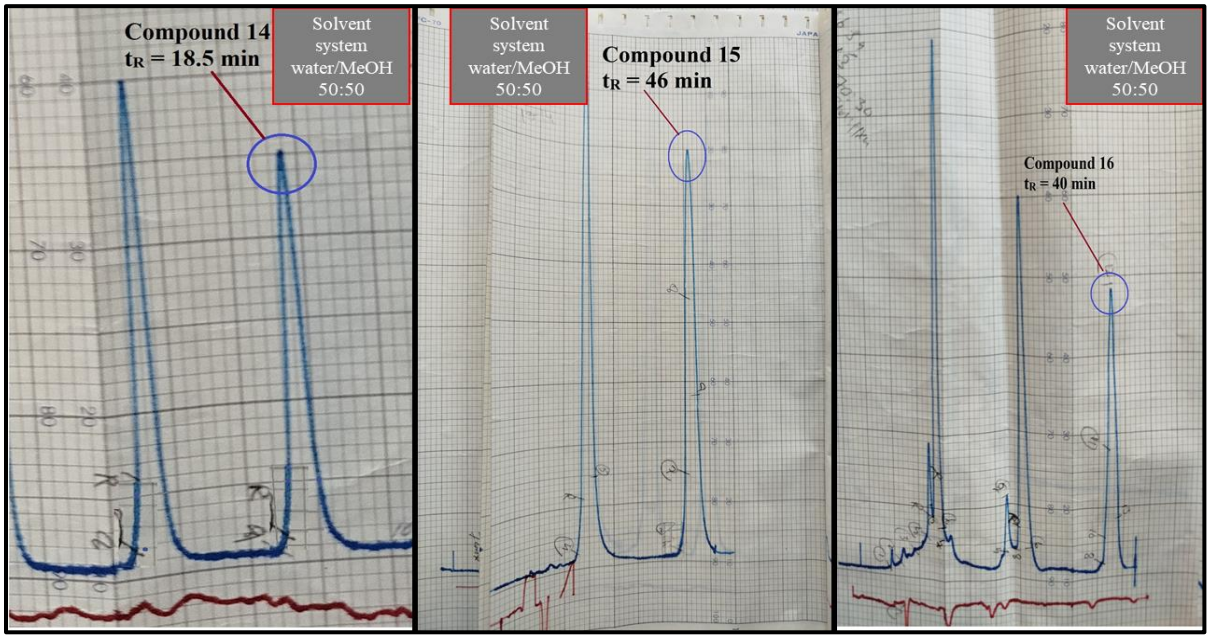


Figure S1 – HPLC (reverse phase) chromatogram of compound 14, 15 and 16

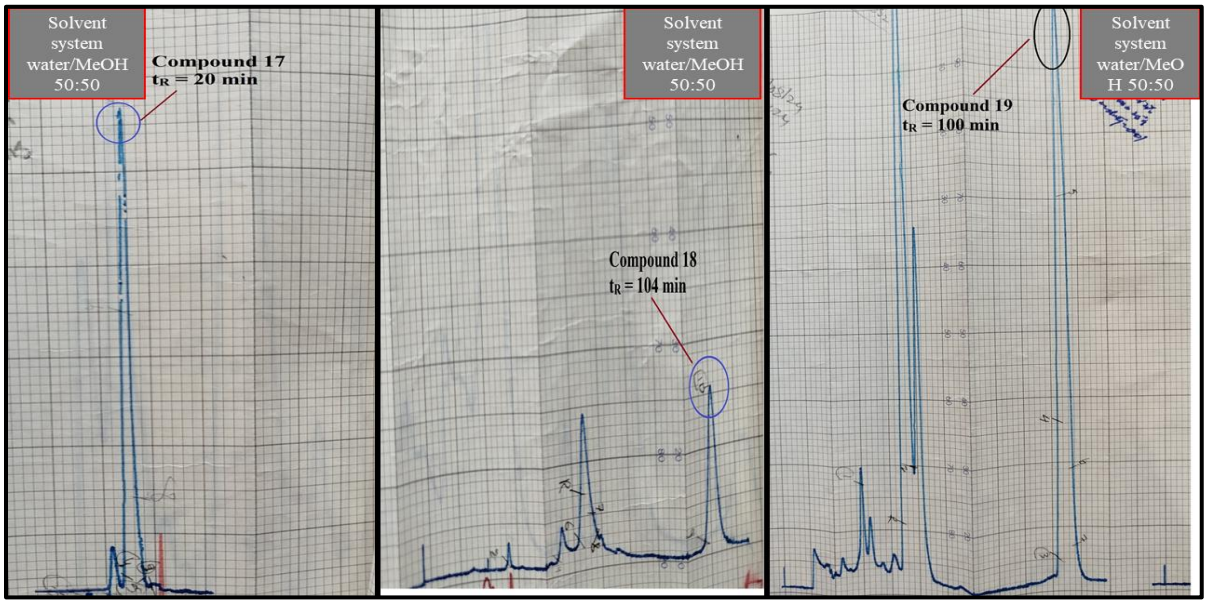


Figure S2 – HPLC (reverse phase) chromatogram of compound 17, 18 and 19

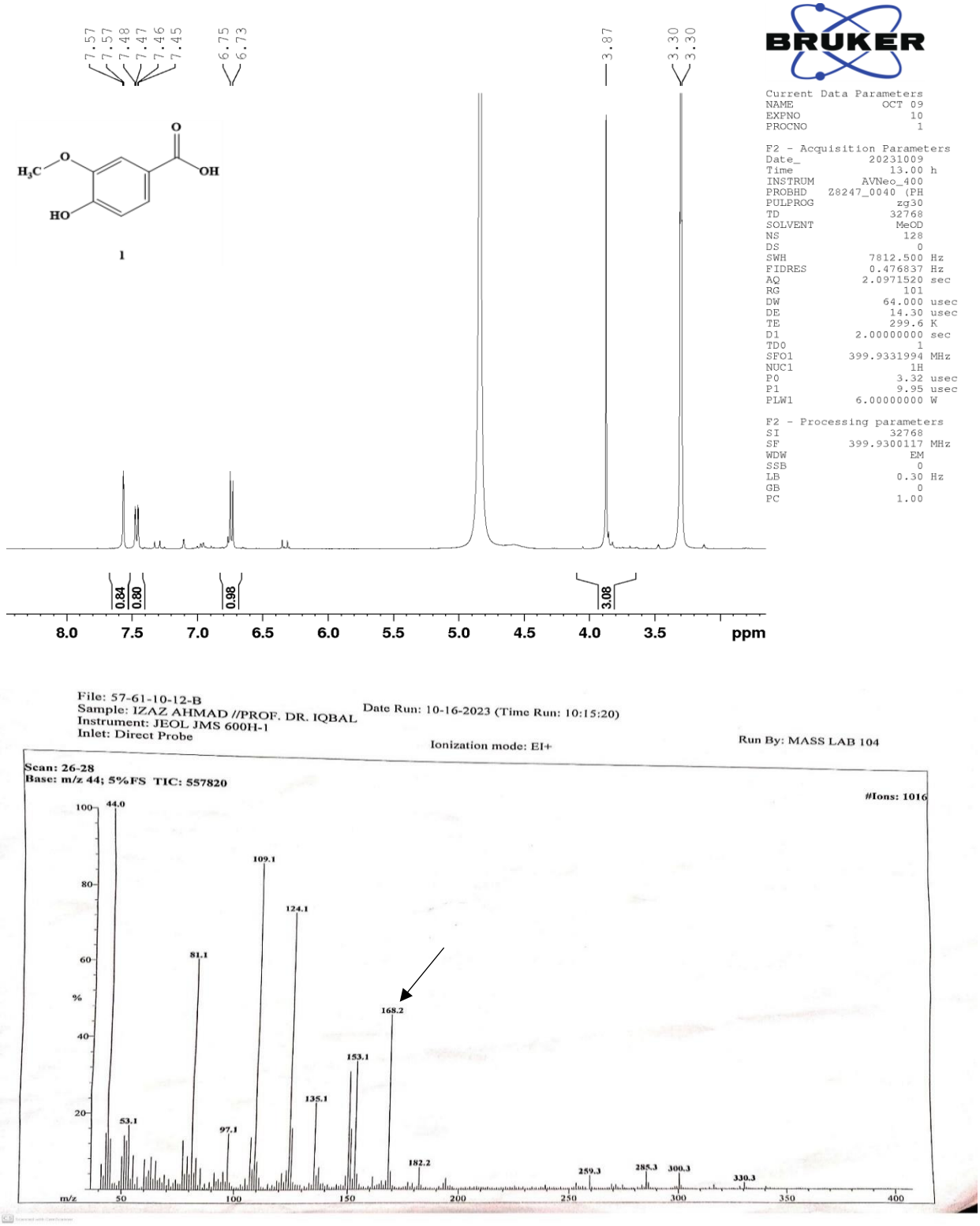


Figure S3 – The ^{1}H-NMR (400 MHz, CD_3OD) and EI-MS $[M]^{+}$ spectra of vanillic acid (1)

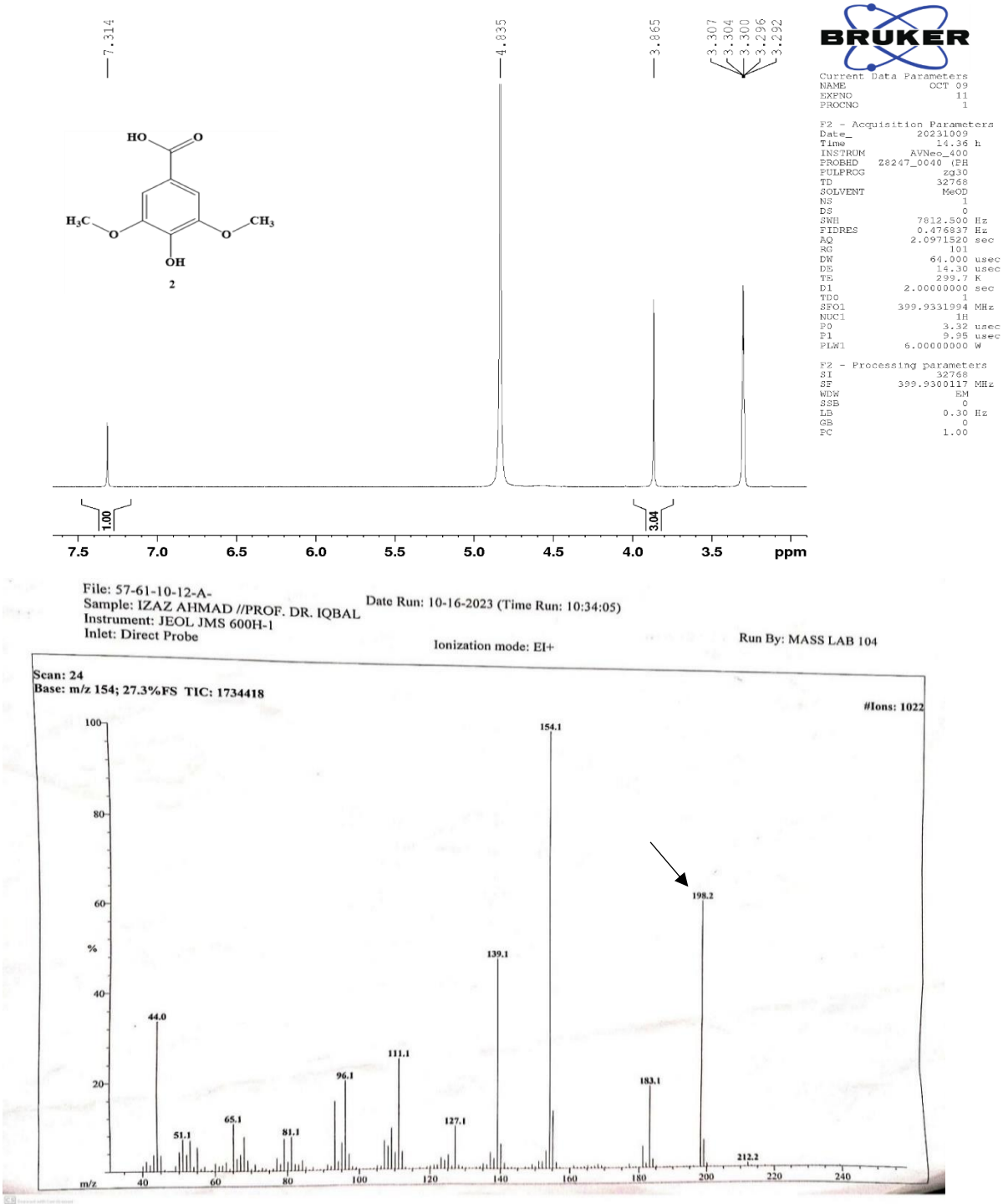
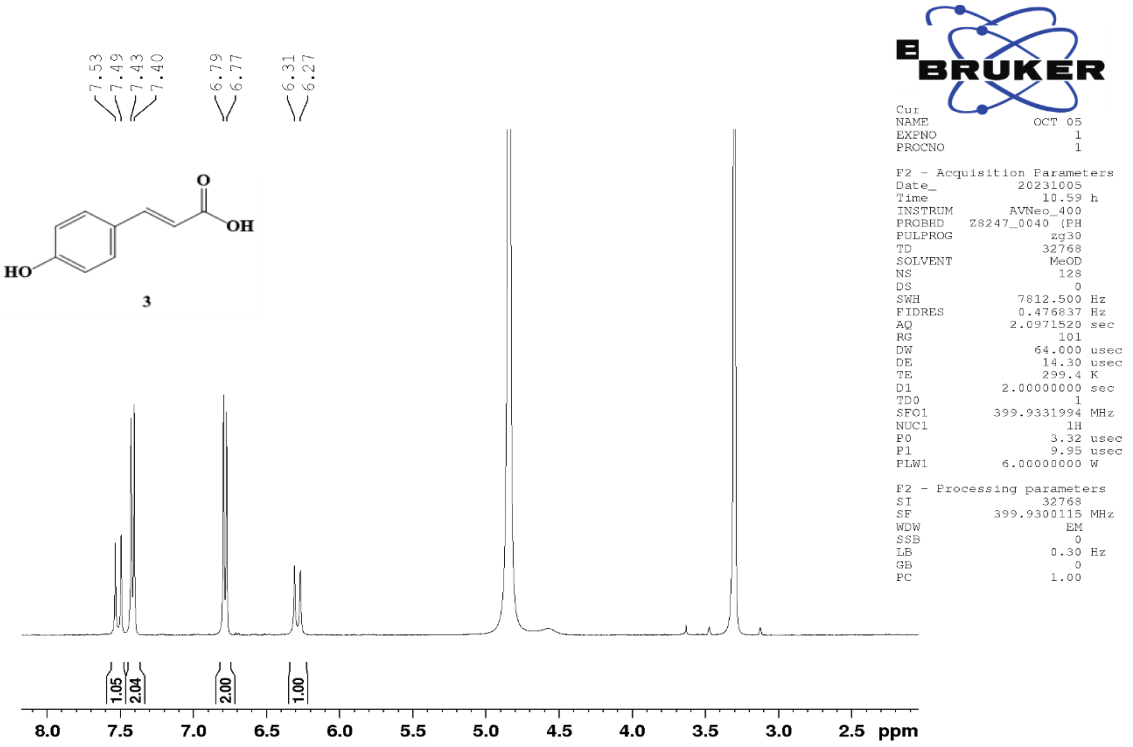


Figure S4 – The ^{1}H-NMR (400 MHz, CD_3OD) and EI-MS $[M]^{+}$ spectra of syringic acid (2)



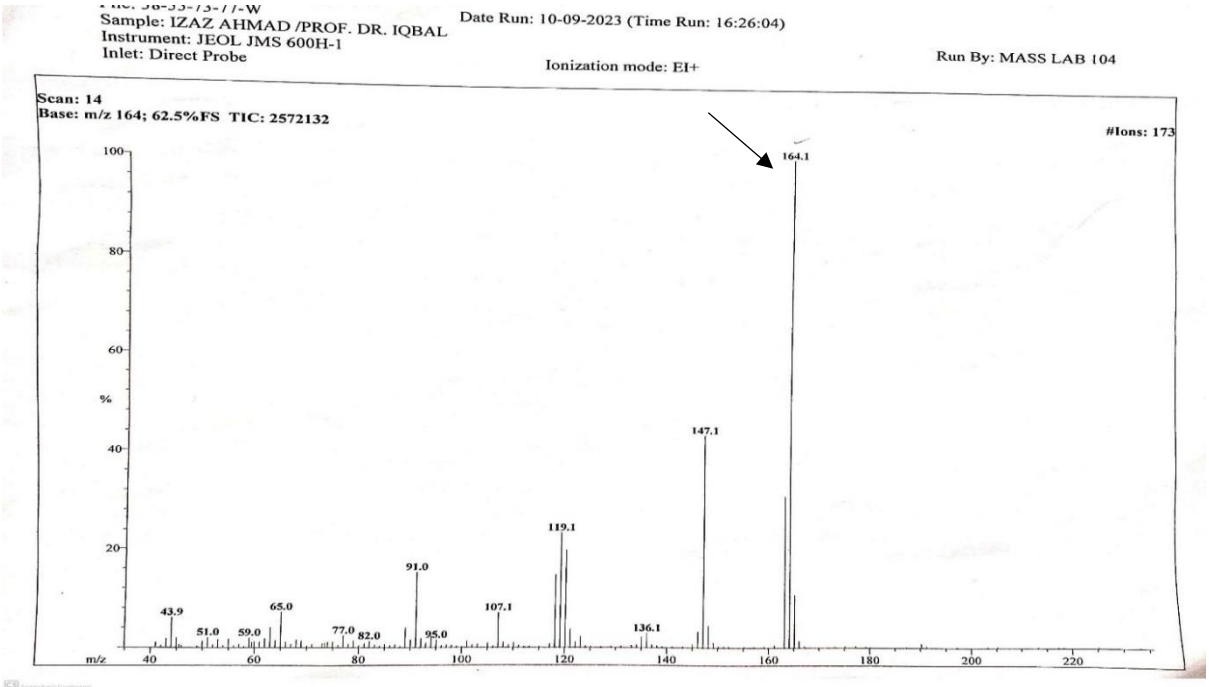
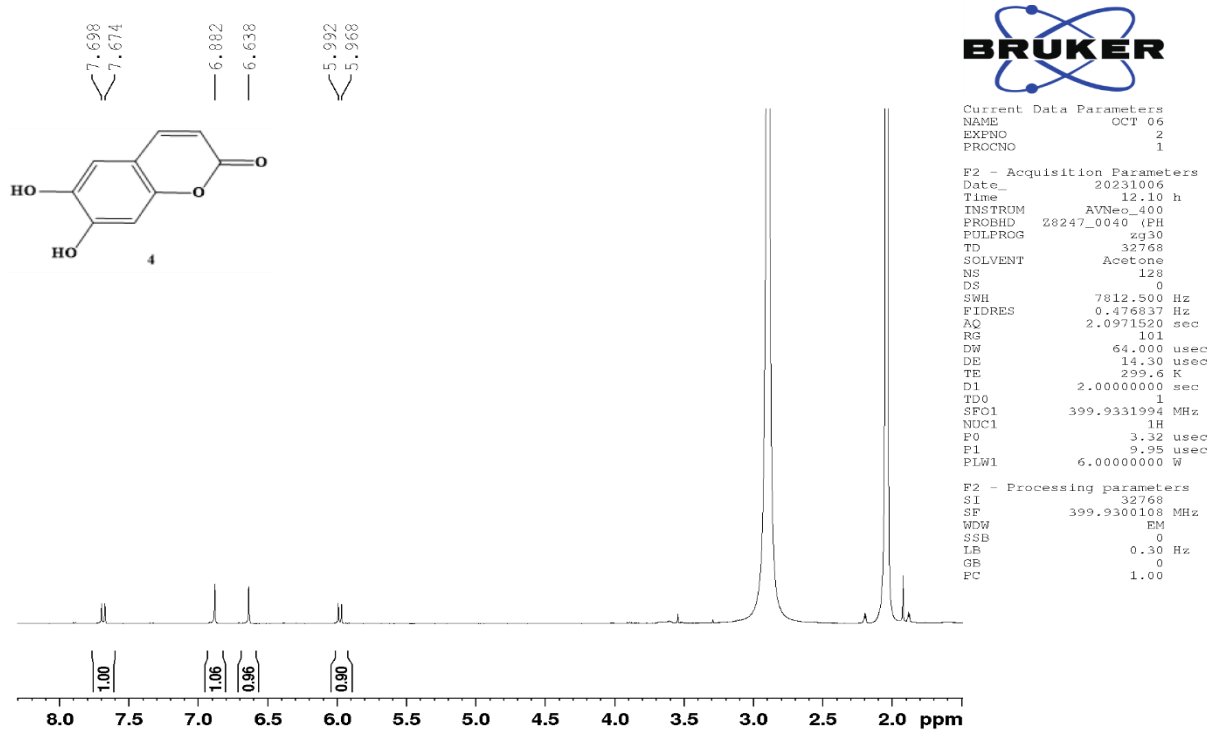


Figure S5 – The ^{1}H-NMR (400 MHz, acetone-d_6) and EI-MS $[M]^{+}$ spectra of *trans-p*-coumaric acid (3)



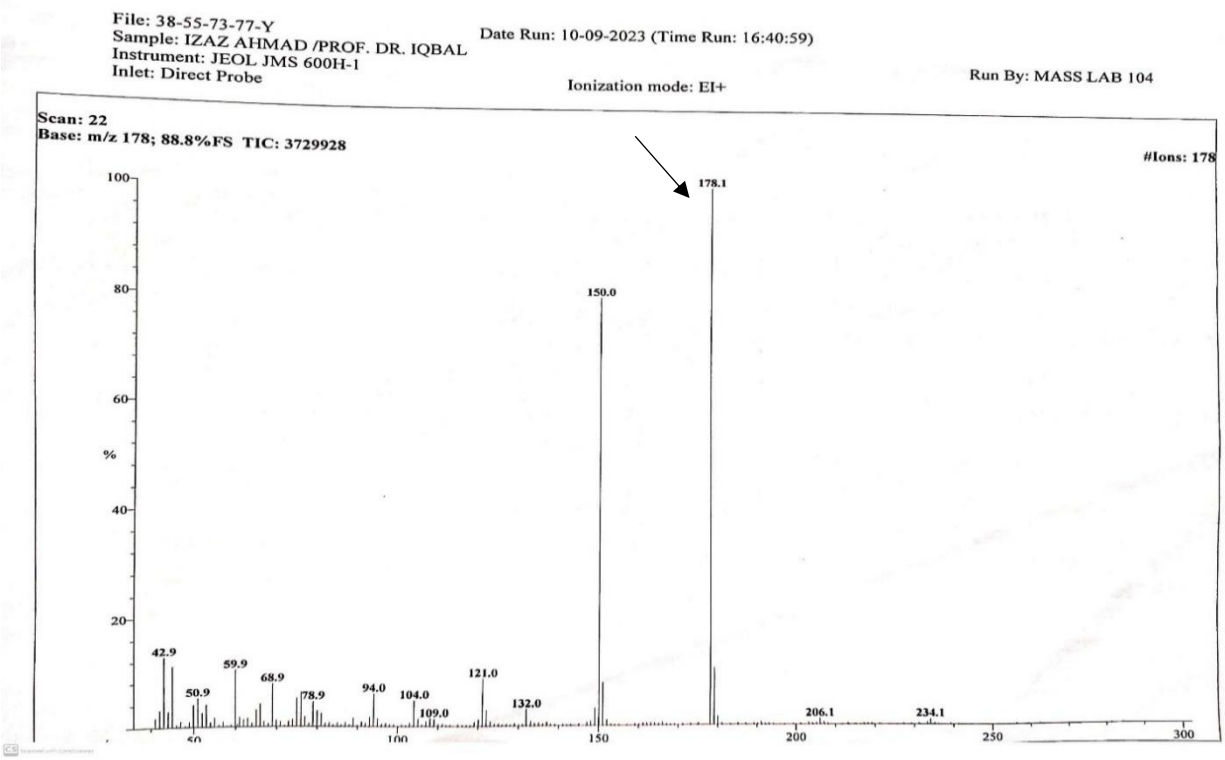
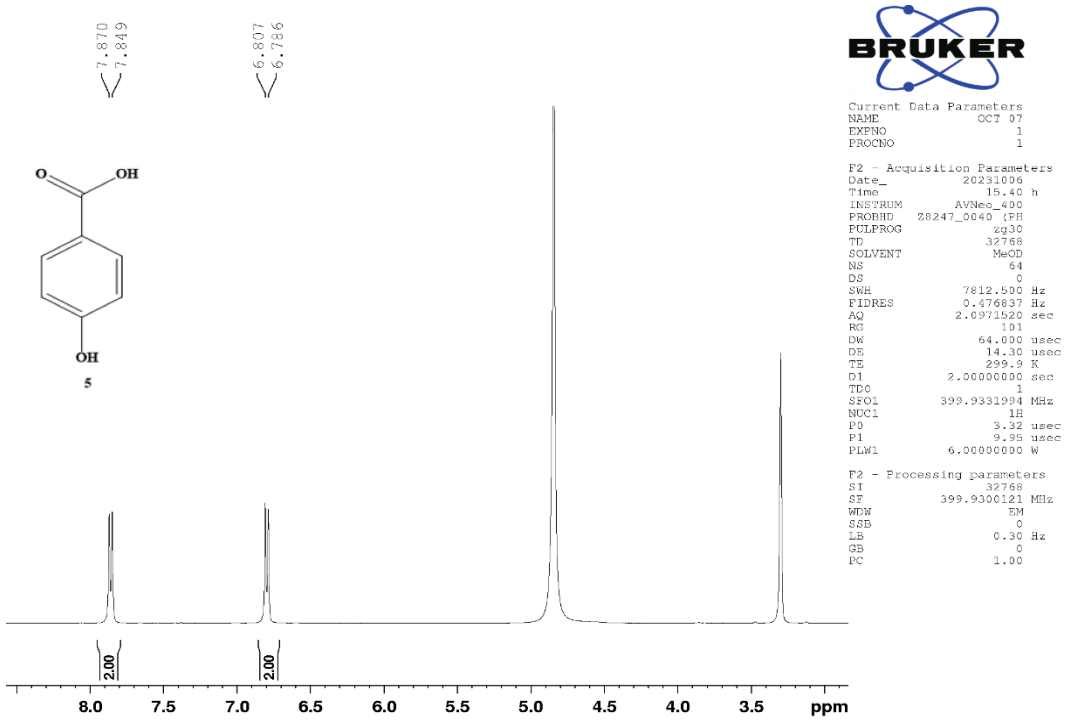


Figure S6 – The ^{1}H-NMR (400 MHz, acetone-d_6) and EI-MS $[M]^{+}$ spectra of esculetin (4)



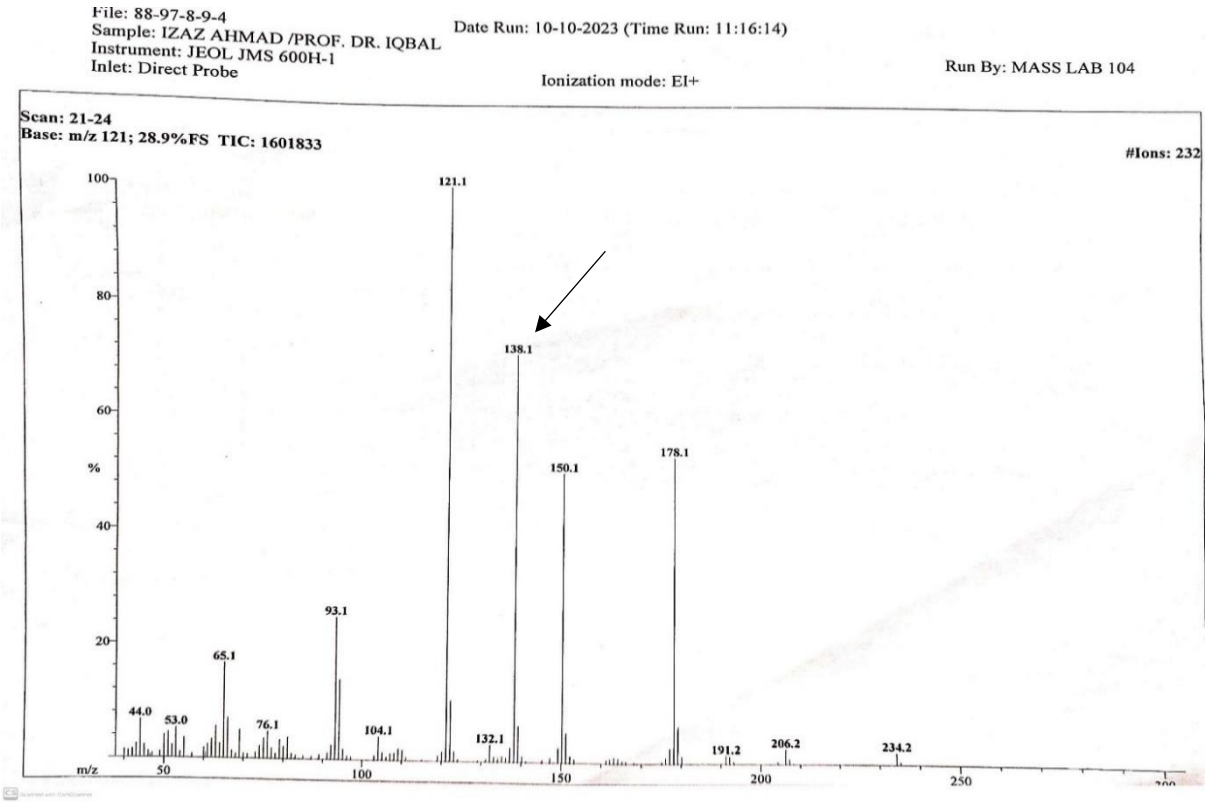
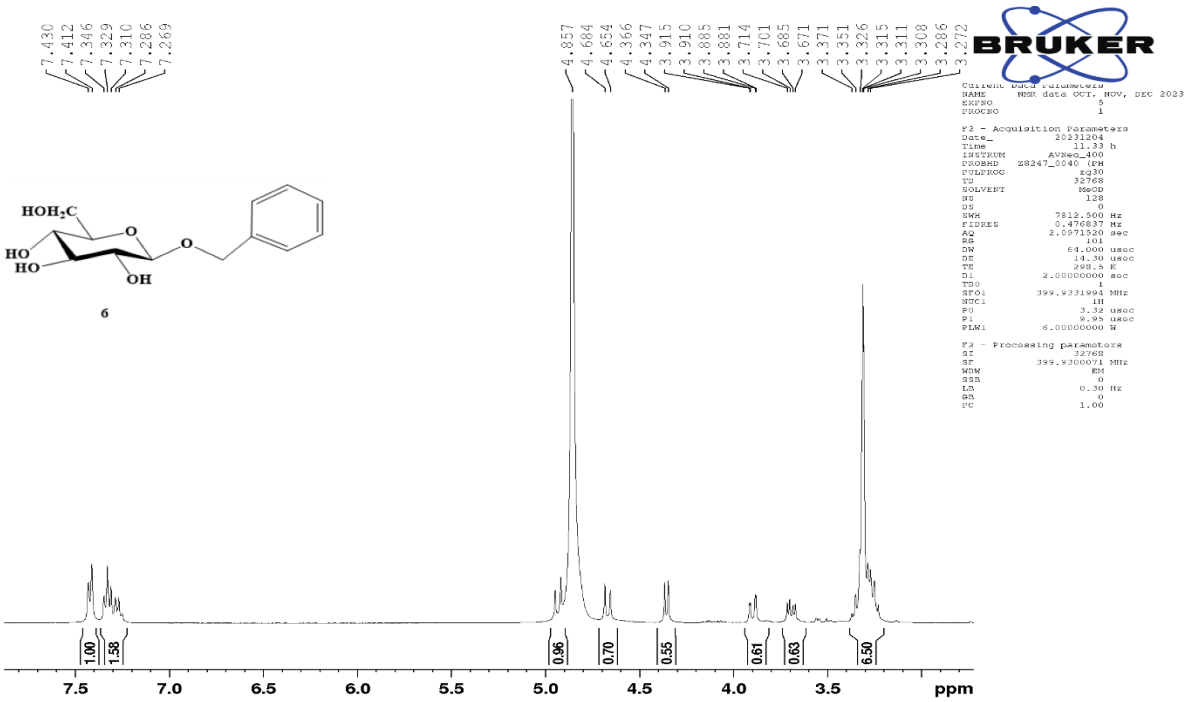


Figure S7 – The ^{1}H-NMR (400 MHz, CD_3OD) and EI-MS $[M]^+$ spectra of *p*-hydroxybenzoic acid (5)



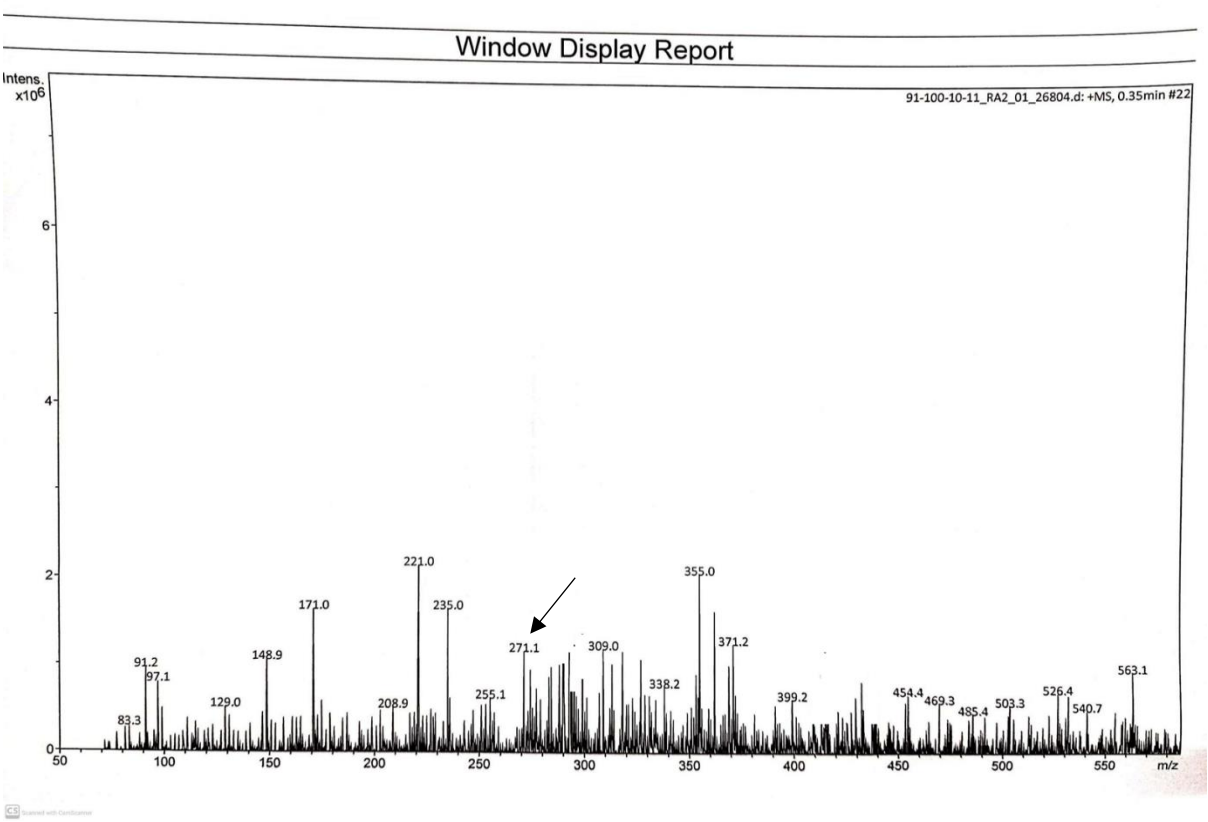
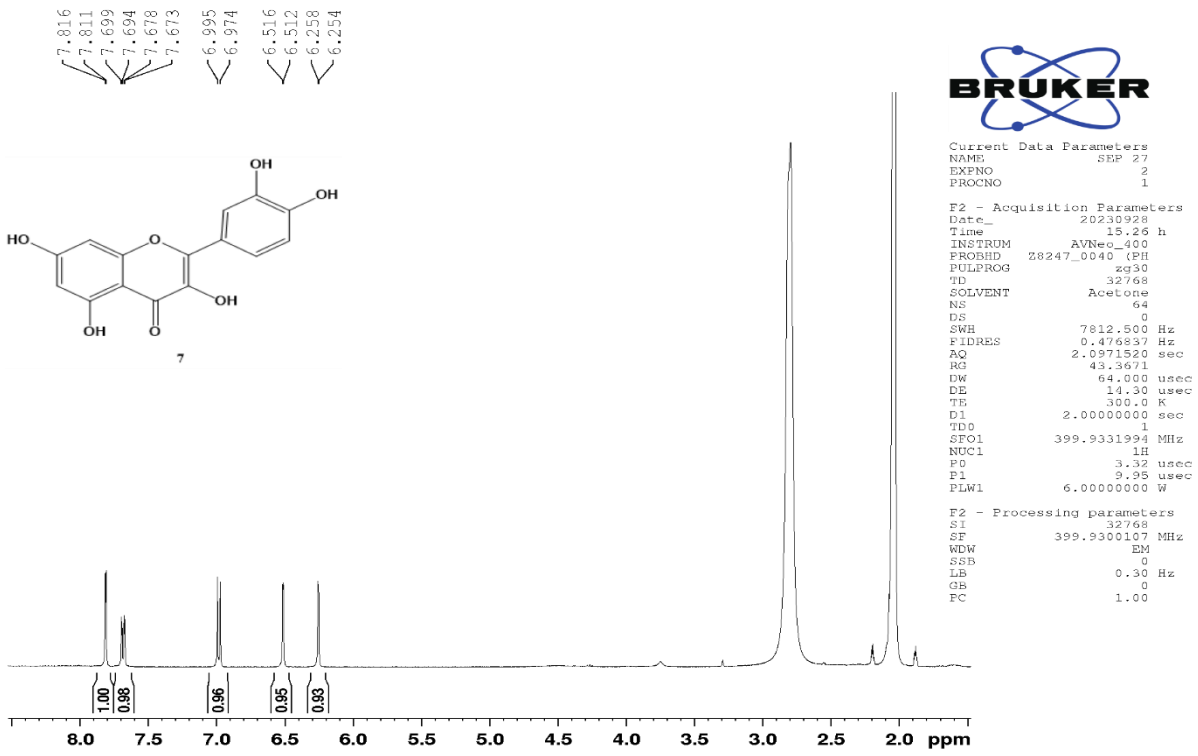


Figure S8 – The ^{1}H-NMR (400 MHz, CD_3OD) and ESI-MS $[M+H]^+$ spectra of benzyl β-D-glucoside (6)



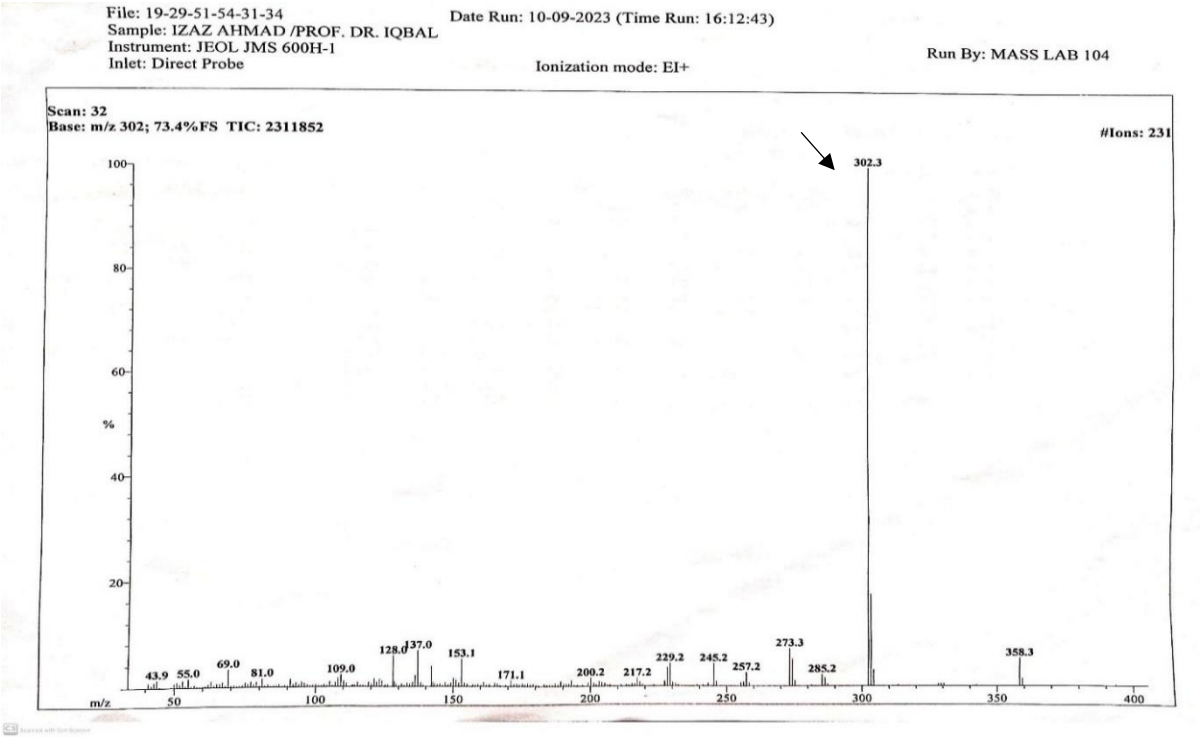


Figure S9 – The ^{1}H-NMR (400 MHz, in CD_3OD) and EI-MS $[M]^+$ spectra of quercetin (7)

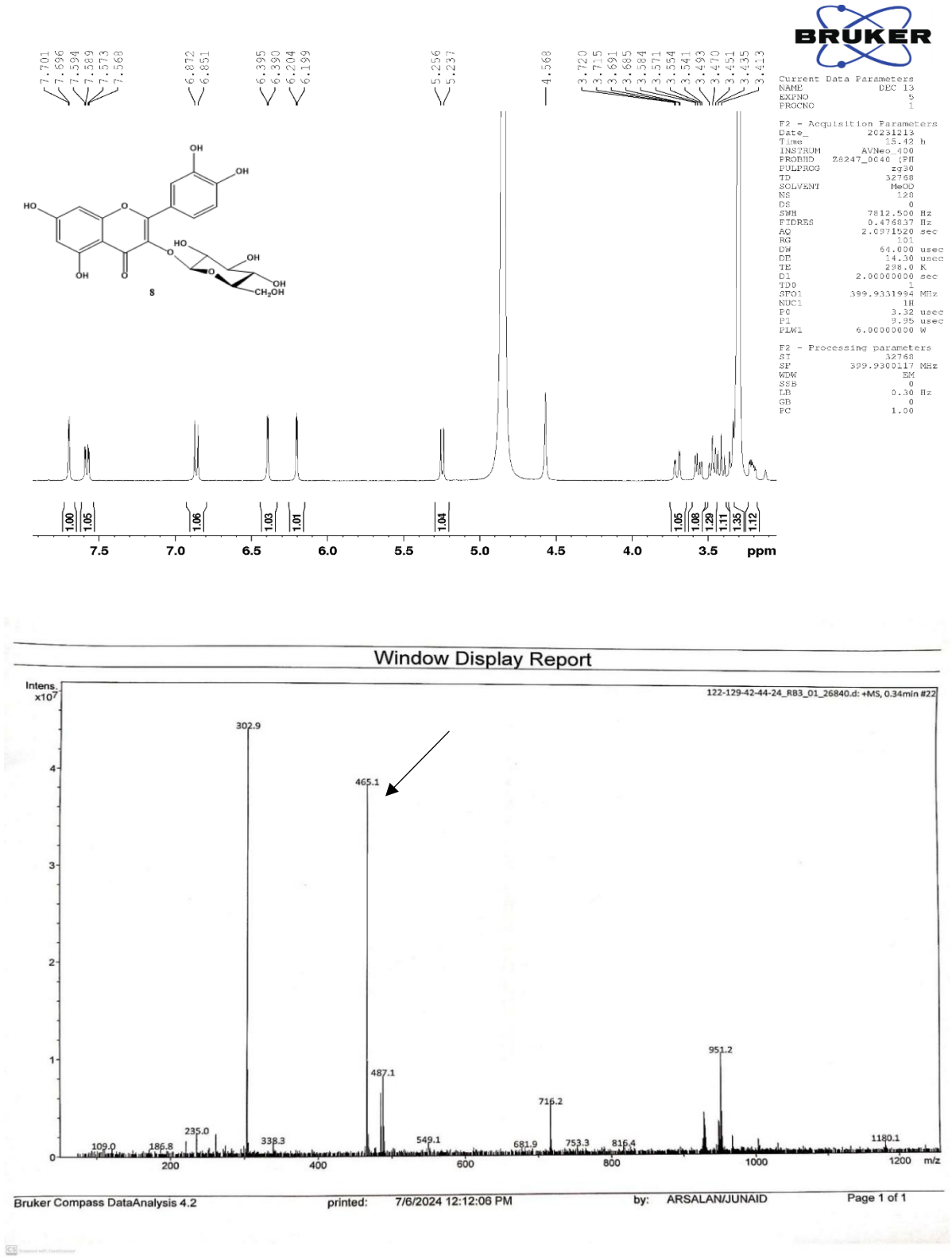
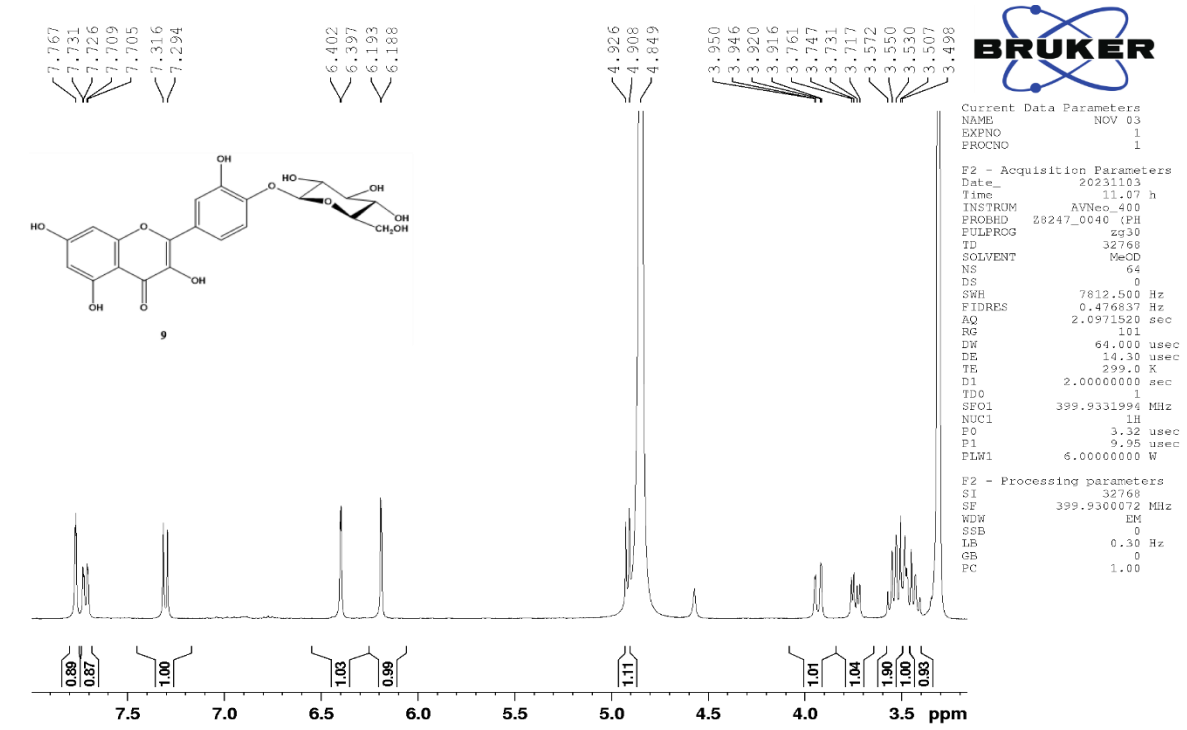


Figure S10 – The ^{1}H-NMR (400 MHz, CD_3OD) and ESI-MS $[M+H]^+$ spectra of quercetin-3-*O*-β-D-glucoside (isoquercitrin; 8)



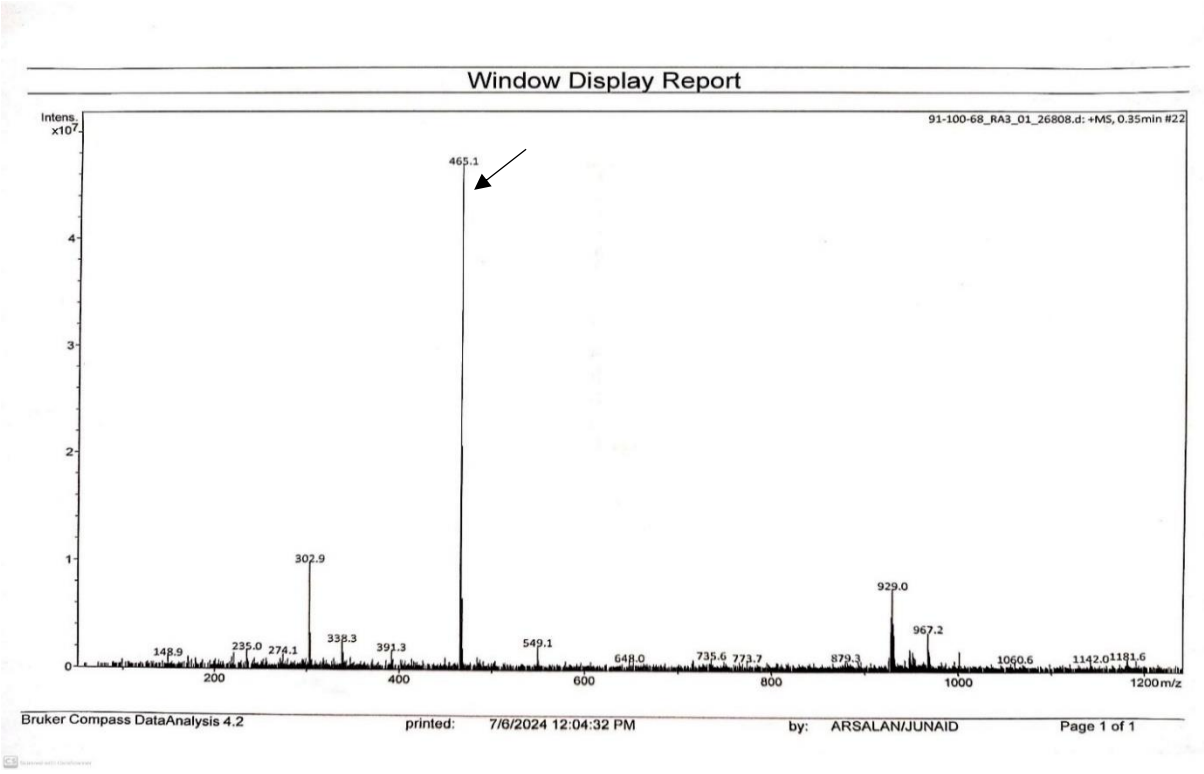


Figure S11 – The ^{1}H-NMR (400 MHz, CD_3OD) and ESI-MS $[M+H]^+$ spectra of quercetin-4′-*O*-glucoside (9)

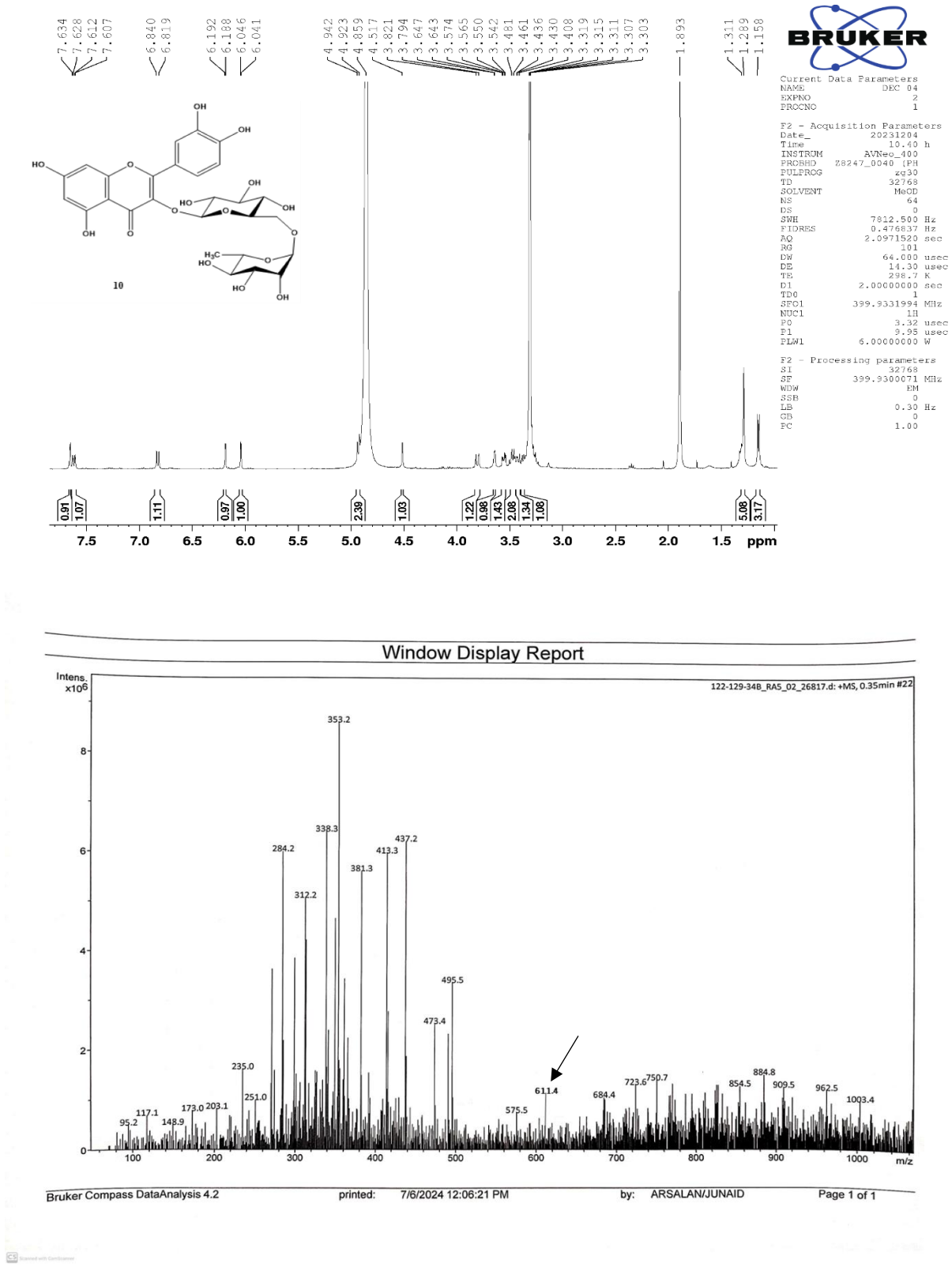


Figure S12 – The ^{1}H-NMR (400 MHz, CD_3OD) and ESI-MS $[M+H]^+$ spectra of quercetin-3-rutinoside (Rutin; 10)

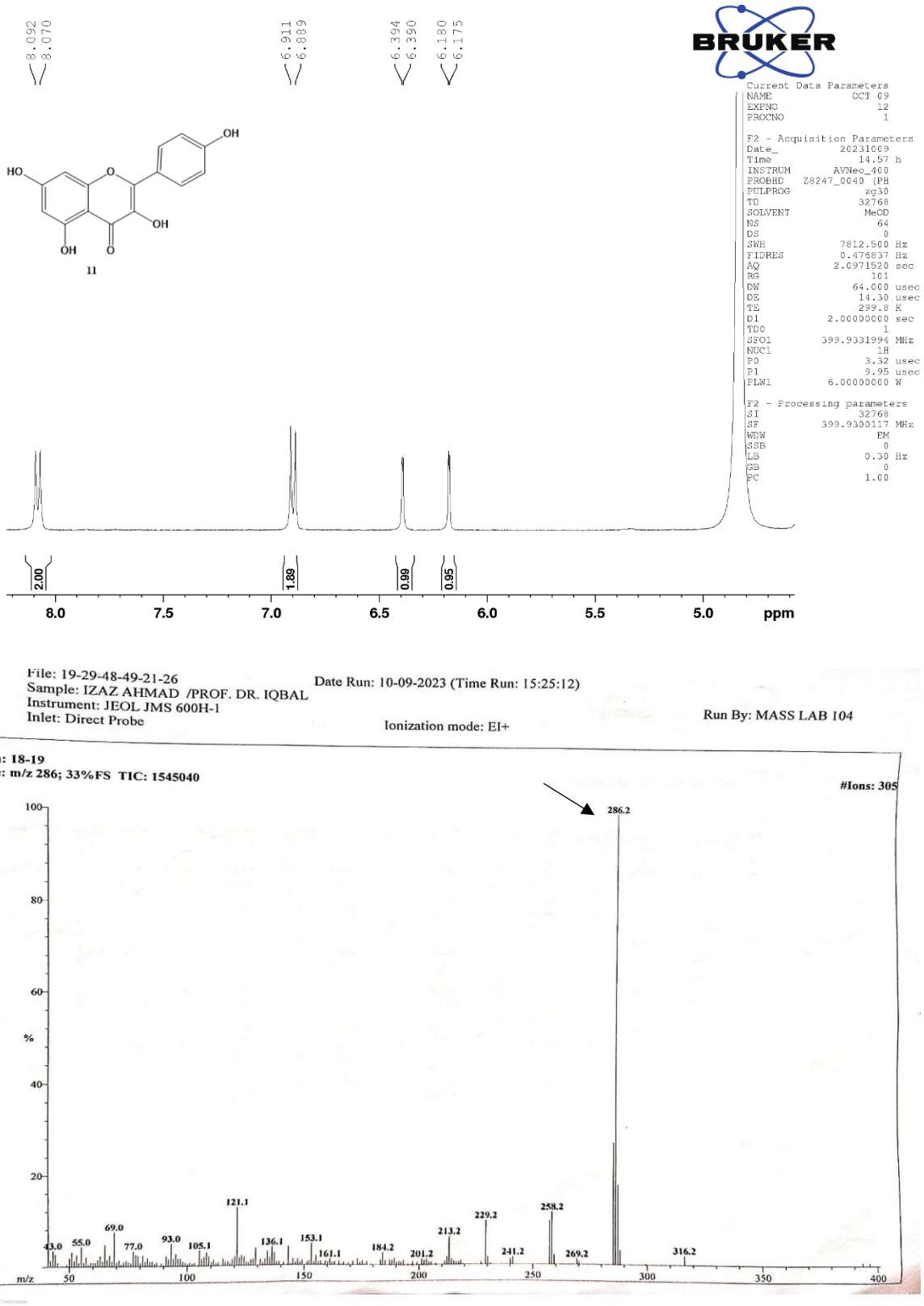
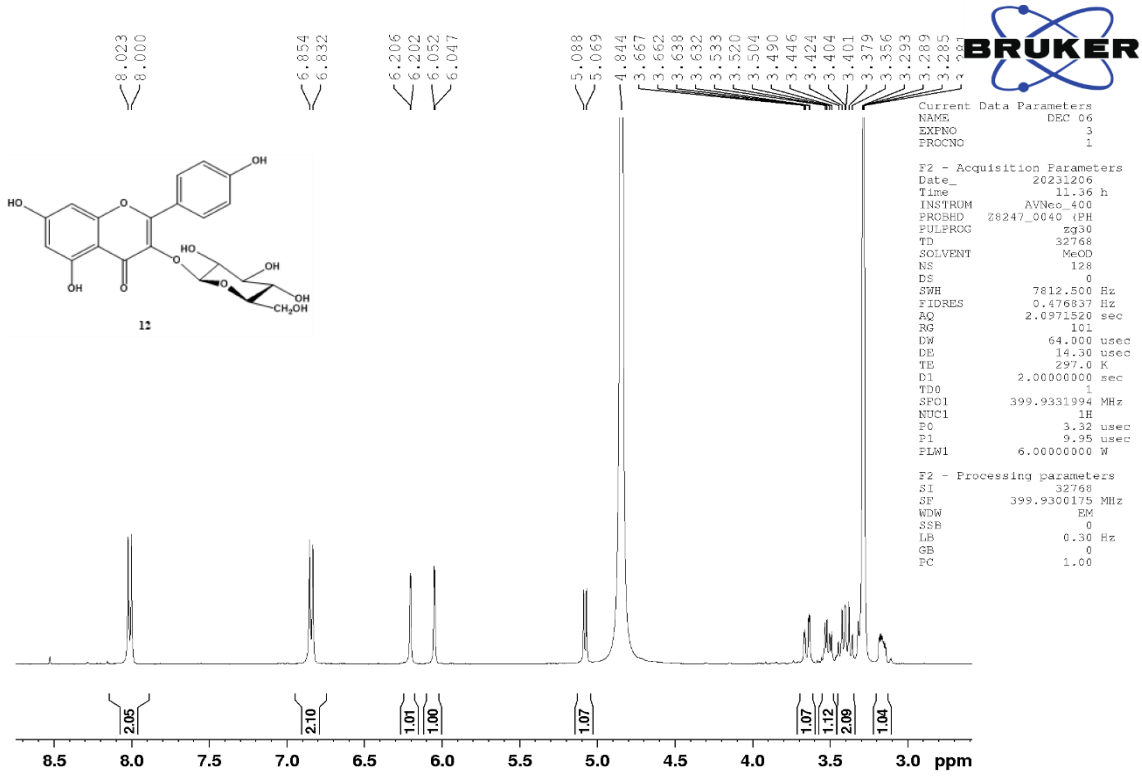


Figure S13 – The ^{1}H-NMR (400 MHz, CD_3OD) and EI-MS $[M]^{+}$ spectra of kaempferol (11)



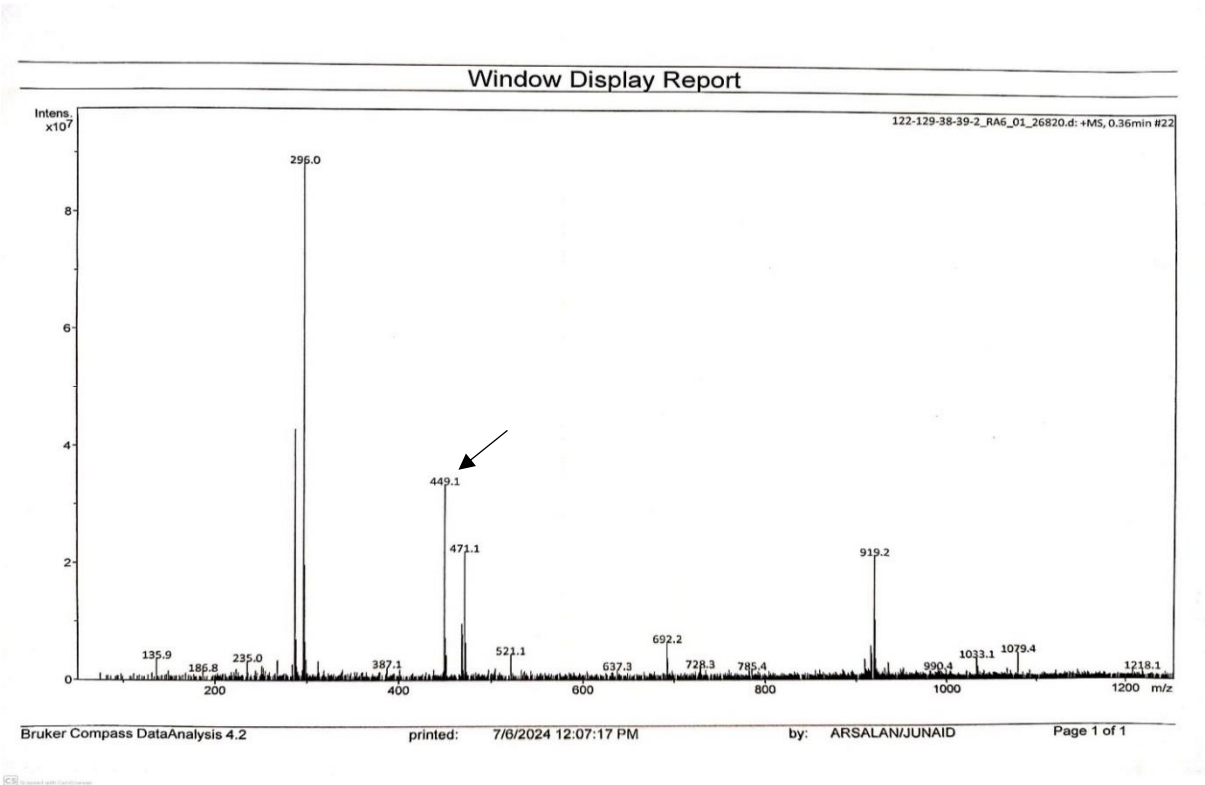
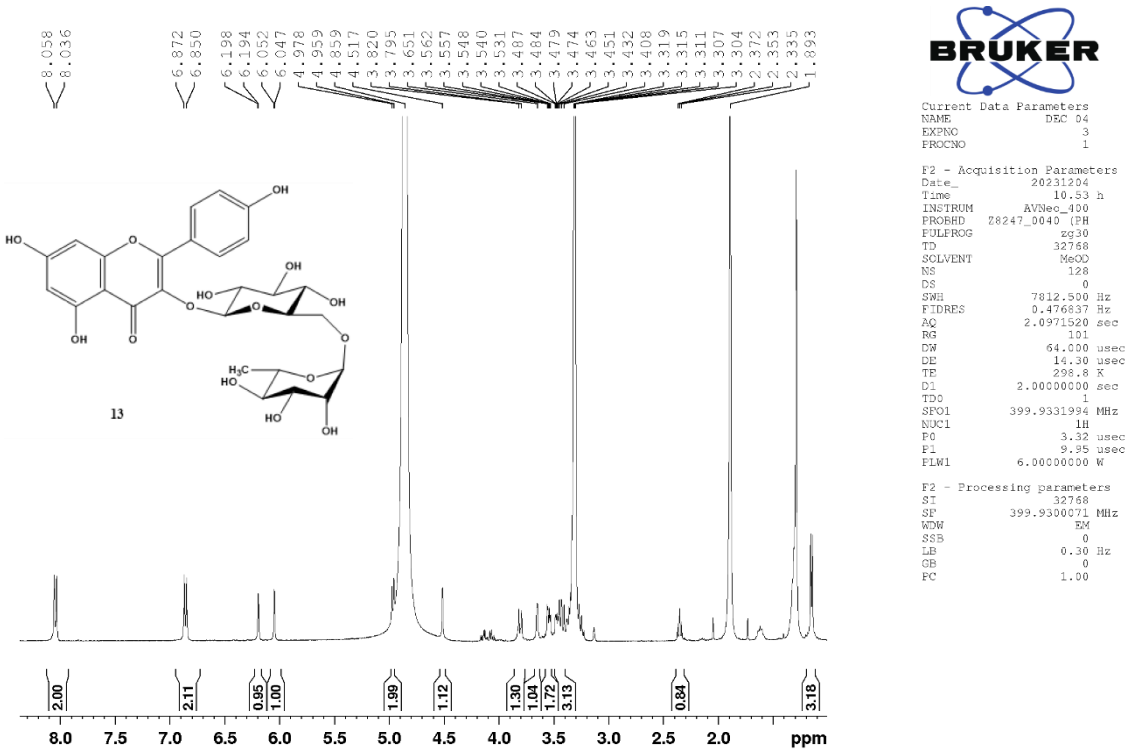


Figure S14 – The ^{1}H-NMR (400 MHz, CD_3OD) and ESI-MS $[M+H]^+$ spectra of Kaempferol 3-*O*-glucoside (Astragalin; 12)



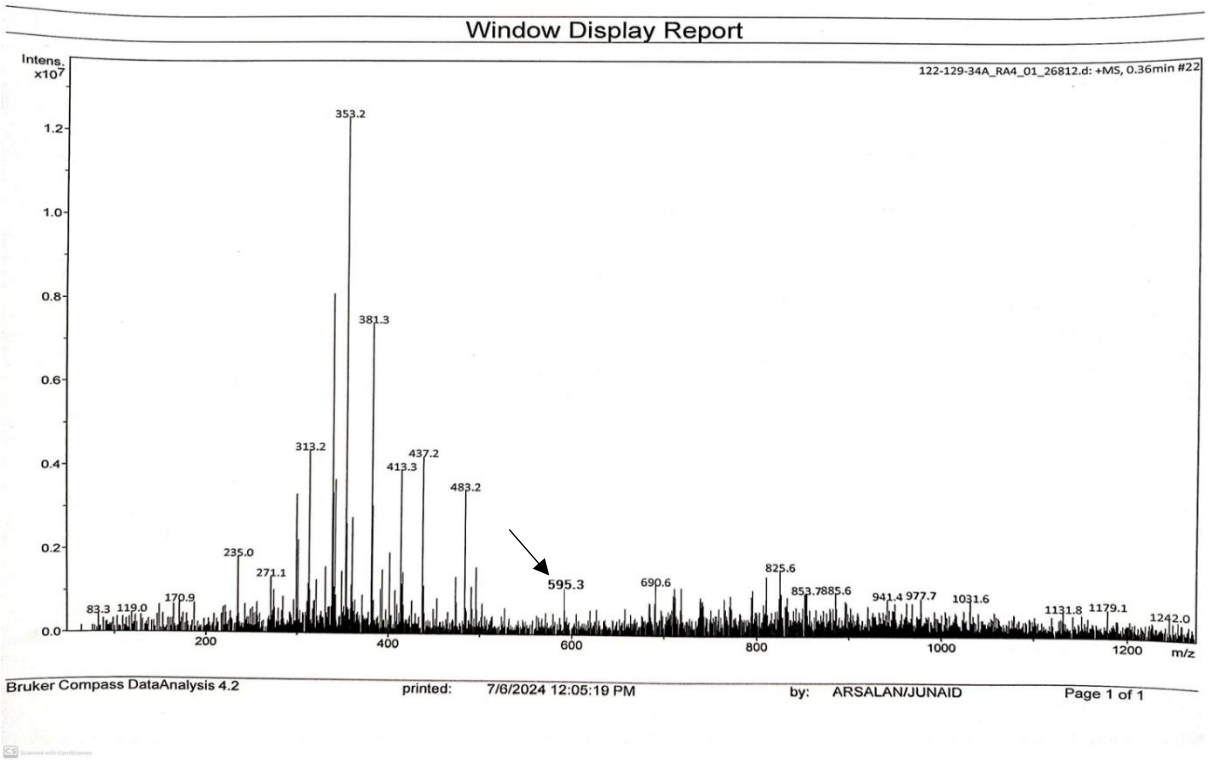
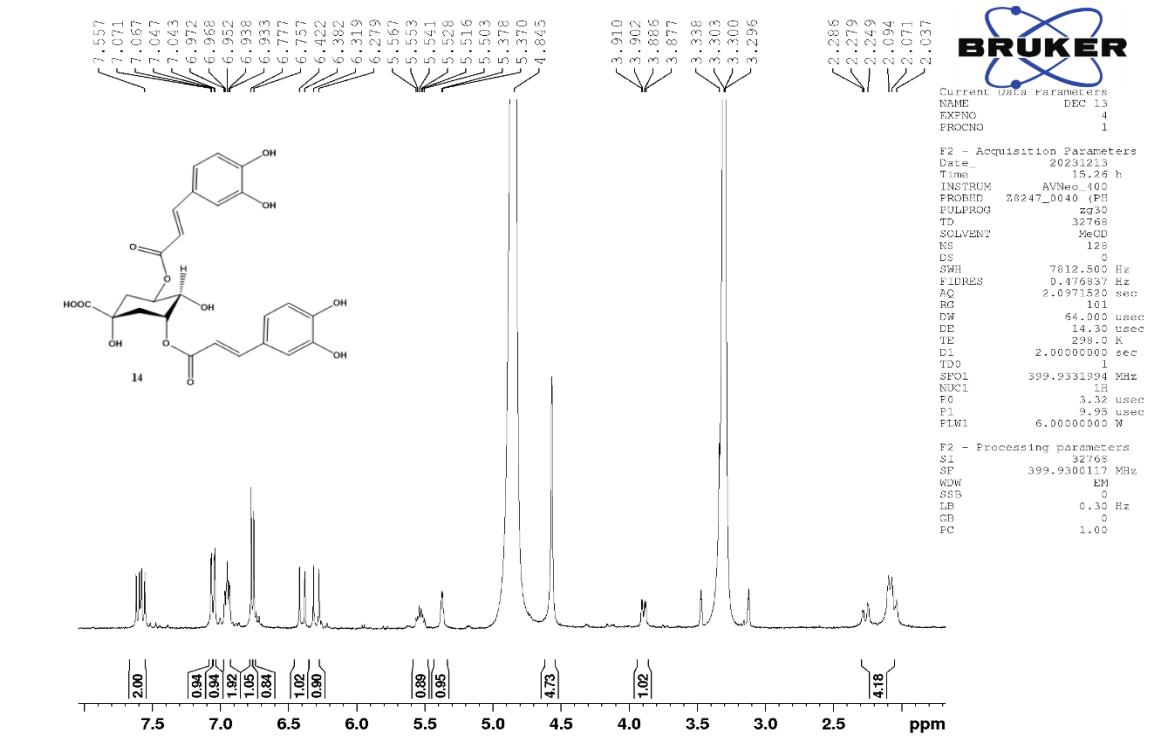


Figure S15 – The ^{1}H-NMR (400 MHz, CD_3OD) and ESI-MS $[M+H]^+$ spectra of kaempferol 3-*O*-rutinoside (13)



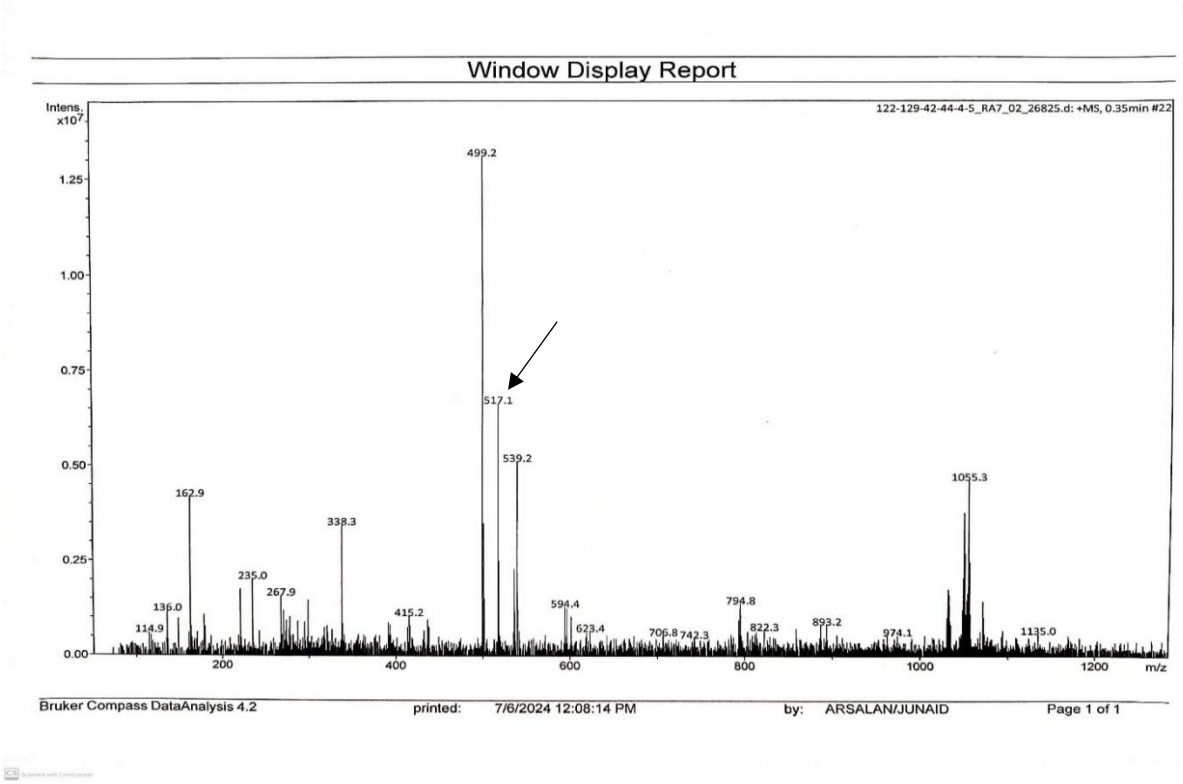


Figure S16 – The ^{1}H-NMR (400 MHz, CD_3OD) and ESI-MS $[M+H]^+$ spectra of (1*S*,3*R*,4*R*,5*R*)-3,5-di-*O*-caffeoylquinic acid (14)

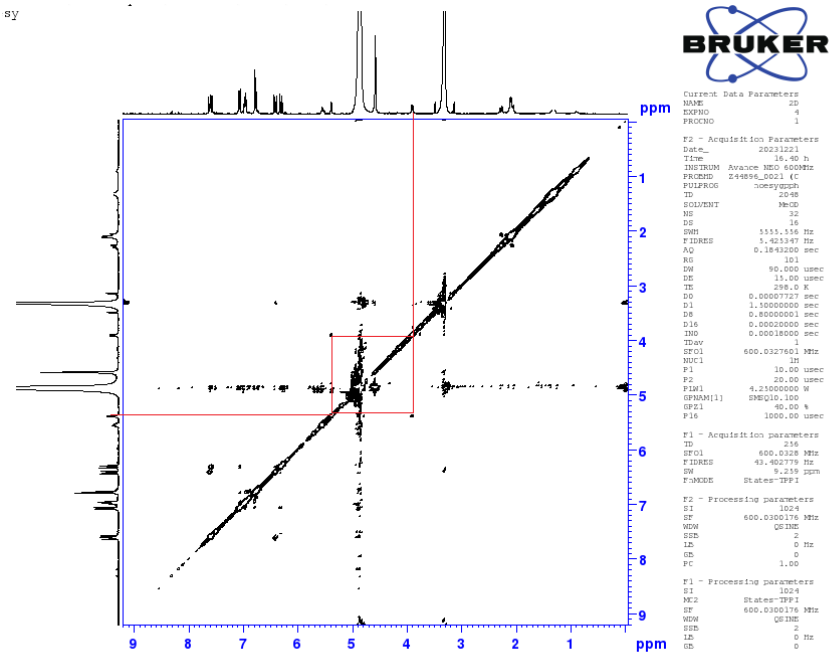
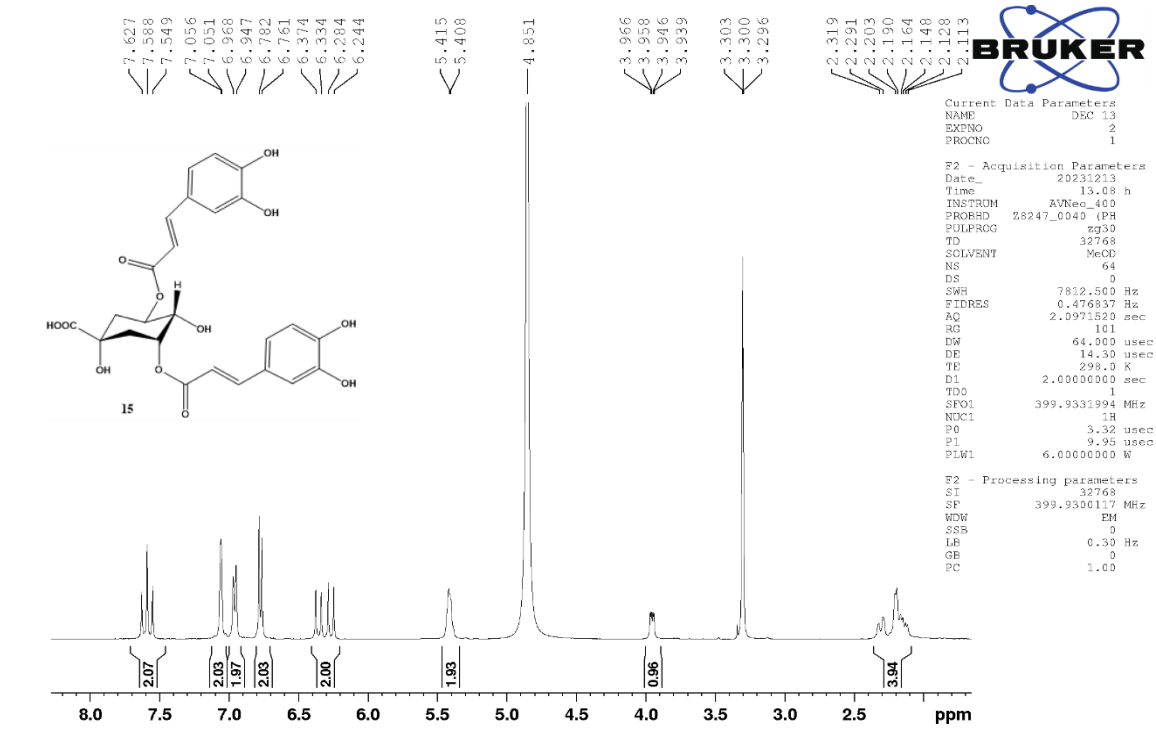


Figure S17– The NOESY spectrum of (1*S*,3*R*,4*R*,5*R*)-3,5-di-*O*-caffeoylquinic acid (14)



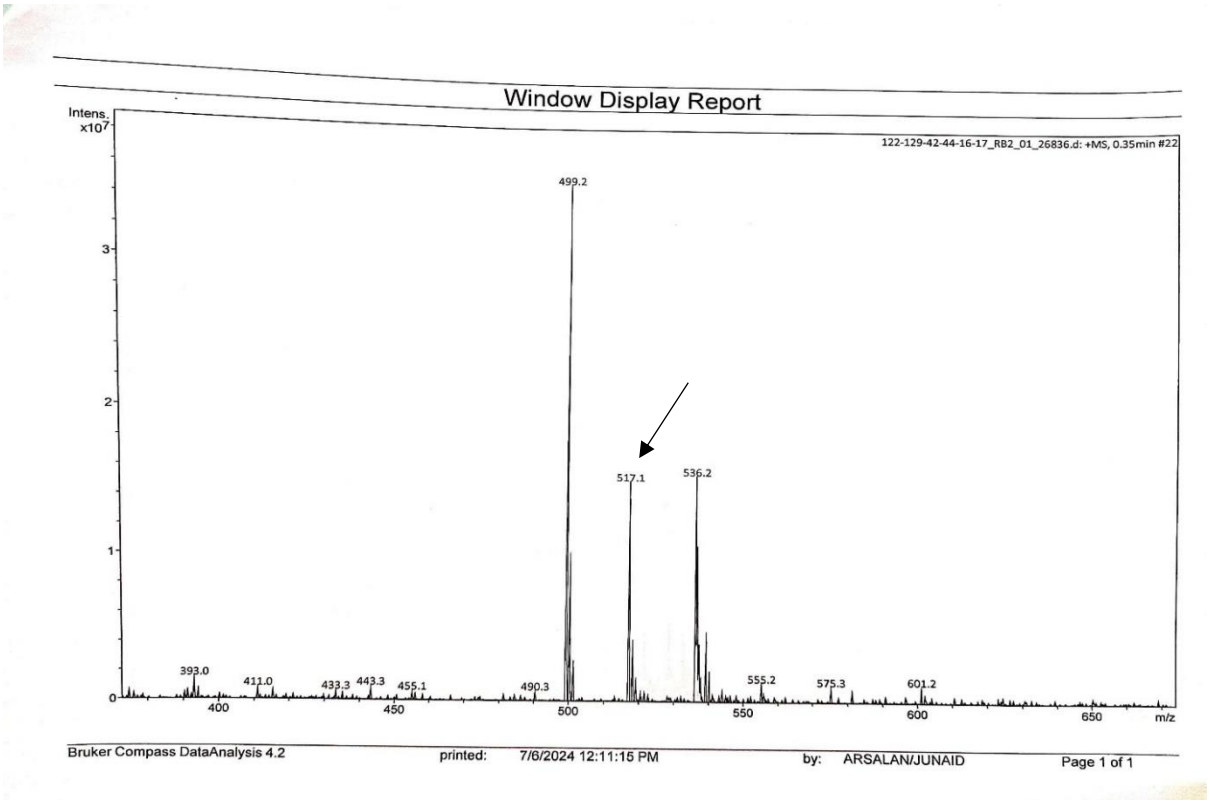


Figure S18 – The ^{1}H-NMR (400 MHz, CD_3OD) and ESI-MS $[M+H]^+$ spectra of (1*S*,3*R*,4*S*,5*R*)-3,5-di-*O*-caffeoylquinic acid (15)

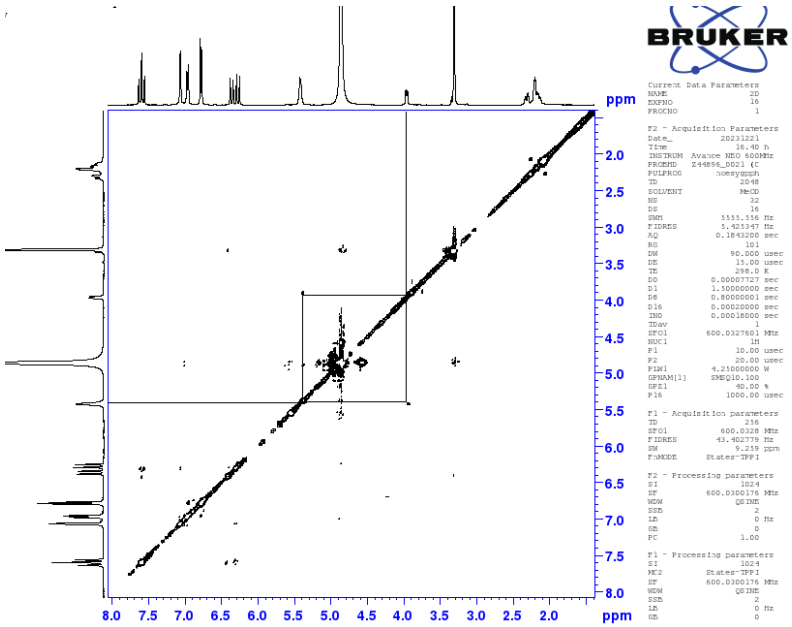


Figure S19 – The NOESY spectrum of (1*S*,3*R*,4*S*,5*R*)-3,5-di-*O*-caffeoylquinic acid (15)

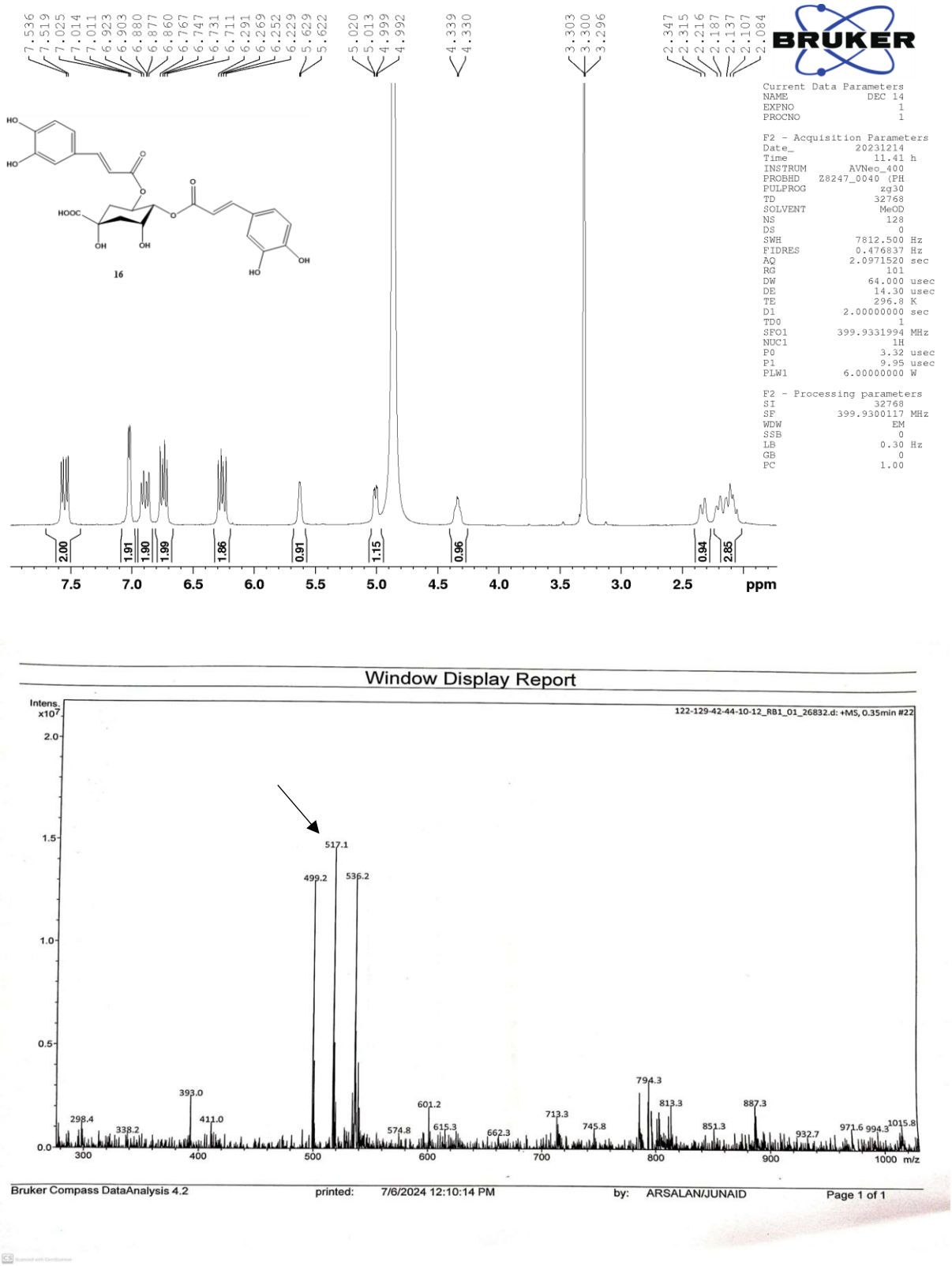
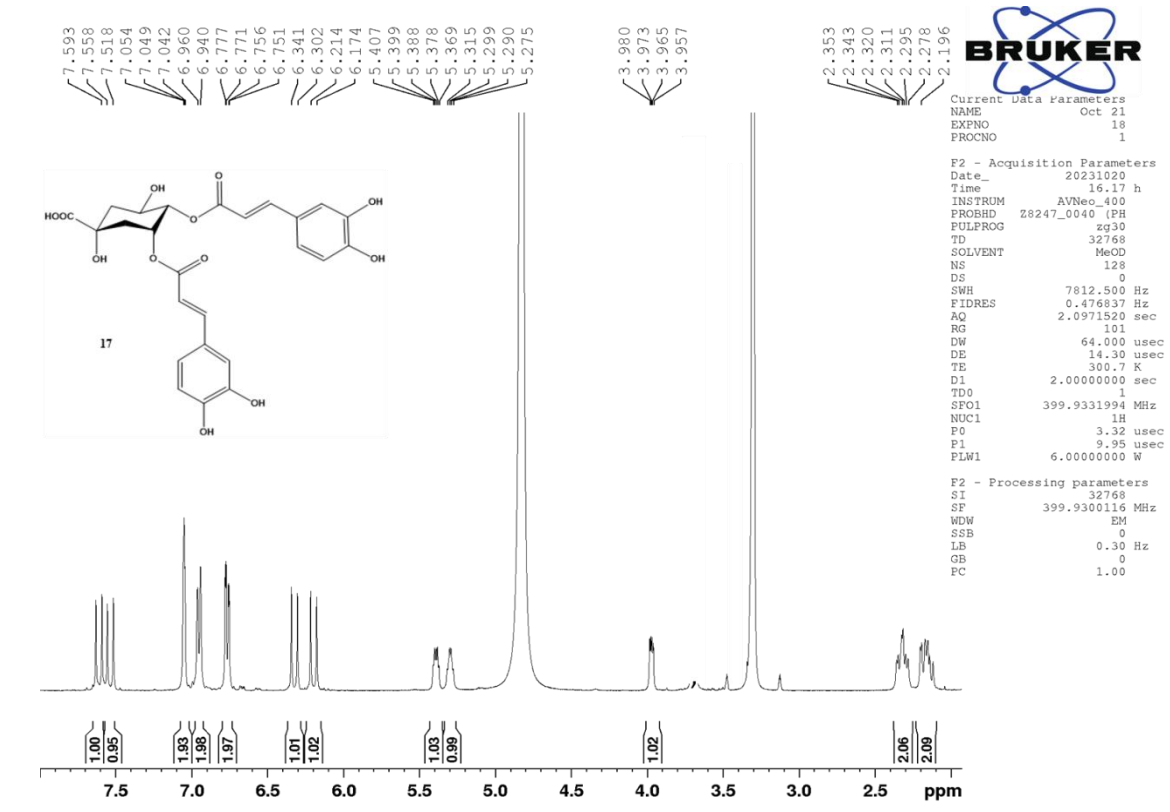


Figure S20 – The ^{1}H-NMR (400 MHz, CD_3OD) and ESI-MS $[M+H]^+$ spectra of 3,4-di-*O*-caffeoylquinic acid (16)



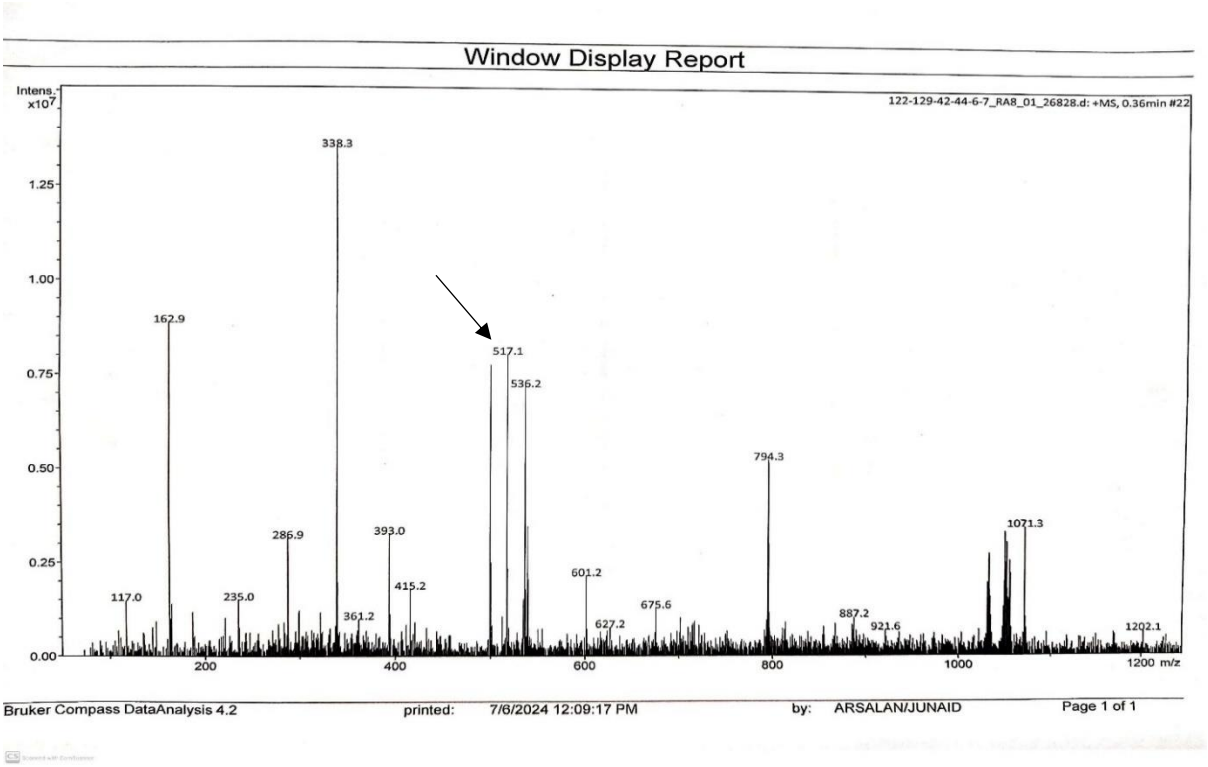


Figure S21– The ^{1}H-NMR (400 MHz, CD_3OD) and ESI-MS $[M+H]^+$ spectra of 4,5-di-*O*-caffeoylquinic acid (17)

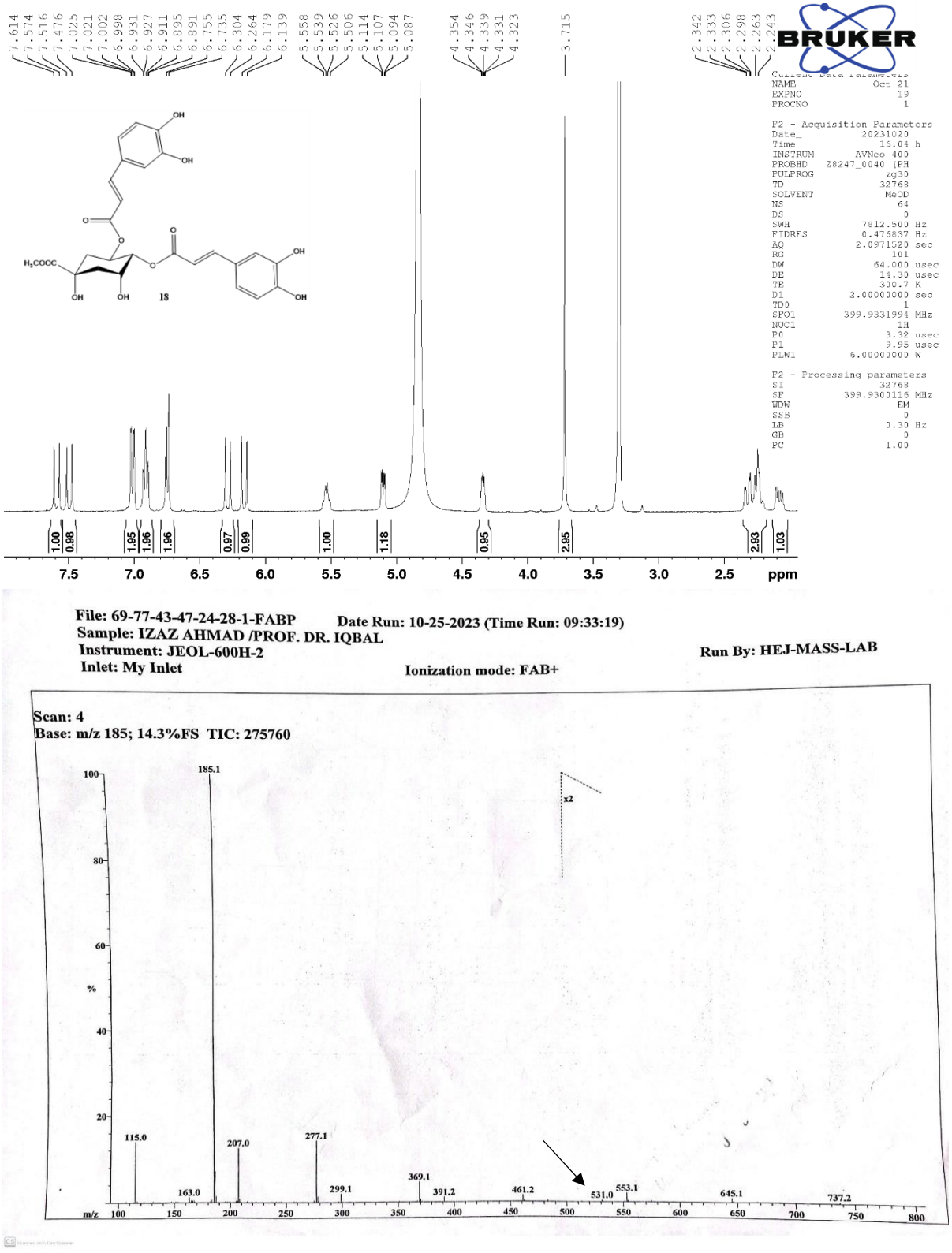


Figure S22 – The ^{1}H-NMR (400 MHz, CD_3OD) and FAB-MS $[M+H]^+$ spectra of 3,4-di-*O*-caffeoylquinic acid methyl ester (18)

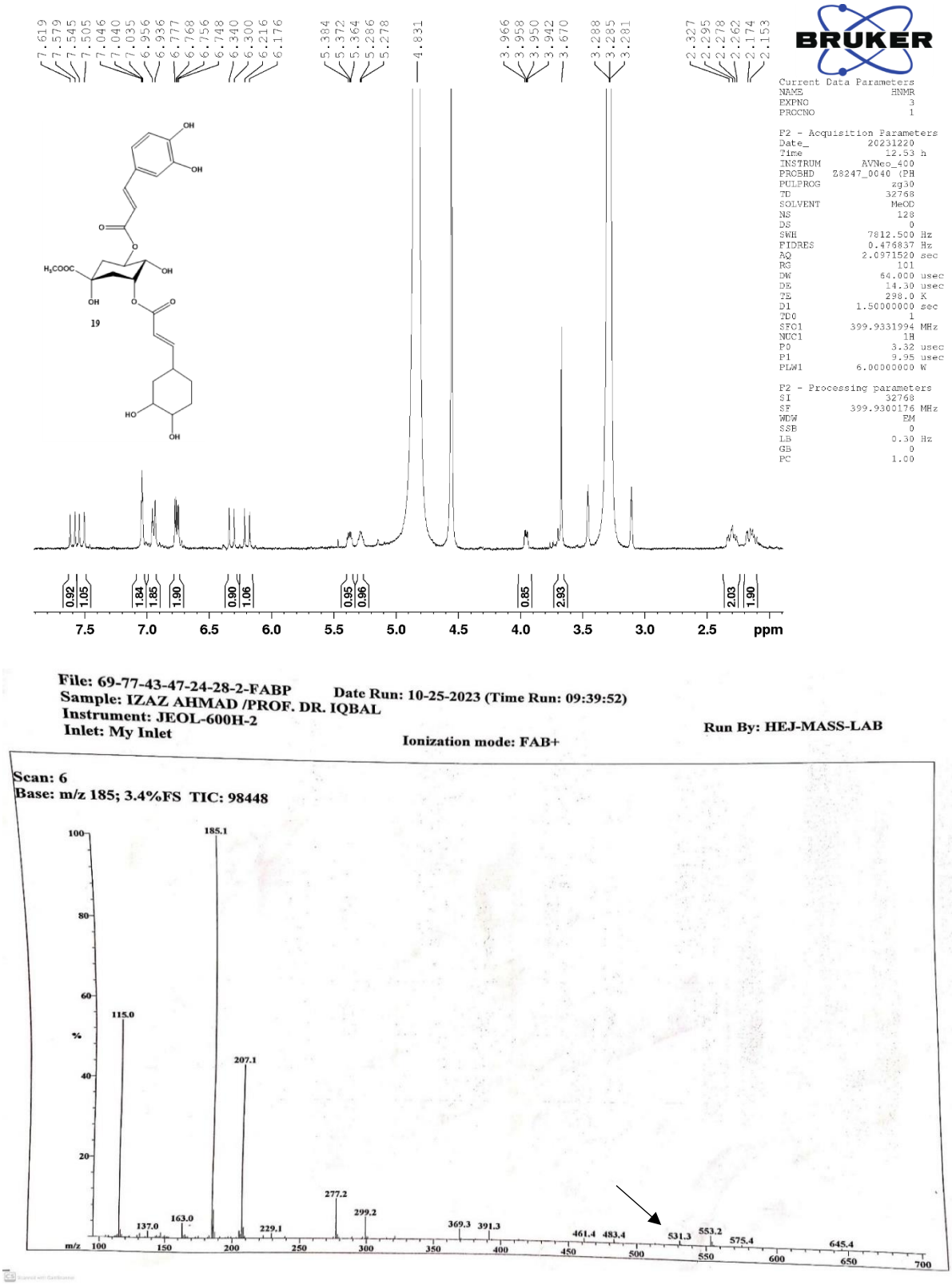


Figure S23 – The ^{1}H-NMR (400 MHz, CD_3OD) and FAB-MS $[M+H]^+$ spectra of 3,5-di-*O*-caffeoylquinic acid methyl ester (19)

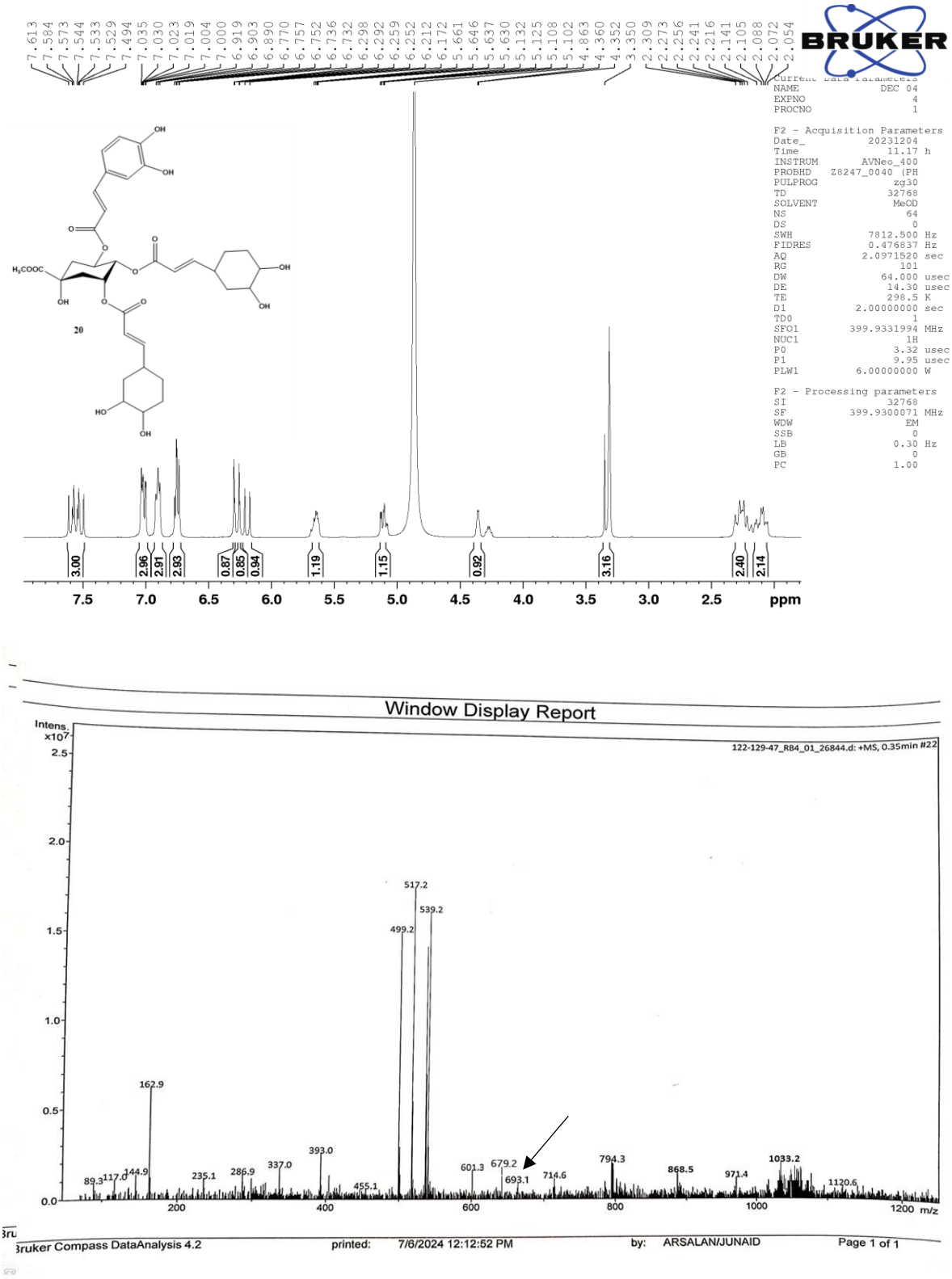


Figure S24 – The ^{1}H-NMR (400 MHz, CD_3OD) and ESI-MS $[M+H]^+$ spectra of 3,4,5-tri-*O*-caffeoylquinic acid methyl ester (20)

Appendix B

Spectroscopic, mass spectrometric, and chromatographic data of biotransformation metabolites

Figures S25–S47 present the spectroscopic, spectrometric, and chromatographic characterization of metabolites obtained through microbial biotransformation, including NMR spectra, EI-MS, ESI-MS/HRMS evidence, and HPLC chromatograms used for structural elucidation and purity assessmen

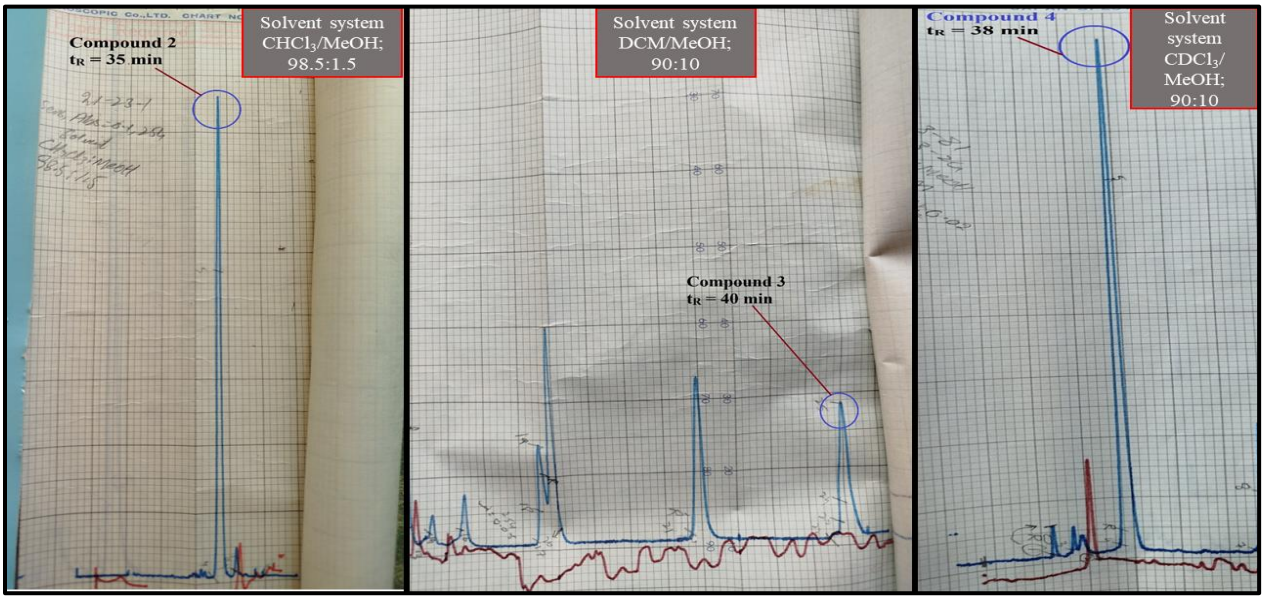


Figure S25 – HPLC (normal phase) chromatogram of metabolite 2, 3 and 4

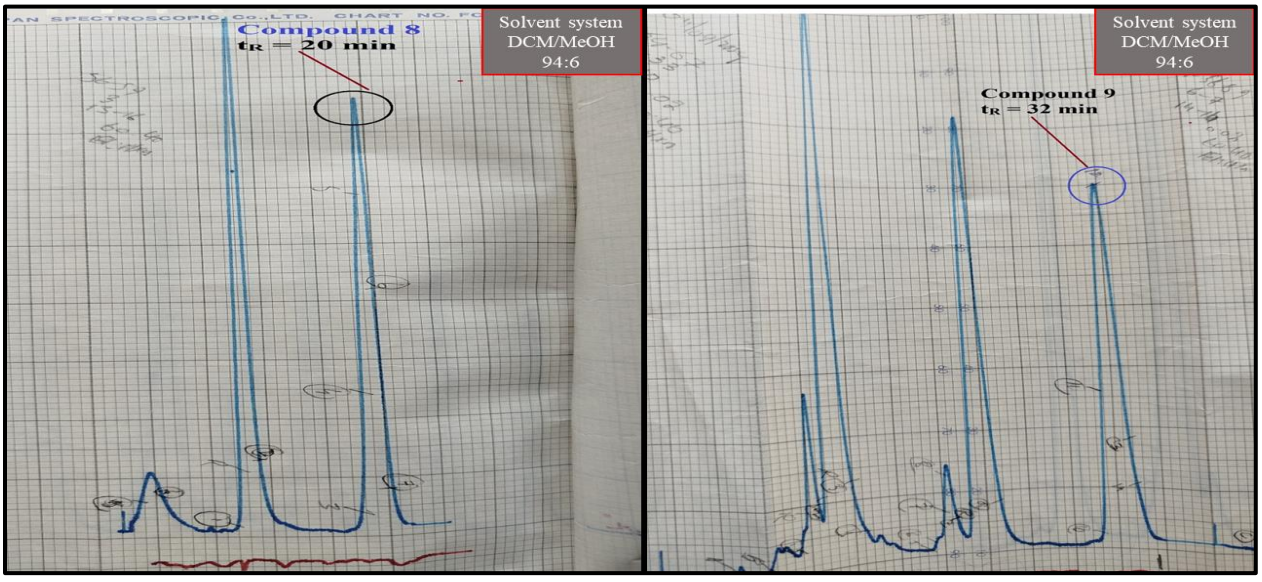


Figure S26 – HPLC (normal phase) chromatogram of metabolite 8 and 9

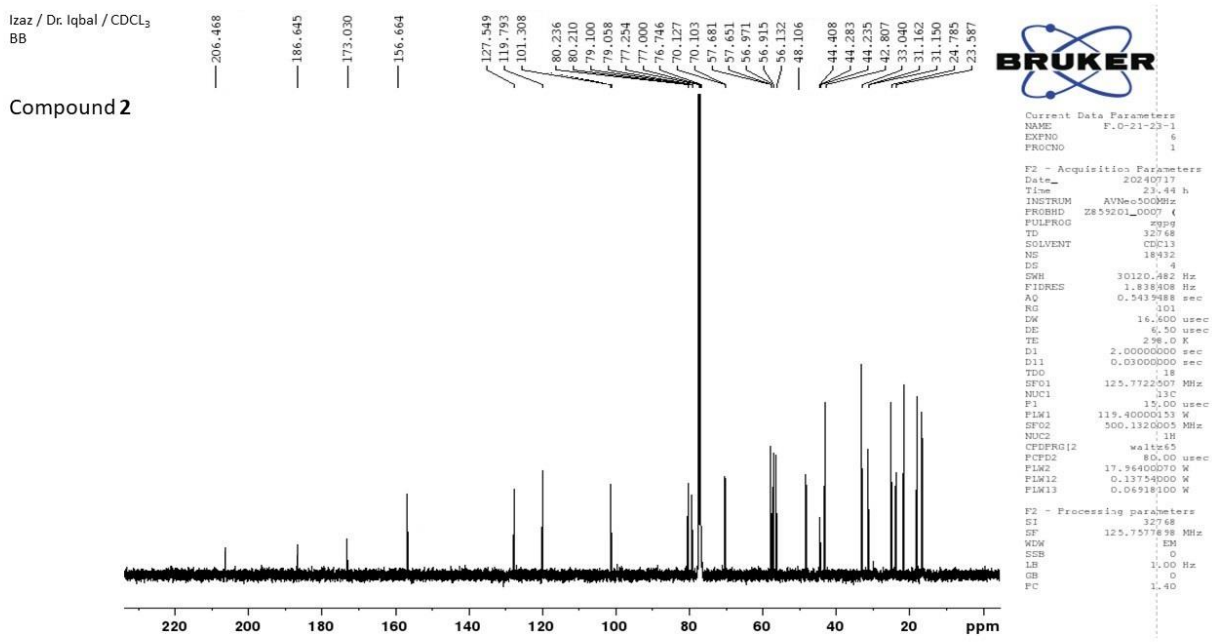


Figure S27 – ^{13}C-NMR (Broad-band decoupled) Spectrum of metabolite 2

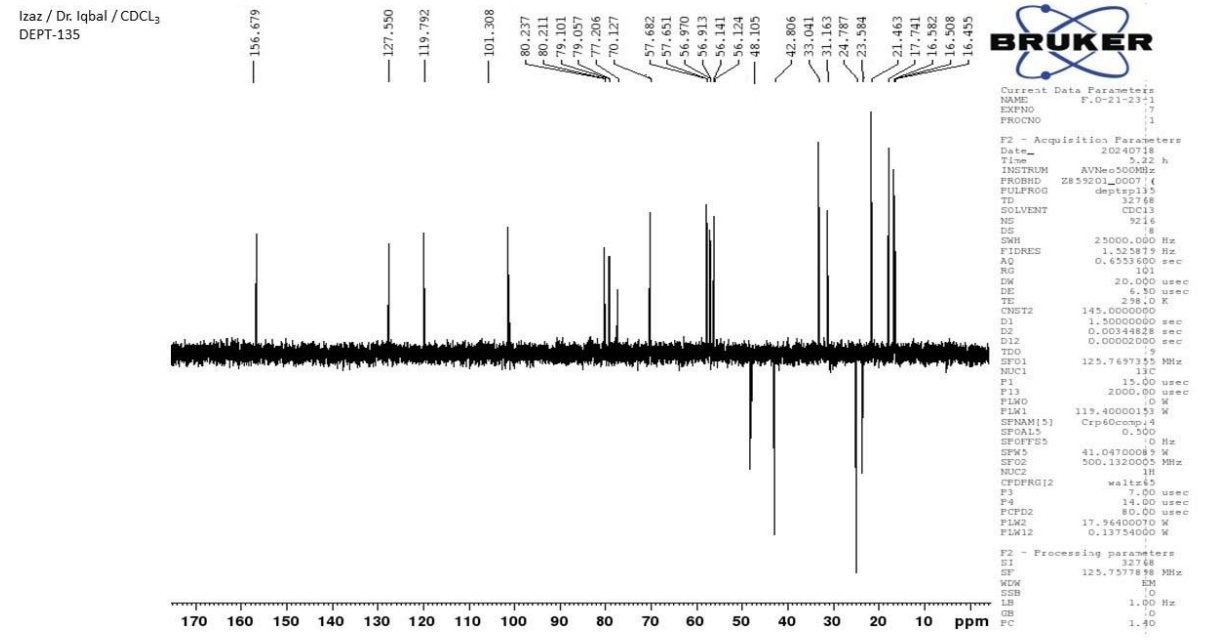


Figure S28 – ^{13}C-NMR (DEPT-135º) Spectrum of metabolite 2

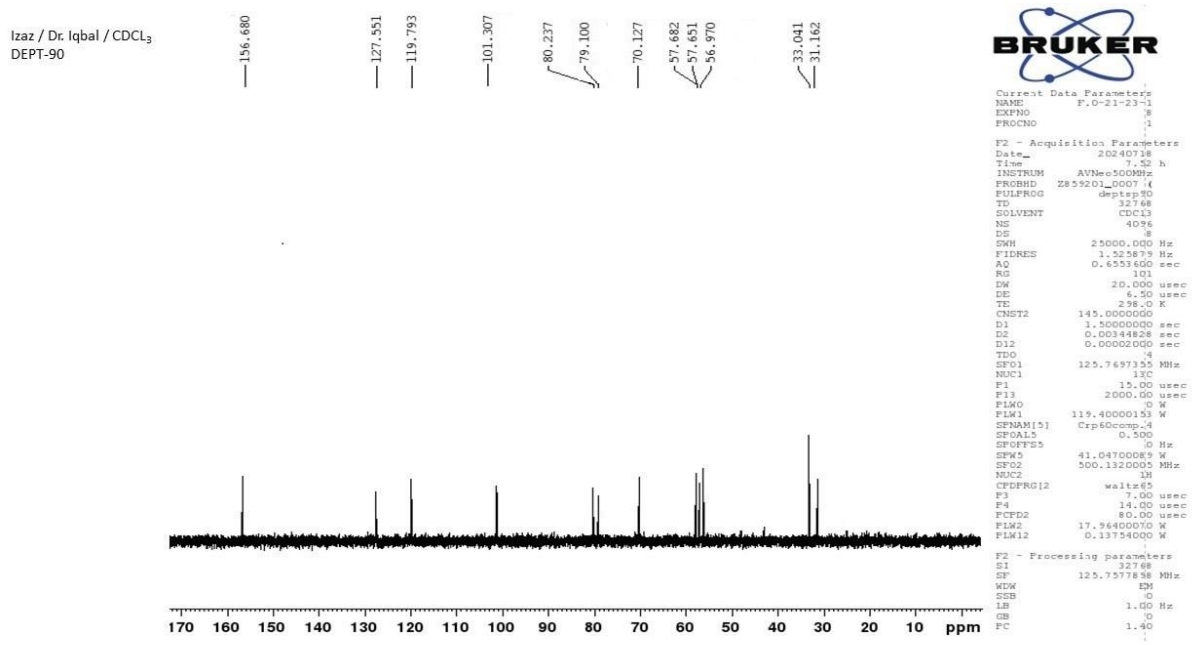


Figure S29 – ^{13}C-NMR (DEPT-90º) Spectrum of metabolite 2

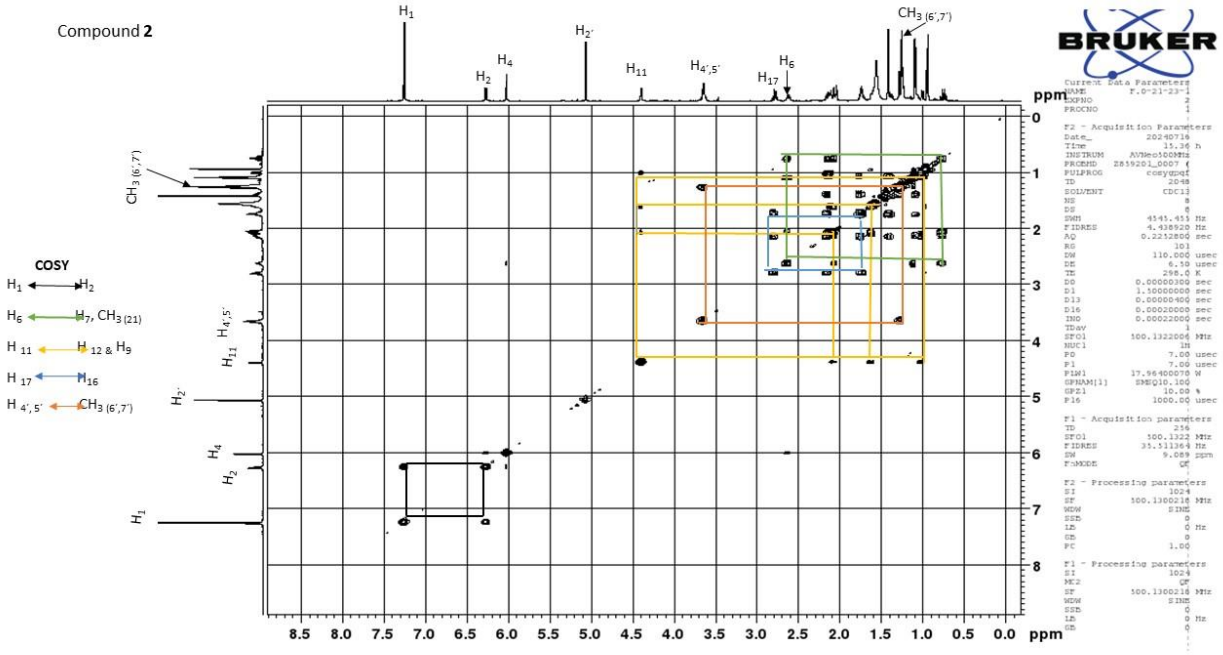


Figure S30 – COSY Spectrum of metabolite 2

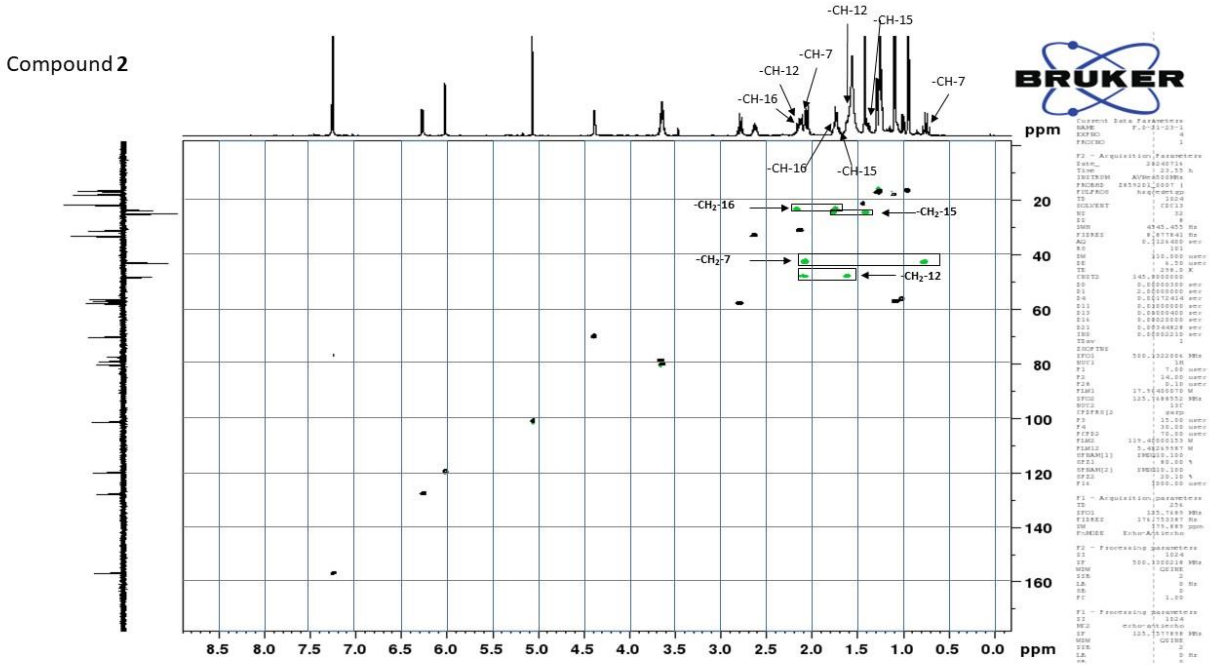


Figure S31 – HSQC Spectrum of metabolite 2

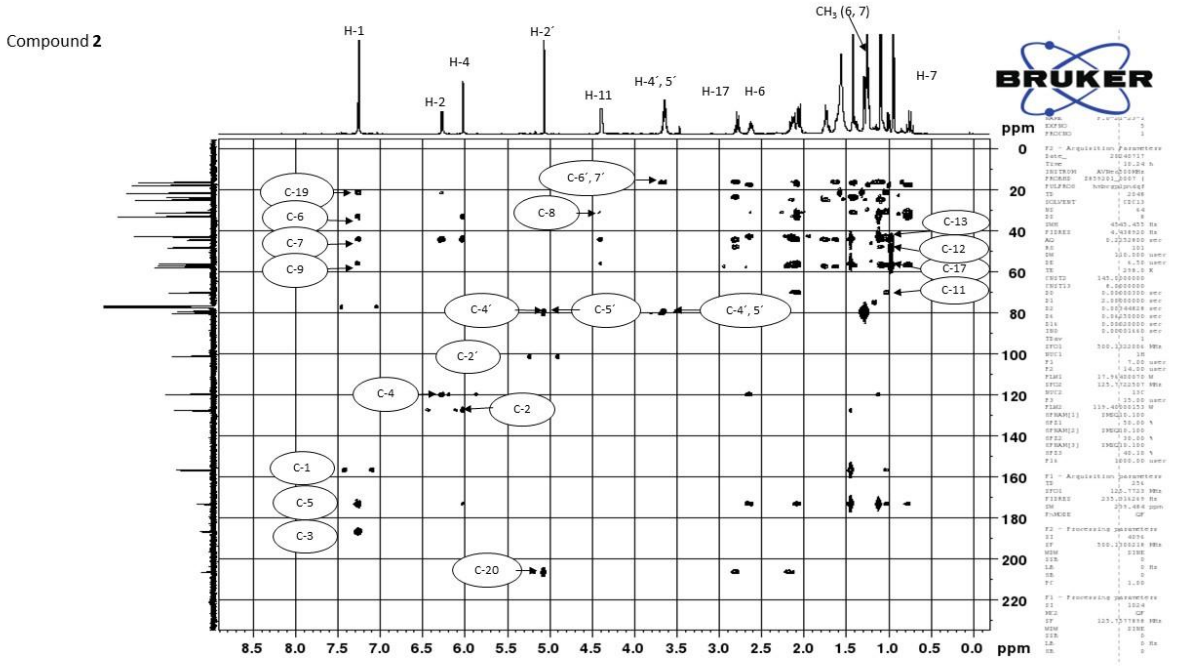


Figure S32 – HMBC Spectrum of metabolite 2

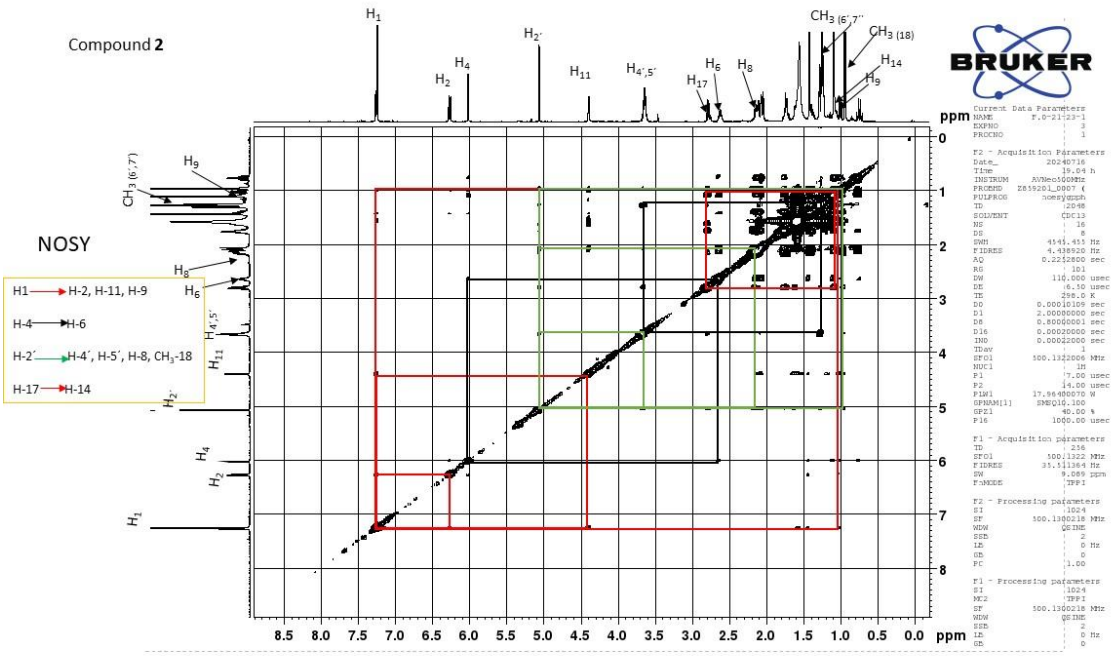


Figure S33 – NOESY Spectrum of metabolite 2

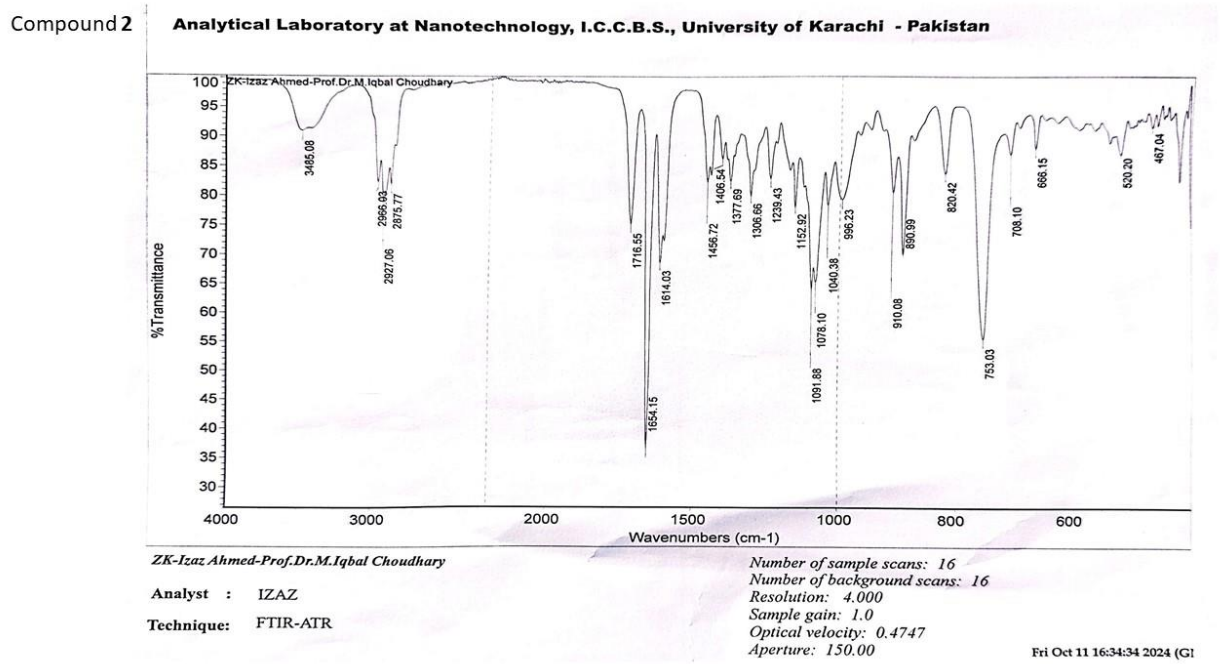


Figure S34 – FT-IR Spectrum of metabolite 2

Compound **2**

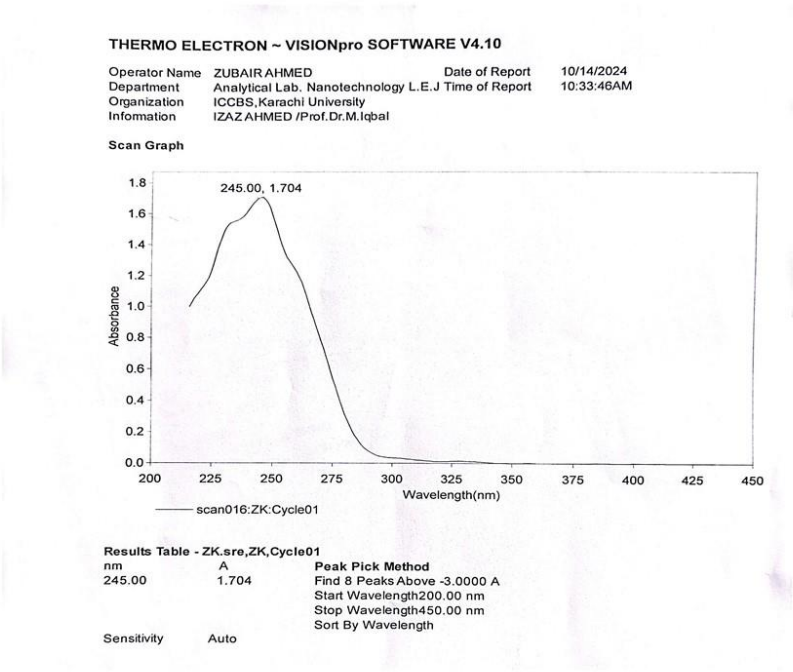
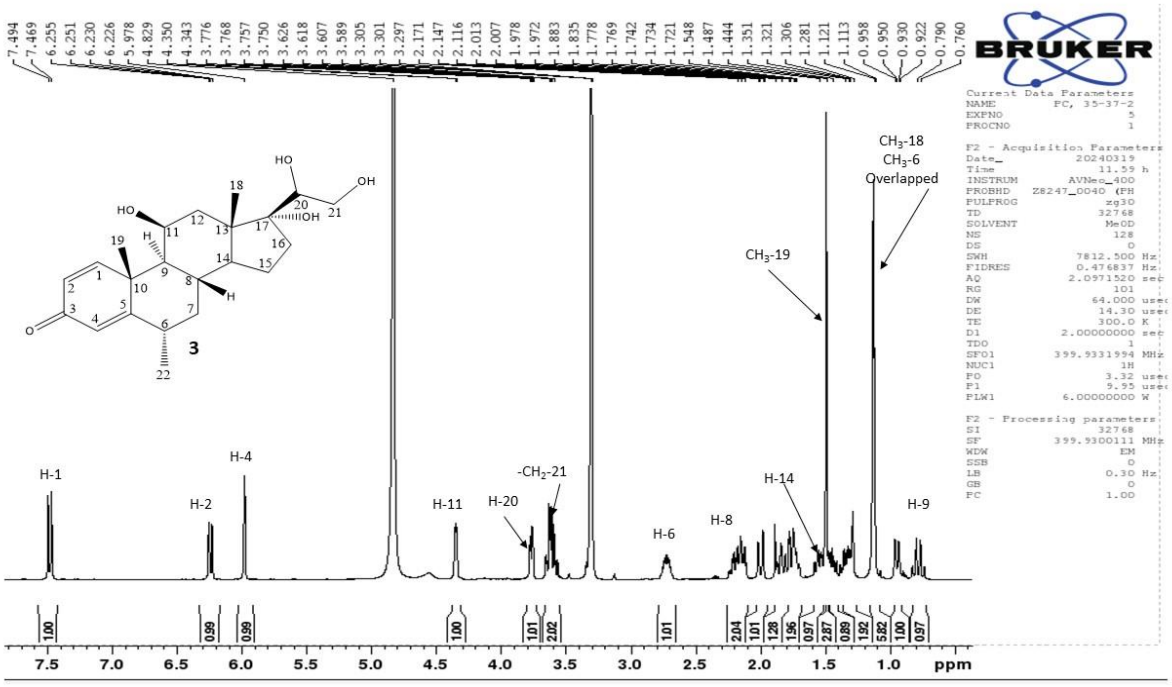


Figure S35 – UV Spectrum of metabolite 2



Compound **3**

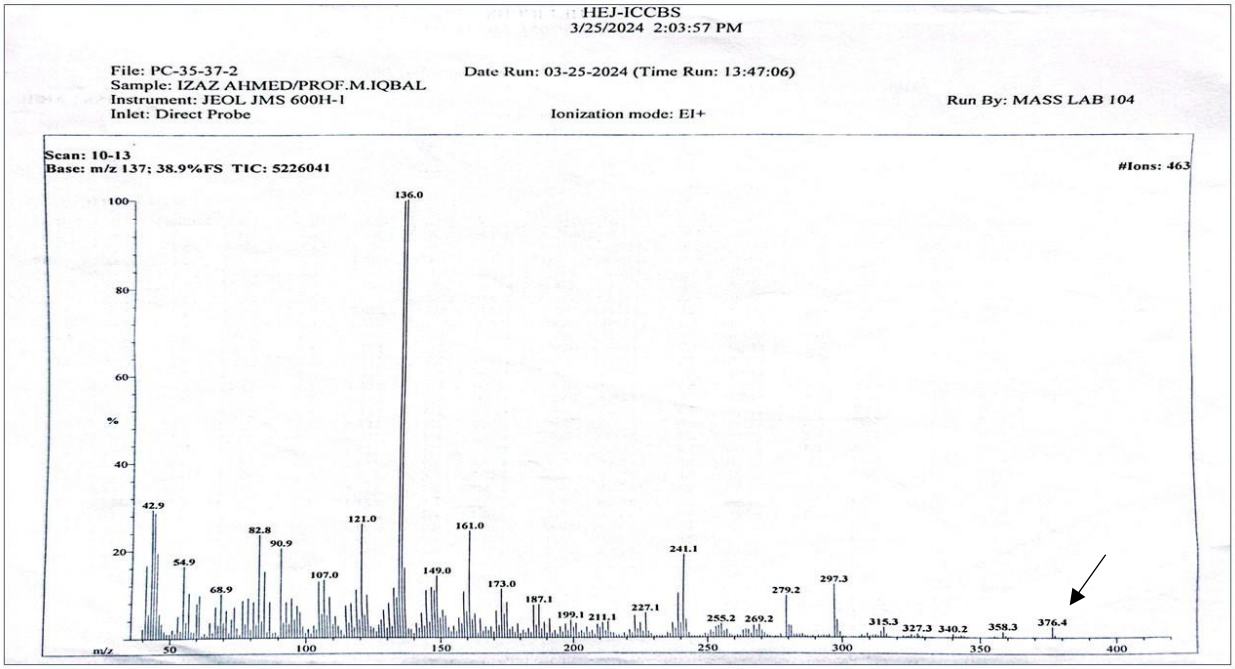


Figure S36 – ^{1}H-NMR, and EI-MS spectra of metabolite 3

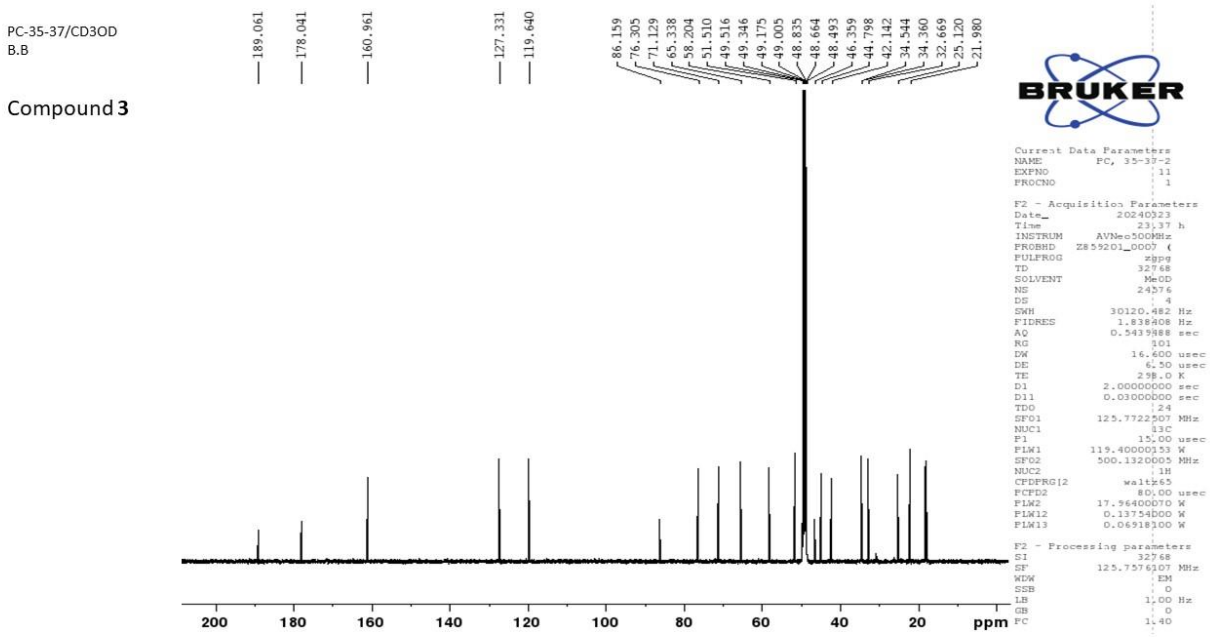
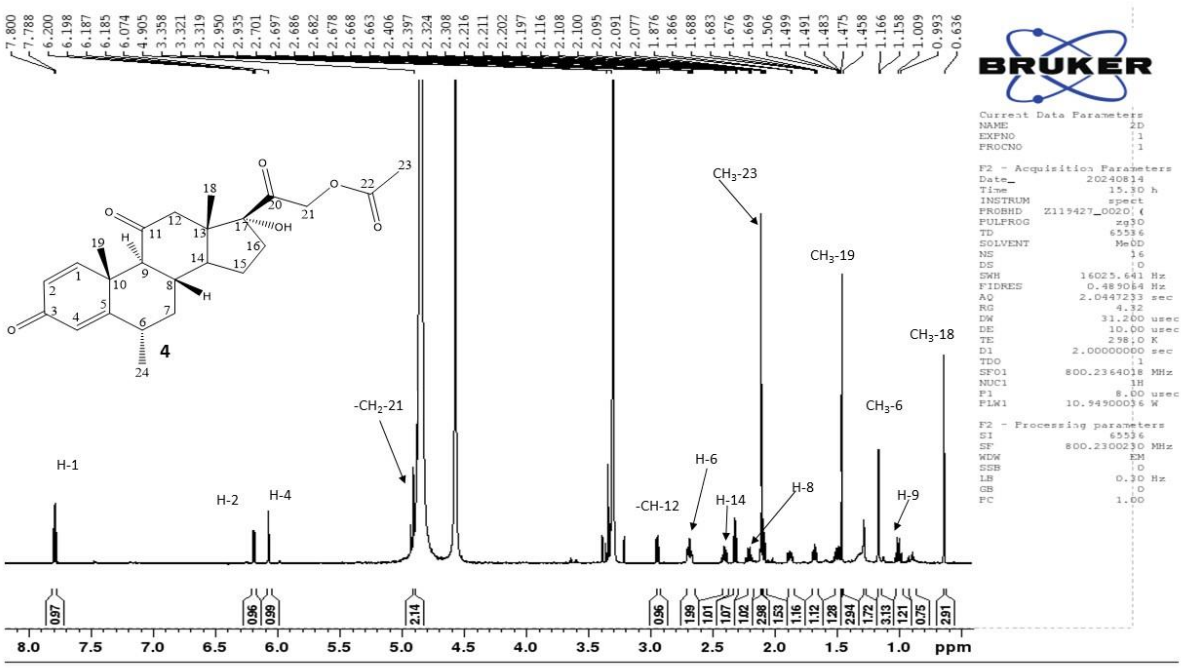


Figure S37 – ^{13}C-NMR (BB) Spectrum of metabolite 3



Compound **4**

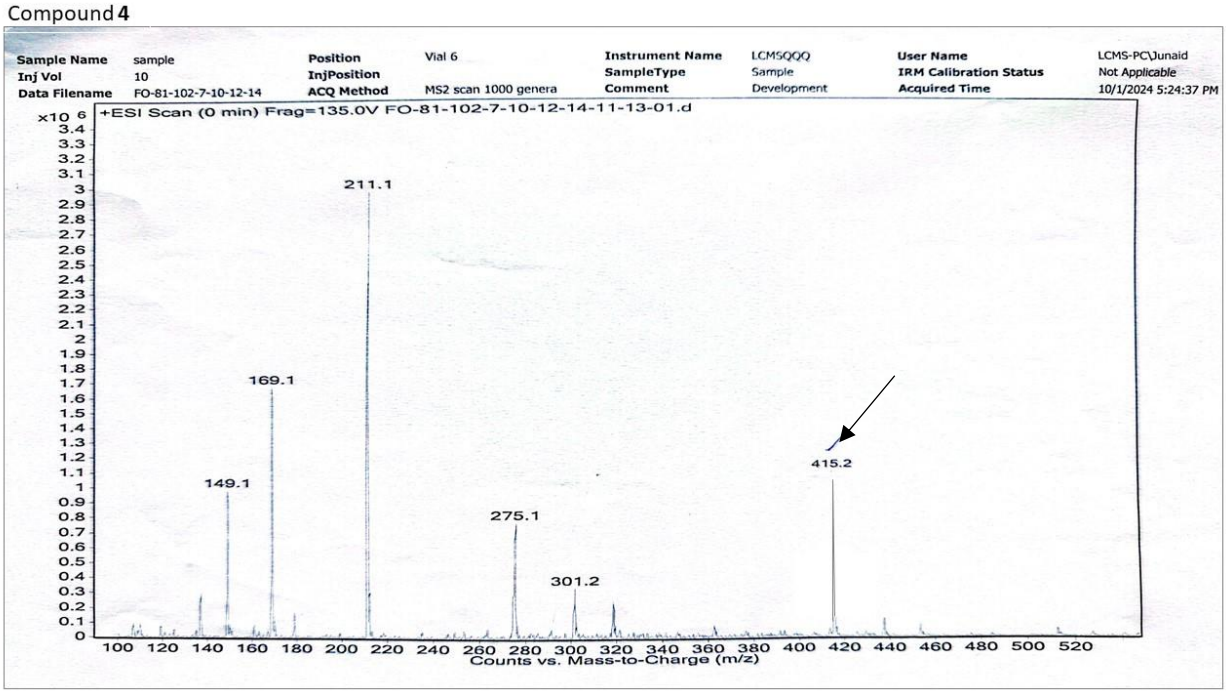


Figure S38 – ^{1}H-NMR, and ESI-MS spectra of metabolite 4

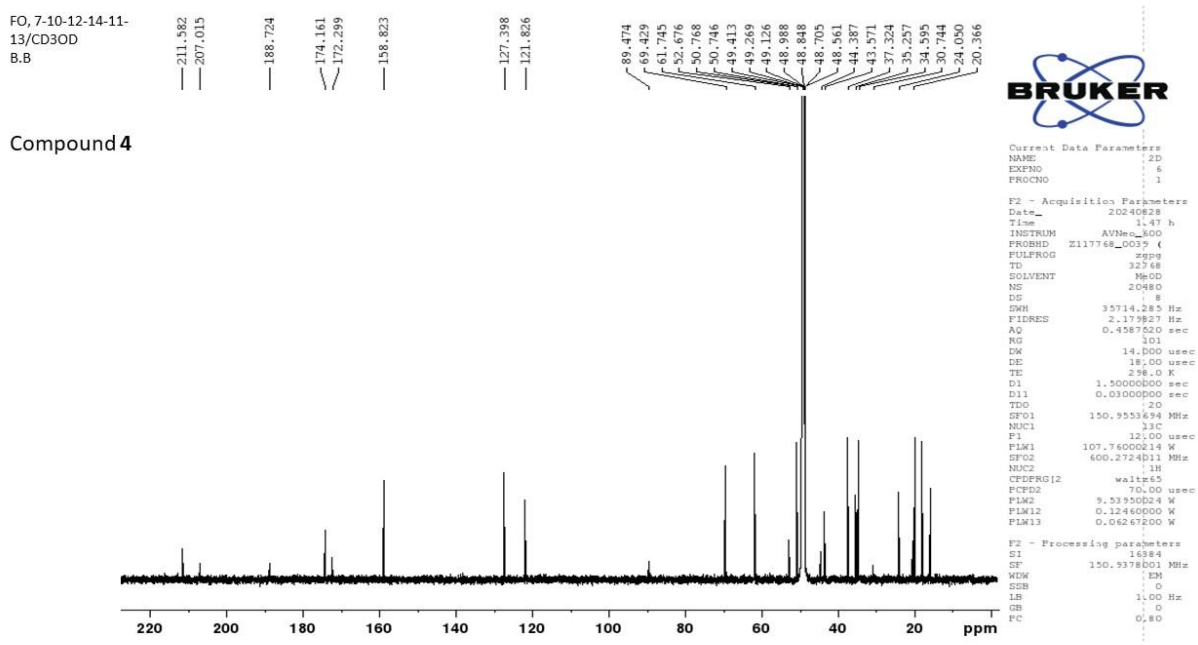
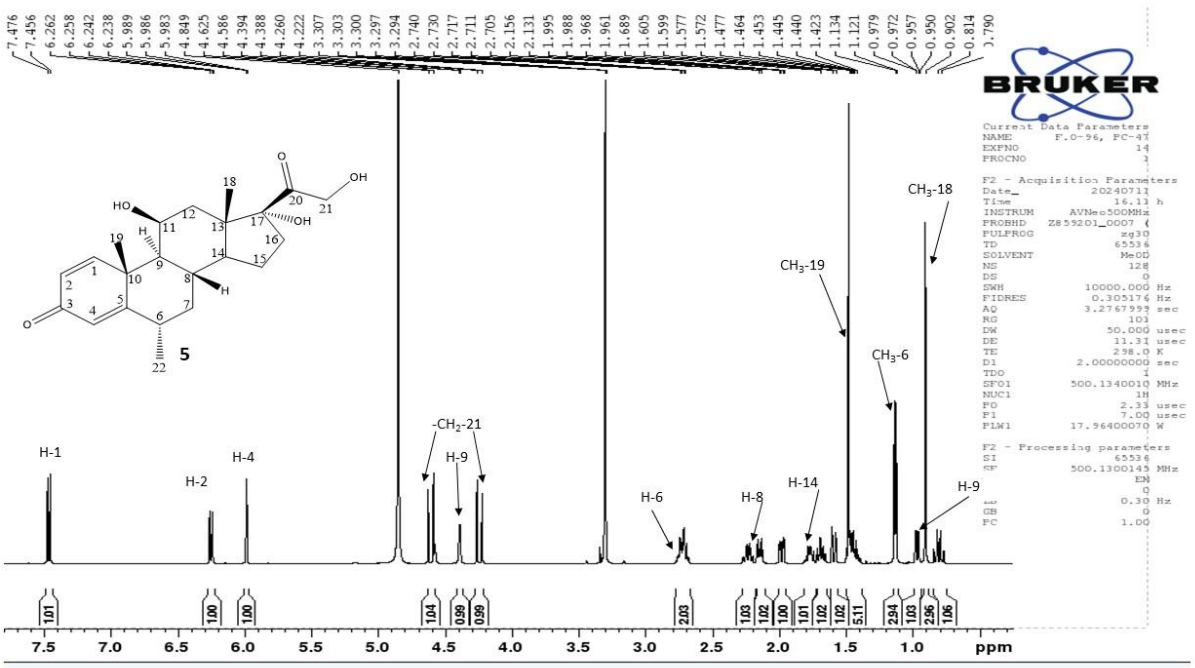


Figure S39 – ^{13}C-NMR (Broad-band decoupled) Spectrum of metabolite 4



Compound **5**

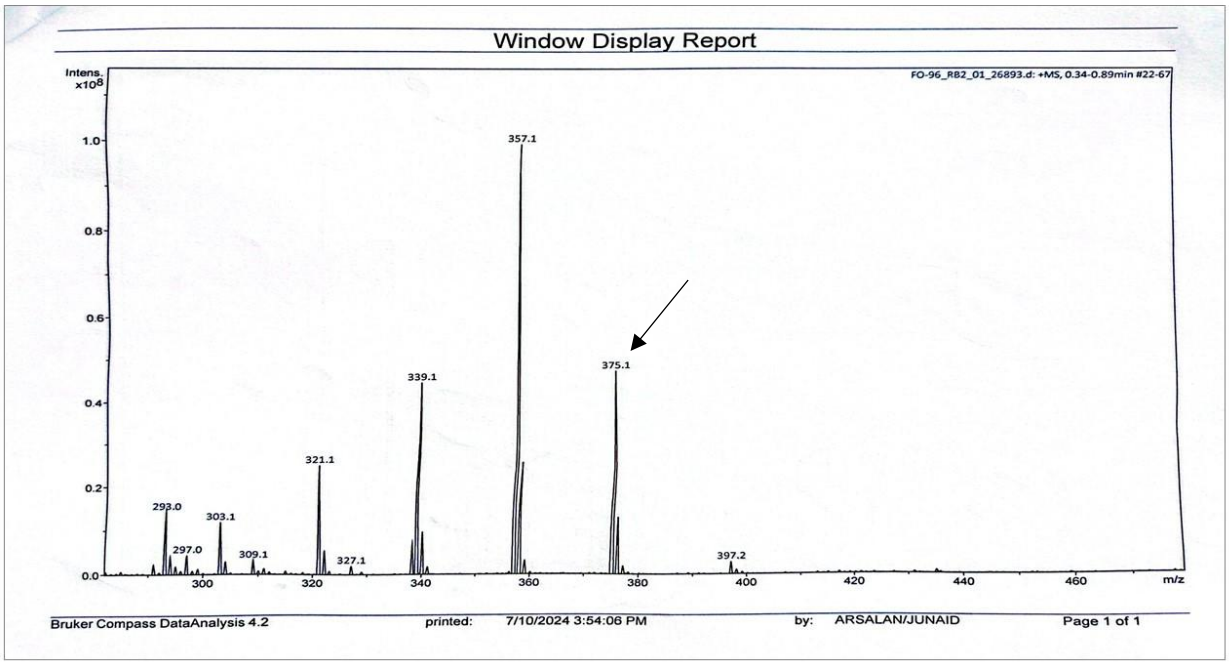


Figure S40 – ^{1}H-NMR, and ESI-MS spectra of metabolite 5

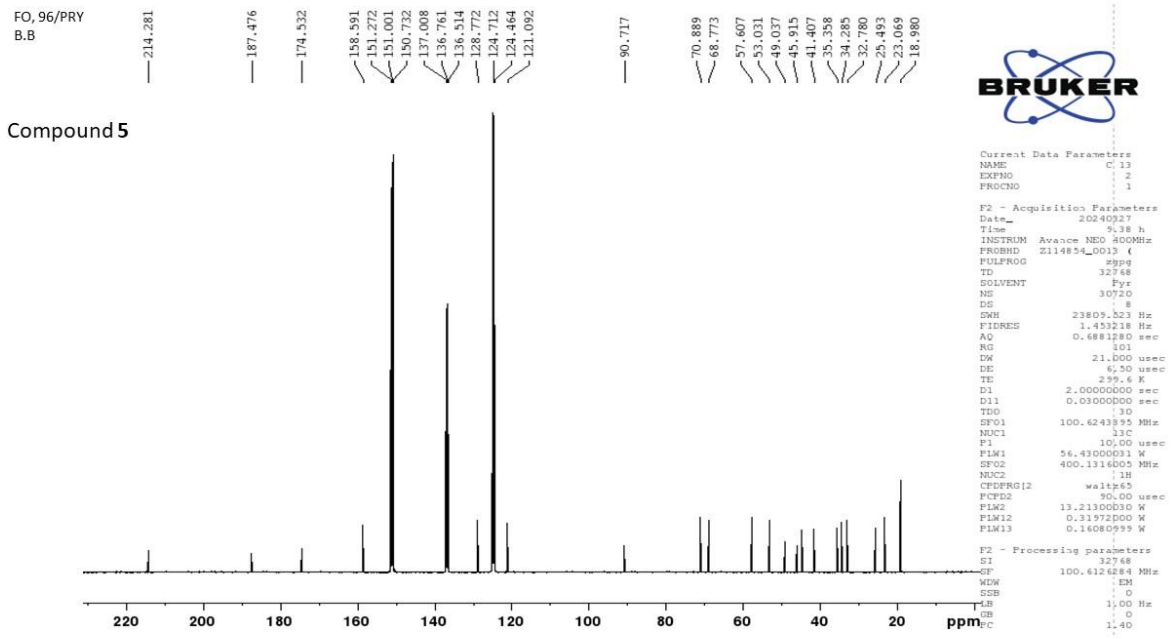
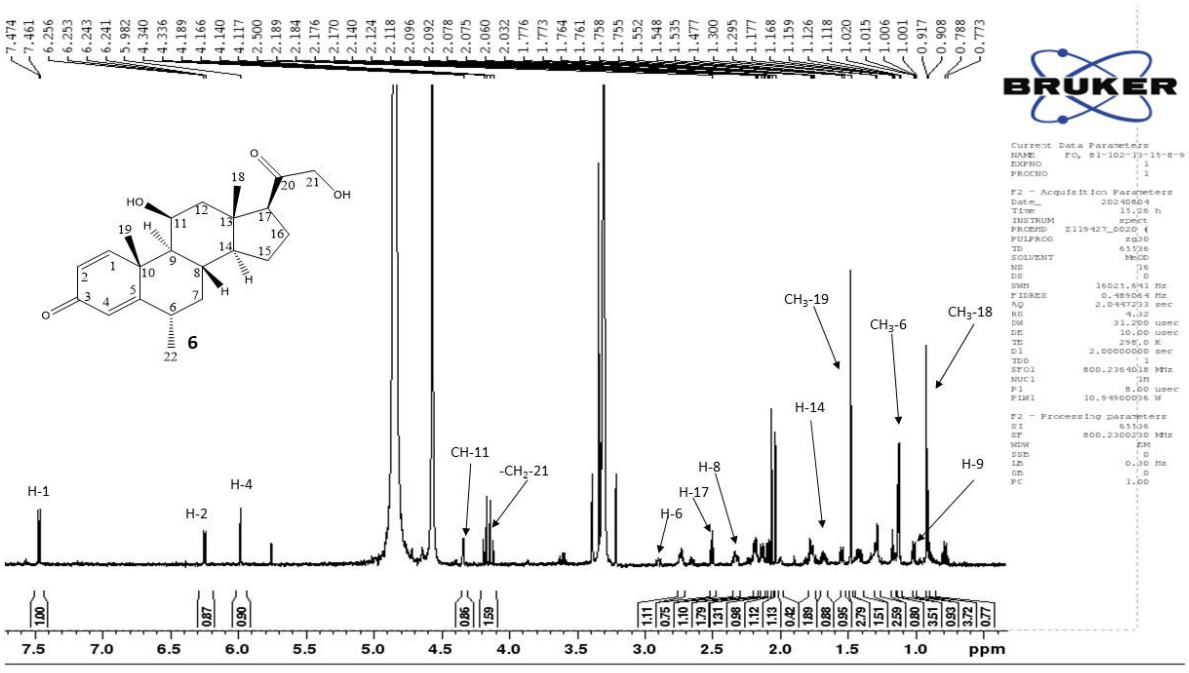


Figure S41 – ^{13}C-NMR (Broad-brand decouple) Spectrum of metabolite 5



Compound **6**

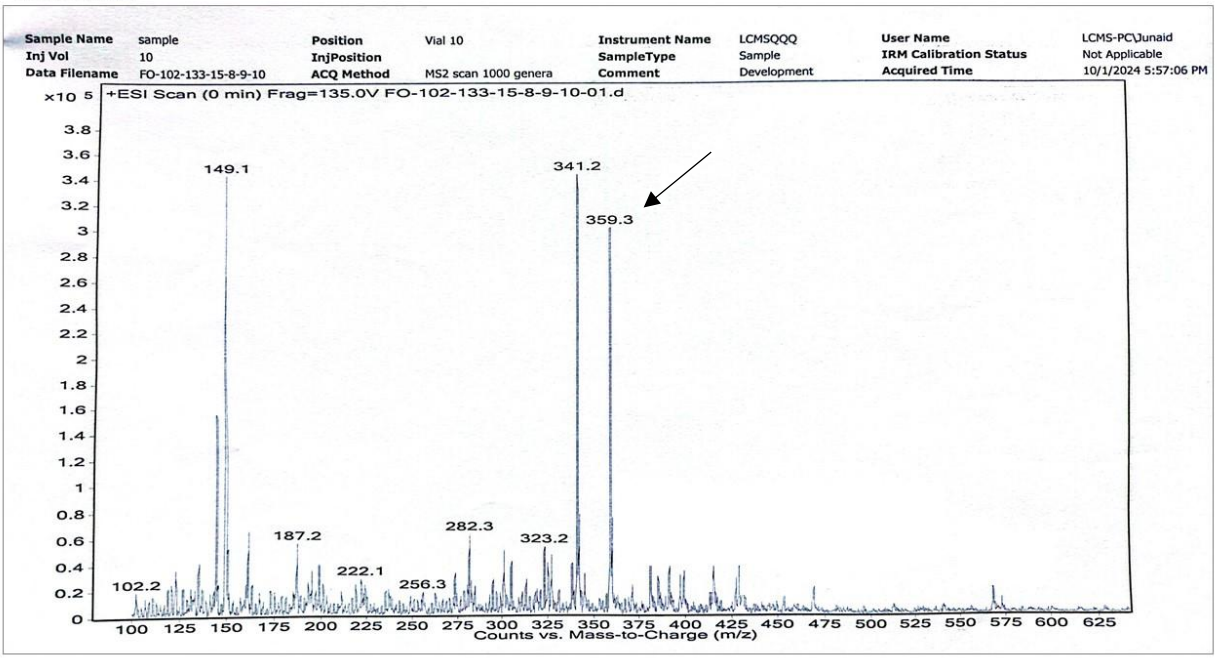


Figure S42 – ^{1}H-NMR, and ESI-MS spectra of metabolite 6

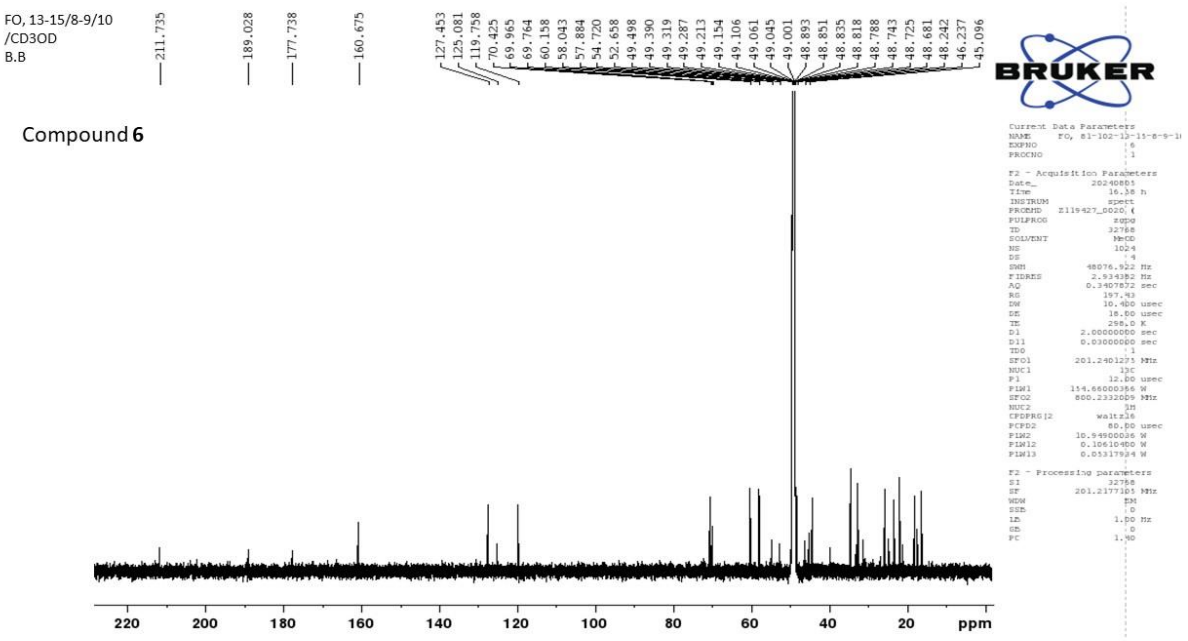
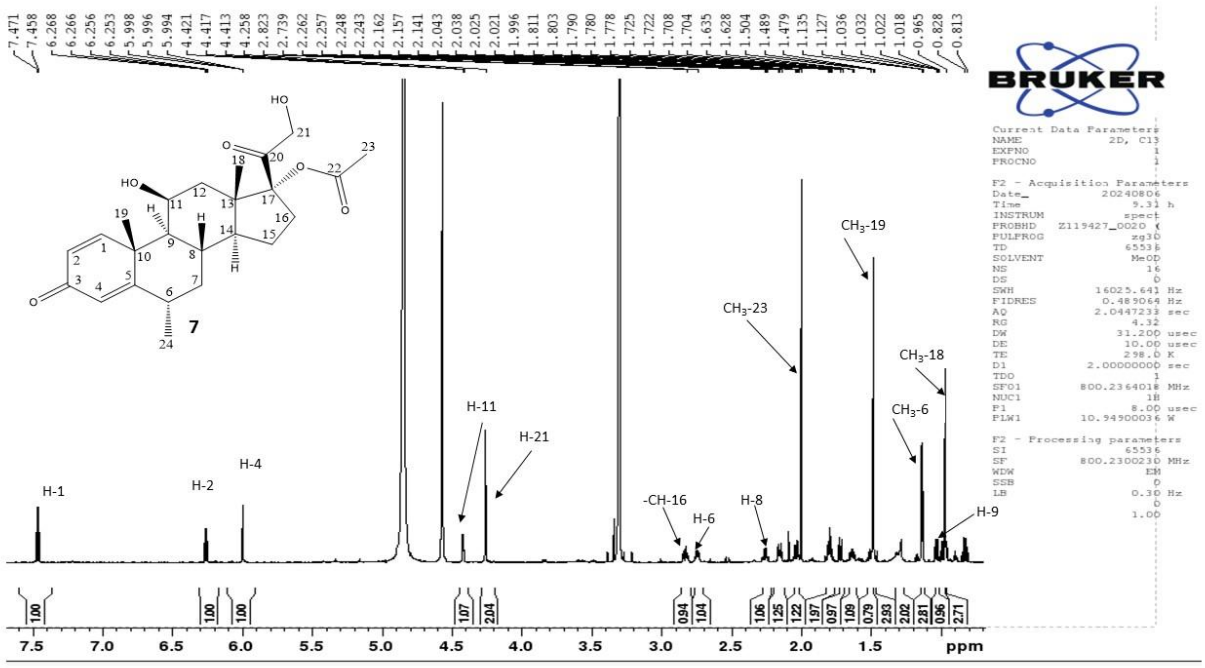


Figure S43 – ^{13}C-NMR (Broad-band decoupled) Spectrum of metabolite 6



Compound **7**

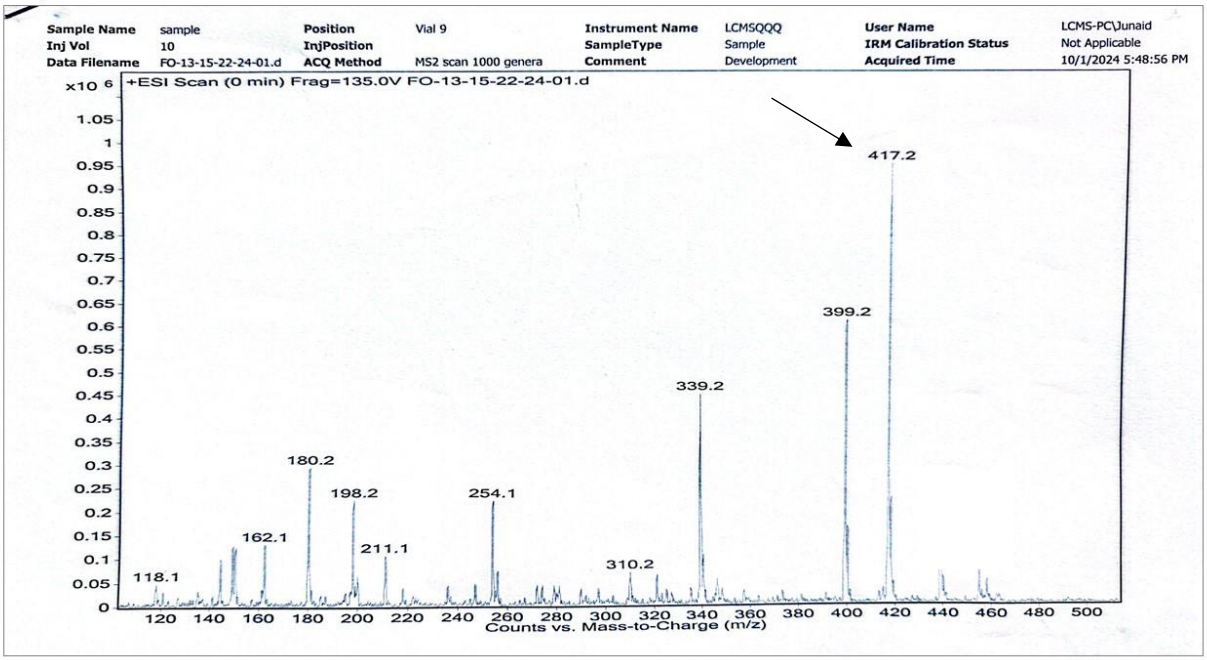
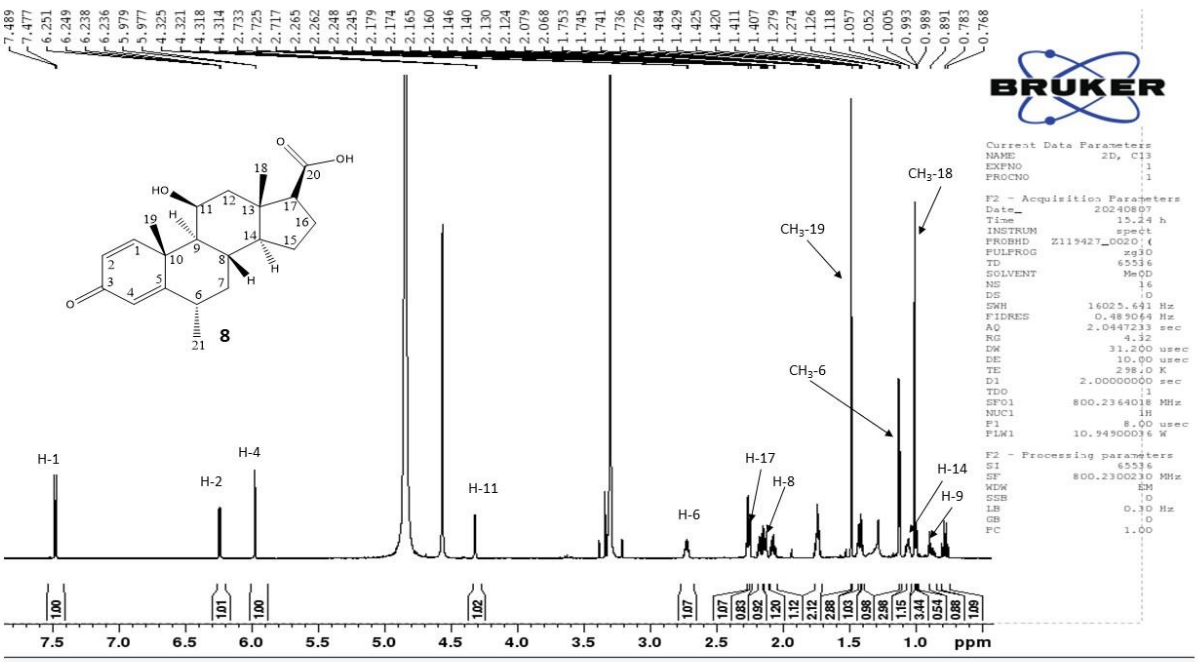


Figure S44 – ^{1}H-NMR, and ESI-MS spectra of metabolite 7



Compound **8**

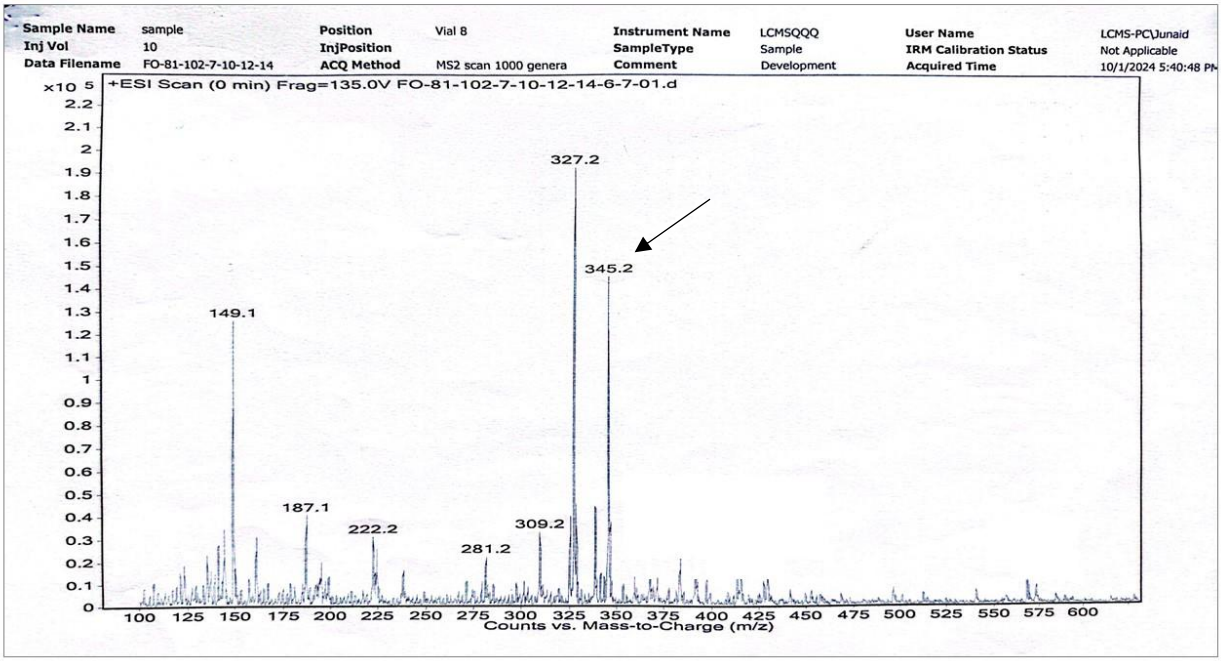
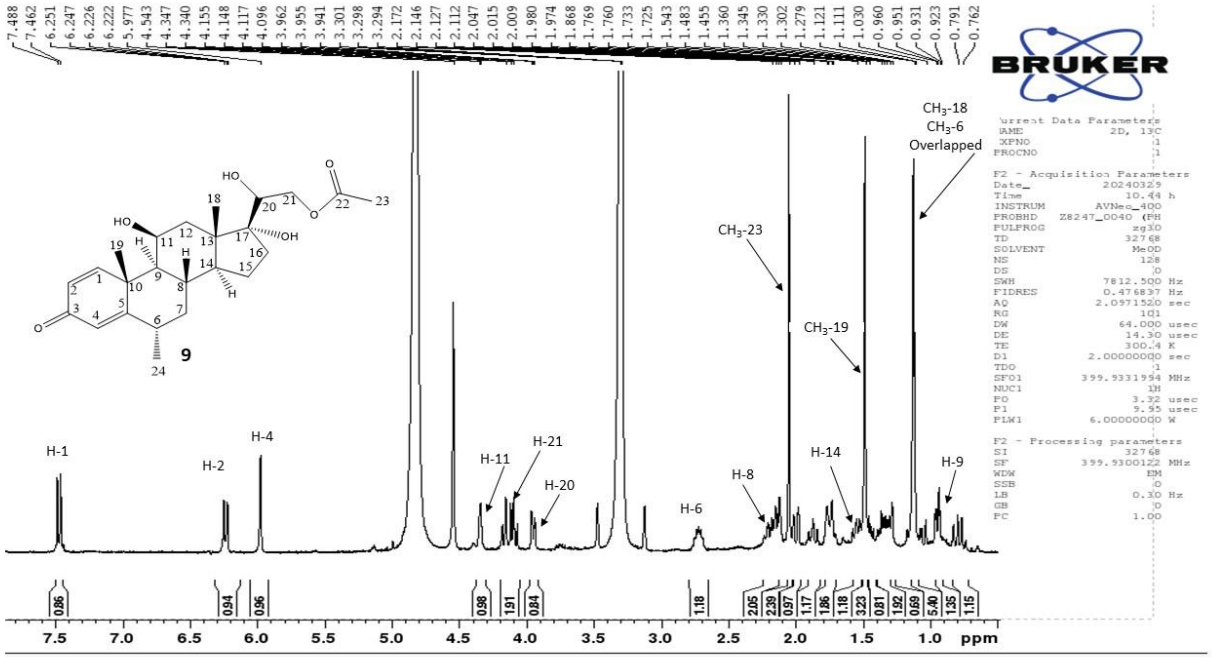


Figure S45 – ^{1}H-NMR, and ESI-MS spectra of metabolite 8



Compound **9**

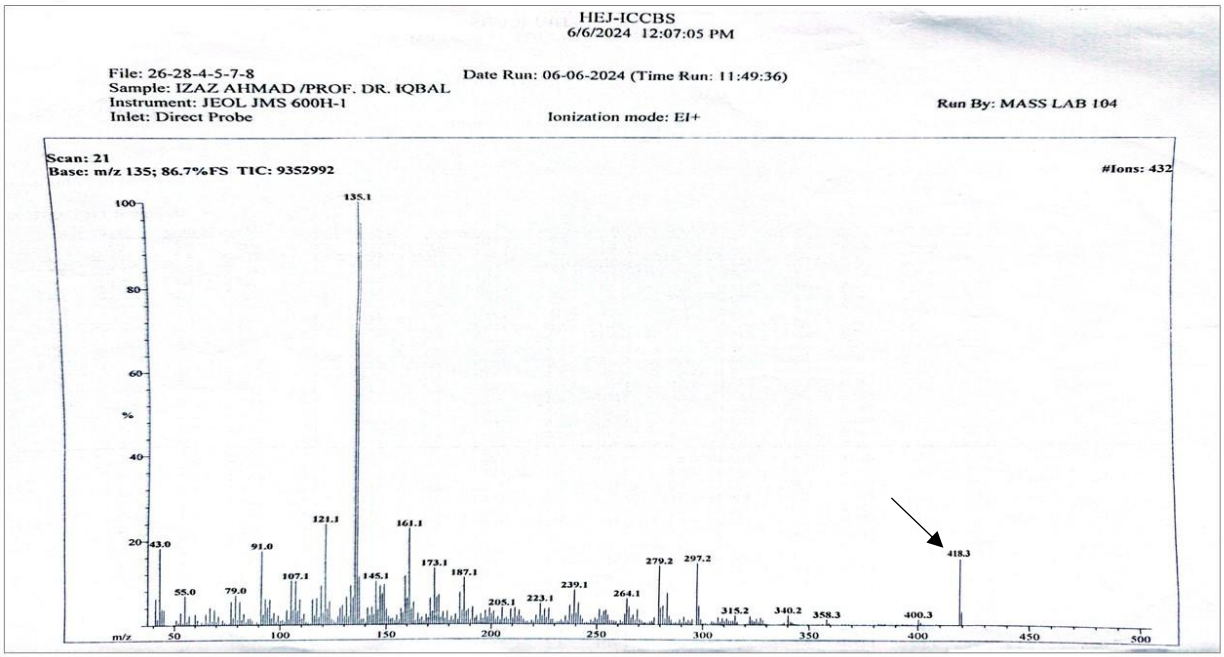


Figure S46 – ^{1}H-NMR, and EI-MS Spectra of metabolite 9

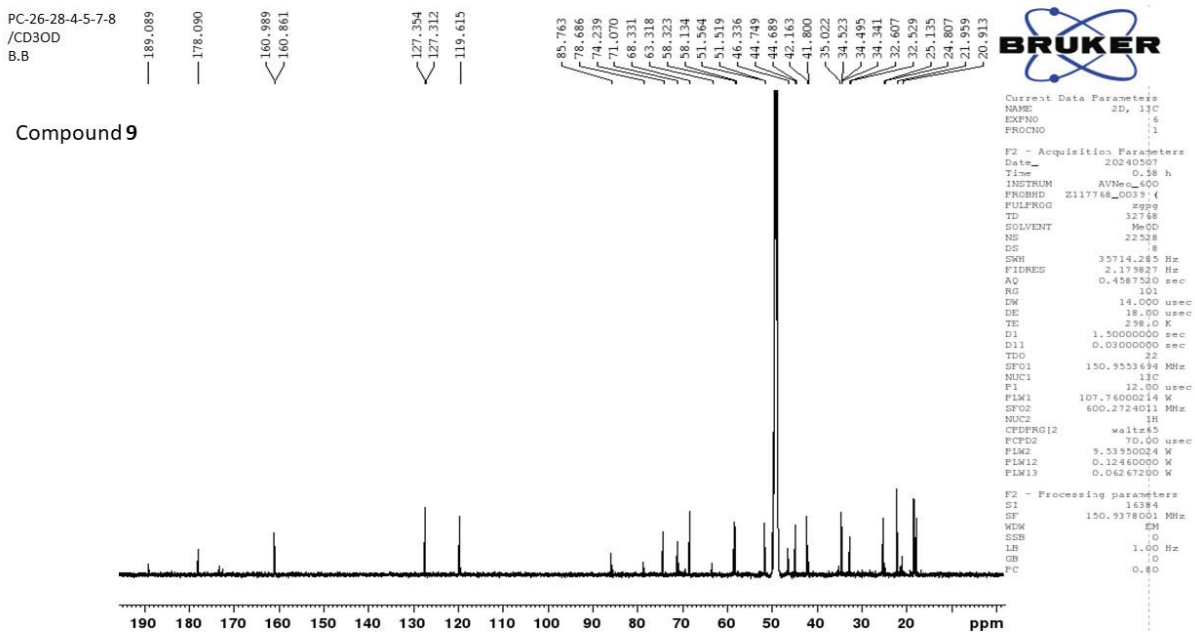


Figure S47 – ^{13}C-NMR (Broad-band decoupled) Spectrum of metabolite 9